A Molecular Toolkit for Immunological Imaging



A thesis submitted for the degree of

Doctor of Philosophy

In Inorganic Chemistry

Grace Tamara McMullon

St. Anne's College

University of Oxford

April 2022

Abstract

“Molecular Toolkit for Immunological Imaging”

Chronic inflammation is prevalent in society with a wide range of inflammatory diseases, such as rheumatoid arthritis and inflammatory bowel disease, as well as association with cancer, strokes, and neurodegenerative conditions. Due to the complexity in the inflammatory pathways and a lack of understanding of those processes, there are limited therapeutic options available that aim to resolve the causes of inflammation, with most treatments instead aiming to manage symptoms. More bespoke imaging agents are required to help advance our understanding of the fundamental processes governing these disease states.

To overcome current imaging limitations such as quantification, correlation, depth penetration and resolution quality, this work takes a multimodal molecular imaging approach to study one type of immune cells, macrophages, that are of particular importance in rheumatoid arthritis. Such methods aim to aid the non-invasive characterisation of disease phenotypes and therapeutic response in inflammatory diseases such as IBD and rheumatoid arthritis.

The general structure of selective imaging probes is an imaging moiety, a targeting group to localise at a specific site and a linker group to attach the two. The work within this thesis focusses on designing a toolkit of imaging probes that target macrophages by using folate and tuftsin derivatives to target receptors with macrophage selective expression. A variety of imaging modalities are explored in this work such as lanthanide luminescence, magnetic resonance and photoacoustic, with the aim to permit the choice of the most appropriate modality required for a given spatial resolution, scale, and depth penetration. In addition, different bioconjugation strategies have been investigated, such as amide linkages and azide-alkyne cycloadditions, to enable access to a wider variety of macrophage imaging agents. By using a toolkit of molecular components that can be easily combined, this work demonstrates preliminary work for luminescent microscopy, magnetic resonance, and photoacoustic imaging to enable the study of macrophage populations in tissue and model systems. Chapter 1 outlines the processes governing inflammation and the current methods of imaging inflammation. It provides a general overview of the different imaging modalities, with a specific focus on lanthanide chemistry and its photophysics, magnetism and stability in relation to its *in vivo* imaging. Moreover, the suitability of the targeting moieties – folate and tuftsin – are discussed and the prior work in these areas.

Chapter 2 outlines the synthesis, paramagnetic NMR spectroscopy and photophysical characterisation of alkyne appended DO3A derivatives. The purpose of these alkynes is for use in bioconjugation to the targeting moieties with an azide functionality for use in CuAAC and SPAAC.

Chapter 3 describes the synthesis of multiple terbium-folate conjugates using solid-phase synthesis, as well as the generation of folate-azides for conjugation to the alkynes discussed in chapter 2. The NMR spectroscopy and photophysical properties of these terbium-folate conjugates are discussed.

Chapter 4 details the synthesis of lanthanide-tuftsin conjugates for use in optical and magnetic resonance imaging. The relaxivity and cell diffusion NMR spectroscopy of the gadolinium complexes were studied in blood plasma and whole blood and was compared to a commercially available non-specific gadolinium complex, DOTAREM.

Chapter 5 discusses the preparation of macrophage-targeted photoacoustic probes and their optical properties. The probes are investigated for their photoacoustic properties and stability.

Chapter 6 provides a summary of work and conclusions that can be drawn, with opportunities for future work proposed.

Finally, chapter 7 contains the experimental procedures.

Acknowledgements

The first thank you must go to Steve who accepted me into his group and managed to make a lot of awkward CDT pieces fit together. You were endlessly reassuring even when I didn't believe you. I would also like to thank my industrial supervisors at GSK: Dr. Phil Murphy and Dr. Pilar Jimenez-Royo, who provided guidance and support to the project to help it navigate a tricky time in history.

I would like to thank all the members of the Faulkner group that I've encountered over the years special thanks goes to Carlson, Agnes, Kezi, Deb, Dani, Tom, Marie, Louis, Laura, Cam and anyone who has kept me company or sane by going for a tea/walk/dinner. Deb and Dani have especially made me into a much better chemist than I was before by answering countless questions and challenging my initially questionable chemistry. Special thanks also goes to Anna Booth, for the collaboration on the challenging work that was folate and Virginia Casablancas-Antras, for the INDIANA collaboration and the encouragement to socialise more and stress less.

I would like to thank Dr. Nick Rees for helping to answer my NMR questions and to the mass spec department, especially Dr. Victor Mikhailov and Dr. John Walsby-Tickle. I would also like to thank the incredibly helpful maintenance team in the CRL, especially Ron, Colin, Jude and John, who have answered many Pemac requests of mine.

Thank you also to our collaborators, past, present, and future: Prof. Andrew Baldwin and Dr. Gogulan Karunanithy for INDIANA; Dr. Anant Shah and Dr. Aoife Ivory of NPL for photoacoustic measurements; and Prof. Conny van der Laken, Dr. Gerrit Jansen and Aiarpi Ezgolian for folate cell studies.

Finally, I would like to thank my family, my Mum and Dad, Naomi, Rory and Hannah. Our family is looking quite different to how I began the PhD, but I am grateful for all your love and encouragement to get this far. I reckon the grandparents would be quite chuffed there was a doctor in the family.

My deepest thanks go to my husband, Josh who has always loved and supported me throughout my PhD. It probably wasn't our brightest idea to do simultaneous PhDs, but I hope the future will be substantially easier than our first four years of marriage.

Finally, the glory deserves to be given to my God, the rock on whom I depend.

"Yes, my soul finds rest in God; My hope comes from him.

Truly he is my rock and my salvation;He is my fortress, I will not be shaken."

Psalm 62 v 5-6

Contents

Abstract ..... **i**

Acknowledgements ..... **iii**

Contents ..... **iv**

Abbreviations ..... **viii**

1 Introduction **14**

1.1 Inflammation 14

1.1.1 Overview of the inflammatory response 15

1.1.2 Imaging inflammation 16

1.2 Imaging modalities 19

1.2.1 Optical 19

1.2.2 MRI/NMR 19

1.2.3 Photoacoustic imaging 22

1.3 Lanthanide chemistry 23

1.3.1 Lanthanide Photophysics 24

1.3.2 Mechanisms of Energy transfer 26

1.3.3 Lanthanide luminescence quenching 27

1.3.4 Isomerism 28

1.4 Bioconjugation 30

1.4.1 Bioorthogonal reactions 31

1.4.2 Folate 32

1.4.3 Tuftsin 35

1.5 Aims and Objectives 36

1.6 References 39

2 Ligands for azide-alkyne cycloadditions **48**

2.1 Introduction 48

2.2 Synthesis of alkyne complexes 49

2.2.1 Alkynes for copper-catalysed click chemistry, L^1 and L^2 49

2.2.2 Alkynes for strain-promoted click chemistry 51

2.2.3 Synthesis of ligand, L^3 51
2.2.4 Synthesis of ligand, L^4 55
2.2.5 Scope of the probes 58
2.3 Characterisation of the complexes 58
2.3.1 Paramagnetic ^{1}H NMR spectroscopy 58
2.3.2 Photophysical properties 61
2.4 Conclusions 65
2.5 References 66
3 Folate-derived luminescent probes 68
3.1 Introduction 68
3.2 Synthetic approaches 69
3.2.1 Initial Approach: Ethylene-diamine linker 69
3.2.2 Solid-phase synthesis approach 71
3.2.3 Click chemistry: FA-$(PEG)_n$-azide 76
3.3 Paramagnetic ^{1}H NMR spectroscopy 80
3.4 Photophysical characterisation 82
3.4.1 UV-Visible spectroscopy 82
3.4.2 Fluorescence and Phosphorescence emission 82
3.4.3 Lifetimes and q values 84
3.5 Conclusion 85
3.6 References 86
4 Tuftsin-derived imaging agents 88
4.1 Introduction 88
4.1.1 INDIANA 88
4.1.2 Design of tuftsin-labelled probes 88
4.2 Synthesis of complexes 89
4.3 Characterisation of the complexes 91
4.3.1 Paramagnetic ^{1}H NMR spectroscopy 91
4.3.2 Photophysical characterisation 93

4.3.3 ^{1}H Relaxivity 98
4.4 NMR techniques 100
4.4.1 INDIANA 100
4.4.2 diffCEST 105
4.5 Conclusions 106
4.6 References 108
5 Macrophage targeted photoacoustic contrast agents 110
5.1 Introduction 110
5.1.1 Principles of PA imaging 110
5.1.2 Design of a macrophage-targeted PA contrast agent 113
5.2 Synthesis 115
5.2.1 Synthesis of the heptamethine cyanine dye 115
5.2.2 Synthesis of the macrophage binding moieties 117
5.2.3 Scope of probes 120
5.3 Photophysical characterisation 120
5.3.1 Photophysical properties 120
5.3.2 Photostability 122
5.4 Photoacoustic characterisation 122
5.4.1 Pre-clinical iThera photoacoustic imaging 122
5.4.2 Optimal transmit parameters 123
5.4.3 Linearity 125
5.4.4 Sensitivity of the PA probes 125
5.4.5 Photostability 126
5.5 Conclusions 127
5.6 References 129
6 Conclusions 132
7 Experimental Procedures 135
7.1 General Procedures 135
7.2 References 182

A. Appendix - HPLC conditions 184

Abbreviations

aq.	aqueous
BODIPY	boron-dipyrromethene/4,4-difluoro-4-bora-3a,4a-diaza-s-indacene
CEST	chemical exchange saturation transfer
CHO	chinese hamster ovary cells
COSY	correlation spectroscopy
COX	cyclooxygenase
cyclen	1,4,7,10-tetraazacyclododecane
CuAAC	copper-catalysed azide alkyne cycloaddition
DBCO	dibenzocyclooctyne
DCC	*N,N'*-dicyclohexylcarbodiimide
DCM	dichloromethane
DI	deionised
DIC	*N,N'*-diisopropylcarbodiimide
DIPEA	*N,N*-diisopropylethylamine
DMF	*N,N*-dimethylformamide
DMSO	dimethyl sulfoxide
DO3A	1,4,7,10-tetraazacyclododecane-1,4,7-triacetic acid
DOTA	1,4,7,10-tetraazacyclododecane-1,4,7,10-tetraacetic acid
ESMS	electrospray mass spectrometry
EtOAc	ethyl acetate
EtOH	ethanol
FA	folic acid
FDA	United States food and drug administration
FITC	fluorescein isothiocyanate
FLIM	fluorescence-lifetime imaging microscopy
Fmoc	9-fluorenylmethoxycarbonyl
FPR	formyl peptide receptor
FR	folate receptor
GBCA	gadolinium-based contrast agent
GPI	glycosylphosphatidylinositol
HATU	1-[bis(dimethylamino)methylene]-1*H*-1,2,3-triazolo[4,5-*b*]pyridinium 3-oxide hexafluorophosphate
HMBC	heteronuclear multiple bond correlation
HOBt	1-hydroxybenzotriazole
HPLC	high-performance liquid chromatography

HRMS	high resolution mass spectrometry
HSQC	heteronuclear single quantum coherence
IC_{50}	half maximal inhibitory concentration
ICG	indocyanine green
IgG	immunoglobulin G
IL	interleukin
INDIANA	in cell diffusion analysis
i-PrOH	*iso*-propanol/propan-2-ol
ISC	intersystem crossing
LCMS	liquid chromatography – mass spectrometry
Ln	lanthanide
MALDI	matrix-assisted laser desorption/ionisation
MeCN	acetonitrile
MeOH	methanol
MMP	matrix metalloproteins
MR	mannose receptor
MRI	magnetic resonance imaging
MS	mass spectrometry
MSOT	multispectral optoacoustic tomography
MWCO	molecular weight cut-off
NaOH	sodium hydroxide
NHS	*N*-hydroxysuccinimide
NIR	near-infrared
NMR	nuclear magnetic resonance
NSF	nephrogenic systemic fibrosis
OD	optical density
PA	photoacoustic
PAI	photoacoustic imaging
PET	positron emission tomography
Pbf	2,2,4,6,7-pentamethyl-dihydro-benzofuran-5-sulfonyl
PBS	phosphate buffered saline
PCFT	proton coupled folate transporter
PEG	polyethylene glycol
PET	positron emission tomography
R_f	retention factor
RFC	reduced folate carrier

RF	radiofrequency
RP-HPLC	reverse-phase high-performance liquid chromatography
SAP	square antiprism
SPAAC	strain-promoted azide-alkyne cycloaddition
SPECT	single-photon emission computerised tomography
SWNT	single-walled nanotubes
TAM	tumour associated macrophage
*t*Bu	*tert*-butyl
TBTU	2-(1H-benzotriazole-1-yl)-1,1,3,3-tetramethylaminium tetrafluoroborate
TEA	triethylamine
TFA	trifluoroacetic acid
THPTA	tris(3-hydroxypropyltriazolylmethyl)amine
TIPS	triisopropylsilane
TLC	thin layer chromatography
TLRs	toll-like receptors
τ_m	water residence time
t_R	retention time
Triester	1,4,7-tris(tert-butoxycarbonylmethyl)-1,4,7,10-tetraazacyclododecane hydrobromide salt
TSAP	twisted square antiprism
TSPO	translocator proteins
UV	ultraviolet
WBC	white blood cell

1 Introduction

Molecular imaging has the potential to become a widely applied platform to study drug properties *in vivo* and mechanistic measures of pharmacology. However, despite the emergence of new measurement methods (e.g. clinical optical) and a wide range of molecular probes, there remains a reliance upon well-established tracers (e.g. [^{18}F]-fluorodeoxyglucose-PET). These do not address the demands of disciplines such as immunology where better tools are needed to study the behaviour of inflammatory cells *in vivo*, with a view to understanding disease and developing effective therapeutics.

Addressing these dichotomous demands remains a challenge: whole-body measurements are needed in addition to high spatial resolution in disease relevant tissue areas; high specificity to a target is required in addition to high detection sensitivity. This can only be addressed with a multi-modal approach that combines the primary benefits of each method within a single experiment. While some of this may potentially be achieved using label-free measurements (e.g. 2-photon fluorescence of NADH) only probe-based approaches are likely to provide the necessary specificity required for imaging cells and a broad range of molecular processes.

Photoacoustic imaging is an emerging technique that has potential to provide molecular specificity at tissue depths not accessible through optical techniques. However, imaging probes for photoacoustic imaging remain limited and new probes are required. Furthermore, multimodal approaches will enable the potential of photoacoustic imaging to be evaluated by comparison with whole body readouts. This will be achieved by developing a series of probe molecules that are specific to macrophages and able to report through measurement platforms across scales (e.g. localised measurements with optical, whole body with MR and bridging between those scales through photoacoustic techniques).

Given the broad imaging methods, it is necessary to outline a basic scaffold for the molecules developed. Typically, imaging probes comprise of a target moiety - such as a peptide, oligosaccharide or small organic molecule that will bind to a receptor on the cell surface, be internalised into the cell or merge into the lipid bilayer - that is covalently linked to a component that will produce a signal.[1]

1.1 Inflammation

Inflammation is known to play a central role in a broad range of disease state progressions including cancer,[2] diabetes, cardiovascular disease and neuroinflammatory diseases such as multiple sclerosis and Alzheimer's disease,[3] in addition to the more commonly associated inflammatory conditions such as rheumatoid arthritis, osteoarthritis, ulcerative colitis, Crohn's disease, gout,

psoriasis and asthma. Inflammation is pivotal in many disease conditions and to improve our understanding and therapeutic options it is necessary to develop imaging probes that will help to visualise the different stages in the inflammatory response.

1.1.1 Overview of the inflammatory response

Inflammation is a cascade of responses that are triggered in the body as defence against harmful stimuli (pathogen, physical and chemical agents) that cause damage to tissues (Figure 1.1).[4] The primary aim of the inflammation is to restore the system to homeostasis and has most likely evolved as an adaptive response.[5] When applied as a controlled response, inflammation is considered to be beneficial to the individual at providing protection against harmful stimuli; however dysregulation (i.e. abnormality) of inflammatory pathways can have detrimental results.[5]

Acute inflammation is the body's rapid response to eliminate a pathogen or noxious compound followed by a reduction in the number of leukocytes, repair of tissue damage and restoration of tissue function.[4] Meanwhile, chronic inflammation is a prolonged response and can arise from a persistent antigenic stimulus, such as a resistant infectious organism that evaded the host's acute inflammatory response (e.g. *Mycobacterium tuberculosis*); autoimmune disorders where the body incorrectly recognises healthy tissue as foreign (e.g. rheumatoid arthritis); or exposure to irritants that are unable to be removed from the body (e.g. silica dust or asbestos). The cell populations differ for acute and chronic inflammation, with sites of acute inflammation being characterised by large quantities of neutrophils and activated helper T cells,[4] while higher proportions of macrophages, cytotoxic T cells and B cells are found in sites experiencing prolonged chronic inflammation.[4]

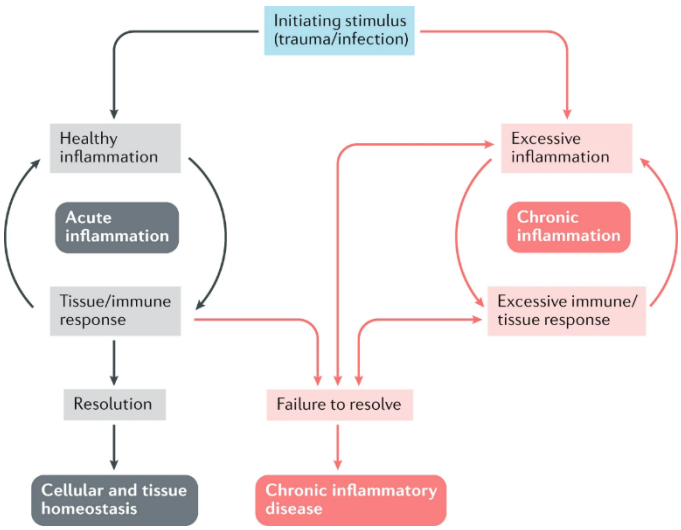


Figure 1.1. Pathways to acute versus chronic inflammation. Reprinted with permission from Nat. Rev. Rheumatol., 2020, 16, 496-513.[6] Copyright 2020 Springer Nature.

A simplified pathway of a bacterial infection involves detection of the pathogen by receptors of the innate immune system such as toll-like receptors (TLRs) expressed on macrophages that reside in the tissue.[7] This induces the production and release of inflammatory chemical mediators by tissue-

resident macrophages such as cytokines (e.g. TNF, IL-1), chemokines (e.g. CCL2 and CXCL8), prostaglandins and eicosanoids.[7] These chemical signals initiate responses on both their local environment and target tissues including vasodilation of blood vessels and increased permeability to allow extravasation of leukocytes (mainly neutrophils) to reach the site of infection.[7] Upon reaching the damaged tissue, the neutrophils are activated by endogenous chemical signal from surrounding cells or directly by the pathogen itself and work to destroy the invading pathogen. They do this by releasing toxic effectors from their granules such as reactive oxygen species (singlet oxygen, H_2O_2 and hypohalous acids) and cathepsin G.[5, 8] These effectors are highly potent and non-specific so, as well as damage to the pathogen, the host tissues are also damaged.[8]

1.1.2 Imaging inflammation

Given the diversity of the immune cells involved in inflammation, as well as the small molecules and proteins involved in orchestrating the inflammatory response, it is expected that there would be a vast number of targeting options. The inflammatory response can be classified by three main components: increased blood supply to the site of infection; increased permeability of capillaries to allow larger molecules to escape; and migration of immune cells towards the site of infection (neutrophils at early stages and monocytes and leukocytes are later stages).[4]

One method of probe accumulation relies on passive localisation of imaging agents using the physiological changes associated with inflammation such as the increased blood supply and higher rate of metabolism to focus the density of the probe. A frequently used radiotracer in clinical imaging is ^{18}F-fluorodeoxyglucose (FDG) (Figure 1.2) which is used in positron emission tomography (PET) imaging in situations where there is high glucose metabolism.[9] Although commonly used in tumour detection, it has found use in imaging of inflammatory diseases where there is increased glucose uptake by immune cells including atherosclerosis and arthritis.[10] However due to the lack of specificity, it is often used in combination with other imaging techniques such as computed tomography (CT) or magnetic resonance (MR) imaging to increase diagnostic accuracy.[11]

Historically, ^{67}Ga-citrate has been used as it has been reported to localise in sites of infection.[12] Due to its similarities to ferric iron, Fe^{3+}, ^{67}Ga-citrate binds to transferrin in the blood and circulates until it reaches the site of inflammation.[13] It is then released and binds to bacterial siderophores and lactoferrin which is released by leukocytes; this exchange occurs as ^{67}Ga-citrate binds more strongly to lactoferrin than transferrin.[13] However its use in clinic is reducing as a result of its long acquisition time, high number of false positives and slow clearance from the body.[12, 13]

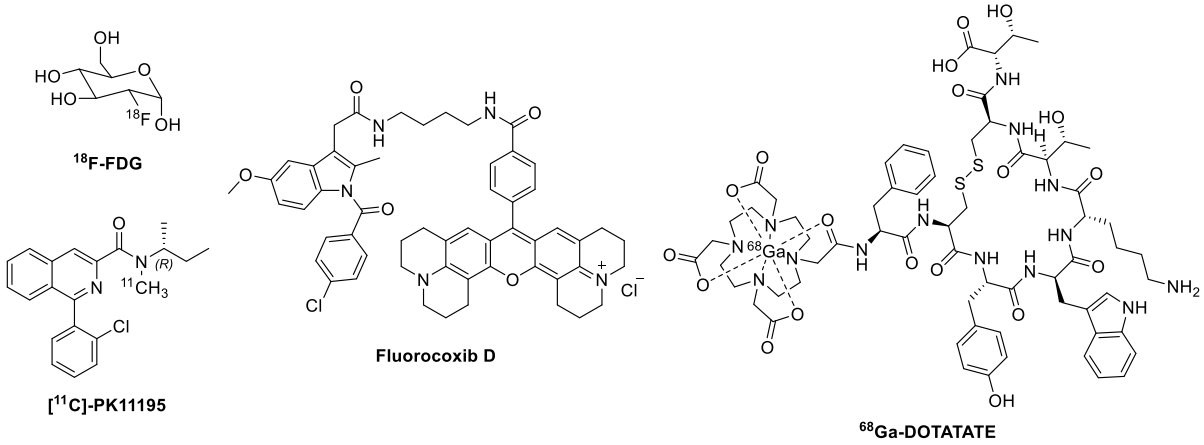


Figure 1.2. Examples of inflammation imaging probes.

Active targeting strategies initially relied on ^{99m}Tc or ^{111}In labelled leukocytes that involved the extraction of blood for *ex-vivo* labelling and reinjection of cells - typically neutrophils - which are recruited to the active site of inflammation. Although this technique can result in good localisation of the probe, it is expensive, time-consuming to allow for the labelling of leukocytes and requires extensive expertise.[10] Advances in this area have produced a plethora of imaging agents that target inflammatory mediators such as the cytokines and chemokines released at the site of inflammation or immune cells including neutrophils, monocytes/macrophages and T-cells; a summary of these is outlined in Table 1.1.

Table 1.1. Summary of examples of cytokines and membrane markers of inflammatory cells that have been target for imaging probes.

a. Inflammatory cytokines			
Name	**Location/cell type**	**Disease expression**	**Ref**
COX (cyclooxygenase)	COX-2[14-16]	osteoarthritis[14], colon cancer[15]	[14-17] (detailed review[18])
MMPs (matrix metalloproteins)	MMP-3[19]	rheumatoid arthritis[19]	[19, 20]
IL-2 (interleukin-2)	T-cells/macrophages	Crohn's disease,[21] atherosclerotic plaques[22]	[21-23]
b. Membrane markers of inflammatory cells			
TSPO (translocator protein)	activated microglia/brain macrophages, neutrophils, lymphocytes	Alzheimer's disease (C11-PBR28), (C11-PK11195), ALS (Amyotrophic Lateral Sclerosis)	[24-26]

		Stroke, Multiple sclerosis, atherosclerotic inflammation[24]	
CB2R (type 2 cannabinoid receptor)	activated microglial, CNS/brain	neuroinflammatory disease	[27]
MRs (mannose receptor)	macrophage/M2 and tumour associated macrophage (TAM)[28]	atherosclerotic inflammation[29], rheumatoid arthritis[30]	[28-30]
FPRs (formyl peptide receptor)	leukocytes/neutrophils/	Klebsiella pneumonia	[31-33]
FRs (folate receptor)	macrophages	arthritis,[34, 35] atherosclerotic inflammation[24]	[24, 34, 35]
Tuftsin receptor	peritoneal macrophages		[36, 37]
Somatostatin receptor	SSTR2 M1 macrophage	atherosclerotic inflammation[24]	[24, 38]

An example of a targeted chemokine is cyclooxygenase (COX); these are enzymes that catalyse the conversion of arachidonic acid into prostaglandins. COX-2 is highly expressed following inflammatory stimulation and has attracted great interest in medicinal chemistry with the development of the COX-2 specific non-steroidal anti-inflammatory drug, Celecoxib. It is used to treat osteoarthritis and rheumatoid arthritis while minimising the gastrointestinal side effects associated with unselective pain medications such as ibuprofen which inhibits both COX-1 and 2 enzymes.[39] Derivatives of celecoxib have been used to develop imaging agents which target COX-2 released in inflammation; an example of this is Fluorocoxib D (Figure 1.2), a water-soluble fluorescent rhodamine dye with selectivity for COX-2 reported to detect inflammation in a mouse model of osteoarthritis.[14]

Alternatively, receptors on immune cells are common targets such as the translocator protein (TSPO) receptor found on activated microglia, neutrophils and lymphocytes.[25] The radiolabelled [^{11}C]-PK11195 (Figure 1.2) has been used for over 20 years and paved the way for the development of second generation TSPO radiotracers (both ^{11}C and ^{18}F).[24] Similarly, the somatostatin receptor, SST_2R is highly expressed in activated macrophages and the PET probe, ^{68}Ga-DOTATATE (Figure 1.2) has demonstrated promise for imaging atherosclerotic plaque inflammation.[24, 38]

The work in this thesis focusses on targeting macrophages, which shows greater correlation with the chronic inflammatory state, with the purpose of improving understanding of the mechanisms of inflammation as well as monitoring disease progression and aiding development of new therapeutics.

1.2 Imaging modalities

Molecular imaging is a powerful non-invasive tool used by researchers and clinicians for visualising the biochemical processes that occur at the molecular and cellular levels up to tissue and whole-body scale.[40] Generally molecular imaging requires specialised imaging equipment, and can either be used alone or in combination with an administered contrast agent to help to improve the signal and reduce the background noise.[40] The data obtained from molecular imaging can be used to help understand the complex biochemical pathways, monitor disease progression and in drug development to measure the success of potential therapeutics. Given the many opportunities for using molecular imaging, a wide range of imaging modalities have been developed which each offer benefits and challenges; some will be discussed in the following sections but more detailed information is found in these reviews.[40-42] Therefore prior to selection of an imaging modality, it is necessary to consider the scale of imaging (cellular or whole body) which dictates the spatial resolution and depth of penetration required, as well as the biochemical process to visualised.[41]

1.2.1 Optical

Optical imaging is a non-invasive modality that is used in cellular and *in vivo* imaging and is primarily used for its high spatial resolution in the region of few millimetres and high sensitivity to the probes.[40] Fluorescence imaging is relatively inexpensive compared to other imaging modalities, easy to use and portable.[43] It is desirable for fluorescent probes to operate in the near infrared (NIR) wavelengths (650-900 nm) to minimise overlap with tissue autofluorescence, reduce tissue absorbance and improve depth penetration.[43]

Organic dyes are commonly used fluorophores in optical imaging and use conjugated systems which allows for delocalisation of electrons within a molecule; these include rhodamines, cyanines, methylene blue, BODIPY and fluorescein isothiocyanate (FITC). Inorganic probes have also been developed for optical imaging. Compared to organic probes, lanthanide based probes benefit from long luminescent lifetimes (μs to ms range), which can be used with time-gating techniques to distinguish the lanthanide signal from biological background fluorescence.[44]

As a result of using low-energy photons, the main limitation of optical imaging is the depth penetration which is limited to only a few centimetres as the energy is attenuated (absorbed and scattered) by the tissue. Therefore, the optical probes are mainly used in preclinical imaging such as in cell and small animal studies. This restricts the utility of optical imaging in clinical applications, although they have been used for near surface applications such as intraoperative fluorescence guided surgery and endoscopic imaging.[43, 45]

1.2.2 MRI/NMR

Imaging technologies that are less invasive and enable measurements from multiple organ systems include magnetic resonance imaging (MRI), positron emission tomography (PET) and

ultrasound. MRI provides high quality soft tissue imaging based on changes to the relaxation rate of water protons,[46] and can capture whole body images with voxel resolution around 1 mm. However, the detection limit of classical Gd contrast MRI is of the order of 0.1 μM, meaning that improved strategies are necessary to achieve imaging of surface receptors. The poor sensitivity of all nuclear magnetic resonance (NMR) methods dictates that a large concentration of contrast agent be used in MRI methods. PET and SPECT offer much lower detection limits, allowing direct measurement of surface receptors, but the use of radioisotopes limits some clinical application, particularly where serial monitoring of treatment response requires multiple scanning sessions. Also, the limited spatial resolution of these methods significantly complicates interpretation in some diseases.

MRI is widely used for *in vivo* studies due to its high spatial resolution and unlimited penetration depth; moreover as it does not use ionising radiation it can be used for long term studies.[47] MRI is derived from the same principles as NMR spectroscopy and probes the local magnetic field around a nucleus with a net nuclear spin.[46] The ^{1}H nucleus is used for the majority of MR imaging applications due to the high abundance of water in the human body (~65% water by weight) and will be the focus of discussion in this section.

Figure 1.3 gives an overview of the mechanisms of NMR spectroscopy than underpin the processed governing MRI. The image is acquired by subjecting a sample to a constant external magnetic field (B_0) to give net alignment of the nuclear spins (most are in the low energy state aligned with B_0). This is followed by a short radiofrequency (RF) pulse at resonant frequency.[48, 49] When the RF pulse stops, the protons relax back to their position at equilibrium which is aligned to the constant external magnetic field. As they relax, the protons release radio waves which are recorded by a receiver coil to obtain the signal that is followed by an analogue-to-digital conversion of the signal.[48, 49] The magnetisation in the xy-plane decreases exponentially with a time constant, T_2, whilst the magnetisation along the z-axis increases exponentially with the time constant, T_1.[48, 49] Transverse relaxation or "spin-spin" relaxation is faster than longitudinal relaxation or "spin-lattice" relaxation ($T_2<T_1$).[49] It is the difference in water content in different tissues that generates variations in signal and contrast and that allows for the generation of an anatomical image.[48]

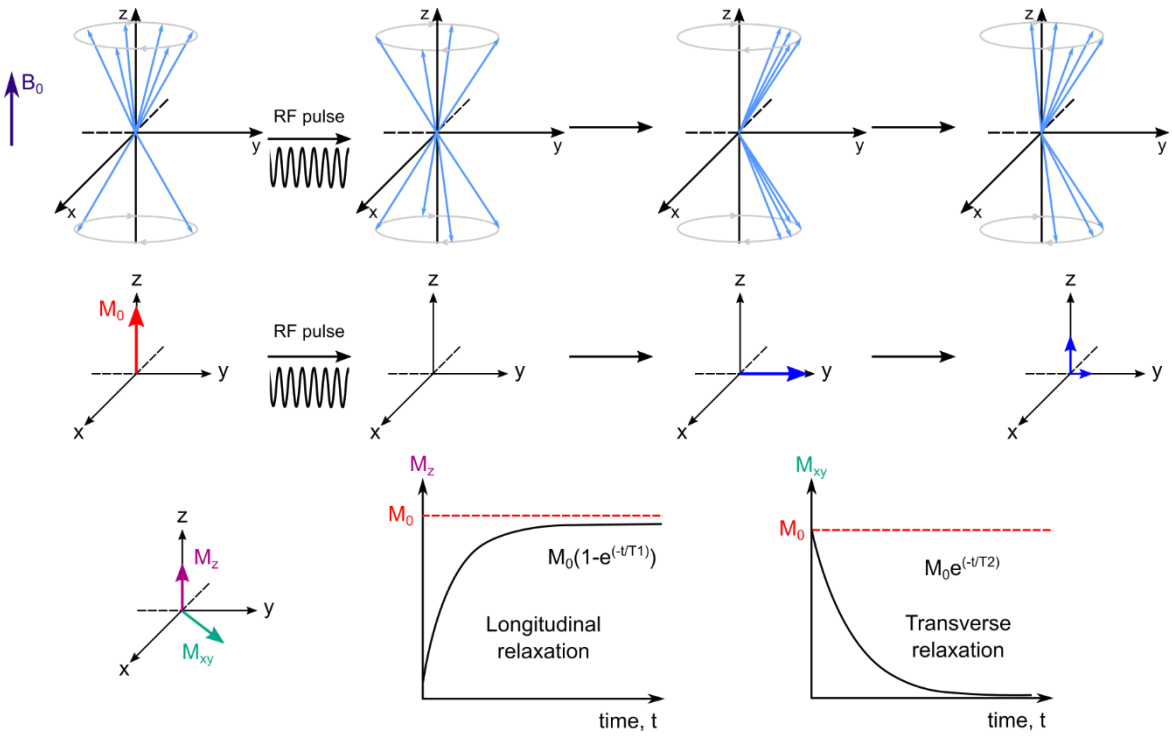


Figure 1.3. Illustration of the mechanisms of NMR spectroscopy that govern MRI. Protons precess under a permanent magnetic field B_0. A radiofrequency (RF) pulse causes loss of magnetisation in the z plane and increase in signal in the xy plane. When the RF pulse is removed the protons return to equilibrium.

To extend the principles of NMR spectroscopy to 2D or 3D imaging, spatial resolution of signal is required. In MRI, there are 3 directions over which linear magnetic field gradients can be applied, helping to localise the signal (Figure 1.4a). Starting along the z-axis, a magnetic field gradient is applied from high to low strength. Selecting a slice occurs by sending a selective excitation which is at the resonance frequency for the field strength at that location in the z-axis (the bandwidth of the excitation pulse therefore determines the slice width, Figure 1.4b).[49] Within each slice, the x- and y-axes also need to be resolved. A frequency encoding gradient is applied along the x-axis so that spins in different positions along the x-axis precess at different frequencies.[49] Along the y-axis, a phase encoding gradient is applied before the measurement resulting in a unique phase for each spin in the y-axis.[49] Therefore, each voxel in a given slice is encoded in phase and frequency which corresponds to a localisation in 3D space. Mathematical processing of the raw signal yields an image comprised of a matrix of voxels.

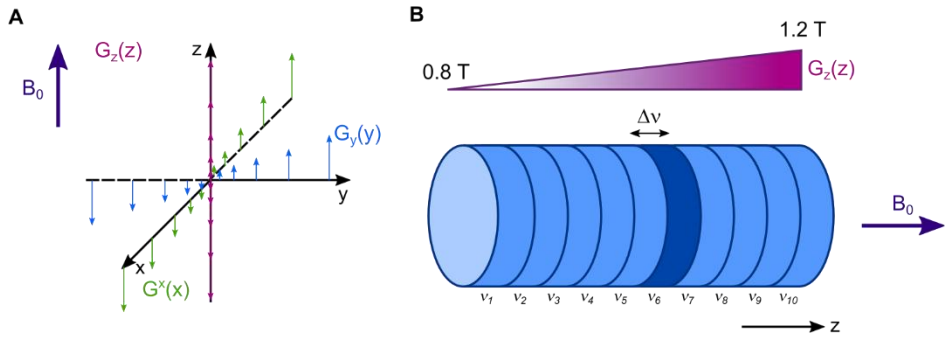


Figure 1.4. a) Magnetic field gradients in used to localise signal in three-dimensions for MRI; b) Slice selection by choosing a specific frequency and bandwidth along the varied magnetic field along z-axis. Redrawn from reference.[49]

Contrast agents that are used for MRI, such as gadolinium or manganese probes, influence the rates of T_1 or T_2 relaxation.[50] The most used class of contrast agents are longitudinal T_1 relaxation agents that increase the rate of relaxation of the H_2O protons back to equilibrium by interaction with unpaired electrons.[49] Gadolinium is paramagnetic, with seven unpaired electrons, and is the main metal used in commercially available contrast agents and is effective in inducing relaxation in nearby water molecules.[50] A limit of the effectiveness of the gadolinium-based contrast agent (GBCA) is the transfer of the relaxation effect to the bulk of the water, which relies of the fast exchange of the water bound to the metal ion and the bulk water.[50]

1.2.3 Photoacoustic imaging

Another imaging modality explored in this project is photoacoustic (PA) imaging. The benefit of photoacoustic imaging is that it can reach greater depths in the body than optical microscopy, beyond superficial skin measurements. With these attributes it has potential to bridge between optical, MR and PET imaging, in both depth and resolution. Photoacoustic imaging derives from the "photoacoustic effect", whereby light is absorbed by a chromophore and converted into heat, which generates measurable sound waves.[51] In practice, a pulsed laser is directed at the tissue, photons are absorbed by the chromophore, converting into thermal energy with a resultant increase in pressure.[51] Thermoelastic expansion that occurs as a result of the absorbed photon then transmits as an acoustic wave because of the elasticity of the tissue, which can be recorded by a detector.[51, 52]

To achieve good imaging contrast between the target and the biological background, it is necessary to have a signalling chromophore that can absorb and emit in the near-infrared region between 600 and 900 nm, as this region is poorly absorbed by endogenous photoabsorbers such as haemoglobin and lipids.[1] One type of PA contrast agent that has been thoroughly explored is molecular dyes such as cyanine, phthalein, xanthene and squaraine and croconaine dyes.[53] For this work, we have chosen a heptamethine cyanine dye structure, given that the indocyanine green (ICG) structure is already FDA approved. Heptamethine cyanine dyes have an absorption maximum within the optical window, around 790 nm, and a large molar extinction coefficient (~240,000 M^{-1} cm^{-1}),

and has been shown as a suitable PA imaging agent for receptors targeted in the brain by Parker and colleagues.[54]

1.3 Lanthanide chemistry

The lanthanides are a series of elements represented by the gradual filling of the 4*f* orbital with electrons. The chemistry of the lanthanides is largely governed by the +3 oxidation state which arises from the high fourth ionisation energy being unable to be offset by the energetic gains from bond formation.[55] The 4*f* valence electrons are penetrating with most of the electron density situated close to the nucleus; this prevents any substantial orbital overlap with ligands.[55] Therefore bonding in lanthanide complexes is strongly ionic and non-directional with small crystal field effects. Even though the lanthanides are large and the ionic charge is distributed over a large area, as the most common oxidation state is +3, they have a high charge density and act as hard Lewis acids.[55] Given this, lanthanide ions prefer to coordinate to hard Lewis acids such as O, N or F donor atoms. The coordination geometry of the surrounding ligands is mainly determined by size of the metal ion and steric requirements of the ligands;[56] the large ionic radii of the lanthanides means that the early lanthanides can accommodate geometries of around 9-12 coordinates whilst the contracted later lanthanides tend to adopt an 6-8 coordinate geometry.

Like *d*-metal complexes, stable lanthanide complexes can be made by exploitation of the chelate and macrocyclic effects. Lanthanides complexes with polydentate ligands afford additional stability due to the entropic gains from the release of monodentate ligands or solvent molecules.[56] Whilst macrocyclic polydentate ligands display even greater stability over their linear analogues owing to the macrocyclic effect when there is a good alignment between the diameter of the cavity and the size of the metal ion. This is demonstrated most clearly through the kinetic stability reported as the acid dissociation rate, k_{obs} at pH 1, where $k_{obs} = 2.1 \times 10^{-5}$ s^{-1} for Gd-DOTA and 1.2×10^{-3} s^{-1} for Gd-DTPA (Figure 1.5).[57]

Due to the neurotoxicity of the free Ln^{3+} ions, stability of the lanthanide complexes is of great importance when used *in vivo* to ensure the complex retains the metal until excreted.[50, 58] The safety hazards associated with complex instability have been highlighted recently with gadolinium contrast agents used for magnetic resonance imaging, where a link between patients with reduced renal function and nephrogenic systemic fibrosis (NSF) has been reported.[59] Examples of linear and macrocyclic GBCA used for MRI are shown in Figure 1.5. In 2017, following the link between NSF in patients with compromised renal function and the linear GBCAs, Magnevist and Omniscan, their general use in clinics was suspended.[60]

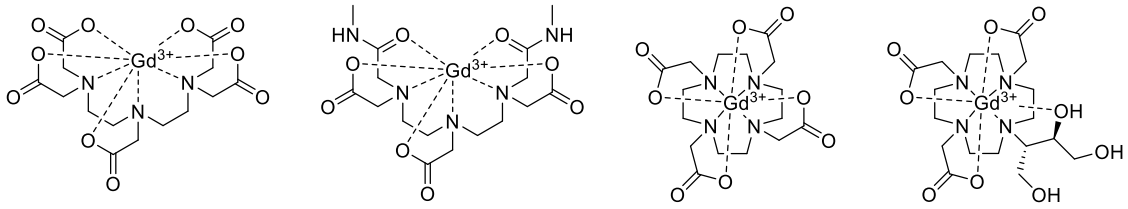


Figure 1.5. Structures of commercially available gadolinium contrast agents for MRI showing both linear and macrocyclic ligands, and neutral and anionic complexes.

1.3.1 Lanthanide Photophysics

Theoretically lanthanide electric dipole transitions are "forbidden" under Laporte's parity selection rule. However, in a ligand environment the interaction of the 4f electrons with the crystal field can result in a relaxation of the selection rules and the transition becomes partially allowed; this is known as an induced electric dipole transition.[61] As a result, the transitions can occur as a magnetic dipole with weak intensity and exhibit characteristic, sharp 4f-4f transitions.[61] This results in very little change between the internuclear distances in the excited state and ground state giving narrow bands and small Stokes' shifts.[61]

Direction excitation of lanthanides is inefficient and gives weak emission and this can be overcome by incorporating a chromophore which can be used to indirectly excite electrons into the 4f excited state as shown in Figure 1.6. The typical pathway involves the absorption of photons by the chromophore, which is usually an organic or d-block chromophore, into the excited singlet (S_1) state. Intersystem crossing within the chromophore into the longer-lived triplet (T_1) state then allows energy transfer into the excited state on the lanthanide. Using this simplified view of lanthanide emission, some generalisations have been noted for chromophore design with Eu^{3+} and Tb^{3+}.[62] To maximise the quantum yield of the overall process (excitation – energy transfer – emission), for cases where the ligand triplet state is the primary donor, the triplet state energy should be at least 1500 cm^{-1} (ideally 2000 – 4000 cm^{-1}) above the main lanthanide emissive state in order to minimise energy losses via back energy transfer.[62]

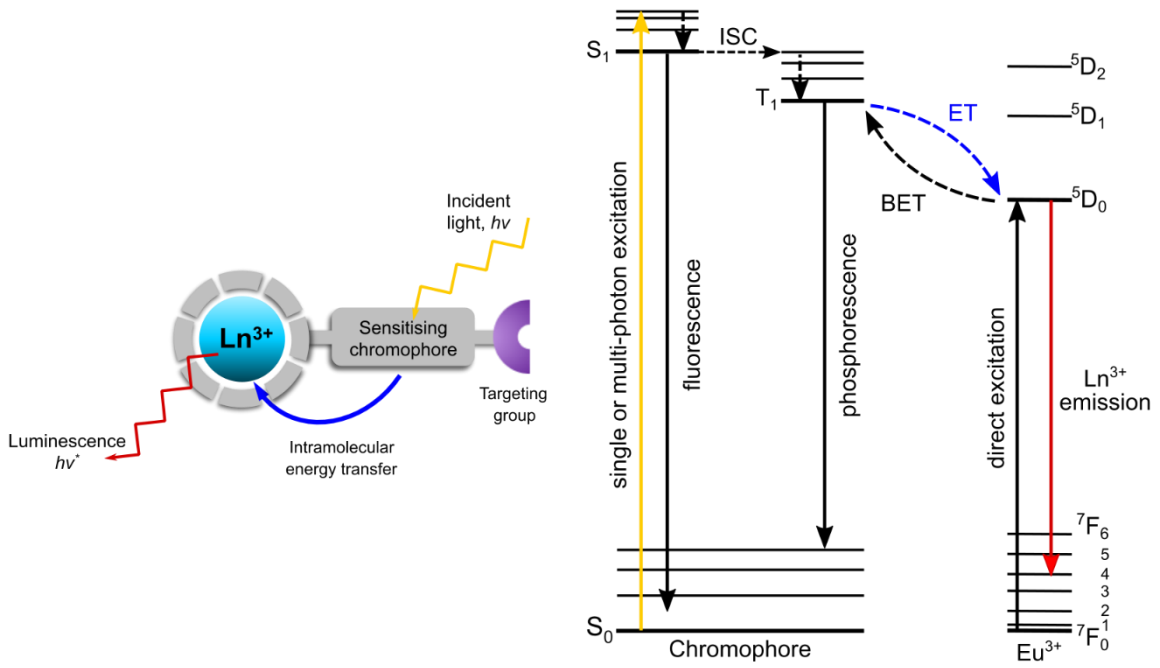


Figure 1.6. Cartoon depiction of indirect lanthanide excitation via a chromophore. Simplified Jablonski diagram showing some pathways for energy transfer for Eu^{3+}. ISC: Intersystem crossing; ET: Energy transfer; BET: Back energy transfer.

Another important aspect of lanthanide emission is where changes in the coordination environment can produce small changes in the emission spectra seen as hypersensitive transitions.[63, 64] These are generally seen for the $\Delta J = 2$ transition and can be used to interpret changes at the lanthanide which may be sensitive to changes in solvent coordination, pH change and ligand binding.[63]

Some key ground and emissive states for the f-f emission bands are shown in Table 1.2 with Eu^{3+}, Tb^{3+} and Gd^{3+} being especially relevant to this work. Europium and terbium are the most suitable candidates for luminescence studies as they have the largest energy gap between their main emissive and ground states, excluding gadolinium, and, unlike gadolinium, emit in the visible range.

Another benefit of the parity forbidden nature of f-f transitions is that they exhibit longer luminescent lifetimes than typical fluorescent probes. This allows for the lanthanide emission to be separated from short lived autofluorescence from biological tissues by using time-gating techniques.[44]

Table 1.2. Ground, main emissive and final states for the f-f emission bands with the corresponding wavelengths and energy gap between the emissive state and highest SO level of the receiving state. Reproduced from reference.[61]

Ln	**Ground State**	**Main emissive state**	**Final states**	**λ (nm)**[a]	**Energy gap (cm^{-1})**[a]	**Radiative life of Ln^{3+} ions (ms)**
Nd	$^4I_{9/2}$	$^4F_{3/2}$	^4I_J (J = 9/2-13/2)	900, 1060, 1350	5400	0.42 (0.2-0.5)
Eu[b]	$^7F_0$	$^5D_0$	^7F_J (J =0-6)	580, 590, 615, 650, 720, 750, 820	12300	9.7 (1-11)
Gd	$^8S_{7/2}$	$^6P_{7/2}$	$^8S_{7/2}$	315	32100	10.9
Tb	$^7F_6$	$^5D_4$	^7F_J (J =0-6)	490, 540, 580, 620, 650, 660, 675	14800	9.0 (1-9)
Dy	$^6H_{15/2}$	$^4F_{9/2}$ $^4I_{15/2}$	^6H_J(J = 15/2-9/2) ^6H_J(J = 15/2-9/2)	475, 570, 660, 750 455, 540, 615, 695	7850 100	1.85 (0.15-1.9) -
Yb	$^2F_{7/2}$	$^2F_{5/2}$	$^2F_{7/2}$	980	10250	1.3

[a]Values for the aqua ions, otherwise stated. [b]Luminescence from $^5D_1$, $^5D_2$, and $^5D_3$ is sometimes observed as well.

1.3.2 Mechanisms of Energy transfer

There are two mechanisms of energy transfer from the excited state of the chromophore (donor*) to the lanthanide ion (acceptor)– Dexter and Förster as shown in Figure 1.7. A Dexter energy transfer is a double electron exchange that depends on the distance *d* separating the donor from the acceptor (e^{-2d}) and requires electronic coupling that is facilitated by direct orbital overlap.[65-67] Dexter exchange is important for lanthanide sensitisation by chromophores as it is the ligand-based triplet excited state that transfers energy to the Ln^{3+} centre but primarily occurs over distances of ~50 pm, although distances up to 2000 pm are possible by superexchange.[66, 68] Meanwhile, Förster energy transfer is a through-space mechanism that arises from the dipole-dipole interaction and relies on good spectral overlap of the donor and acceptor. It can occur over much longer distances than Dexter energy transfer (up to 1000 pm) and has a distance dependency of d^{-6}.[6, 65, 66, 69]

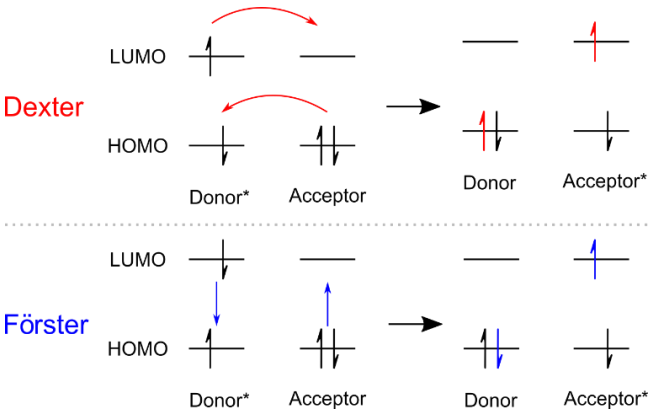


Figure 1.7. Dexter and Förster energy transfer.

1.3.3 Lanthanide luminescence quenching

Bound ligands or coordination of solvent molecules to lanthanide complexes can act as quenchers that shorten the excited state lifetimes of the metal ions.[70] The quenchers deactivate the excited lanthanide ions through non-radiative energy transfer to high frequency X-H oscillators (X = O, N or C) (Figure 1.8). The most effective quenchers were found to be O-H oscillators such as bound water molecules.[70] This is a result of the large overlap in vibrational energy levels between the Ln^{3+} ions and O-H oscillators, which is especially observed for Yb^{3+} and Eu^{3+}, but less efficient quenching is found for Tb^{3+} where the Franck-Condon overlap is weaker.[70] Meanwhile, the analogous X-D oscillators have lower stretching frequencies that display less favourable vibrational energy overlap with the Ln^{3+} ions and are seen only for higher energy harmonics,[70] with the deuterated oscillators being found to be at least 200 times less effective quenchers than the protonated counterparts.[71]

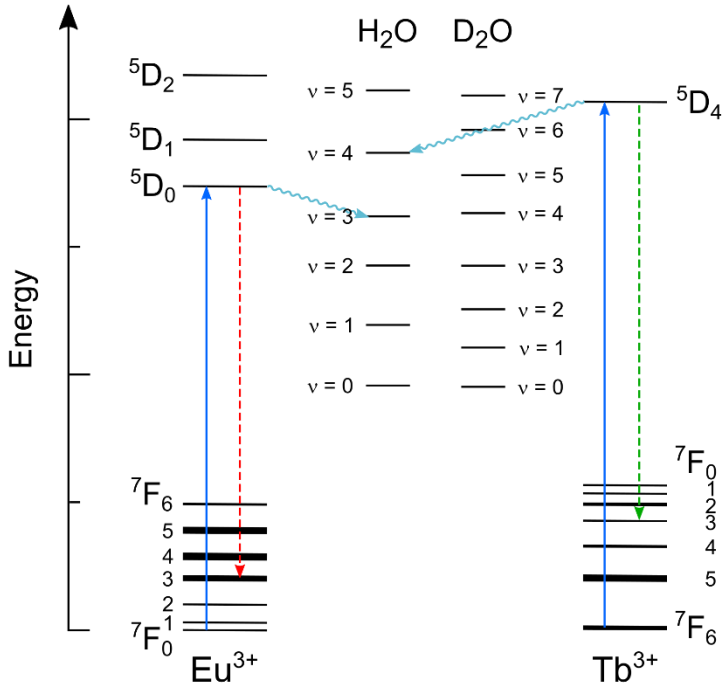


Figure 1.8. Energy level diagrams for Eu(III) and Tb(III) showing quenching via O-H and O-D oscillators; measurement of luminescent lifetime decay using to calculate q. Redrawn from reference.[72]

This difference has been exploited to assess the number of water molecules, *q*, that interact in the inner coordination sphere of the lanthanide complex using the luminescence lifetimes measured with water and deuterated water via the modified Horrocks' equation (Eq. 1.1) with constants given in Table 1.3.

$$q = A\left(k_{H_2O} - k_{D_2O} - B\right) = A\left(\frac{1}{\tau_{H_2O}} - \frac{1}{\tau_{D_2O}} - B\right)$$

Eq. 1.1. Modified Horrocks equation[70] *where q is the number of coordinating water molecules, A is the proportionality contrast, k is the rate constant, B is the correction factor to account for other deactivation vibrations.*

Table 1.3. Proportionality constant, A and correction factor, B for the Eu^{3+} and Tb^{3+} ions when using the modified Horrocks' equation.[70]

Metal ion	A (ms)	B (ms^{-1})
Eu^{3+}	1.2	0.25
Tb^{3+}	5	0.06

1.3.4 Isomerism

DOTA is an 8-coordinate ligand that binds strongly and irreversibly to Ln^{3+} ions; for these reasons, its gadolinium complex has been in widespread clinical use for over thirty years. It is well suited as it has a preorganised structure of eight "hard" Lewis bases (N and O), and a cavity within the ligand that matches the ionic radii of Ln^{3+} ions.[73] Ln(III) DOTA and DO3A-derived complexes exist as two diastereoisomers: square antiprism (SAP) and twisted-square antiprism (TSAP), with water molecule residing in the ninth axial coordination site.[73] The two isomers of $[LnDOTA]^-$ are observed by ^1H NMR spectroscopy as they are in slow exchange in solution at room temperature.[74] The structures of the conformations is such that the lanthanide metal resides in a central cavity with a plane of 4 donor atoms above and below (Figure 1.9).[75] The SAP isomer has a twist angle of 40° between the O-Ln-N, whereas the equivalent angle in the TSAP isomer is between ~25-30°, with interconversion between the two occurring by arm rotation or ring inversion.[73, 76] However it is important to note that the complexes are likely to resemble one of these limiting isomers rather than exhibit the exact geometries provided which is of relevance to responsive luminescence probe design.[75]

In addition to solid state crystal structures, NMR spectroscopy has been pivotal in helping to distinguish the conformation of DOTA- and DO3A-derived structures. Due to the more closed structure of the SAP conformation, the axial ring protons display larger paramagnetic shifts due to their larger susceptibility anisotropy.[74] It has been found that there is correlation between the metal ion size and the adopted geometries of the complex with later, smaller lanthanides (Sm^{3+} to Lu^{3+}) preferring a SAP conformation, whereas earlier, larger lanthanides (Ln^{3+} to Pm^{3+}) prefer a TSAP geometry.[74] In addition to the size of the ion, the relative concentrations of the isomers varies with temperature, solvent, anion binding, ligand chirality, sterics and pH.[74, 77-80] The geometry of the complexes is important to their function, particularly for MRI contrast agents design, as it has been found that the axial coordinated water undergoes exchange 50 times faster when bound to TSAP conformers compared to SAP.[81]

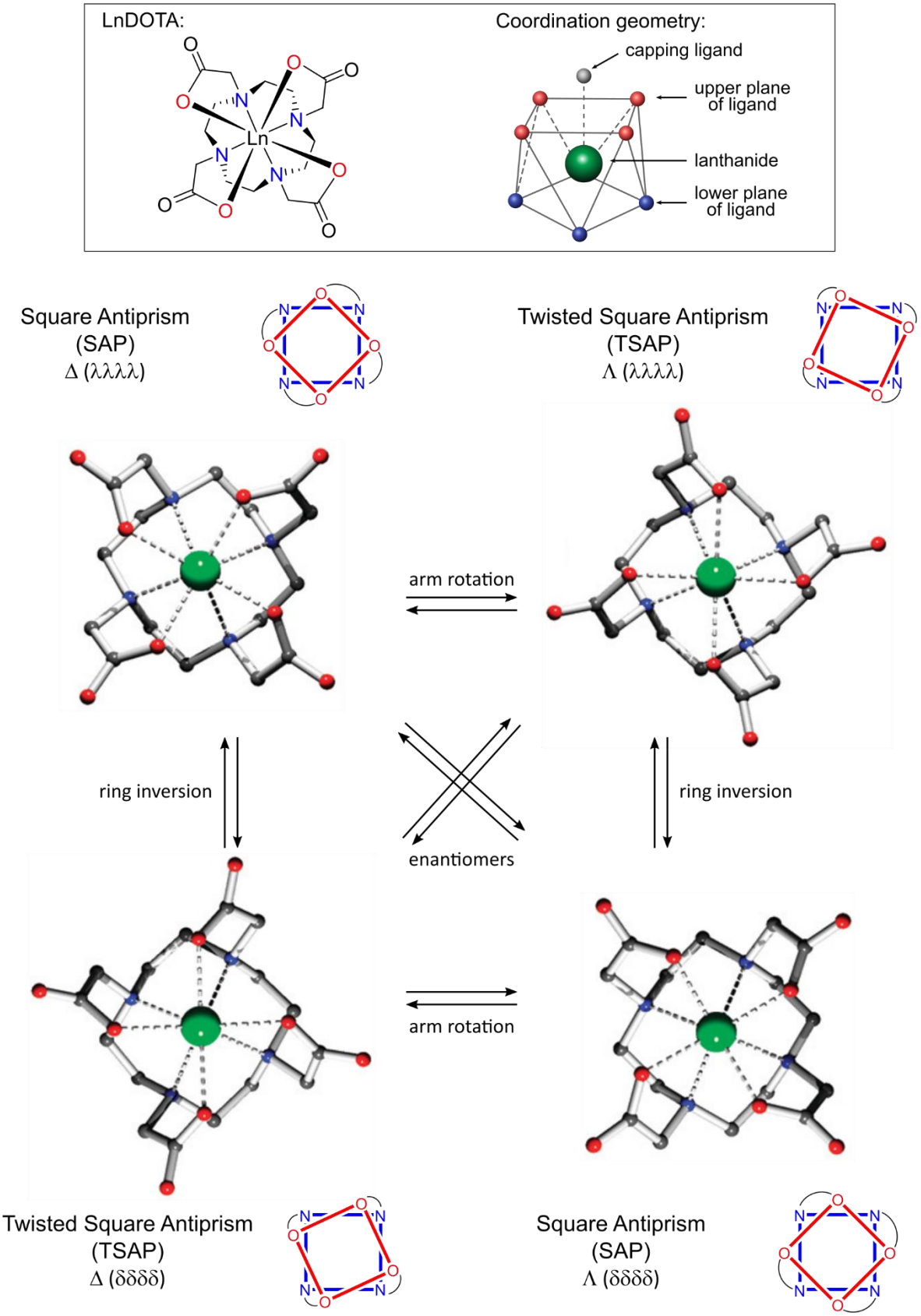


Figure 1.9. Isomerism of the LnDOTA complexes. Reprinted (adapted) with permission from Inorg. Chem., 2009, 48, 2, 466–475.[82] Copyright 2008 American Chemical Society.

1.4 Bioconjugation

Most of the contrast agents for PET and MR imaging used in clinical applications are contrast agents, such as ^{19}F-FDG and [GdDOTA]$^{-}$, that accumulate in the body through non-specific mechanisms; however, these are limited in their use for more complex disease conditions. In contrast, approaches using bioconjugation allow for the development of probes with high specificity that will localise and accumulate in one location. Bioconjugation is the attachment of a targeting vector (peptide, protein, antibody or nucleic acid) to a diagnostic or therapeutic agent to produce a compound that is directed to a disease (Figure 1.10).[83] For imaging agents, the aim is to improve selectivity to visualise a particular biological state while reducing localisation at non-specific locations, thereby increasing the signal to noise ratio.

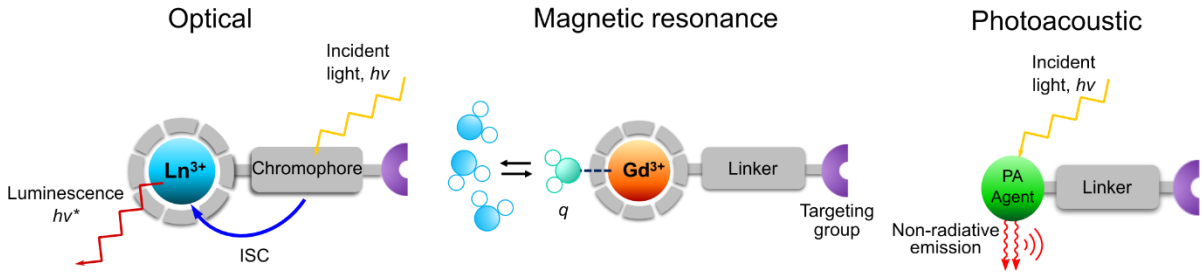


Figure 1.10. Illustration showing the key components of the imaging probes for optical, magnetic resonance and photoacoustic imaging. ISC: Intersystem crossing; PA: photoacoustic; q: number of water molecules bound.

Routine bioconjugation involves a limited number of frequently used reactions to form the covalent bonds such as amides, thioethers, disulfide and ester; an important aspect is to select the appropriate reactive groups and suitable crosslinking reagents for the different moieties to be joined together.[83] Some examples of typical bioconjugation reactions are shown in Figure 1.11, this topic is covered more in depth in a book by Hermanson.[84]

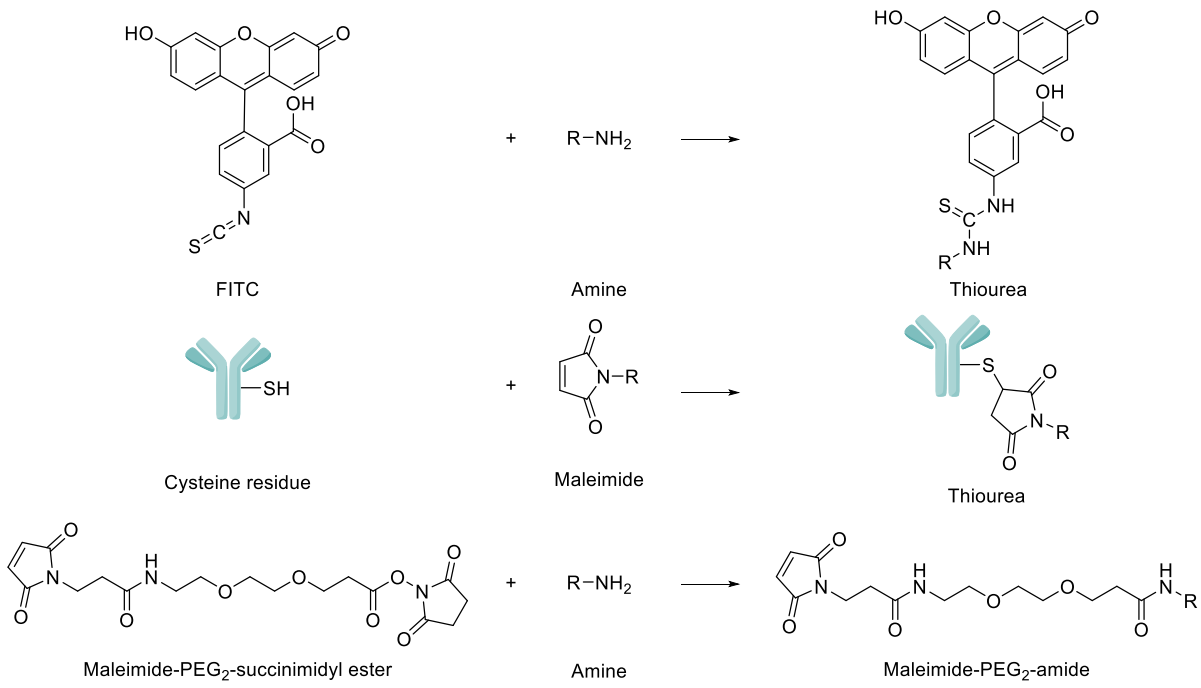


Figure 1.11. Examples of bioconjugation reactions. FITC: fluorescein isothiocyanate; PEG: polyethylene glycol.

In addition, linking molecules can have significant effects on the properties of the final compound such as hydrophobic or hydrophilic linking molecules.[83] Polyethylene glycol (PEG) is a hydrophilic chain that is incorporated into therapeutics to modify the pharmacokinetic properties, such as reducing renal clearance, increased water solubility and reduced toxicity.[85, 86] Low and van der Laken have developed PET imaging agents targeting folate receptors that incorporate PEG_6 and PEG_{12} units and report a reduction in radioactivity accumulation in the liver.[35, 86]

1.4.1 Bioorthogonal reactions

Whilst bioconjugation reactions are designed to use the functional groups typically used by biological molecules, bioorthogonal reactions allow chemical reactions to occur *in vivo* whilst avoiding side reactions by using reactive functional groups that are inert to biological moeities.[87, 88] There are requirements for a reaction to be considered a bioorthogonal reaction: it reacts selectively, is chemically inert once formed, is non-toxic and compatible in biological environments.[88] For more detail, McKay and Finn provide an excellent review on bioothorgonal bioconjugation.[89]

Over the years, the formation of triazoles by the azide-alkyne cycloaddition has attracted a lot of interest. Initially Huisgen reported that 1,3-dipolar cycloaddition of azides reacted slowly with unstrained, linear alkynes.[90] It was then found that this reaction could be catalysed with metal catalysts, such as copper(I), by Sharpless *et al.* with stereospecificity that led to the concept of click chemistry.[91] The Cu^+ catalyst can either be used directly or be generated *in situ* from Cu^{2+} species with appropriate reducing agents (typically sodium ascorbate). Recently, evidence in support of the copper catalysis occurring via both mononuclear and dinuclear mechanisms has been reported which

are shown in Figure 1.12.[92, 93] Moreover it has been found that the reaction can be accelerated further by using copper-binding ligands such as THPTA (tris(3-hydroxypropyltriazolylmethyl)amine).[94, 95]

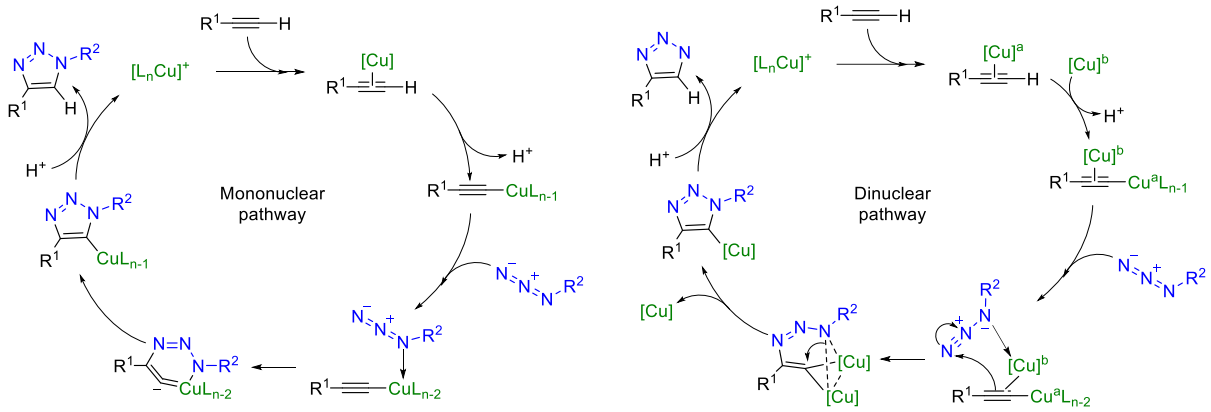


Figure 1.12. Proposed catalytic cycles for mononuclear and dinuclear copper catalysed azide-alkyne cycloaddition, CuAAC.[92, 96]

Despite its popularity, there remains concern over copper's toxicity *in vivo*, so the best way to improve the biocompatibility of cycloaddition is to eliminate the use of copper.[97, 98] This led to the development of strain-promoted azide-alkyne cycloaddition (SPAAC) as a route for Cu-free click chemistry by Bertozzi and Sletten.[88] The strain on the alkyne bond reduces the energy barrier required for the reaction to proceed resulting in the non-stereoselective formation of the 1,3- and 1,4 triazoles.[99] Meanwhile, biocompatibility has been demonstrated with SPAAC reactions *in vivo* for zebrafish and mice.[100, 101] The work in this project has utilised both Cu- and Cu-free click chemistry with the synthesis of DO3A-derived complexes containing linear and strained alkynes detailed in Chapter 2.

Further to the earlier discussion on imaging inflammation (Section 1.1.2), macrophages were identified as the target immune cell due to their significance in chronic inflammation for rheumatoid arthritis.[102, 103] There were a few receptors on the surface of macrophages that have been identified as prominent in arthritic diseases (folate, mannose, tuftsin).[30, 104] For the focus of this work, folate and tuftsin were chosen to act as the targeting moieties for imaging macrophages and are discussed in detail below.

1.4.2 Folate

Folate is a generic term for the family of B9 vitamins, including folic acid and its reduced forms tetrahydrofolic acid and methyltetrahydrofolate. Folates are important one-carbon donors in the synthesis of DNA and RNA.[105] However, as human bodies lack the ability to synthesise folate, it is vital that it is acquired from dietary sources.[105] There are three methods through which folates can enter the cell: the reduced folate carrier (RFC), the proton coupled folate transporter (PCFT), and folate receptors.[105-107] The RFC is an anion exchange protein where the import of folate derivatives into the cell requires outward release of organic negatively charged phosphates using their

concentration gradient as the driving force.[105, 108] The binding affinity for folic acid, however is low with an IC_{50} value of 890 μM reported against the [^{3}H]-methotrexate.[105, 109] The PCFT works as a symport co-transporter whereby two protons and one folate molecule (a dianion at physiological pH) are simultaneously transported into the cell to balance the overall charge of the complex.[105, 106] The most relevant mode of folate transport for this work is performed by the family of folate receptors (FR).

The family of folate receptors exists as several isoforms: α, β, γ and δ, and bind with high affinity to folic acid (Figure 1.13a).[110] The α- and β-receptors are located within the cell membrane attached via a glycosylphosphatidylinositol (GPI) anchor and mediate folate transport, whilst the FR-γ lacks the GPI anchor and resides within the cytoplasm. The α- and β-isoforms have high sequence homology (with 68-79% identical amino acid sequences).[105] Greater expression of FR-α is found in cancerous cells,[111, 112] while FR-β is overexpressed in activated macrophages[34, 110, 113-116] compared to low levels of expression in normal, healthy cell types. The limited distribution of the FRs make them ideal targets for selective therapeutic and imaging purposes. For this reason, FR-β has been identified as a suitable target for the imaging of inflammation, as activated macrophages are associated with inflammatory diseases such as rheumatoid arthritis,[35, 114, 115, 117-119] osteoarthritis, and ulcerative colitis;[120] while expression is not observed for quiescent macrophages.[34]

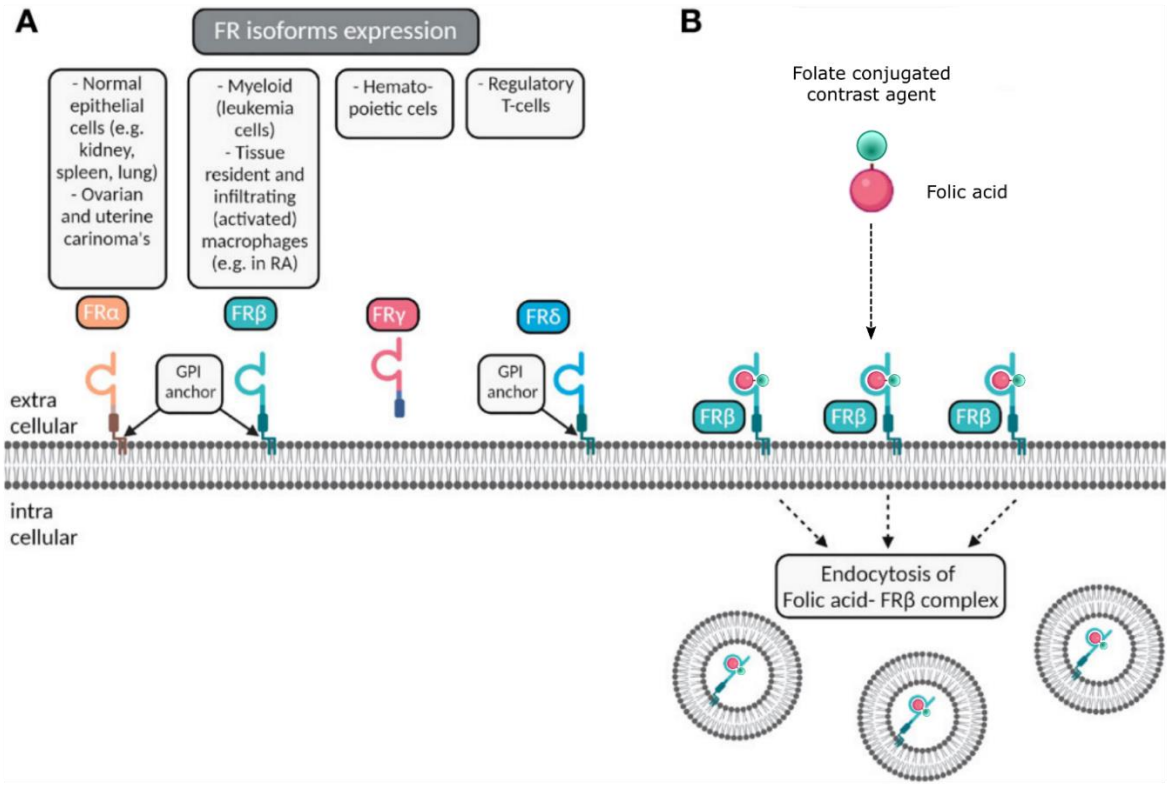


Figure 1.13. a) Isoforms of folate receptors: α, β, γ, δ and their tissue expression. b) Internalisation of folate conjugated contrast agents and upon binding to FR- β either remain bound on the cell surface or are internalised via endocytosis.

Binding of folic acid or folate-conjugates to FR initiates internalisation into cells via receptor-mediated endocytosis (Figure 1.13b). Cross-linking of these receptors leads to the cell membrane pinching off to form vesicles (caveolae) that transport the folate-receptor complex into the cell and targets them for the endosome.[107, 121, 122] The vesicle fuses with the endosome, and it has been postulated that the lower pH in the endosome induces a conformational change in the FR to release the receptor-bound species.[123, 124] Following this, the caveolae returns the FR to the cell surface for reuse;[125] this recycling of the FR therefore enables further accumulation of folate-conjugates within the cell.

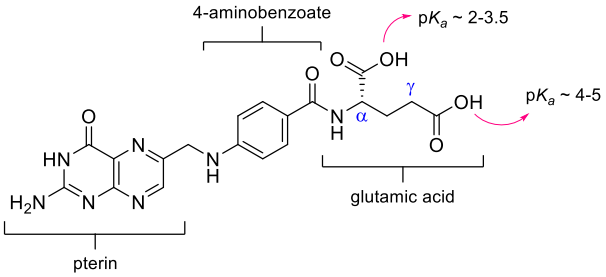


Figure 1.14. Chemical structure of folic acid highlighting α- and γ- carboxylate conjugation sites.

Folic acid consists of three distinguishable fragments: pterin, 4-aminobenzoic acid and glutamic acid (Figure 1.14). The crystal structure of FR-α[126] and FR-β[123] complexed with folic acid and some antifolates (pemetrexed, aminopterin and methrotexate) have been reported, helping to elucidate the important structural features of the folate-derivates within the FR binding pocket. Figure 1.15 shows the interactions between folic acid and the residues in the FR-β binding pocket. The pteroic acid binds furthest within the FR binding cavity, with the ring π-π stacking between tryptophan 187 and tyrosine 101 residues; the pterin ring is also further stabilised by hydrogen bonding and charge-charge interactions with surrounding residues.[123] The 4-aminobenzoic acid moiety interacts only via hydrophobic interactions with the phenylalanine 78, tyrosine 76 and tryptophan 118.[123] The terminal glutamic acid resides closest to the entrance of the receptor cavity with the glutamic acid carboxylates forming hydrogen bonds and charge-charge interactions with three tryptophans, glycine 153 and arginine 152.[123] These structures provide support for the functionalisation at the γ-carboxyl moiety of glutamic acid,[123] which is the most prolific position for attachment of an imaging or therapeutic group.[35, 86, 125, 127-131] The Low group reported binding of a γ-folate regioisomer to FR-α as having a binding affinity comparable to free folic acid ($K_d \sim 10^{-9}$ M).[127] Nevertheless, positions of functionalisation remain widely debated amongst the community, reporting little to no difference between the α- and γ-regioisomers,[132, 133] in some cases leading to use of a mixture of the regioisomers.[134, 135]

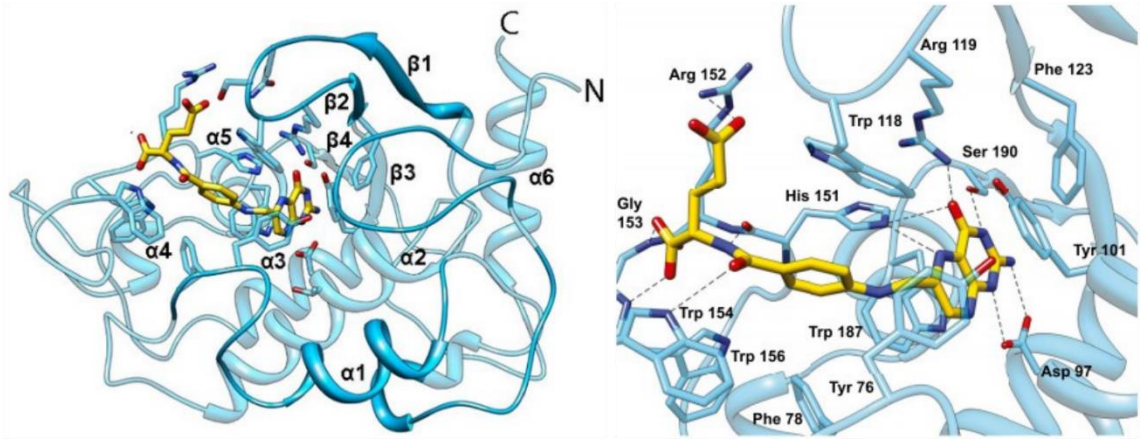


Figure 1.15. Human folate receptor-β-folate complex where the FR-β is represented as a ribbon diagram in cyan and the folate is shown as a yellow stick structure.[123] Interactions between folate and the residues on the receptor are shown on the right. Reproduced with permission.[123]

Unsurprisingly, extensive work has been carried out to make use of the specificity and high binding affinity of folic acid to the FRs for therapeutic and imaging applications. Initial work involved the development of folate-targeted toxins.[136] Following this, work expanded into imaging probes to improve the understanding of off-target locations of the therapeutics beginning with radiolabelled-folate imaging agents for SPECT imaging (^{67}Ga, ^{99m}Tc, ^{111}In and ^{3}H).[34, 114-116, 125, 127, 137-139] Since then, considerable research has resulted in compounds for PET[140] (^{18}F, ^{68}Ga),[35, 86, 119, 130] MRI,[128, 129, 141] and optical (NIR fluorescence and lanthanides)[34, 35, 45, 131, 133-135, 142, 143] imaging modalities. Folate targeting has also been utilised for treatment using antifolates – such as methotrexate,[135] or pemetrexed - as well as for newer techniques such as liposomal drug delivery[144] and nanopharmaceuticals.[145] More detailed discussion of folate-lanthanide conjugates is reviewed in Chapter 3.

1.4.3 Tuftsin

Tuftsin is one of the targeting approaches employed for the attachment and internalisation of the designed probes in this project. Tuftsin is a tetrapeptide with the sequence Thr-Lys-Pro-Arg (TKPR), Figure 1.16a.[146] It is a naturally occurring peptide that derives from the antibody tail (or Fc region) of its larger parent molecule, immunoglobin G (IgG) which is a major class of antibodies/immunoglobin found in the blood. Tuftsin is released from IgG (also known as leukokinin) via proteolytic cleavage by leukokinase[147] or by an enzyme located in the spleen (tuftsin-endocarboxypeptidase).[148] The release of tuftsin from IgG and synthetic tuftsin are reported to stimulate a multitude of downstream effects such as phagocytosis,[149, 150] chemotaxis and cell motility,[151] as well as anti-bactericidal[152, 153] and anti-tumouricidal[154, 155] activity.

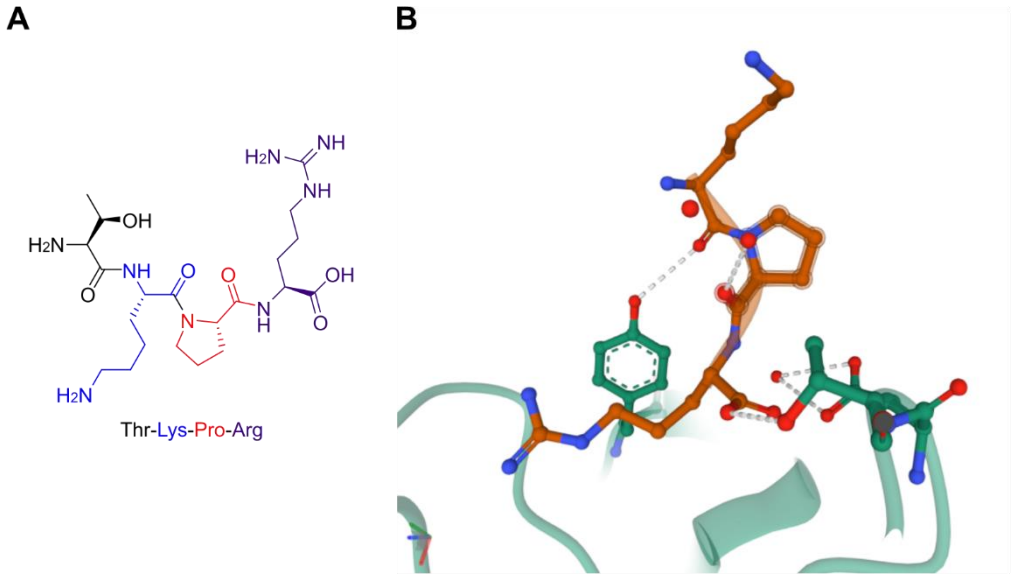


Figure 1.16. a) Structure of tuftsin; b) Binding of tuftsin in Nrp-1 domain (PDB 2ORZ) RCSB PDB.: https://www.rcsb.org/3d-view/2ORZ/1 generated using Mol.*[156]

Tuftsin binds to specific receptors that are found on macrophages and neutrophils (known as Fc receptors) and more recently tuftsin has been found to bind to neuropilin-1 (Np-1) receptor, Figure 1.16b, which is understood to regulate at least some of the downstream effects of tuftsin.[157] Studies involving the attachment of tuftsin to a fluorescent marker, rhodamine or FITC, demonstrated that tuftsin and its analogues are able to be internalised into cells via receptor-mediated endocytosis.[158, 159] The benefit of internalisation of probes, rather than just residing on the cell surface, is that it allows for a greater accumulation of the contrast agent in a specific location. For surface localised contrast agents, the limiting factor is the number of receptors on the cell's surface, as once occupied there are no further locations for the contrast agent to bind. On the other hand, probes that are able to enter the cell, via a receptor or otherwise, are able to accumulate in the cell whilst the receptors are returned to the cell's surface to aid further entry into the cell for the probe.

1.5 Aims and Objectives

Imaging inflammation using macrophage-targeting imaging agents is important in the development of a greater set of diagnostic tools and monitoring patient response to therapeutic treatments with inflammatory or autoimmune diseases. The main aim of this research is to develop novel imaging agents for inflammation targeting macrophages across a range of modalities: fluorescent, MR and photoacoustic.

Aims:

- To design and synthesise a series of alkyne-containing DOTA based imaging agent precursors for use in copper and strain-promoted alkyne-azide cycloaddition (Chapter 2, Figure 1.17).

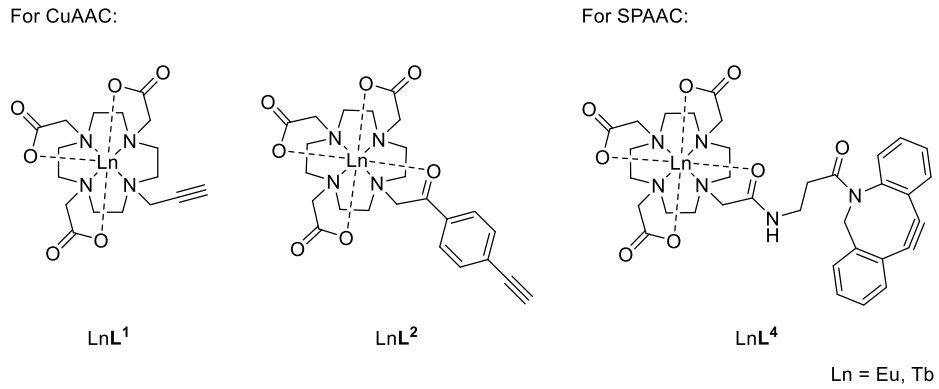


Figure 1.17. Series of alkyne-containing DOTA based imaging precursors for alkyne-azide cycloaddition.

- To design and synthesise a series of folate labelled DOTA based imaging agents and assess their photophysical properties for use as luminescent probes (Chapter 3, Figure 1.18).

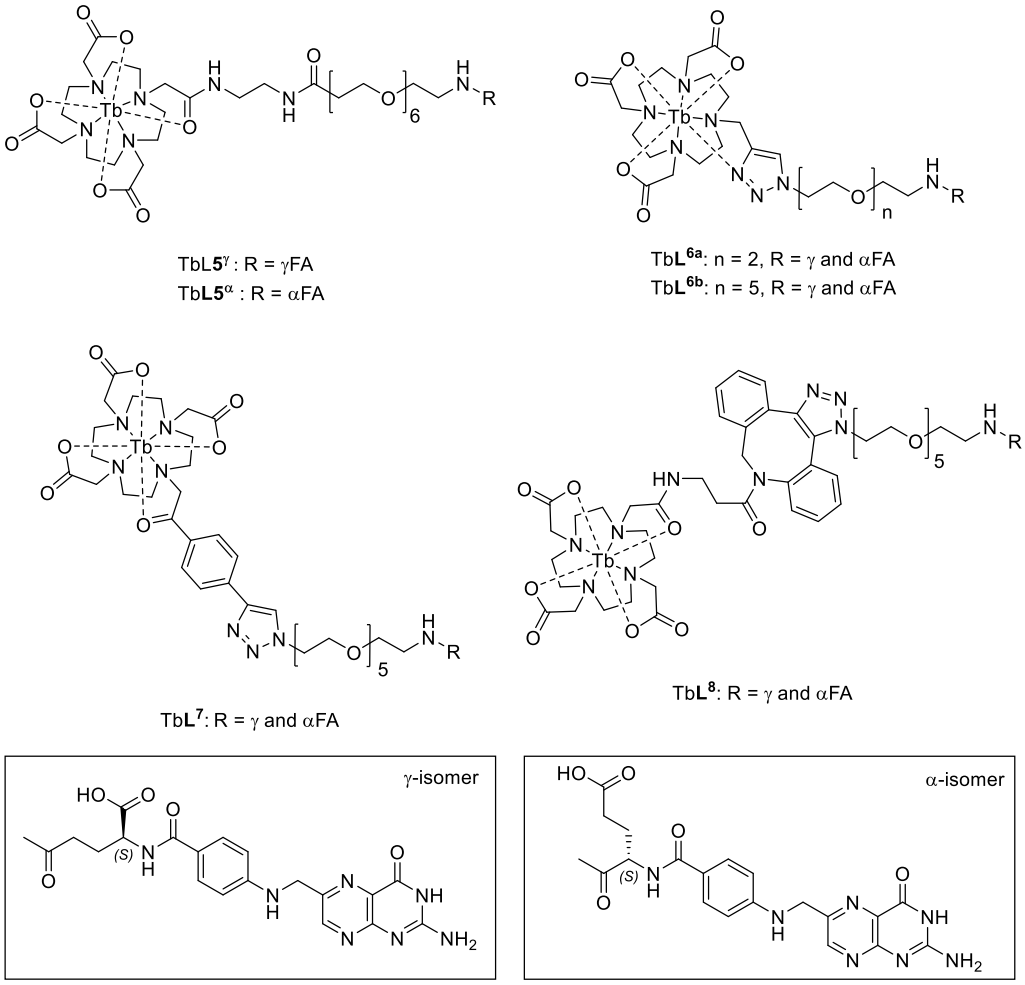


Figure 1.18. Series of folate labelled DOTA based fluorescent imaging agents.

- To synthesise tuftsin-labelled DOTA based imaging agents and assess their suitability as luminescent probes and MRI contrast agents. Using a diffusion NMR technique, INDIANA (in cell diffusion analysis), they will be compared to the commercially available DOTAREM in

human blood plasma and whole human blood, aiming to understand the effect of the targeting moiety for cell internalisation (Chapter 4, Figure 1.19).

- To design and synthesise a macrophage targeting photoacoustic imaging agent and assess the photophysical and photoacoustic properties (Chapter 5, Figure 1.19).

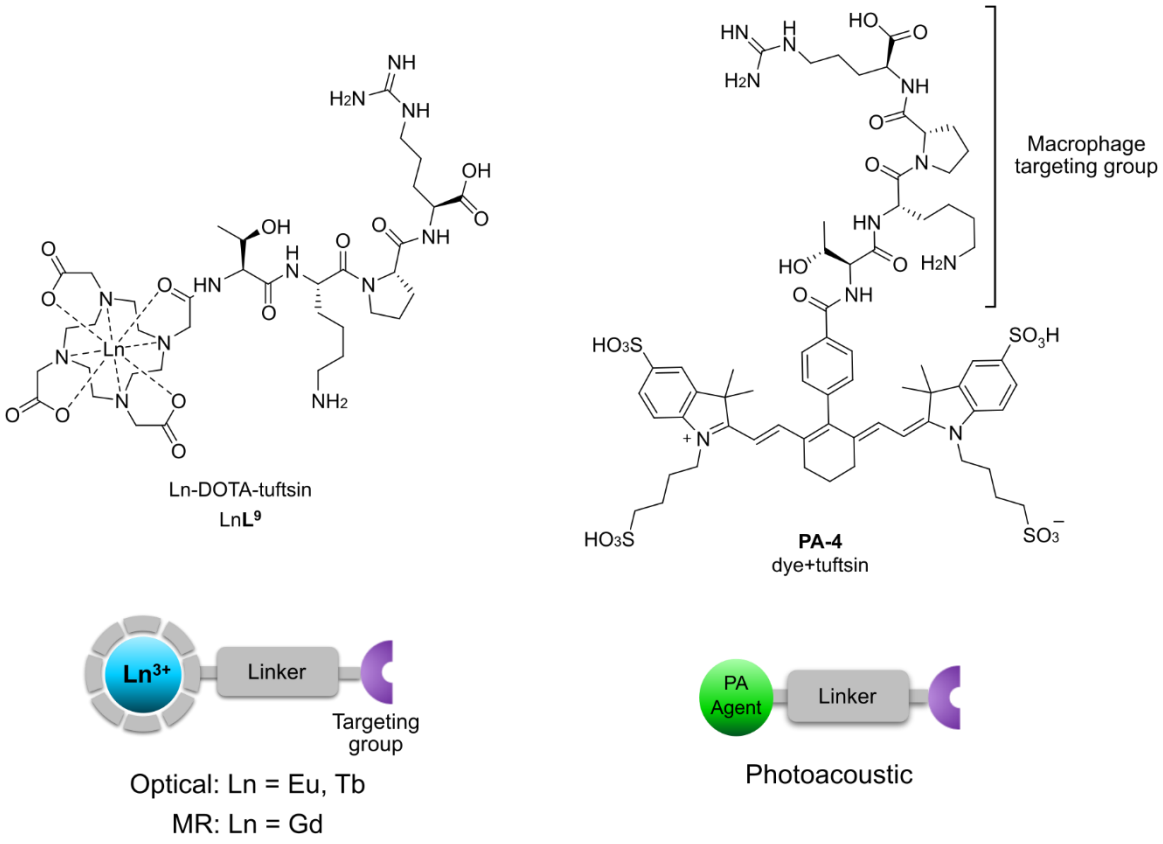


Figure 1.19. Macrophage targeting probes using the tuftsin targeting moiety for optical and MR imaging (left) and photoacoustic imaging (right).

1.6 References

1. M. Y. Berezin, K. Guo, W. Akers, J. Livingston, M. Solomon, H. Lee, K. Liang, A. Agee and S. Achilefu, *Biochemistry*, 2011, **50**, 2691-2700.
2. S. Reuter, S. C. Gupta, M. M. Chaturvedi and B. B. Aggarwal, *Free Radical Biol. Med.*, 2010, **49**, 1603-1616.
3. F. L. Heppner, R. M. Ransohoff and B. Becher, *Nat. Rev. Neurosci.*, 2015, **16**, 358-372.
4. *Immunology*, ed. D. Male, S. Peebles and V. Male, Elsevier, Edinburgh, 9th edn., 2021.
5. R. Medzhitov, *Nature*, 2008, **454**, 428-435.
6. H. Anderton, I. P. Wicks and J. Silke, *Nat. Rev. Rheumatol.*, 2020, **16**, 496-513.
7. R. Medzhitov, *Cell*, 2010, **140**, 771-776.
8. C. Nathan, *Nat. Rev. Immunol.*, 2006, **6**, 173-182.
9. C. M. Le, *Nat. Chem.*, 2022, **14**, 476.
10. S. Basu, H. M. Zhuang, D. A. Torigian, J. Rosenbaum, W. G. Chen and A. Alavi, *Semin. Nucl. Med.*, 2009, **39**, 124-145.
11. C. X. Wu, F. Li, G. Niu and X. Y. Chen, *Theranostics*, 2013, **3**, 448-466.
12. C. Giraudo, L. Evangelista, A. S. Fraia, A. Lupi, E. Quaia, D. Cecchin and M. Casali, *Int. J. Mol. Sci.*, 2020, **21**, 894.
13. W. B. Saunders, in *Nuclear Medicine*, ed. H. A. Zeissman, J. P. O'Malley, J. H. Thrall, Elsevier Mosby, Philadelphia, PA, 4th edn., 2014, ch. 14, pp. 322-349.
14. M. J. Uddin, A. Vemulapalli, H. Niitsu, B. C. Crews, C. G. Oltman, P. J. Kingsley, T. E. Kavanaugh, S. K. Bedingfield, J. O. McIntyre, M. Milad, A. M. Aleem, R. J. Coffey, C. L. Duvall and L. J. Marnett, *ACS Med. Chem. Lett.*, 2020, **11**, 1875-1880.
15. A. Bhardwaj, J. Kaur, F. Wuest and E. E. Knaus, *ChemMedChem*, 2014, **9**, 109-116.
16. C. F. Liu, C. Yang, L. H. Lu, W. H. Wang, W. H. Tan, C. H. Leung and D. L. Ma, *Chem. Comm.*, 2017, **53**, 2822-2825.
17. S. Dasari, A. K. Maparu, Z. Abbas, P. Kumar, H. Birla, S. Sivakumar and A. K. Patra, *Eur. J. Inorg. Chem.*, 2020, **31**, 2998-3009.
18. M. Laube, T. Kniess and J. Pietzsch, *Molecules*, 2013, **18**, 6311-6355.
19. J. H. Ryu, A. Lee, J. U. Chu, H. Koo, C. Y. Ko, H. S. Kim, S. Y. Yoon, B. S. Kim, K. Choi, I. C. Kwon, K. Kim and I. Youn, *Arthritis Rheum.*, 2011, **63**, 3824-3832.
20. W. C. Parks, C. L. Wilson and Y. S. Lopez-Boado, *Nat. Rev. Immunol.*, 2004, **4**, 617-629.
21. A. Signore, M. Chianelli, A. Annovazzi, E. Bonanno, L. G. Spagnoli, P. Pozzilli, F. Pallone and L. Biancone, *J. Nucl. Med.*, 2000, **41**, 242-249.
22. A. Annovazzi, E. Bonanno, M. Arca, C. D'Alessandria, A. Marcoccia, L. G. Spagnoli, F. Violi, F. Scopinaro, G. De Toma and A. Signore, *Eur. J. Nucl. Med. Mol. Imaging*, 2006, **33**, 117-126.

23. V. Di Gialleonardo, A. Signore, A. Glaudemans, R. Dierckx and E. F. J. De Vries, *J. Nucl. Med.*, 2012, **53**, 679-686.
24. R. S. Sriranjan, J. M. Tarkin, N. R. Evans, E. P. V. Le, M. M. Chowdhury and J. H. F. Rudd, *Br. J. Pharmacol.*, 2021, **178**, 2186-2203.
25. W. C. Kreisl, M. Fujita, Y. Fujimura, N. Kimura, K. J. Jenko, P. Kannan, J. Hong, C. L. Morse, S. S. Zoghbi, R. L. Gladding, S. Jacobson, U. Oh, V. W. Pike and R. B. Innis, *Neuroimage*, 2010, **49**, 2924-2932.
26. P. Corcia, C. Tauber, J. Vercoullie, N. Arlicot, C. Prunier, J. Praline, G. Nicolas, Y. Venel, C. Hommet, J. L. Baulieu, J. P. Cottier, C. Roussel, M. Kassiou, D. Guilloteau and M. J. Ribeiro, *PLOS One*, 2012, **7**, DOI: 10.1371/journal.pone.0052941.
27. A. G. Horti, Y. J. Gao, H. T. Ravert, P. Finley, H. Valentine, D. F. Wong, C. J. Endres, A. V. Savonenko and R. F. Dannals, *Bioorg. Med. Chem.*, 2010, **18**, 5202-5207.
28. C. Jiang, H. W. Cai, X. D. Peng, P. Zhang, X. A. Wu and R. Tian, *Mol. Imaging*, 2017, **16**, 1-10.
29. N. Tahara, J. Mukherjee, H. J. de Haas, A. D. Petrov, A. Tawakol, N. Haider, A. Tahara, C. C. Constantinescu, J. Zhou, H. H. Boersma, T. Imaizumi, M. Nakano, A. Finn, Z. Fayad, R. Virmani, V. Fuster, L. Bosca and J. Narula, *Nat. Med.*, 2014, **20**, 215-219.
30. S. Put, S. Schoonooghe, N. Devoogdt, E. Schurgers, A. Avau, T. Mitera, M. D'Huyvetter, P. De Baetselier, G. Raes, T. Lahoutte and P. Matthys, *J. Nucl. Med.*, 2013, **54**, 807-814.
31. G. J. Stasiuk, H. Smith, M. Wylezinska-Arridge, J. L. Tremoleda, W. Trigg, S. K. Luthra, V. M. Iveson, F. N. E. Gavins and N. J. Long, *Chem. Commun.*, 2013, **49**, 564-566.
32. L. W. Locke, M. D. Chordia, Y. Zhang, B. Kundu, D. Kennedy, J. Landseadel, L. Xiao, K. D. Fairchild, S. S. Berr, J. Linden and D. F. Pan, *J. Nucl. Med.*, 2009, **50**, 790-797.
33. T. Boltersdorf, J. Ansari, E. Y. Senchenkova, L. J. Jiang, A. J. P. White, M. Coogan, F. N. E. Gavins and N. J. Long, *Dalton Trans.*, 2019, **48**, 16764-16775.
34. M. J. Turk, G. J. Breur, W. R. Widmer, C. M. Paulos, L. C. Xu, L. A. Grote and P. S. Low, *Arthritis Rheum.*, 2002, **46**, 1947-1955.
35. Y. Y. J. Gent, K. Weijers, C. F. M. Molthoff, A. D. Windhorst, M. C. Huisman, D. E. C. Smith, S. A. Kularatne, G. Jansen, P. S. Low, A. A. Lammertsma and C. J. van der Laken, *Arthritis Res. Ther.*, 2013, **15**, DOI: 10.1186/ar4191.
36. R. Aarons, PhD thesis, University of Manchester, 2004.
37. R. J. Aarons, J. K. Notta, M. M. Meloni, J. H. Feng, R. Vidyasagar, J. Narvainen, S. Allan, N. Spencer, R. A. Kauppinen, J. S. Snaith and S. Faulkner, *Chem. Commun.*, 2006, 909-911.
38. J. M. Tarkin, F. R. Joshi, N. R. Evans, M. M. Chowdhury, N. L. Figg, A. V. Shah, L. T. Starks, A. Martin-Garrido, R. Manavaki, E. Yu, R. E. Kuc, L. Grassi, R. Kreuzhuber, M. A. Kostadima, M. Frontini, P. J. Kirkpatrick, P. A. Coughlin, D. Gopalan, T. D. Fryer, J.

R. Buscombe, A. M. Groves, W. H. Ouwehand, M. R. Bennett, E. A. Warburton, A. P. Davenport and J. H. F. Rudd, *J. Am. Coll. Cardiol.*, 2017, **69**, 1774-1791.

39. F. E. Silverstein, G. Faich, J. L. Goldstein, L. S. Simon, T. Pincus, A. Whelton, R. Makuch, G. Eisen, N. M. Agarwal, W. F. Stenson, A. M. Burr, W. W. Zhao, J. D. Kent, J. B. Lefkowith, K. M. Verburg and G. S. Geis, *JAMA, J. Am. Med. Assoc.*, 2000, **284**, 1247-1255.
40. M. L. James and S. S. Gambhir, *Physiol. Rev.*, 2012, **92**, 897-965.
41. N. Sim and D. Parker, *Chem. Soc. Rev.*, 2015, **44**, 2122-2134.
42. I. Steinberg, D. M. Huland, O. Vermesh, H. E. Frostig, W. S. Tummers and S. S. Gambhir, *Photoacoustics*, 2019, **14**, 77-98.
43. T. Nagaya, Y. A. Nakamura, P. L. Choyke and H. Kobayashi, *Front. Oncol.*, 2017, **7**, DOI: 10.3389/fonc.2017.00314.
44. S. Faulkner, S. J. A. Pope and B. P. Burton-Pye, *Appl. Spectrosc. Rev.*, 2005, **40**, 1-31.
45. E. De Jesus, J. J. Keating, S. A. Kularatne, J. Jiang, R. Judy, J. Predina, S. Nie, P. Low and S. Singhal, *Int. J. Mol. Imaging*, 2015, **2015**, DOI: 10.1155/2015/469047.
46. D. B. Plewes and W. Kucharczyk, *J. Magn. Reson. Imaging*, 2012, **35**, 1038-1054.
47. M. C. Heffern, L. M. Matosziuk and T. J. Meade, *Chem. Rev.*, 2014, **114**, 4496-4539.
48. Y. Cao, L. J. Xu, Y. Kuang, D. S. Xiong and R. J. Pei, *J. Mater. Chem. B*, 2017, **5**, 3431-3461.
49. *The chemistry of contrast agents in medical magnetic resonance imaging*, ed. A. E. Merbach, L. Helm and É. Tóth, Wiley, Chichester, 2nd edn., 2013.
50. J. Wahsner, E. M. Gale, A. Rodríguez-Rodríguez and P. Caravan, *Chem. Rev.*, 2019, **119**, 957-1057.
51. B. Cox, J. G. Laufer, S. R. Arridge and P. C. Beard, *J. Biomed. Opt.*, 2012, **17**, 061202-1-061202-22
52. L. H. V. Wang and S. Hu, *Science*, 2012, **335**, 1458-1462.
53. R. E. Borg and J. Rochford, *Photochem. Photobiol.*, 2018, **94**, 1175-1209.
54. N. Sim, PhD thesis, Durham University, 2014.
55. N. Kaltsoyannis and P. Scott, *The f elements*, Oxford : Oxford University Press, Oxford New York, 1999.
56. G. A. Lawrance, *Introduction to coordination chemistry*, Wiley, Chichester, West Sussex, 2010.
57. J. M. Idee, M. Port, I. Raynal, M. Schaefer, S. Le Greneur and C. Corot, *Fundam. Clin. Pharmacol.*, 2006, **20**, 563-576.
58. S. Aime and P. Caravan, *J. Magn. Reson. Imaging*, 2009, **30**, 1259-1267.
59. C. Rydahl, H. S. Thomsen and P. Marckmann, *Invest. Radiol.*, 2008, **43**, 141-144.

60. U.K. Government, Drug Safety Update, https://www.gov.uk/drug-safety-update/gadolinium-containing-contrast-agents-removal-of-omniscan-and-iv-magnevist-restrictions-to-the-use-of-other-linear-agents, (accessed 08/04/2022).
61. J.-C. G. Bünzli and S. V. Eliseeva, in *Lanthanide Luminescence: Photophysical, Analytical and Biological Aspects*, eds. P. Hänninen and H. Härmä, Springer Berlin Heidelberg, Berlin, Heidelberg, 2011, pp. 1-45.
62. J.-C. G. Bunzli, *Coord. Chem. Rev.*, 2015, **293**, 19-47.
63. C. K. Jorgensen and B. R. Judd, *Molecular Physics*, 1964, **8**, 281-290.
64. B. R. Judd, *J. Chem. Phys.*, 1966, **44**, 839.
65. *Lanthanide Luminescence: Photophysical, Analytical and Biological Aspects*, eds. P. Hänninen and H. Härmä, Springer Berlin Heidelberg, Berlin, Heidelberg, 2011.
66. M. D. Ward, *Coord. Chem. Rev.*, 2010, **254**, 2634-2642.
67. D. L. Dexter, *J. Chem. Phys.*, 1953, **21**, 836-850.
68. T. Lazarides, D. Sykes, S. Faulkner, A. Barbieri and M. D. Ward, *Chem. Eur. J.*, 2008, **14**, 9389-9399.
69. T. Forster, *Discuss. Faraday Soc.*, 1959, 7-17.
70. A. Beeby, I. M. Clarkson, R. S. Dickins, S. Faulkner, D. Parker, L. Royle, A. S. de Sousa, J. A. G. Williams and M. Woods, *J. Chem. Soc., Perkin Trans. 2*, 1999, 493-503.
71. Y. Haas and G. Stein, *J. Phys. Chem.*, 1972, **76**, 1093-1104.
72. L. M. Manus, R. C. Strauch, A. H. Hung, A. L. Eckermann and T. J. Meade, *Anal. Chem.*, 2012, **84**, 6278-6287.
73. S. Aime, M. Botta and G. Ermondi, *Inorg. Chem.*, 1992, **31**, 4291-4299.
74. S. Aime, M. Botta, M. Fasano, M. P. M. Marques, C. Geraldes, D. Pubanz and A. E. Merbach, *Inorg. Chem.*, 1997, **36**, 2059-2068.
75. L. G. Nielsen and T. J. Sorensen, *Inorg. Chem.*, 2020, **59**, 94-105.
76. M. Purgel, Z. Baranyai, A. de Blas, T. Rodriguez-Blas, I. Banyai, C. Platas-Iglesias and I. Toth, *Inorg. Chem.*, 2010, **49**, 4370-4382.
77. K. J. Miller, A. A. Saherwala, B. C. Webber, Y. Wu, A. D. Sherry and M. Woods, *Inorg. Chem.*, 2010, **49**, 8662-8664.
78. M. Woods, Z. Kovacs, S. R. Zhang and A. D. Sherry, *Angew. Chem. Int. Ed.*, 2003, **42**, 5889-5892.
79. R. S. Ranganathan, N. Raju, H. Fan, X. Zhang, M. F. Tweedle, J. F. Desreux and V. Jacques, *Inorg. Chem.*, 2002, **41**, 6856-6866.
80. O. A. Blackburn, N. F. Chilton, K. Keller, C. E. Tait, W. K. Myers, E. J. L. McInnes, A. M. Kenwright, P. D. Beer, C. R. Timmel and S. Faulkner, *Angew. Chem. Int. Ed.*, 2015, **54**, 10783-10786.

81. S. Aime, A. Barge, M. Botta, A. S. De Sousa and D. Parker, *Angew. Chem. Int. Ed.*, 1998, **37**, 2673-2675.
82. M. Polasek, J. Kotek, P. Hermann, I. Cisarova, K. Binnemans and I. Lukes, *Inorg. Chem.*, 2009, **48**, 466-475.
83. G. T. Hermanson, in *Bioconjugate Techniques*, ed. G. T. Hermanson, Elsevier Inc, 3rd edn., 2013, ch.1, pp. 1-125.
84. G. T. Hermanson, in *Bioconjugate Techniques*, ed. G. T. Hermanson, Elsevier Inc, 3rd edn., 2013, ch.3, pp. 229-258.
85. J. M. Harris, N. E. Martin and M. Modi, *Clin. Pharmacokinet.*, 2001, **40**, 539-551.
86. Q. S. Chen, X. J. Meng, P. McQuade, D. Rubins, S. A. Lin, Z. Z. Zeng, H. Haley, P. Miller, D. G. Trotter and P. S. Low, *Mol. Pharmaceutics*, 2017, **14**, 4353-4361.
87. G. T. Hermanson, in *Bioconjugate Techniques*, ed. G. T. Hermanson, Elsevier Inc, 3rd edn., 2013, ch.17, pp. 757-785.
88. E. M. Sletten and C. R. Bertozzi, *Acc. Chem. Res.*, 2011, **44**, 666-676.
89. C. S. McKay and M. G. Finn, *Chem. Biol.*, 2014, **21**, 1075-1101.
90. R. Huisgen, *Angew. Chem. Int. Ed.*, 1963, **2**, 565-598.
91. H. C. Kolb, M. G. Finn and K. B. Sharpless, *Angew. Chem. Int. Ed.*, 2001, **40**, 2004-2021.
92. B. T. Worrell, J. A. Malik and V. V. Fokin, *Science*, 2013, **340**, 457-460.
93. L. Q. Jin, D. R. Tolentino, M. Melaimi and G. Bertrand, *Sci. Adv.*, 2015, **1**, DOI: 10.1126/sciadv.1500304.
94. V. Hong, S. I. Presolski, C. Ma and M. G. Finn, *Angew. Chem. Int. Ed.*, 2009, **48**, 9879-9883.
95. S. I. Presolski, V. P. Hong and M. G. Finn, *Current Protocols in Chemical Biology*, 2011, **3**, 153-162.
96. V. V. Rostovtsev, L. G. Green, V. V. Fokin and K. B. Sharpless, *Angew. Chem. Int. Ed.*, 2002, **41**, 2596-2599.
97. C. L. Dupont, G. Grass and C. Rensing, *Metallomics*, 2011, **3**, 1109-1118.
98. L. M. Gaetke and C. K. Chow, *Toxicology*, 2003, **189**, 147-163.
99. N. J. Agard, J. A. Prescher and C. R. Bertozzi, *J. Am. Chem. Soc.*, 2005, **127**, 11196-11196.
100. K. W. Dehnert, J. M. Baskin, S. T. Laughlin, B. J. Beahm, N. N. Naidu, S. L. Amacher and C. R. Bertozzi, *ChemBioChem*, 2012, **13**, 353-357.
101. P. V. Chang, J. A. Prescher, E. M. Sletten, J. M. Baskin, I. A. Miller, N. J. Agard, A. Lo and C. R. Bertozzi, *Proc. Natl. Acad. Sci. U.S.A.*, 2010, **107**, 1821-1826.
102. J. S. Smolen, D. Aletaha, A. Barton, G. R. Burmester, P. Emery, G. S. Firestein, A. Kavanaugh, I. B. McInnes, D. H. Solomon, V. Strand and K. Yamamoto, *Nat. Rev. Dis. Primers*, 2018, **4**, DOI: 10.1038/nrdp.2018.1

103. M. A. Boutet, G. Courties, A. Nerviani, B. Le Goff, F. Apparailly, C. Pitzalis and F. Blanchard, *Autoimmun. Rev.*, 2021, **20**, DOI: 10.1016/j.autrev.2021.102758.
104. M. M. Steinz, A. Ezdoglian, F. Khodadust, C. F. M. Molthoff, M. Srinivasarao, P. S. Low, G. J. C. Zwezerijnen, M. Yaqub, W. Beaino, A. D. Windhorst, S. W. Tas, G. Jansen and C. J. van der Laken, *Front. Immunol.*, 2022, **13**, DOI: 10.3389/fimmu.2022.819163.
105. R. B. Zhao, L. H. Matherly and I. D. Goldman, *Expert Rev. Mol. Med.*, 2009, **11**, e4, DOI: 10.1017/S1462399409000969.
106. Z. J. Hou and L. H. Matherly, *Exchangers*, 2014, **73**, 175-204.
107. S. Sabharanjak and S. Mayor, *Adv. Drug Delivery Rev.*, 2004, **56**, 1099-1109.
108. R. B. Zhao, N. Diop-Bove, M. Visentin and I. D. Goldman, *Ann. Rev. Nutr.*, 2011, **31**, 177-201.
109. G. R. Westerhof, G. Jansen, N. Vanemmerik, I. Kathmann, G. Rijksen, A. L. Jackman and J. H. Schornagel, *Cancer Res.*, 1991, **51**, 5507-5513.
110. A. Puig-Kroger, E. Sierra-Filardi, A. Dominguez-Soto, R. Samaniego, M. T. Corcuera, F. Gomez-Aguado, M. Ratnam, P. Sanchez-Mateos and A. L. Corbi, *Cancer Res.*, 2009, **69**, 9395-9403.
111. S. D. Weitman, R. H. Lark, L. R. Coney, D. W. Fort, V. Frasca, V. R. Zurawski and B. A. Kamen, *Cancer Res.*, 1992, **52**, 3396-3401.
112. N. Parker, M. J. Turk, E. Westrick, J. D. Lewis, P. S. Low and C. P. Leamon, *Anal. Biochem.*, 2005, **338**, 284-293.
113. W. Xia, A. R. Hilgenbrink, E. L. Matteson, M. B. Lockwood, J. X. Cheng and P. S. Low, *Blood*, 2009, **113**, 438-446.
114. C. M. Paulos, M. J. Turk, G. J. Breur and P. S. Low, *Adv. Drug Delivery Rev.*, 2004, **56**, 1205-1217.
115. J. W. van der Heijden, R. Oerlemans, B. A. C. Dijkmans, H. Qi, C. J. van der Laken, W. F. Lems, A. L. Jackman, M. C. Kraan, P. P. Tak, M. Ratnam and G. Jansen, *Arthritis Rheum.*, 2009, **60**, 12-21.
116. V. B. Kraus, G. McDaniel, J. L. Huebner, T. V. Stabler, C. F. Pieper, S. W. Shipes, N. A. Petry, P. S. Low, J. Shen, T. A. McNearney and P. Mitchell, *Osteoarthr. Cartil.*, 2016, **24**, 1613-1621.
117. D. M. S. H. Chandrupatla, G. Jansen, E. Mantel, P. S. Low, T. Matsuyama, R. P. Musters, A. D. Windhorst, A. A. Lammertsma, C. F. M. Molthoff and C. J. van der Laken, *Contrast Media Mol. Imaging*, 2018, **2018**, DOI: 10.1155/2018/8092781.
118. D. Chandrupatla, C. F. M. Molthoff, A. A. Lammertsma, C. J. van der Laken and G. Jansen, *Drug Delivery Transl. Res.*, 2019, **9**, 366-378.

119. D. M. S. H. Chandrupatla, G. Jansen, R. Vos, M. Verlaan, Q. Chen, P. S. Low, A. D. Windhorst, A. A. Lammertsma, C. J. van der Laken and C. F. M. Molthoff, *Arthritis Res. Ther.*, 2017, **19**, DOI: 10.1186/s13075-017-1325-x.
120. P. S. Low, W. A. Henne and D. D. Doorneweerd, *Acc. Chem. Res.*, 2008, **41**, 120-129.
121. J. Sudimack and R. J. Lee, *Adv. Drug Delivery Rev.*, 2000, **41**, 147-162.
122. C. P. Leamon and P. S. Low, *Biochem. J.*, 1993, **291**, 855-860.
123. A. S. Wibowo, M. Singh, K. M. Reeder, J. J. Carter, A. R. Kovach, W. Y. Meng, M. Ratnam, F. M. Zhang and C. E. Dann, *Proc. Natl. Acad. Sci. U.S.A.*, 2013, **110**, 15180-15188.
124. R. J. Lee, S. Wang and P. S. Low, *Biochim. Biophys. Acta - Mol. Cell Res.*, 1996, **1312**, 237-242.
125. S. Wang, J. Luo, D. A. Lantrip, D. J. Waters, C. J. Mathias, M. A. Green, P. L. Fuchs and P. S. Low, *Bioconjugate Chem.*, 1997, **8**, 673-679.
126. C. Chen, J. Y. Ke, X. E. Zhou, W. Yi, J. S. Brunzelle, J. Li, E. L. Yong, H. E. Xu and K. Melcher, *Nature*, 2013, **500**, 486-489.
127. S. Wang, R. J. Lee, C. J. Mathias, M. A. Green and P. S. Low, *Bioconjugate Chem.*, 1996, **7**, 56-62.
128. C. Corot, P. Robert, E. Lancelot, P. Prigent, S. Ballet, I. Guilbert, J. S. Raynaud, I. Raynal and M. Port, *Magn. Reson. Med.*, 2008, **60**, 1337-1346.
129. T. L. Kalber, N. Kamaly, P. W. So, J. A. Pugh, J. Bunch, C. W. McLeod, M. R. Jorgensen, A. D. Miller and J. D. Bell, *Mol. Imaging Biol.*, 2011, **13**, 653-662.
130. Q. S. Chen, X. J. Meng, P. McQuade, D. Rubins, S. A. Lin, Z. Z. Zeng, H. Haley, P. Miller, D. G. Trotter and P. S. Low, *Mol. Pharmaceutics*, 2016, **13**, 1520-1527.
131. S. G. Konig and R. Kramer, *Chem. Eur. J.*, 2017, **23**, 9306-9312.
132. *World pat.*, WO99/59640, 1999.
133. S. Quici, A. Casoni, F. Foschi, L. Armelao, G. Bottaro, R. Seraglia, C. Bolzati, N. Salvarese, D. Carpanese and A. Rosato, *J. Med. Chem.*, 2015, **58**, 2003-2014.
134. Z. L. Du, G. N. Borlace, R. D. Brooks, R. N. Butler, D. A. Brooks and S. E. Plush, *Inorg. Chim. Acta*, 2014, **410**, 11-19.
135. Z. L. Du, J. Sun, C. A. Bader, D. A. Brooks, M. Q. Li, X. Li and S. E. Plush, *J. Inorg. Biochem.*, 2018, **178**, 32-42.
136. C. P. Leamon, I. Pastan and P. S. Low, *J. Biol. Chem.*, 1993, **268**, 24847-24854.
137. C. J. Mathias, S. Wang, R. J. Lee, D. J. Waters, P. S. Low and M. A. Green, *J. Nucl. Med.*, 1996, **37**, 1003-1008.
138. W. Xia, A. R. Hilgenbrink, E. L. Matteson, M. B. Lockwood, J.-X. Cheng and P. S. Low, *Blood*, 2009, **113**, 438-446.

139. B. A. Siegel, F. Dehdashti, D. G. Mutch, D. A. Podoloff, R. Wendt, G. P. Sutton, R. W. Burt, P. R. Ellis, C. J. Mathias, M. A. Green and D. M. Gershenson, *J. Nucl. Med.*, 2003, **44**, 700-707.

140. S. A. Kularatne, M. J. Belanger, X. J. Meng, B. M. Connolly, A. Vanko, D. L. Suresch, I. Guenther, S. B. Wang, P. S. Low, P. McQuade and D. G. Trotter, *Mol. Pharmaceutics*, 2013, **10**, 3103-3111.

141. O. Saborowski, G. H. Simon, H. J. Raatschen, M. F. Wendland, Y. J. Fu, T. Henning, R. Baehner, C. Corot, M. H. Chen and H. E. Daldrup-Link, *Contrast Media Mol. Imaging*, 2007, **2**, 72-81.

142. C. H. Tung, Y. H. Lin, W. K. Moon and R. Weissleder, *ChemBioChem*, 2002, **3**, 784-786.

143. D. Messeri, PhD thesis, University of Durham, 2001.

144. S. M. Lee, H. M. Chen, T. V. O'Halloran and S. T. Nguyen, *J. Am. Chem. Soc.*, 2009, **131**, 9311-9320.

145. M. Dzwonek, D. Zalubiniak, P. Piatek, G. Cichowicz, S. Meczynska-Wielgosz, T. Stepkowski, M. Kruszewski, A. Wieckowska and R. Bilewicz, *RSC Adv.*, 2018, **8**, 14947-14957.

146. V. A. Najjar, *Ann. N.Y. Acad. Sci.*, 1983, **419**, 1-11.

147. V. A. Najjar and K. Nishioka, *Nature*, 1970, **228**, 672-673.

148. K. Nishioka, J. McMurray, F. AlObeidi and B. M. Pettitt, *Curr. Med. Chem.*, 1996, **3**, 153-166.

149. A. Wardowska, K. Dzierzbicka, P. Trzonkowski and A. Myśliwski, *Acta Pol. Pharm.*, 2006, **63**, 378-385.

150. M. Fridkin and V. A. Najjar, *Crit. Rev. Biochem. Mol. Biol.*, 1989, **24**, 1-40.

151. I. Z. Siemion and A. Kluczyk, *Peptides*, 1999, **20**, 645-674.

152. Z. Baranyai, M. Kratky, R. Vosatka, E. Szabo, Z. Senoner, S. David, J. Stolarikova, J. Vinsova and S. Bosze, *Eur. J. Med. Chem.*, 2017, **133**, 152-173.

153. G. Mezo, A. Kalaszi, J. Remenyi, Z. Majer, A. Hilbert, O. Lang, L. Kohidai, K. Barna, D. Gaal and F. Hudecz, *Biopolymers*, 2004, **73**, 645-656.

154. V. A. Najjar, D. Konopinska, M. K. Chaudhuri, D. E. Schmidt and L. Linehan, *Mol. Cell. Biochem.*, 1981, **41**, 3-12.

155. K. Nishioka, *Br. J. Cancer*, 1979, **39**, 342-345.

156. D. Sehnal, S. Bittrich, M. Deshpande, R. Svobodova, K. Berka, V. Bazgier, S. Velankar, S. K. Burley, J. Koca and A. S. Rose, *Nucleic Acids Res.*, 2021, **49**, W431-W437.

157. M. A. von Wronski, N. Raju, R. Pillai, N. J. Bogdan, E. R. Marinelli, P. Nanjappan, K. Ramalingam, T. Arunachalam, S. Eaton, K. E. Linder, F. Yan, S. Pochon, M. F. Tweedle and A. D. Nunn, *J. Biol. Chem.*, 2006, **281**, 5702-5710.

158. P. Gottlieb, E. Hazum, E. Tzehoval, M. Feldman, S. Segal and M. Fridkin, *Biochem. Biophys. Res. Commun.*, 1984, **119**, 203-211.

159. A. A. Amoscato, P. J. A. Davies, G. F. Babcock and K. Nishioka, *Ann. N.Y. Acad. Sci.*, 1983, **419**, 114-134.

2 Ligands for azide-alkyne cycloadditions

2.1 Introduction

"Click" chemistry has risen to prominence because of the ease and versatility of producing new carbon-heteroatom bonds with consistently high yields using high energy reactants to control the outcome, and it shows good tolerance for different functional groups.[1] The Huisgen 1,3-cycloaddition of azides with terminal alkynes to produce 1,2,3-triazoles typifies click chemistry, because of its functional-group tolerance, ease of synthesis of the azides and alkyne precursors and the kinetic stability of the resultant triazole.[2, 3] Azide-alkyne cycloaddition was further developed by the Meldal and Sharpless groups as a variation involving copper(I) to catalyse the reaction between terminal alkynes and azides, accelerating the rate of reaction by $\sim 10^6$ compared to the Huisgen cycloaddition.[1, 4] Previously within the Faulkner group, it has been demonstrated that CuAAC provides a convenient way to attach a lanthanide imaging agent to a targeting group and could be extended to our application.[5] However, due to the cytotoxicity of residual copper ions, it reduces the *in vivo* applicability.[6, 7]

Therefore, alternative 1,3-cycloadditions have been widely researched to allow the reaction to proceed without a copper catalyst. The alkyne is a poor 1,3-dipolar acceptor, so two methods can be employed to narrow the HOMO-LUMO energy gap to promote the azide-alkyne cycloaddition: destabilise the reactants or lower the energy of the transition state. First reported by Wittig and Krebs in 1961, "explosive" reactivity was observed between cyclooctyne and phenylazide stemming from the strain in cyclooctyne ring.[8] Following on from their work, Bertozzi and coworkers demonstrated that cyclooctyne rings could be used for *in vivo* detection of azides through strain-promoted azide-alkyne cycloaddition (SPAAC) (Figure 2.1).[9-12] They summarised their work on cyclooctyne reactions in a key review.[13]

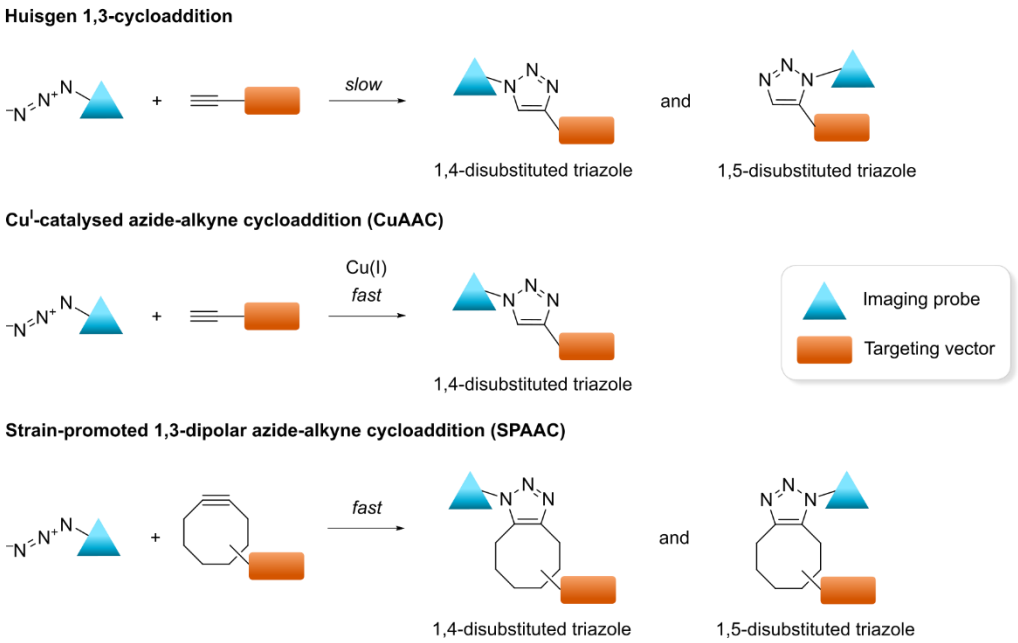


Figure 2.1. Huisgen 1,3-cycloaddition, copper(I)-catalysed azide-alkyne cycloaddition (CuAAC) and strain-promoted azide-alkyne cycloaddition (SPAAC).

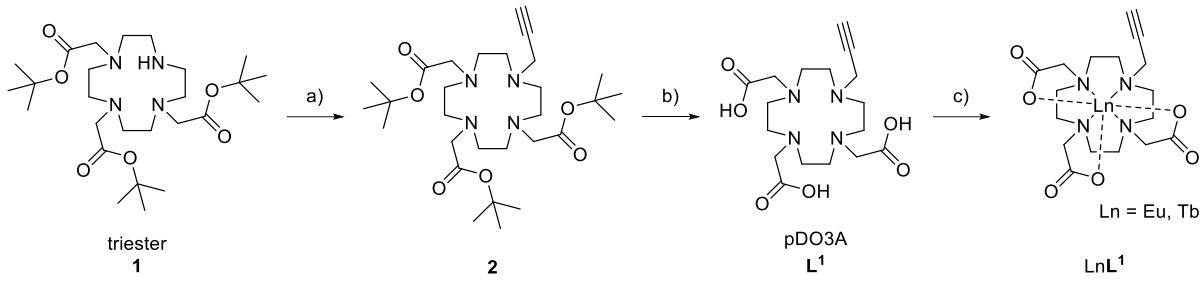
The strain imposed on the acetylene bond causes a deformation to 163° from the preferred linear state; this corresponds to ~18 kcal/mol of destabilisation which is able to increase the rate of cycloaddition with azides compared to unstrained alkynes.[12] Strained alkynes were further explored by addition of electron-withdrawing groups to make the cyclooctyne electron-poor;[11] alternatively, extra ring strain can be forced through the introduction of two conjugated benzene rings (dibenzocyclooctyne, DBCO), which both increased the rate of cycloaddition.[12] Earlier work by the Faulkner group demonstrated that DBCO can be attached to the 1,4,7,10-tetraazacyclododecane-1,4,7-triacetate (DO3A) free pendant arm[14] and that cycloaddition is unhindered by the metal complex. Given the ability of the DBCO to react with azides in the absence of a copper(I) catalyst, and their ability for functionalisation with DO3A, this was selected for this project. The azide can be further functionalised which can link to groups that target cells of interest, in this case it was proposed that tuftsin and folate azide groups could be used for cycloaddition.

2.2 Synthesis of alkyne complexes

2.2.1 Alkynes for copper-catalysed click chemistry, L^1 and L^2

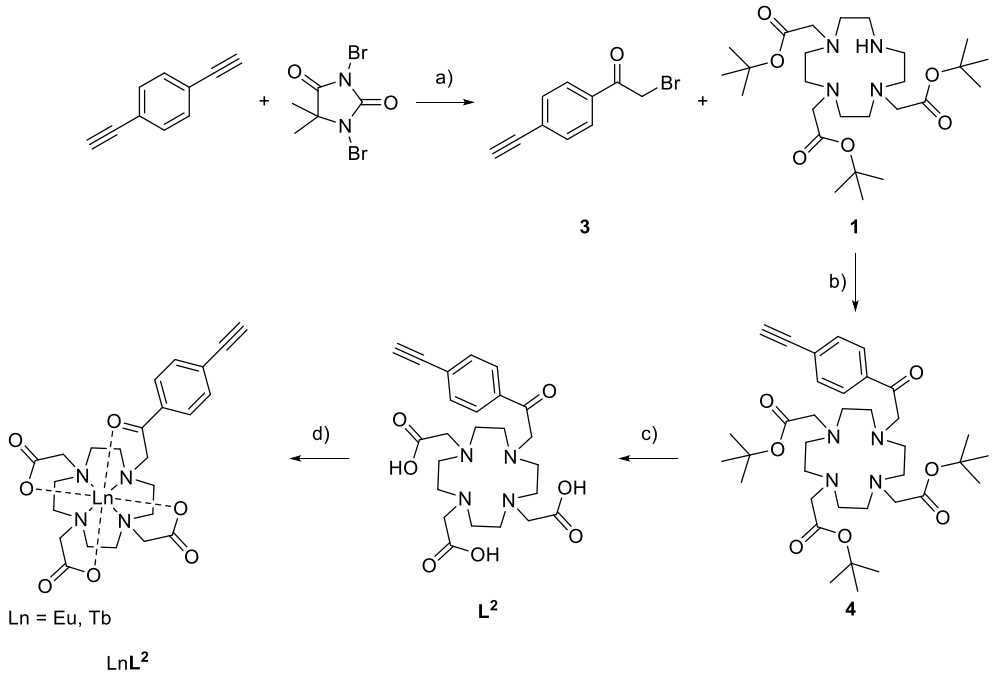
For the purpose of CuAAC, propargyl DO3A (pDO3A, $\mathbf{L^1}$) was synthesised, which had been previously reported for click chemistry.[5, 15, 16] The synthesis of LnpDO3A, Ln$\mathbf{L^1}$ complex is outlined in Scheme 2.1. Firstly, triester, **1**, was synthesised following literature procedures,[17] and then the fourth nitrogen was alkylated using potassium carbonate as base before slow addition of propargyl bromide (70% yield). Deprotection of the *tert*-butyl ester was achieved by using TFA in DCM followed by precipitation of the triacid in diethyl ether as the triflate salt (64% yield). Lanthanide

complexation used a slight excess of the lanthanide salt (1.05 eq.) with the ligand heated in methanol for 48 hours (86% yield).



Scheme 2.1. Synthesis of Ln-propargyl DO3A complex. Reagents and conditions: a) propargyl bromide, K_2CO_3, MeCN, 0 °C → r.t., 16 h, 70%; b) TFA/DCM (1:1), r.t., 16-24 h, 64%; c) Ln(OTf)$_3$, MeOH, pH 5, 60 °C, 48 h, 86%.

The second alkyne synthesised for CuAAC was ethynylacetophenone DO3A (**L^2**, Scheme 2.2). This expanded structure includes a chromophore to act as a sensitiser for the metal centred luminescence, while the ketone oxygen acts an additional coordination donor site for the lanthanide centre – an 8-coordinate ligand compared to the 7-coordinate ligand, **L^1**. Similar acetophenone complexes have been previously prepared by Beeby *et al.* and were found to promote efficient lanthanide sensitisation.[18]



Scheme 2.2. Synthesis of ethynylacetophenoneDO3A. Reagents and conditions: a) ethylene thiourea, acetone:H_2O (100:1), 45 °C, 4 h, 19%; b) K_2CO_3, MeCN, r.t. → 60 °C, 16 h, 35%; c) TFA/DCM (1:1), r.t, 16-24 h, 90%; d) Ln(OTf)$_3$, MeOH, pH 5, 60 °C, 48 h, Eu = 31%; Tb = 79%.

The α-monobromo ketone, **3** was prepared following a slight adaptation of a one-step procedure reported by Wu *et al.* where the 1,4-diethynylbenzene reacted with 1,3-dihalo-5,5-dimethylhydantoin and water to form the 4'-ethynyl-2-bromoacetophenone.[19] The paper reports that

the more water-rich solvent mixture resulted in the formation of the dibrominated product, whereas with less water exclusively the monobrominated product was obtained in high yield, despite the two potential alkynyl groups and the four potential bromination products.[19] Unfortunately this was not found when the reaction was repeated and even with optimisation of the acetone:water ratios, multiple byproducts were observed when monitoring the reaction by TLC. Following purification, the α-monobromo ketone, **3** was obtained in sufficient yield (19% yield) to carry forward and was attached to triester, **1** by alkylation with potassium carbonate as base to give compound **4**, Scheme 2.2. Afterwards, the *tert*-butyl esters were cleaved using TFA to yield the ligand, $\mathbf{L^2}$. Complexation of the ligand, $\mathbf{L^2}$ was performed using triflate salts of europium and terbium and the complexes were subsequently purified on an alumina column.

2.2.2 Alkynes for strain-promoted click chemistry

As a result of difficulties in producing the strained alkynes, two different routes to produce a strained dibenzocyclooctyne attached to the DO3A macrocycle were investigated, resulting in two structures with differing linker groups (Figure 2.2). The principal difference between the two routes is the step at which the DO3A ligand (protected or deprotected) is attached to the dibenzocyclooctene/yne precursor. This will be discussed in the following sections. An additional benefit for both DBCO functionalised arms is that the carboxyl group can coordinate to the metal centre and provide further kinetic stability.

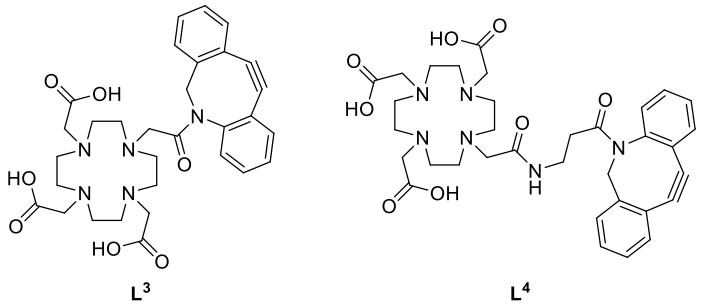


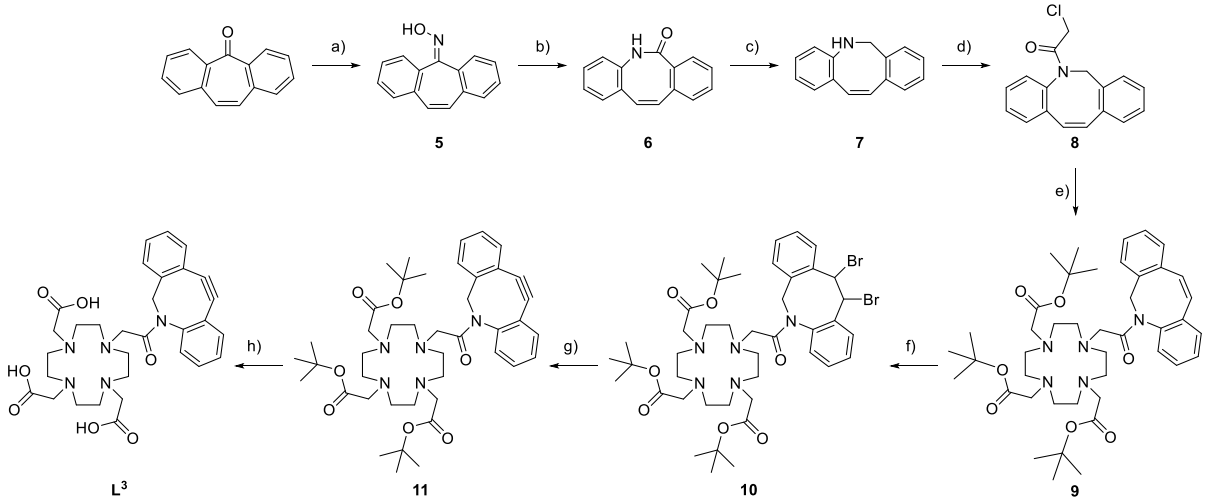
Figure 2.2. Two strained dibenzocyclooctynes attached to a DOTA-based macrocycle.

2.2.3 Synthesis of ligand, $\mathbf{L^3}$

The initial strategy involved attaching dibenzocylcooctene-chloroacetamide to triester, **1**, which had been previously carried out in the Faulkner group,[14] with the aim of using it in a click reaction with a targeting group attached to an azide. The triple bond is formed *in situ*, followed by deprotection of triester and lanthanide complexation to form the strained alkyne attached to the complexed DO3A structure, $\mathbf{L^3}$ (Scheme 2.3).

The chloroacetamide, **8**, and its precursors were synthesised according to literature procedures shown in Scheme 2.3.[20-22] The procedure was based on the Popik methodology due to its experimental simplicity and affordable reagents and this method has been later improved by Adronov

and colleagues to increase the yield.[22, 23] Oxime **5** was formed by reacting dibenzosuberenone with hydroxylammonium chloride in pyridine under reflux for 24 hours. Oxime **5** was precipitated in ice-cold 5% hydrochloric acid to yield a white solid in high purity.



Scheme 2.3. Synthesis of $^{t}Bu_3DO3A$-DIBAC. Reagents and conditions: a) $NH_2OH{\cdot}HCl$, pyridine, reflux, 20 h, 93%; b) PPA, 125 °C, 1.5 h, 81%; c) $LiAlH_4$, Et_2O, reflux, 40 h, 89%; d) $ClCOCH_2Cl$, DCM, Cs_2CO_3, 93%; e) $^{t}Bu_3DO3AH$, K_2CO_3, reflux, 48 h, 21%; f) pyridinium tribromide, r.t, overnight, 94%; g) 1.0 M $^{t}BuOK$ in THF, 65 h, 29%; h) TFA:DCM (1:1), r.t., 16 h.

Oxime **5** was used without further purification and was reacted with polyphosphoric acid to form the amide **6**, via the Beckmann rearrangement under acid catalysis. Following work up, amide **6** was produced as a grey powder in reasonable yield (45%). Minor polyphosphoric acid contamination was present but was not detrimental to the next step of the reaction and so was taken forward.

The amide **6** was reduced to amine **7** by lithium aluminium hydride under reflux in anhydrous diethyl ether overnight. There were initial difficulties with this step as, even when fitted with a water condenser, it was prone to drying out overnight, due to the low boiling point of diethyl ether (34.6 °C). To overcome this problem, the reaction was placed under a N_2 atmosphere with greased joints and then sealed to have a closed system to reduce solvent loss. An alternative would have been to use a solvent with a higher boiling point such as tetrahydrofuran (66 °C) or diisopropyl ether (68 °C). Furthermore, the 2 equivalents of lithium aluminium hydride used previously was found to be insufficient for the reaction to reach completion, most likely as a result of degradation of the $LiAlH_4$.[14] Therefore the amount of $LiAlH_4$ used was increased to 2.24 equivalents following the procedure by Meggers and colleagues.[20] Once the reaction had reached completion, the remaining $LiAlH_4$ was quenched by the addition of water and stirred for 30 minutes. Solid precipitates were removed by filtration and 5,6-dihydrodibenzo[b,f]azocine, amine **7**, extracted by washing with diethyl ether, and removing the solvent under reduced pressure. Further compound was extracted by dispersing the filter cake in more ether and repeating the separation process. Amine **7** was produced

in good yield and purity (deduced by NMR spectroscopy, Figure 2.3) as a yellow solid and was used without further purification.

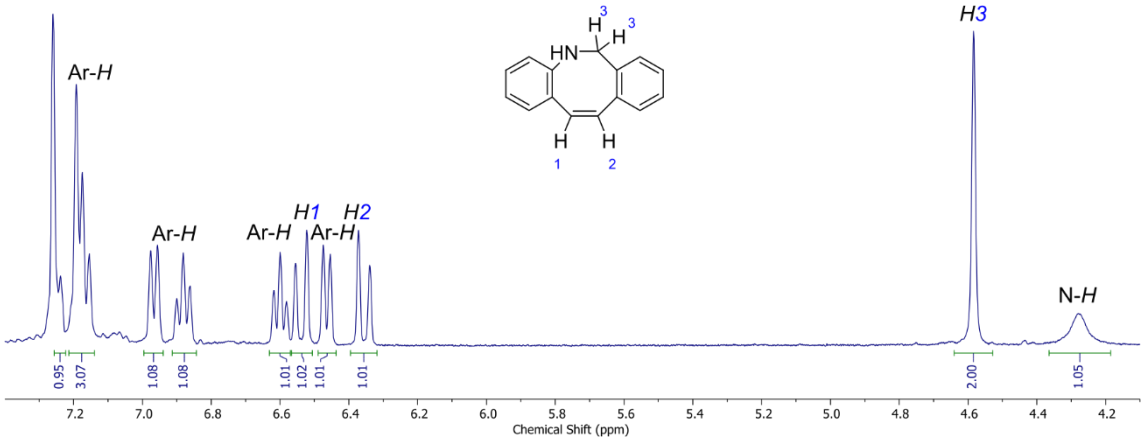


*Figure 2.3. ^{1}H NMR spectrum (400 MHz, $CDCl_3$) of 5,6-dihydrodibenzo[b,f]azocine, **7**.*

Chloroacetamide **8** was prepared by dropwise addition of chloroacetyl chloride to a stirred solution of amine **7** and caesium carbonate in DCM cooled to 0 °C, before being warmed to room temperature and stirred overnight. Following work up, the chloroacetamide **8** was obtained as a brown viscous oil in high yield and good purity (Figure 2.4).

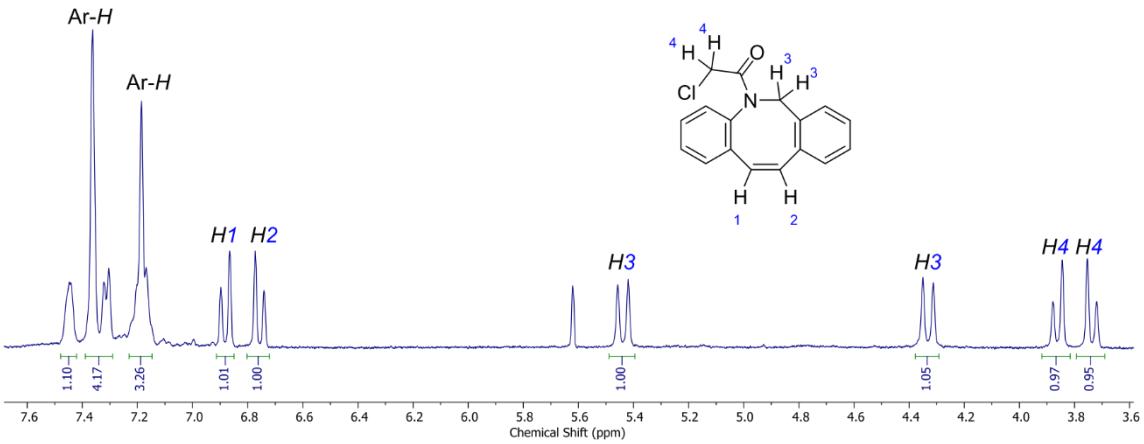


*Figure 2.4. ^{1}H NMR spectrum (400 MHz, acetone-d_6) of 2-chloro-1-(dibenzo[b,f]azocin-5(6H)-yl)ethan-1-one, **8**.*

Before the strained cyclooctyne could be synthesised, the chloroacetamide, **8** was attached to the fourth nitrogen atom of triester, **1**. The order is to avoid breaking the strained alkyne were it to be formed prior to being attached to triester as it involves high heat under basic conditions. Compound **9** was prepared by reacting **1** with chloroacetamide, **8**, in the presence of potassium carbonate (to deprotonate the amine) under reflux for 48 hours. Following removal of inorganic salts and solvent, compound **9** was produced as a brown solid with the correct mass confirmed by electrospray ionisation. The product was used without further purification, however in retrospect

further purification could have been explored, for example by column chromatography but the following reaction step proceeded smoothly.

The conversion of the chromophore on the DO3A pendant arm into DBCO first required the double halogenation of the C-C double bond. This was achieved by reacting compound **9** with pyridinium tribromide in DCM and stirred overnight. The solution was washed with 5% HCl, filtered, and solvent was removed to obtain the compound **10** as a pale brown crystalline solid and was confirmed by HRMS. Compound **10** contained two bromines, with two major isotopes of high natural abundance (^{79}Br - 51%; ^{81}Br - 49%). The HRMS is shown in Figure 2.5 and displays all combinations of the bromine isotopes with good alignment to the theoretical spectrum.

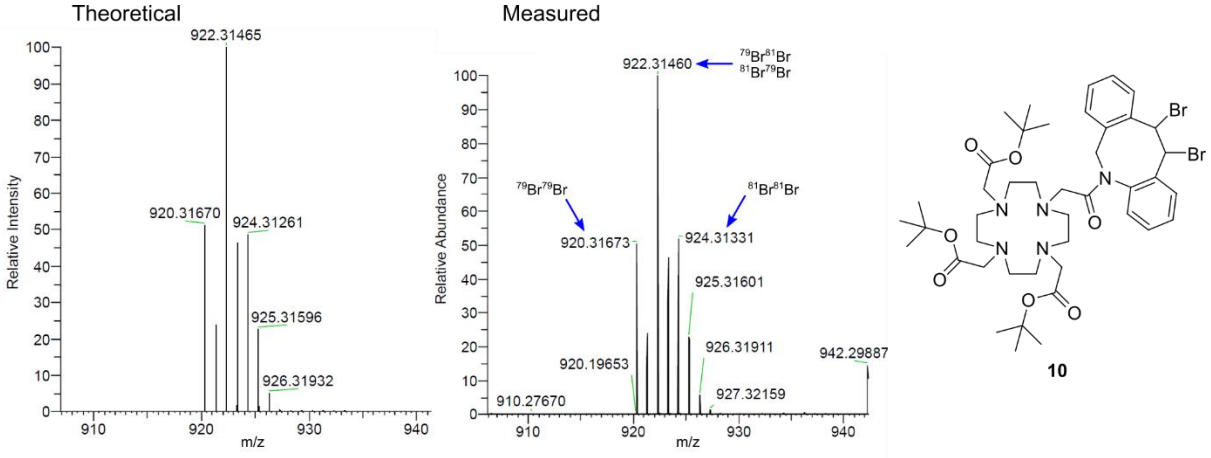


*Figure 2.5. Theoretical (left) and measured (right) mass spectrum of compound **10**.*

The DBCO pendant arm, **11**, proved difficult to synthesise, however this has been found by other research groups for the synthesis of the strained cyclooctyne.[14] Previously reported procedures by the group[14] and in literature[20-22, 24] involving relatively short reaction times (1 hour to overnight) and low temperatures (-40 °C – room temperature) and KOtBu were unsuccessful for obtaining DBCO attached to the DO3A triester. It was previously reported that use of the 1 M solution of KOtBu in THF improved the outcome of the reaction, as the solid KOtBu was found to result in unwanted side reactions.[24] It was also concluded that this would be a more concentrated form of the reagent as it was difficult to dissolve the KOtBu salt in small volumes of anhydrous THF. The reaction was attempted at the reaction conditions listed in Table 2.1. It was found that even when left for 64 hours to react at 45 °C that 2.5 equivalents of KOtBu was insufficient to reach completion, although analysis for the mass spectrum showed the presence of both the starting material and a compound with the same mass as the cyclooctyne, **11**. The most aggressive reaction conditions followed a similar approach to that of Adronov and coworkers where a further portion of KOtBu was added after the majority of the reaction had completed,[22] the aim being that this would ensure the second elimination of HBr was finished. Using this approach, the desired cyclooctyne, **11** was obtained as a reddy-brown solid but in relatively low yield (29%).

Table 2.1. Reaction conditions attempted for the didehalogenation step in the production of DIBAC attached to the DO3A-tBu ester.

Reaction temperature	**Form of KO*t*Bu**	**Equ. of KO*t*Bu**	**Reaction time (h)**	**Success**
Room temperature	KO*t*Bu salt	2.5	1	No
Room temperature	KO*t*Bu salt	2.5	2	No
Room temperature	1.0 M KO*t*Bu in THF	2.5	18	No
45 °C	1.0 M KO*t*Bu in THF	2.6	64	Partially
i) Room temperature ii) 45 °C	1.0 M KO*t*Bu in THF	i) 3 ii) 1.6	46 24	Yes

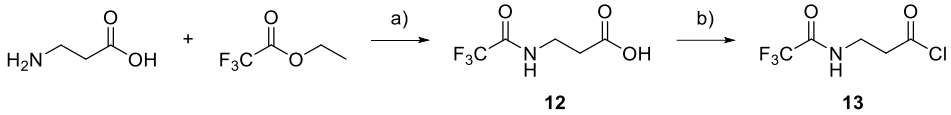
Although the correct mass (determined by electrospray mass spectrometry) is indicative of the formation of the alkyne bond, it has been previously found that similar systems underwent rearrangements to a molecule of equivalent mass.[25] It has also been reported that double HBr elimination is problematic for ester protecting groups on side chains attached to DBCO, so the tert-butyl ester protecting groups on the triester may be interfering with the reaction.[22] For the final step however to make ligand **L^3**, it was found that removal of the tert-butyl protecting groups with TFA destroyed the alkyne bond; this was in agreement with findings by Chigrinova *et al.*[25] Therefore an alternative synthesis of a strained alkyne ligand was needed.

2.2.4 Synthesis of ligand, L^4

An alternative synthetic strategy was employed to synthesise a dibenzocyclooctyne-amine (DBCO-amine) linker suitable for strain-promoted copper-free click chemistry. Commercially available DBCO-amine has also been used in this research,[26, 27] although it is currently expensive and only available in small quantities giving it limited practicality. Therefore, the aim was to synthesise larger quantities of DBCO-amine and bypass the cost restriction. In this synthesis, the alkyne linking group is synthesised initially and attached to DOTA-NHS ester; by synthesising it in this way, it avoids using TFA to deprotect the tert-butyl protecting groups and so prevents destruction of the alkyne bonds.

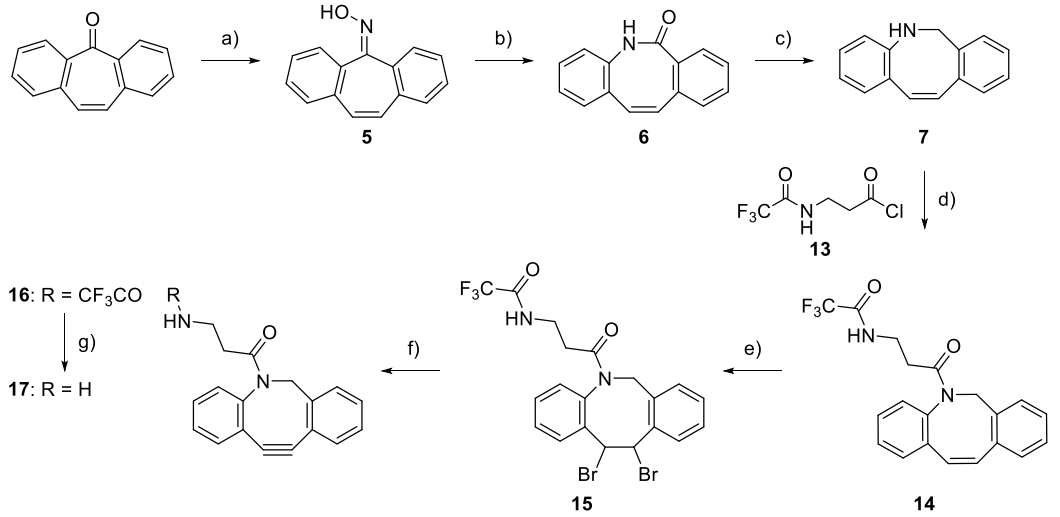
Initially *N*-trifluoroacetyl-β-alanyl chloride was synthesised to act as a linker to attach the dibenzocyclooctyne to the DOTA macrocycle. The synthesis is outlined in Scheme 2.4 following literature procedures.[21, 28] 4-Aminopropanoic acid was stirred in methanol and triethylamine to deprotonate the amine before reacting with the ethyl trifluoracetate to yield the *N*-trifluoroacetyl-β-alanine, **12**. The carboxylic acid was then cleanly converted into an acid chloride, **13**, using thionyl

chloride which was then readily attached to the dibenzocyclooctene through alkylation of the free amine.



*Scheme 2.4. Synthesis of N-trifluoroacetyl-β-chloride, **13**. Reagents and conditions: a) triethylamine, MeOH, r.t., 22 h, 87%; b) $SOCl_2$, reflux, 1.5-7 h, 96%.*

The synthetic route used to prepare the DBCO-amine, **17**, was reported by Popik and Adronov[21, 29] and outlined in Scheme 2.5. There is great interest in the synthesis of strained cyclooctynes and so there have been several papers on the optimisation of the synthesis of the DBCO-amine.[22, 29] The initial conversion of dibenzosubernone was carried out using pyridine in ethanol heated to reflux with hydroxylamine hydrochloride to produce the corresponding oxime, **5** at high yield (93%). The Beckmann rearrangement to expand the ring was initially carried out using polyphosphoric acid,[14, 20] but this was very difficult due to the high viscosity of the polyphosphoric acid, resulting in losses in the work up. Instead, it was decided to use Eaton's reagent (phosphorus pentoxide in methansulfonic acid) – the reaction was completed quickly after 30 minutes and quenched with water before multiple extractions with hot ethyl acetate to yield the amide at high yield (93%). The amide, **6** was then reduced to the amine using a larger excess of $LiAlH_4$ than used previously for the synthesis of **7** (Scheme 2.3) (10 eq. compared to 2.24 eq.), and it was necessary to keep this reaction topped up with dry Et_2O because evaporation losses occurred even with a water condenser.



*Scheme 2.5. Synthesis of dibenzocyclooctyne-amine, **17**. Reagents and conditions: a) $NH_2OH{\cdot}HCl$, pyridine, reflux, 20 h, 93%; b) Eaton's reagent, 100 °C, 30 mins, 93%; c) $LiAlH_4$, Et_2O, reflux, 40 h, 89%; d) pyridine, CH_2Cl_2, 89%; e) pyridinium tribromide, 82%; f) KO^{t}Bu, THF, 88%; g) K_2CO_3, aq. MeOH, 27%.*

Acylation of the dibenzocyclooctene was straightforward and this was followed by bromination, both following literature procedures.[21] As found previously, the challenging step was the double elimination of HBr to form the alkyne, **16**, however this was achieved using 2 portions of

KOtBu, 2.5 eq. later followed by an additional 1.25 eq., giving the alkyne in 88% yield. The importance of newly purchased or carefully stored KOtBu should be stressed, as this was pivotal in the formation of the alkyne.

The final step to deprotect the trifluoroacetamide protecting group from the amine on the linking chain, to obtain compound **17** proved challenging. Following literature,[21] it was cleaved using aqueous methanol and potassium carbonate, but poor conversion was found. Different ratios of methanol and water were attempted, as shown in Table 2.2; little difference was observed between conditions A and B as determined by TLC, but when using only methanol, little change from the starting material was found after 3 hours. The amide linkage to the dibenzocyclooctyne was also found to be cleaved (ESI *m/z* 206 $[M+H]^+$) and separation by column chromatography was difficult as the dibenzocyclooctyne and dibenzocyclotyne-amine ran almost analogously on the silica.

Table 2.2. Reaction conditions for the cleavage of the trifluoroacetamide protecting group.

Conditions	**MeOH**	**H_2O**	**K_2CO_3 equivalents**
A	2	1	2.0
B	10	3	2.0
C	1	-	2.0

Following purification by column chromatography multiple times, a small amount of pure DBCO-amine, **17** was obtained (41 mg, 27% yield) - NMR spectrum shown in Figure 2.6. Large scale synthesis was possible for steps a-f (Scheme 2.5) however this is in vain if the final step is not optimised further. For further improvements, alternative bases could be tried e.g. Na_2CO_3, $NaBH_4$ as well as different equivalents of base.[30]

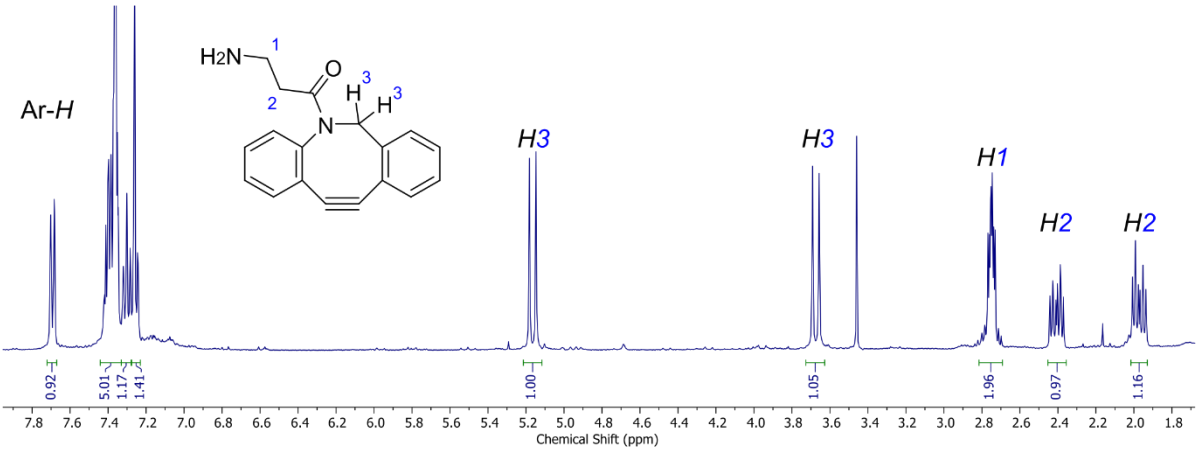
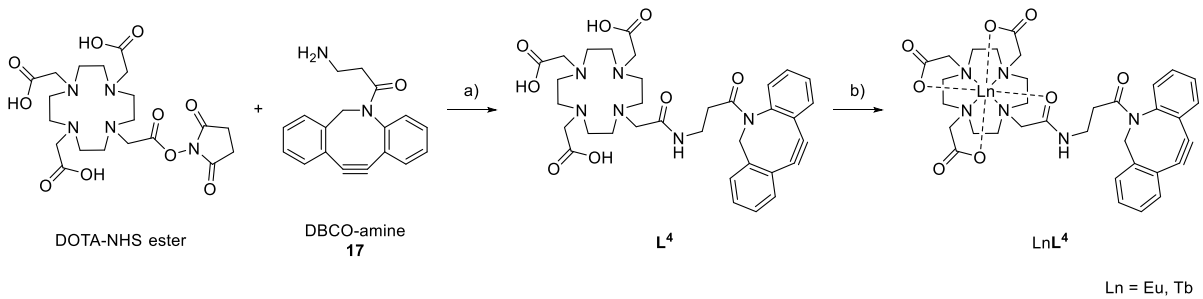


*Figure 2.6. ^1H NMR spectrum (400 MHz, $CDCl_3$) of N-(3-aminopropyl)-5,6-dihydro-11,12-didehydrodibenzo[b,f]azocine /DBCO-amine, **17**.*

Due to time constraints, DBCO-amine was purchased from BroadPharm to prepare the final complexes. DBCO-amine, **17** was reacted with the activated DOTA-NHS-ester which readily formed the amide linkage (Scheme 2.6). This was then purified by RP-HPLC under acidic conditions to obtain the pure DOTA-DBCO, $\mathbf{L^4}$ in reasonable yield (69%). Lanthanide complexation was then carried out with the corresponding triflate salt, and the product was purified on neutral alumina to yield the pure complex, Ln$\mathbf{L^4}$.



Scheme 2.6. Synthesis of Ln-DOTA-DBCO, Ln$\mathbf{L^4}$ Reagents and conditions: a) anhydrous DMF, TEA, r.t, 16 h, Ar, 69%, b) Ln(OTf)$_3$, H_2O/MeCN (7:3), 50 °C, 48 h, Eu = 112%; Tb = 154%*. *Excess mass attributed to salts; product used with salts.*

2.2.5 Scope of the probes

The alkyne probes used for this work are shown in Figure 2.7 and the europium and terbium complexes were made for each. The probes will include a seven-coordinate propargyl DO3A, $\mathbf{L^1}$, which once clicked will made an eight-coordinate complex, Ln$\mathbf{L^1}$. The extension of this was the ethynylacetophenoneDO3A, $\mathbf{L^2}$, which contains a chromophore to access indirect metal sensitisation. The final probe incorporates the strained cyclooctyne for SPAAC, Ln$\mathbf{L^4}$.

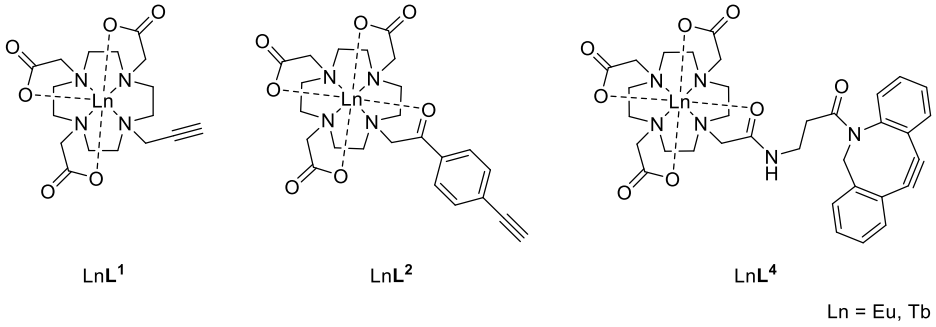


Figure 2.7. Ln-alkyne complexes for click chemistry.

2.3 Characterisation of the complexes

2.3.1 Paramagnetic ^{1}H NMR spectroscopy

2.3.1.1 pDO3A, $\mathbf{L^2}$

The NMR spectra of TbpDO3A are shown in Figure 2.8 and are consistent with those reported in literature.[5] Both Eu$\mathbf{L^1}$ and Tb$\mathbf{L^1}$ are seven coordinate unsymmetrical complexes with all protons being non-equivalent. The most downfield shifted peaks correspond to the axial ring protons of the cyclen ring in the SAP isomer. Due to the 7-coordinate metal centre, the peaks are broad because of

the lower energy barrier to the interconversion between the different isomers. Propargyl DO3A, **L^1**, and other 7-coordinate ligands are well-established to bind to anions such as carbonate, acetate, phosphate, and halides.[31, 32] The changes in the NMR spectrum upon addition of carbonate (Figure 2.8) support the hypothesis that the 7-coordinate complexes, previously bound to two water molecules, are both replaced with one carbonate bidentate binding to the metal centre, meaning the carbonate-bound complex shifts are more characteristic of the TSAP isomer.[31, 32]

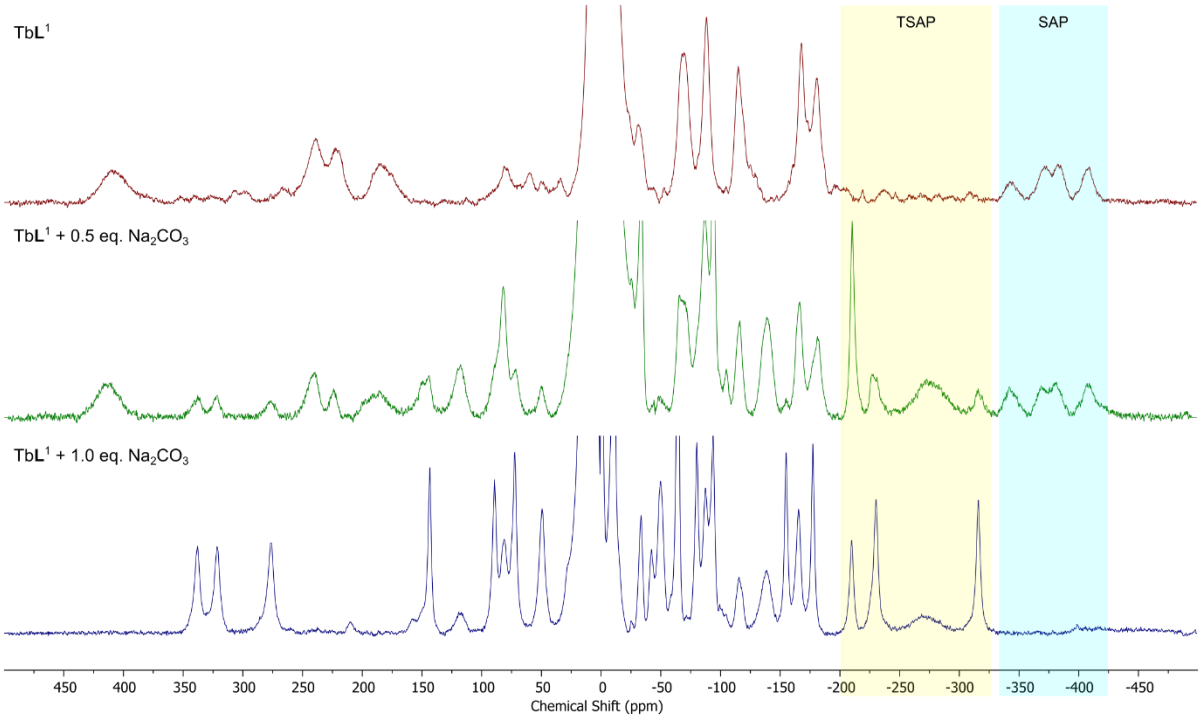


Figure 2.8. ^{1}H NMR spectra of TbpDO3A with different equivalents of Na_2CO_3 added (400 MHz, D_2O).

2.3.1.2 EthynylacetophenoneDO3A, L^2

Figure 2.9 shows the ^{1}H NMR spectra of europium and terbium ethynylacetophenone DO3A, **L^2.** The complexes are 8-coordinate which are more rigid when compared to the 7-coordinate pDO3A complex - this constrains the rate at which the SAP and TSAP isomers can interconvert. This results in the two isomers being resolved by NMR spectroscopy and in sharper peaks: the blue regions correspond to the axial ring protons of the SAP isomers, whilst the TSAP isomers are more clearly seen in the Eu-complex as highlighted by the yellow region. These complexes are observed to exhibit the SAP isomer as the dominant isomer, which is expected given that there is not much steric bulk close to the metal centre and is in agreement with similar acetophenone containing complexes.[18]

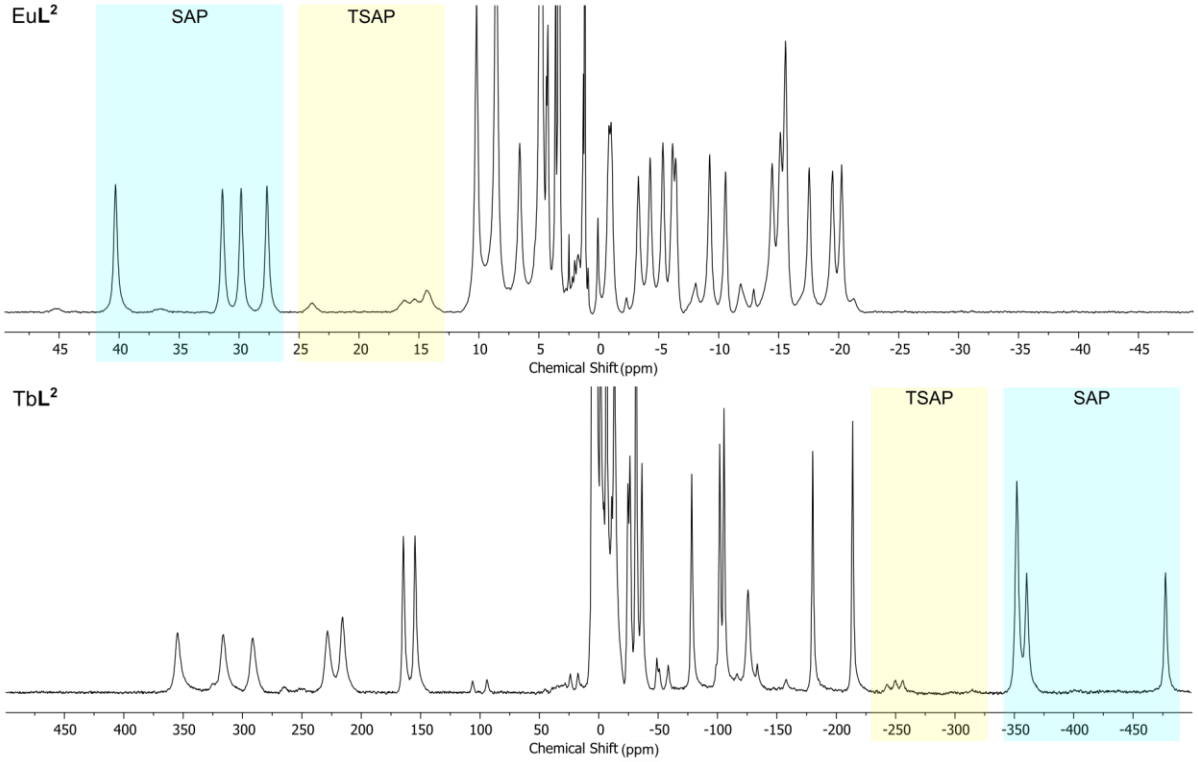


Figure 2.9. ^{1}H NMR spectra of Eu (top) and Tb (bottom) of ethynylacetophenoneDO3A complexes (400 MHz, MeOD). Blue regions (SAP isomer); yellow region (TSAP isomer).

2.3.1.3 DOTA-DBCO, L^{4}

Figure 2.10 shows the europium and terbium ^{1}H NMR spectra for the complexes of DOTA-DBCO. The peaks are sharp as a result of the 8th coordinate site from the amide carboxyl-group, this limits ring inversion and arm rotation between the SAP and TSAP isomer. Both metals show the SAP isomer as the major isomer; for the europium there is more of the minor TSAP isomer due to its larger ionic radii. The ^{1}H NMR spectra of the Ln-DOTA-DBCO complexes differs from that of the Ln-ethynylacetophenoneDO3A in that there are 6 peaks in the SAP isomer region for DOTA-DBCO compared to the 4 peaks for the Ln-ethynylacetophenoneDO3A. These 6 peaks could be attributed to the two enantiomers of the SAP isomers Λ(δδδδ) and Δ(λλλλ).

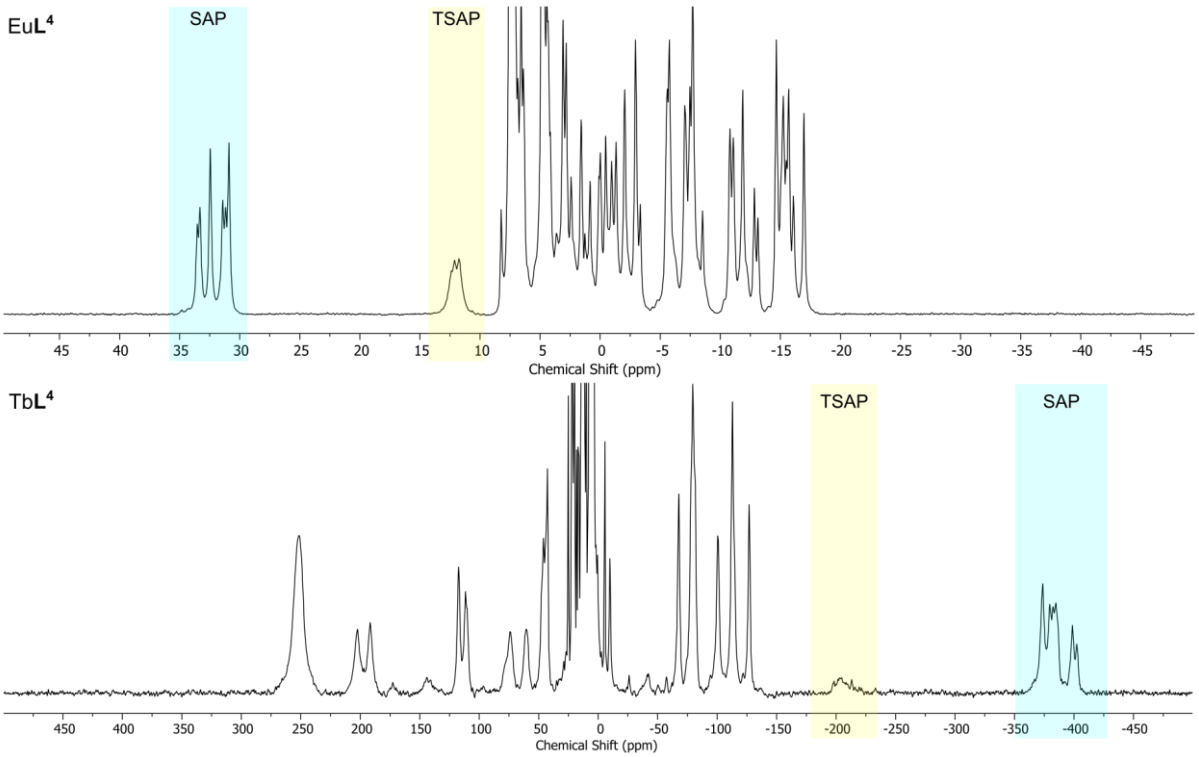


Figure 2.10. ^{1}H NMR spectra of Eu (top) and Tb (bottom) of DOTA-DBCO complexes (400 MHz, D_2O). Blue regions (SAP isomer); yellow region (TSAP isomer).

2.3.2 Photophysical properties

2.3.2.1 pDO3A, L^1

The absorption spectra of the Ln-pDO3A complexes show negligible absorbance as expected of a complex containing no chromophore. Therefore, the use of higher concentration of complexes in solution and direct excitation of the complexes was required to obtain the subsequent lanthanide emission spectra shown of Eu$\mathbf{L}^1$ and Tb$\mathbf{L}^1$ in Figure 2.11.

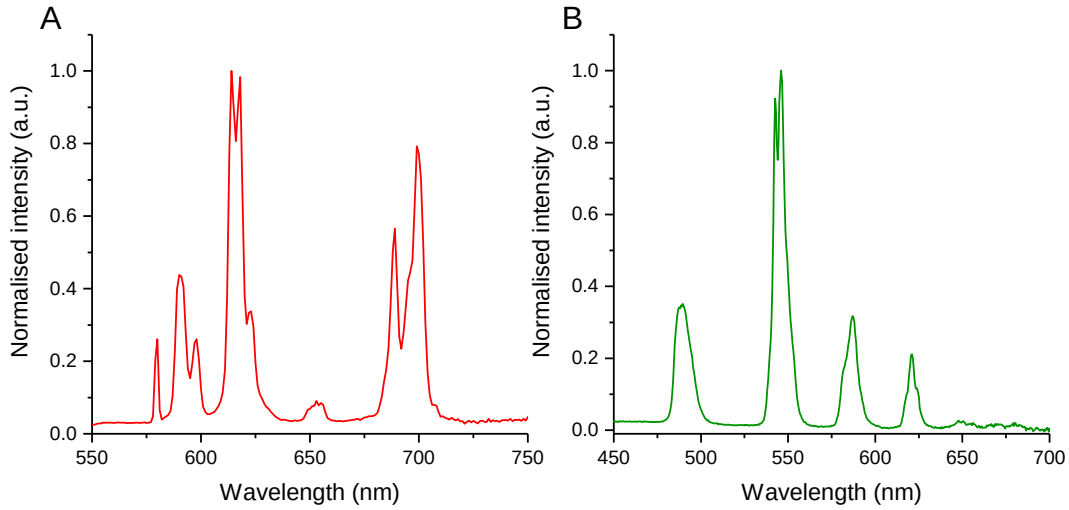


Figure 2.11. Normalised fluorescence emission spectra for a) EupDO3A, λ_{ex} = 397 nm and b) TbpDO3A, λ_{ex} = 366 nm; [Ln$\mathbf{L}^1$] = 1 mM in H_2O.

2.3.2.2 EthynylacetophenoneDO3A, L^2

The lanthanide complexes of ethynylacetophenoneDO3A exhibit an absorption ~291 nm, as shown in Figure 2.12a, from the acetophenone moiety which can be used as a sensitiser to indirectly excite the metal centre. Previous work reports that the triplet state of the ligand is well suited as a sensitiser of europium ([$E(^5D_0)$ = 17 300 cm^{-1}, $E(^5D_1)$ = 19 000 cm^{-1}],[18] it is postulated that sensitisation occurs via the triplet sate of the acetophenone.[33] The emission spectra shown in Figure 2.12b shows the characteristic europium emission spectra. The fluorescence from the chromophore can be observed in black only after 10 × magnification; the red spectra shows that the emission is dominated by the emission from europium even at more dilute concentrations (100 × more dilute than the pDO3A complexes).

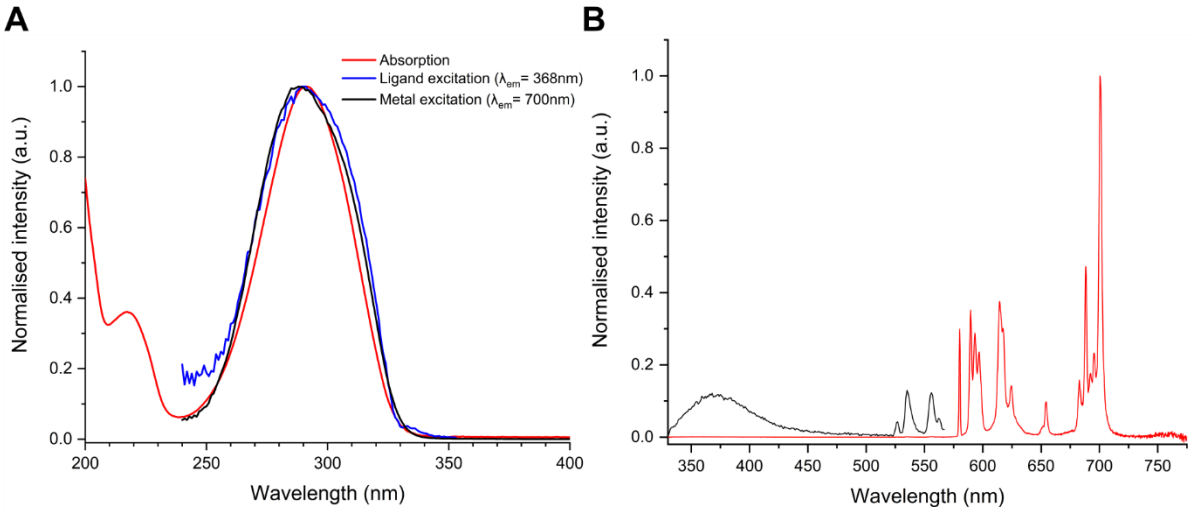


*Figure 2.12. a) Excitation spectra for ligand and metal centred excitation and absorption spectra overlaid; and b) Fluorescence emission spectra for EuethynylacetophenoneDO3A (red), magnified fluorescence from chromophore and emission states for Eu (black), λ_{ex} = 291 nm. [Eu**L²**] = 25 μM.*

Similarly, the terbium complex shows an absorption peak at ~292 nm (Figure 2.13a), corresponding to an electron transition from the non-bonding orbital to a π* antibonding orbital. Also, the peak at 292 nm corresponds to the direct excitation of the weak ligand fluorescence, which is observed at 368 nm, and the indirect terbium excitation. The comparable terbium emission spectra are shown in Figure 2.13b. Indirect excitation is better as it allows for strong fluorescence emission while using lower concentrations of complex – an acetophenone-derived pendant arm has been demonstrated to be suitable for indirect excitation of both europium and terbium.

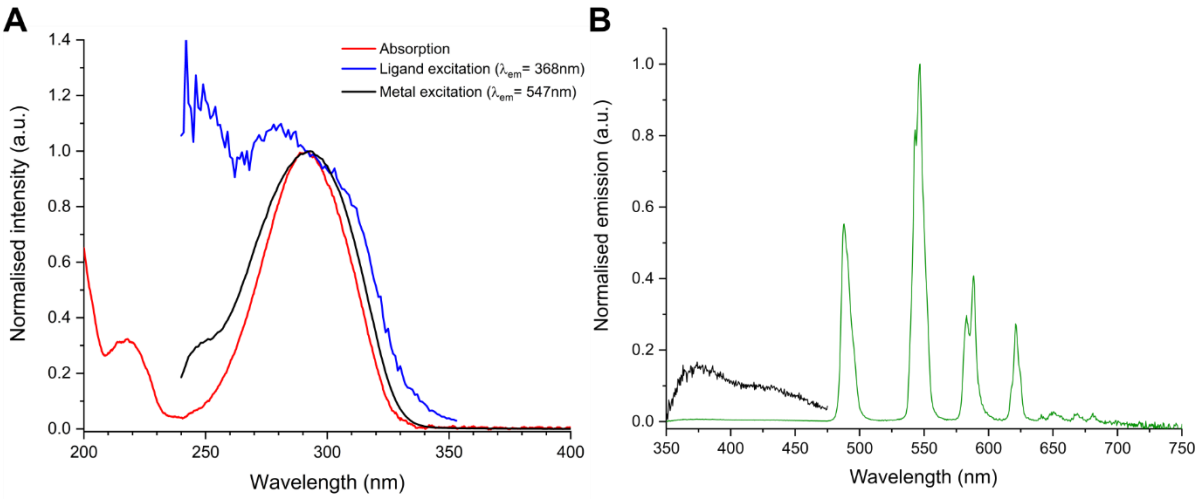


*Figure 2.13. a) Excitation spectra for ligand and metal centred excitation and absorption spectra overlaid; and b) Fluorescence emission spectra for TbethynylacetophenoneDO3A (green), magnified fluorescence from chromophore (black), λ_{ex} = 292 nm. [Tb**L**^{2}] = 25 μM.*

2.3.2.3 DOTA-DBCO, L^4

The DOTA-DBCO ligand, **L**^{4} and europium complex absorption spectra in Figure 2.14a display two peak absorptions at 291 and 308 nm corresponding to an electron transition from the non-bonding orbitals to the π* antibonding orbitals. The metal excitation was able to occur through the chromophore shown by the overlap with the absorption spectra. However, it can be seen in Figure 2.14b that the fluorescence of the chomophore at ~370 nm dominates when excited at 308 nm and 291 nm with the europium emission just visible. The europium emission spectra is stronger for both degassed samples compared to the aerated sample which is indicative of an oxygen quenching pathway.

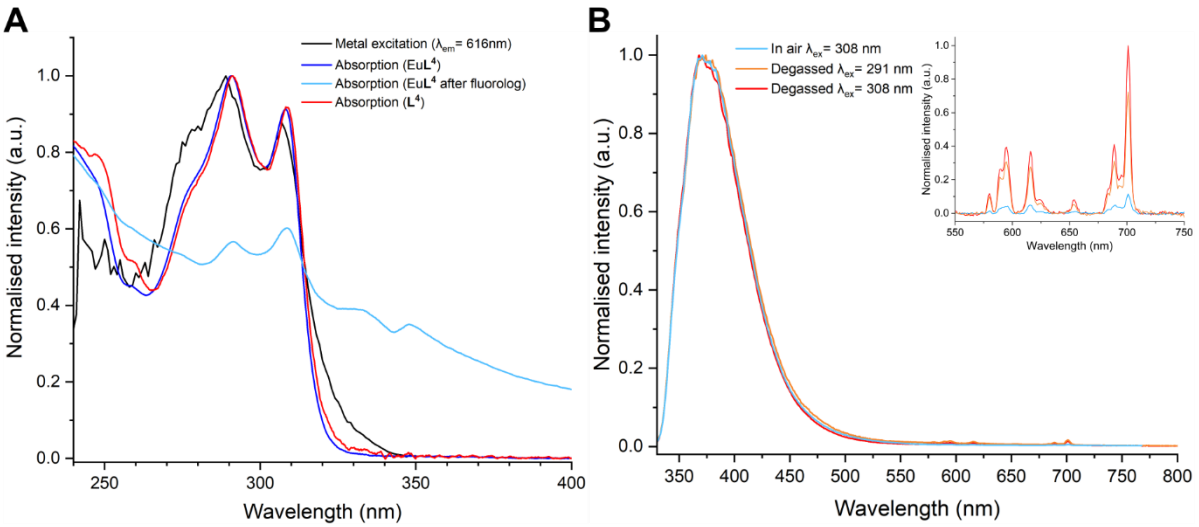


*Figure 2.14. a) Excitation spectra for metal centred excitation and absorption spectra for ligand (DOTA-DBCO, **L**^{4}), Eu**L**^{4}, and Eu**L**^{4} after photodamage; b) Fluorescence emission spectra for Eu**L**^{4} in air (light blue: λ_{ex} = 291 nm; dark blue: λ_{ex} = 308 nm) and degassed (orange: λ_{ex} = 291 nm; red: λ_{ex} = 308 nm). Inset is 550-750 nm region normalised to peak at 701 nm. [Eu] = 25 μM in H_2O.*

Photodegradation of the complex was observed when recording the fluorescence emission spectra, demonstrated by a total loss of the europium emission and reduction in the fluorescence signal. The absorption spectra of the Eu complex was measured following fluorescence emission measurements and the intensity and shape of the spectra has changed (Figure 2.14a, before (dark blue) compared to after (light blue)). It is reasonable to propose that irradiation during excitation provides sufficient energy to break the strained alkyne bond. The fluorescence emission spectra for a degassed sample was compared to the fluorescence of a freshly prepared sample under atmospheric conditions (Figure 2.14b). A reduction in the europium peaks is observed under aerated conditions therefore it is possible that the alkyne could undergo photo-oxidation, or that the oxygen is quenching the signal.

Similar absorption and excitation results were found for Tb**L**^{4} as for Eu**L**^{4}, where it was also possible to indirectly excite terbium through the dibenzocyclooctyne arm (Figure 2.15a). All samples displayed large fluorescence from DBCO at ~ 370 nm. However, a larger difference was observed between the aerated and degassed terbium fluorescence (Figure 2.15b) than for europium. Without oxygen, more efficient transfer to the terbium was possible. Smaller slit widths were used for the terbium samples which resulted in less photodamage, therefore it is likely that oxygen was the source of the energy loss.

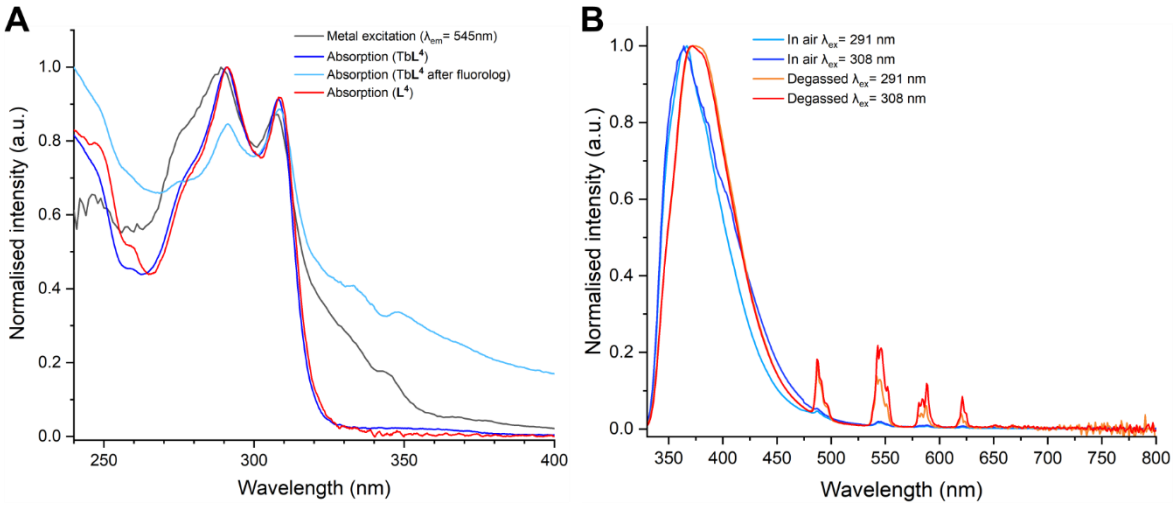


*Figure 2.15. a) Excitation spectra for metal centred excitation and absorption spectra for ligand (DOTA-DBCO, **L**^{4}), Tb**L**^{4}, and Tb**L**^{4} after photodamage; b) Fluorescence emission spectra for Tb**L**^{4} in air (light blue: λ_{ex} = 291 nm; dark blue: λ_{ex} = 308 nm) and degassed (orange: λ_{ex} = 291 nm; red: λ_{ex} = 308 nm). [Tb] = 25 μM in H_2O.*

Given the photodamage of the DOTA-DBCO samples it was chosen not to carry out lanthanide lifetime emission measurements as the rapid damage would make it difficult to distinguish the long-lived phosphorescence from degradation of the compound. The excited state emission lifetimes for Ln**L**^{1} and Ln**L**^{2} are given in Table 2.3. The hydration number for the 7-coordinate pDO3A complexes are approximately equal to 2, which would be in agreement with two water molecules binding to the

metal centre for the nine-coordinate metal centre. Correspondingly, a hydration number of ~1 was found for the 8-coordinate ethynylacetophenone complexes, meaning one water molecule was able to bind.

Table 2.3. Excited state Ln(III) emission lifetimes for alkyne complexes in H_2O and D_2O and calculated hydration number.

Complex	λ_{ex} (nm)	λ_{em} (nm)	τH_2O (ms)	τD_2O (ms)	kH_2O (ms^{-1})	kD_2O (ms^{-1})	*q*
Eu**L**^{1}[a]	393	617	0.38	1.90	2.69	0.53	2.2
Tb**L**^{1}[a]	366	545	1.25	2.90	0.80	0.34	2.0
Eu**L**^{2}[a]	291	615	0.59	2.19	1.71	0.46	1.2
Tb**L**^{2}[b]	292	546	1.42	2.27	0.70	0.44	1.0

*[a] Fit using monoexponential decay; [b] Fit using biexponential decay; Typical errors on measured values are 10%. [Ln**L**^{1}] = 1 mM; [Ln**L**^{2}] = 25 μM in distilled water or D_2O. For Eu: A = 1.2 and B = -0.25; for Tb: A = 5 and B = 0.06 in modified Horrocks' equation (Eq. 1.1).*[34]

2.4 Conclusions

A set of three complexes with alkyne appendages have been synthesised and exhibit photophysical properties in line with their structure. The developed probes will be used with azides bound to targeting moieties to act as a linker to the imaging agent. Previously, pDO3A complexes have been used for copper-mediated click chemistry. This work has extended this, and developed a new alkyne complex, Ln**L**^{2} with an acetophenone chromophore that can sensitise the metal centre. The SPAAC complex, LnDOTA-DBCO, Ln**L**^{4}, shows strong fluorescence with limited energy transfer from the pendant arm to the lanthanide. In isolation, the Ln-DOTA-DBCO is a poor sensitiser and unstable as a result of the strained alkyne; however, it was anticipated that following cycloaddition with an azide, the newly formed triazole, as well as the two benzene rings, could behave as a suitable metal sensitiser.

2.5 References

1. H. C. Kolb and K. B. Sharpless, *Drug Discovery Today*, 2003, **8**, 1128-1137.
2. J. E. Moses and A. D. Moorhouse, *Chem. Soc. Rev.*, 2007, **36**, 1249-1262.
3. V. V. Rostovtsev, L. G. Green, V. V. Fokin and K. B. Sharpless, *Angew. Chem. Int. Ed.*, 2002, **41**, 2596-2599.
4. C. W. Tornoe, C. Christensen and M. Meldal, *J. Org. Chem.*, 2002, **67**, 3057-3064.
5. M. Jauregui, W. S. Perry, C. Allain, L. R. Vidler, M. C. Willis, A. M. Kenwright, J. S. Snaith, G. J. Stasiuk, M. P. Lowe and S. Faulkner, *Dalton Trans.*, 2009, 6283-6285.
6. C. L. Dupont, G. Grass and C. Rensing, *Metallomics*, 2011, **3**, 1109-1118.
7. L. M. Gaetke and C. K. Chow, *Toxicology*, 2003, **189**, 147-163.
8. G. Wittig and A. Krebs, *Chemische Berichte-Recueil*, 1961, **94**, 3260-3275.
9. E. M. Sletten and C. R. Bertozzi, *Org. Lett.*, 2008, **10**, 3097-3099.
10. J. A. Codelli, J. M. Baskin, N. J. Agard and C. R. Berozzi, *J. Am. Chem. Soc.*, 2008, **130**, 11486-11493.
11. J. M. Baskin, J. A. Prescher, S. T. Laughlin, N. J. Agard, P. V. Chang, I. A. Miller, A. Lo, J. A. Codelli and C. R. Bertozzi, *Proc. Natl. Acad. Sci. U.S.A.*, 2007, **104**, 16793-16797.
12. N. J. Agard, J. A. Prescher and C. R. Bertozzi, *J. Am. Chem. Soc.*, 2005, **127**, 11196-11196.
13. E. M. Sletten and C. R. Bertozzi, *Angew. Chem. Int. Ed.*, 2009, **48**, 6974-6998.
14. L. Mason, PhD thesis, University of Oxford, 2017.
15. M. Tropiano, C. J. Record, E. Morris, H. S. Rai, C. Allain and S. Faulkner, *Organometallics*, 2012, **31**, 5673-5676.
16. A. K. R. Junker, M. Tropiano, S. Faulkner and T. J. Sorensen, *Inorg. Chem.*, 2016, **55**, 12299-12308.
17. A. Dadabhoy, S. Faulkner and P. G. Sammes, *J. Chem. Soc., Perkin Trans. 2* , 2002, 348-357.
18. A. Beeby, L. M. Bushby, D. Maffeo and J. A. G. Williams, *J. Chem. Soc., Dalton Trans.*, 2002, 48-54.
19. C. Wu, X. Xin, Z. M. Fu, L. Y. Xie, K. J. Liu, Z. Wang, W. Y. Li, Z. H. Yuan and W. M. He, *Green Chem.*, 2017, **19**, 1983-1989.
20. T. Cruchter, K. Harms and E. Meggers, *Chem. Eur. J.*, 2013, **19**, 16682-16689.
21. A. Kuzmin, A. Poloukhtine, M. A. Wolfert and V. V. Popik, *Bioconjugate Chem.*, 2010, **21**, 2076-2085.
22. R. C. Chadwick, S. Van Gyzen, S. Liogier and A. Adronov, *Synthesis*, 2014, **46**, 669-677.
23. *US Pat.*, US61368775, 2012.
24. M. F. Debets, S. S. van Berkel, S. Schoffelen, F. Rutjes, J. C. M. van Hest and F. L. van Delft, *Chem. Commun.*, 2010, **46**, 97-99.

25. M. Chigrinova, C. S. McKay, L. P. B. Beaulieu, K. A. Udachin, A. M. Beauchemin and J. P. Pezacki, *Org. Biomol. Chem.*, 2013, **11**, 3436-3441.
26. D. X. Zeng, N. S. Lee, Y. J. Liu, D. Zhou, C. S. Dence, K. L. Wooley, J. A. Katzenellenbogen and M. J. Welch, *ACS Nano*, 2012, **6**, 5209-5219.
27. Y. Liang, X. Jiang, R. Yuan, Y. Zhou, C. X. Ji, L. M. Yang, H. F. Chen and Q. Wang, *Anal. Chem.*, 2017, **89**, 538-543.
28. M. S. Cherevin, Z. P. Zubreichuk, L. A. Popova, T. G. Gulevich and V. A. Knizhnikov, *Russ. J. Gen. Chem.*, 2007, **77**, 1576-1579.
29. S. A. McNelles, J. L. Pantaleo and A. Adronov, *Org. Process Res. Dev.*, 2019, **23**, 2740-2745.
30. P. G. M. Wuts, *Greene's protective groups in organic synthesis*, Wiley, Hoboken, New Jersey, 5th edn., 2014.
31. J. I. Bruce, R. S. Dickins, L. J. Govenlock, T. Gunnlaugsson, S. Lopinski, M. P. Lowe, D. Parker, R. D. Peacock, J. J. B. Perry, S. Aime and M. Botta, *J. Am. Chem. Soc.*, 2000, **122**, 9674-9684.
32. R. S. Dickins, T. Gunnlaugsson, D. Parker and R. D. Peacock, *Chem. Commun.*, 1998, 1643-1644.
33. A. Beeby, L. M. Bushby, D. Maffeo and J. A. G. Williams, *J. Chem. Soc., Perkin Trans. 2*, 2000, 1281-1283.
34. A. Beeby, I. M. Clarkson, R. S. Dickins, S. Faulkner, D. Parker, L. Royle, A. S. de Sousa, J. A. G. Williams and M. Woods, *J. Chem. Soc., Perkin Trans. 2* , 1999, 493-503.

3 Folate-derived luminescent probes

3.1 Introduction

One of the methods for targeting macrophages investigated in this work is folic acid to bind to the folate receptor-β which has found to be overexpressed in activated macrophages. The structure of folic acid is shown in Figure 3.1 highlighting the α- and γ- carboxylic acid sites used for conjugation to the imaging agent.

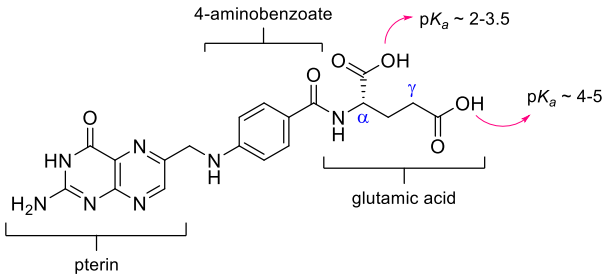


Figure 3.1. Chemical structure of folic acid highlighting α- and γ-carboxylate conjugation sites.

The earliest reported work of lanthanide-folate conjugates was in 2002 by the Parker group[1] and also, independently, a patent was filed by Bracco.[2] Both produced lanthanide-folate conjugates using Gd, with MR imaging the intended use, shown in Figure 3.2. The gadolinium complex **F1** has chiral carboxylate arms to give a high proportion of the TSAP isomer in solution giving enhanced relaxivity as a result of fast water exchange improving its MRI signal.[1] Interestingly, both Parker and Bracco's work included macrocyclic attachment to both the α- and γ-carboxylates on folate, **F2**, allowing for the complexation of two metals.[1, 2]

The first examples of optical imaging using europium- and terbium-folate conjugates were recently reported by Plush *et al.*[3, 4] and Quici *et al.*[5] Plush and colleagues have investigated folic acid, pteroic acid[3] and methotrexate as targeting moieties, where in the second iteration of their probes they reported the incorporation of a carbostyril chromophore to increase lanthanide sensitisation (Figure 3.2, **F3**).[4] Similarly, Quici and co-workers used a benzyl chromophore to act as a lanthanide sensitiser.[5] It is notable that both groups deviated from the strict γ-functionalised approach, with Plush *et al.* leaving complexes as a mixture of the regioisomers.[4] Meanwhile Quici *et al.* attached macrocycles at the α- and γ- carboxylates, and at the nitrogen of the 4-aminobenzoic residue, stating internalisation of all three regioisomers was of a similar value.[5]

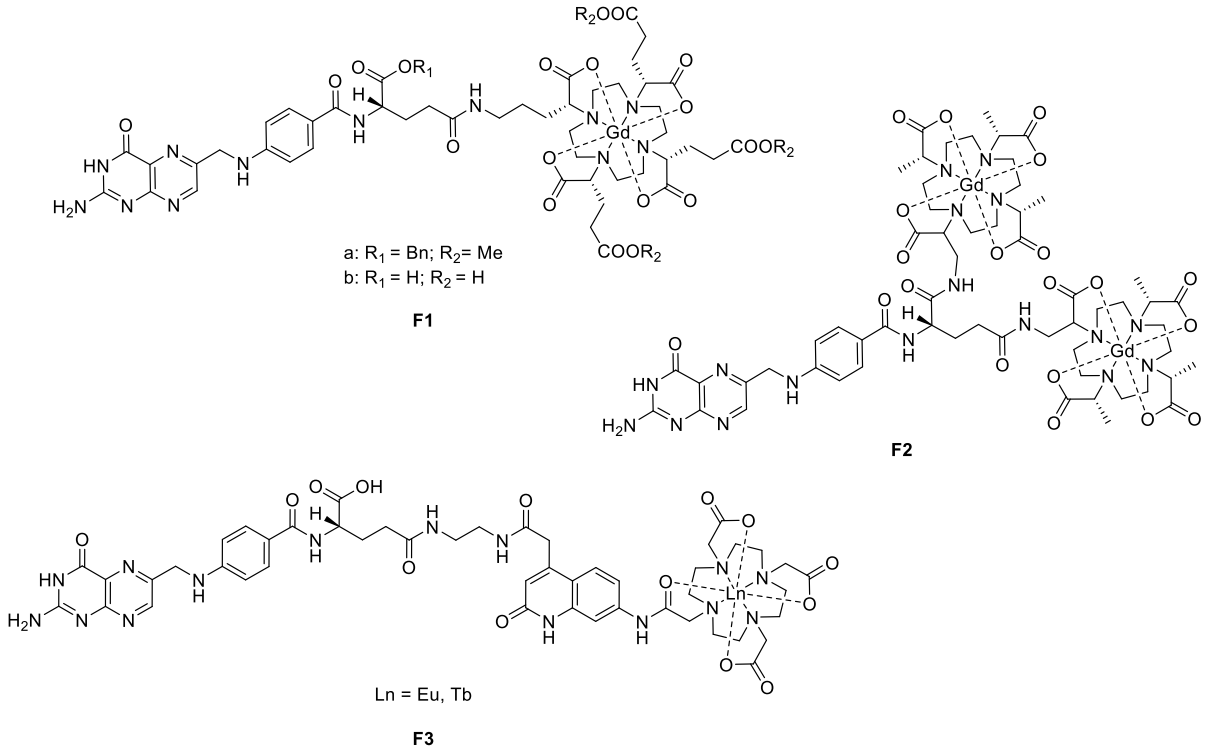


Figure 3.2. Lanthanide folate conjugates reported in literature.[1,2,4]

In this chapter, several folate-based optical imaging probes are discussed. The synthesised molecules comprise a lanthanide containing macrocyclic framework (LnDOTA) which is linked to folic acid. Variation of the linker length is investigated for both polyethylene glycol (PEG) and PEG-1,2,3-triazoles, and the impact of their optical properties. The photophysical properties are studied to assess the requirement of a chromophore in these complexes. Due to terbium being more emissive than europium, a result of the larger energy gap between their main emissive states and ground state,[6] terbium-folate complexes were prioritised.

3.2 Synthetic approaches

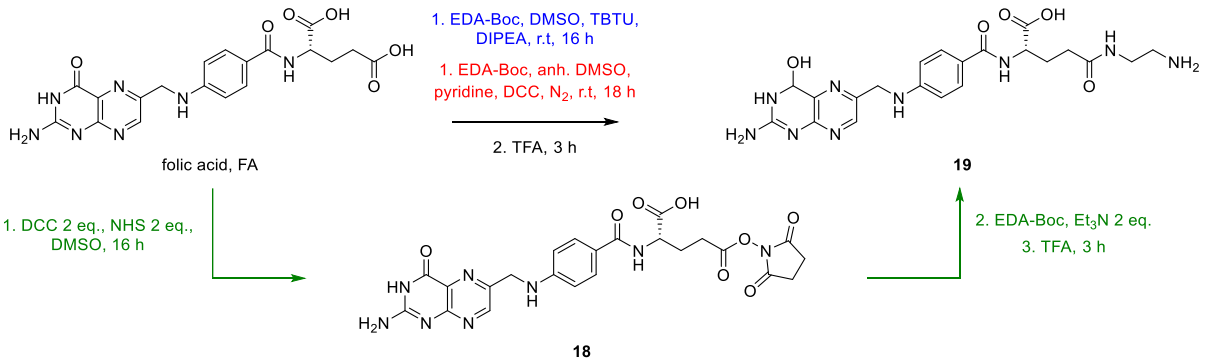
Given that the crystal structure for the complex of folic acid within the folate receptor shows binding with the pteroic acid moiety set furthest within the receptor binding site,[7] the γ-carboxyl has been proposed as the most suitable point for functionalisation. However, there remains many contradictory reports on the selectivity of the α- over the γ-isomer,[5] with some deciding to leave the folate conjugates as a mixture of the two isomers.[3, 4] For this work, where possible, it was aimed to isolate the γ-regioisomer and use these compounds for further testing to align with most of literature.[8-14]

3.2.1 Initial Approach: Ethylene-diamine linker

There were a broad range of synthetic strategies proposed in literature, including dividing the folic acid into smaller fragments to select protecting groups to ensure the γ-regioisomer was obtained in isolation.[1, 12, 15] However, there are also numerous reports of modification of the folic acid[9, 16-18]

and subsequent isolation of each regioisomer by purification techniques such as HPLC.[3, 4] Therefore, for simplicity, this was the initial approach chosen.

The initial strategy was to attach the folic acid using an ethylene diamine linker to functionalise the third triester arm, **1**. However, there was no consistent method reported in literature for synthesising the folic acid ethylene diamine (FA-EDA, **19**), which was indicative of the difficulty in obtaining the desired compound. Scheme 3.1 outlines the strategies attempted. The blue and red routes were reported by König and Kramer[9] and Rutnakornpituk *et al.*[16] respectively, where ethylenediamine (EDA) was conjugated to the terminal (γ-) carboxyl group of the folic acid using uronium or carbodiimide coupling reagents. The reasoning with this approach follows that reaction at the γ- carboxyl group of folic acid is more favoured as it is less sterically hindered, meaning that it is the dominant product formed.[19] Solubility proved an issue in dissolving the folic acid initially and once again in the HPLC purification step reported by König due to large sample loss as a result of insolubility in the H_2O:MeCN HPLC solvent mixture. Even for the dissolved compound, the HPLC trace was difficult to separate out the α and γ-regioisomers.



*Scheme 3.1. Synthetic strategies attempted to yield folic acid N-ethylene diamine, **19**. Blue route reported by König and Kramer[9], red by Rutnakornpituk et al.[16] and green by Trindade et al.[17] and Dzwonek et al.[18]*

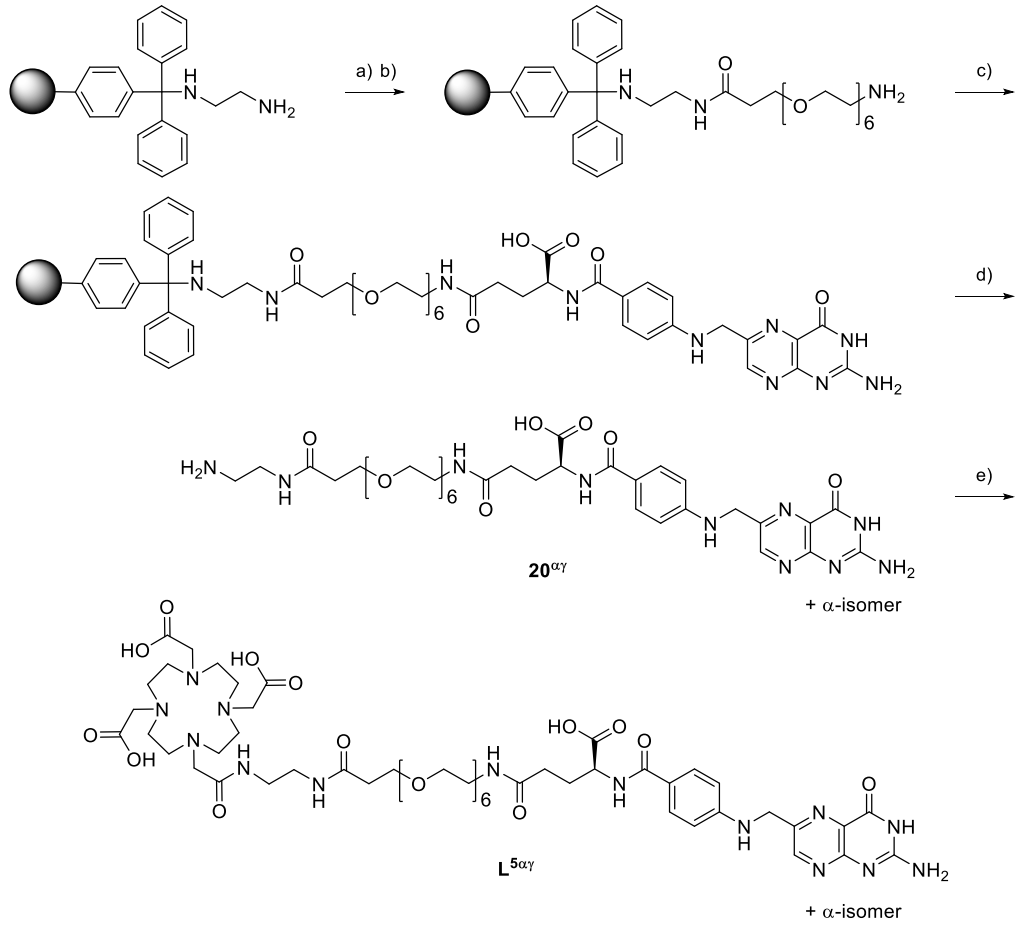
Whilst the method by Rutnakornpituk *et al.* proceeded, when an analytical HPLC run was carried out, it found a mixture of the amide coupling on either available carboxyl group, as well as production of the *bis*-amide. Therefore, to increase selectivity for the terminal carboxylic group, an NHS ester was attached[17, 18] and this resulted in a preference for the *mono*-substituent (Scheme 3.1, green route, **18**). However, problems of compound solubility persisted when connecting the folate targeting vector to the imaging modality and overall poor solubility is an undesirable property of an imaging agent. Therefore, it was concluded that another component should be added to the folic acid to increase its solubility.

3.2.2 Solid-phase synthesis approach

Given the difficulty in purification of the products in the initial routes attempted it was decided to employ solid-phase synthesis with the aim that undesired starting materials would be easily removed by thorough washings between the steps.

3.2.2.1 Approach 1

Work by the Low group introduced a PEG unit into the folate-targeted PET tracer with the aim to improve hydrophilicity and increase retention time in the body.[13, 15] PEG units are introduced to reduce renal clearance times, as well as generally improving the pharmacokinetic properties of pharmaceuticals,[20] thereby providing an additional benefit for the imaging agent. The next synthetic approach was modified from the Low group;[13, 15] the solid phase synthesis of the EDA-PEG moiety and attachment to folic acid used is outlined in Scheme 3.2.



Scheme 3.2. Schematic for solid-phase synthesis of FA-PEG$_6$-EDA-DOTA (mixture of regioisomers, only γ-isomer shown). Conditions and reagents: a) Fmoc-NH-(PEG)$_6$-COOH, HATU, DIPEA, DMF, r.t; b) 20% piperidine in DMF, r.t., 30 mins; c) folic acid, HATU, DIPEA, DMF, r.t.; d) TFA: H$_2$O: TIPS (95: 2.5:2.5), r.t., 3 hrs; e) DOTA-NHS ester, DMSO, DIPEA, r.t., Ar, 16 h.[13, 15]

It deviated from literature in that folic acid is added in one step rather than through addition of the *tert*-butyl protected glutamic acid and N^{10}-TFA-protected pteroic acid, using similar reasoning that the γ- isomer should be the major product due to the less hindered environment. It was proposed that as the reagent was bound onto the solid phase resin, the hindered environment would favour the γ- isomer even more. The folate-PEG_6-EDA, $\mathbf{20}^{\alpha\gamma}$ was purified by HPLC before attaching to DOTA-NHS *via* the amide linkage.[15] The DOTA-PEG_6-FA, $\mathbf{L}^{5\alpha\gamma}$ was purified by RP-HPLC under basic conditions but was still found to contain trace amounts of the $\mathbf{20}^{\alpha\gamma}$ and a cleaved product of $\mathbf{L}^{5\alpha\gamma}$ which breaks between the pterin and the benzoic acid as visible in the MS HPLC trace (Figure 3.3) and by NMR spectroscopy.

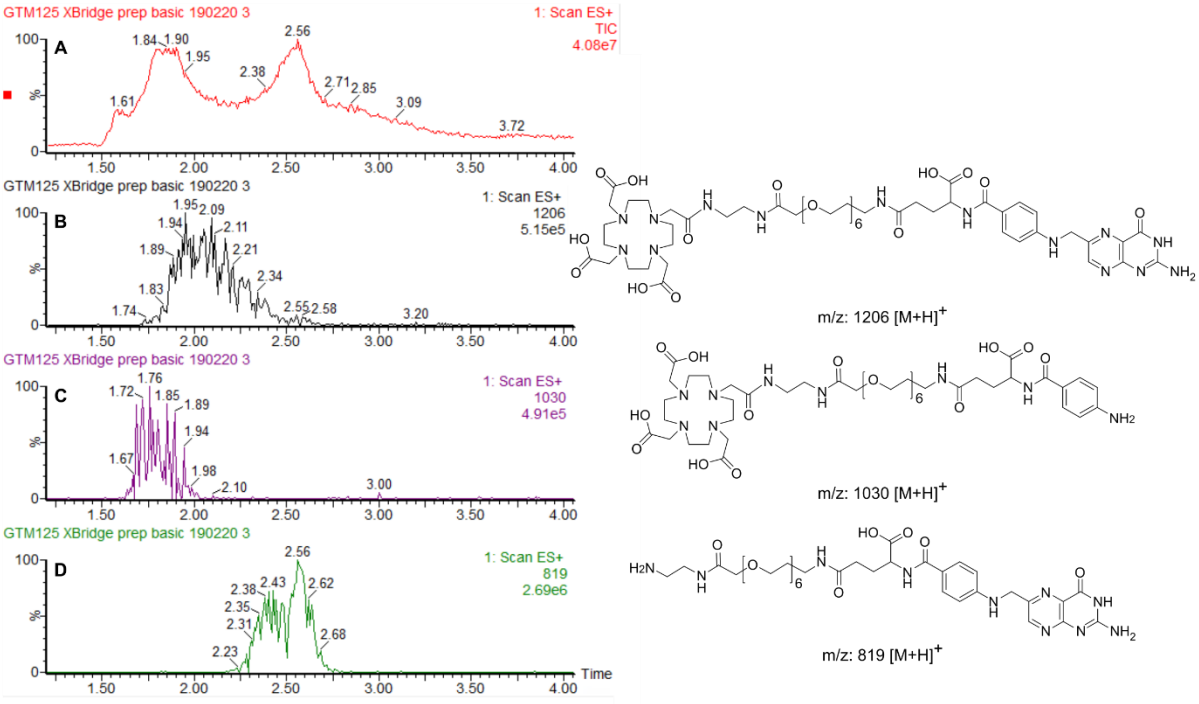
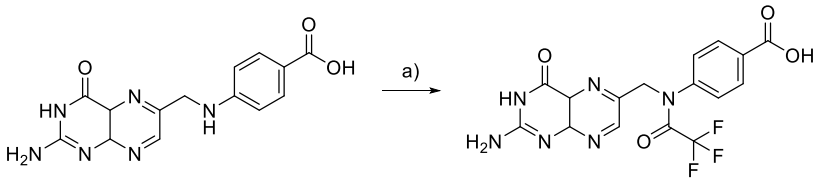


Figure 3.3. Preparative HPLC trace of $\boldsymbol{L}^{5\alpha\gamma}$ *under basic conditions. a) LC-MS trace TIC; b)* $\boldsymbol{L}^{5\alpha\gamma}$, t_R = 2.00 min [1.74-2.58 min]; c) fragment of $\boldsymbol{L}^{5\alpha\gamma}$, t_R = 1.76 min [1.67-2.05 min] and d) $\boldsymbol{20}^{\alpha\gamma}$, t_R = 2.50 min [2.23-2.68 min].

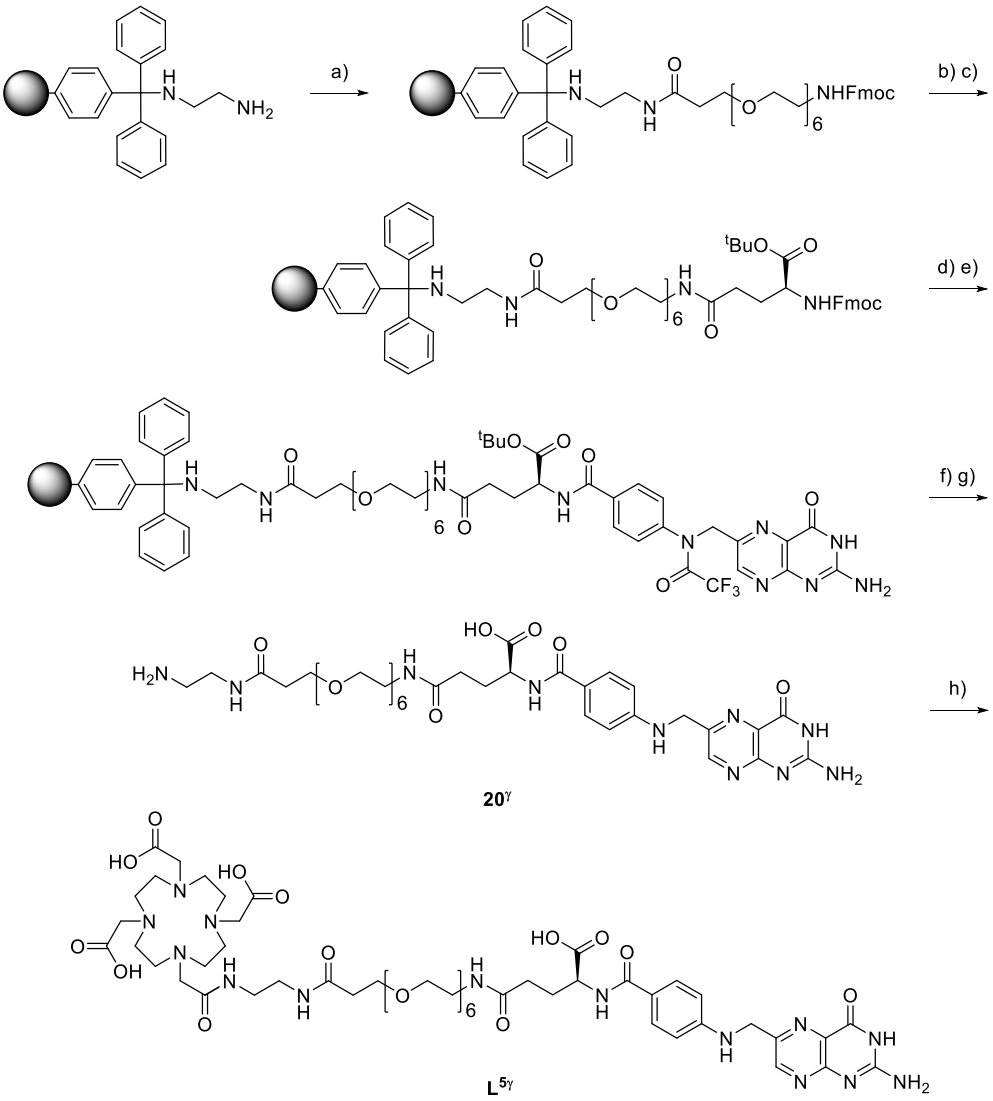
3.2.2.2 Approach 2

Given the difficulty in separation of the isomers, it was decided that the best method would be to use the smaller components of folic acid (pteroic acid and glutamic acid) to build up the separate isomers of folate. The N^{10}-TFA-pteroic acid, **21**, was prepared following literature procedures[21, 22] (Scheme 3.3) and both isomers of the Fmoc-protected glutamic acids were commercially available.



*Scheme 3.3. Synthesis of N^{10}-TFA-Pteroic acid, **21**. a) i) Trifluoroacetic anhydride, r.t., 4 days, Ar, dark; ii) 3% TFA in H_2O, r.t., 2 days, dark, 73%.*

The synthesis of the α- and γ-isomers were carried out as before in an isolute fritted column using 0.1 mmol of the resin agitated by N_2 bubbling through the suspension (Scheme 3.4). To overcome the small scale and low yield of this reaction, multiple reactions were often performed in parallel with between 1-4 reactions occurring at once. The FA-PEG_6-EDA, (Scheme 3.4, **20**$^{\alpha}$ and **20**$^{\gamma}$) were then purified separately by HPLC under basic conditions.



Scheme 3.4. Schematic for solid-phase synthesis of γ-regioisomer of DOTA-EDA-PEG$_6$-FA, ***L$^{5\gamma}$****. Conditions and reagents: a) Fmoc-NH-(PEG)$_6$-COOH, HATU, DIPEA, DMF, r.t; b) 20% piperidine in DMF, r.t., 30 mins; c) Fmoc-Glu(OtBu)-OH, HATU, DIPEA, DMF, r.t.; d) 20% piperidine in DMF, r.t., 30 mins; e) N^{10}-(TFA)pteroic acid,* ***21****, HATU, DIPEA, DMF; f) TFA: H$_2$O: TIPS (95: 2.5:2.5), r.t., 3 hrs g) Saturated Na$_2$CO$_3$, r.t., 30 mins,* ***20$^\gamma$*** *= 19%;* ***20$^\alpha$*** *= 5%; h) DOTA-NHS ester, DMSO, DIPEA, r.t., Ar, 16 h.*[13, 15]

Figure 3.4 shows the ^{1}H NMR spectra of the two regioisomers of **20** highlighting key differences in the glutamic acid residue of the folic acid. Following purification, **20$^\gamma$** and **20$^\alpha$** were then attached to the DOTA using DOTA-NHS ester promoted amide coupling. Each isomer of **L^5** was then purified again by HPLC under basic conditions and then underwent lanthanide complexation.

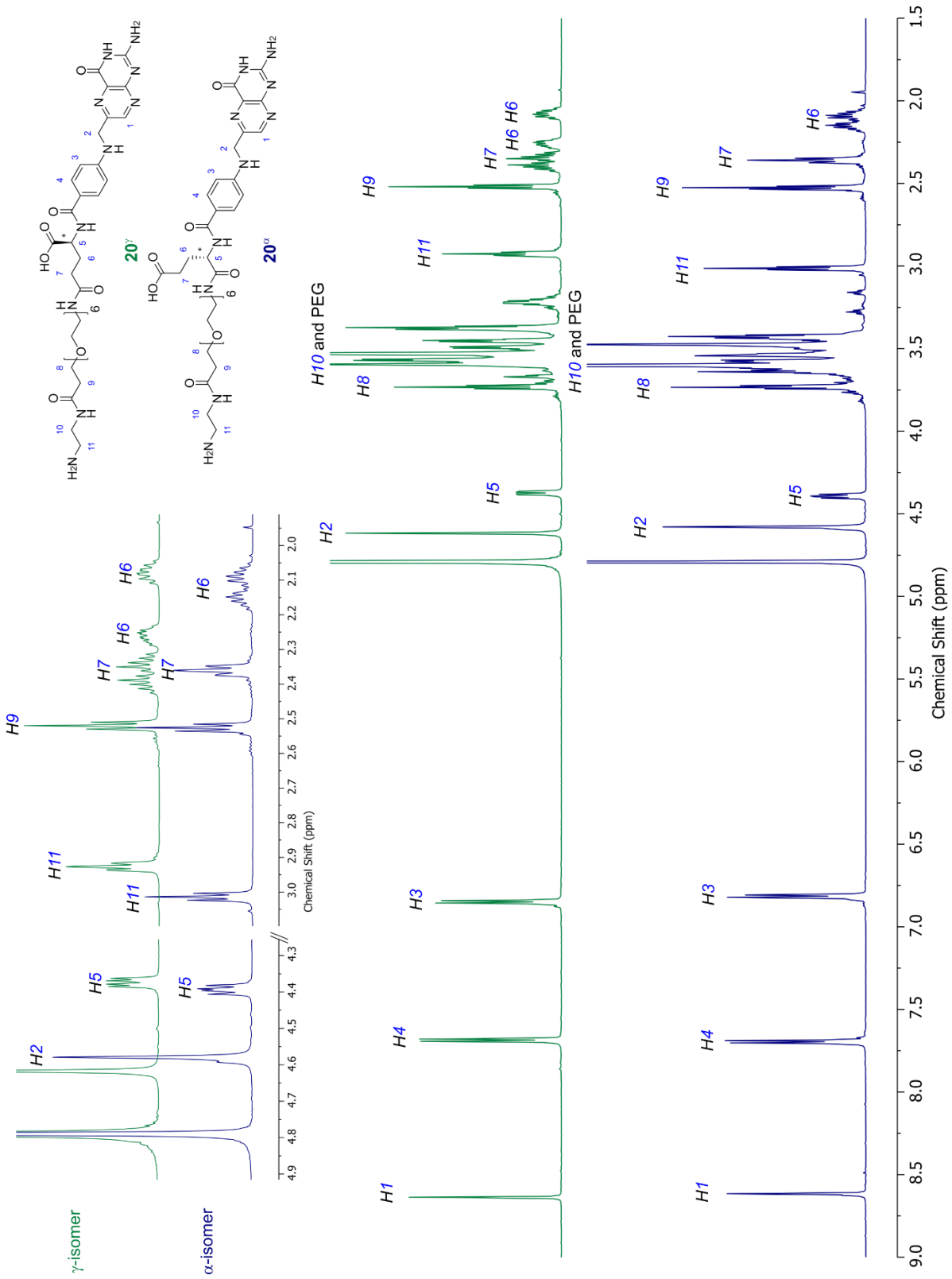
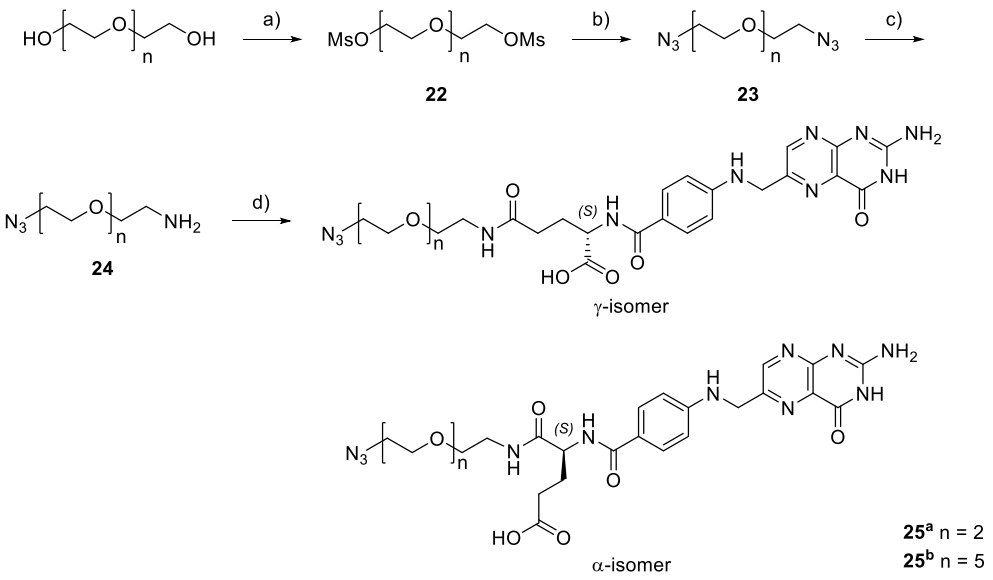


*Figure 3.4. ^{1}H NMR (600 MHz, D_2O) spectra of γ- and α-regioisomers of FA-PEG$_6$-EDA, **20**, highlighting key differences between the two isomers.*

3.2.3 Click chemistry: FA-(PEG)$_n$-azide

Another method of attaching the targeting moiety to the imaging component of the probes explored in this work is click chemistry. To allow for the click reactions to occur with the alkyne functionalised DO3A based ligands, an azide group was attached to the folic acid moiety using polyethylglycol linkers. This synthetic work was carried out in collaboration with Anna Booth who prepared the larger scale of these compounds whilst I worked to optimise the purification. First, the amine-PEG-azide chains, **24** (Scheme 3.5) were synthesised from the respective polyethylene glycol chains following literature procedures.[23] These were then coupled to the folic acid using DCC-mediated amide coupling using a method modified from literature to produce folate-azides, **25**.[19] These folate-azides were then used in various copper-catalysed and copper-free cycloadditions. These were either purified by alumina column chromatography, RP-HPLC or both; problems arose from a contaminant with a m/z = 555 for n=5. Isolation of this contaminant revealed it to be the azide-PEG$_5$-p-aminobenzoyl-L-glutamic acid fragment confirmed by ^{1}H NMR spectroscopy, characterised by the loss of the pterin aromatic peak. Literature reports state that this is a common point for folic acid to cleave, with photodegradation resulting in formation of pterine-6-carboxylic acid and p-aminobenzoyl-L-glutamic acid.[24]

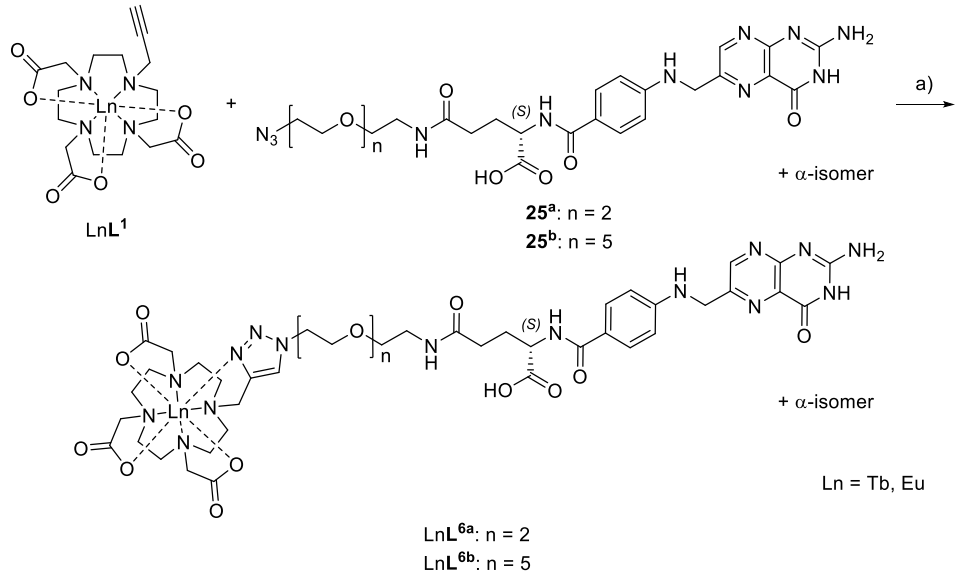


*Scheme 3.5. Synthesis of azide-conjugated folate compounds with polyethylene glycol linkers, **25**. Reagents and conditions: a) MsCl, NEt$_3$, DMC, 0 °C-r.t., 4 h, 97%; b) NaN$_3$, DMF, 65 °C, 16 h, 65%; c) 5% HCl, 0.9 eq. PPh$_3$ in Et$_2$O, r.t., 24 h, 68%; d) folic acid, DCC, pyridine, DMSO, r.t.*

3.2.3.1 Copper-catalysed click chemistry

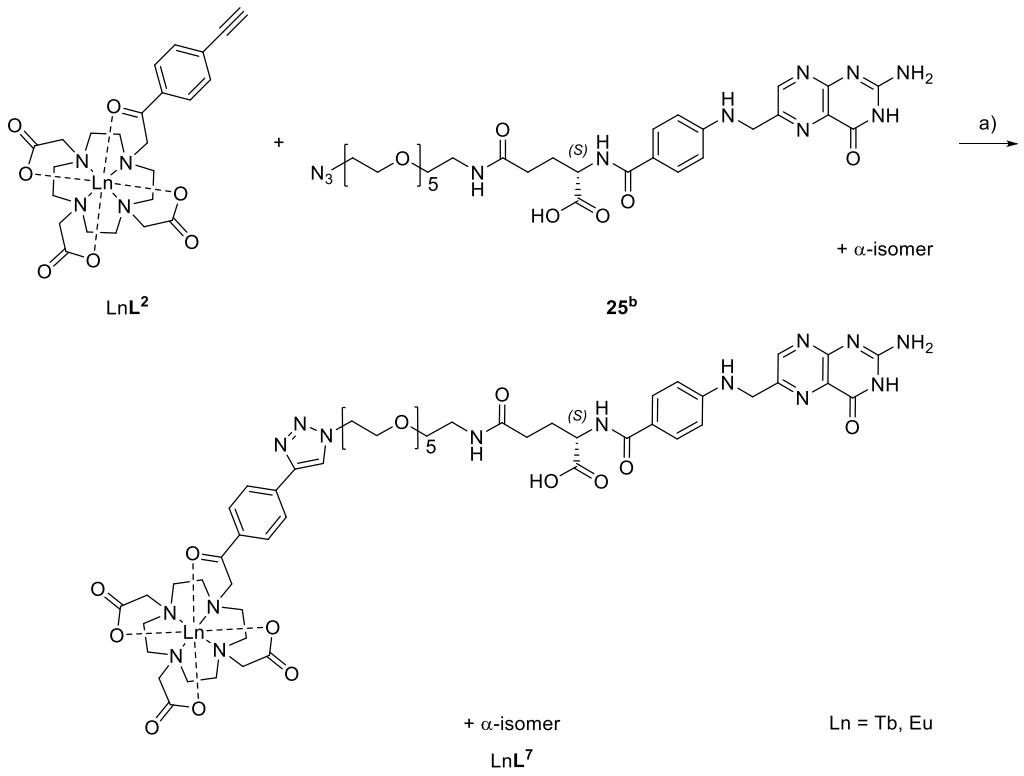
The more detailed synthesis of the alkynes appended to DO3A are included in Section 2.2. The lanthanide complexation was carried out prior to the copper click reaction, otherwise copper would be able to reside in the macrocyclic cavity and coordinate to the ligand. The copper click reactions are outlined in Scheme 3.6 and Scheme 3.7.

Difficulty with the reactions once again arose from solubility issues with the folate-appended azide, however through heating and addition of DMSO the reaction was able to proceed. The copper azide-alkyne cycloaddition was found to proceed with either the Cu^{+} ligand, $(CuOTf)_2 \cdot C_6H_6$, or the Cu^{2+} ligand, $CuSO_4 \cdot 5H_2O$, with sodium ascorbate as the reducing agent to generate the Cu^{+} *in situ*. All final terbium complexes were purified by HPLC by Daniel Gardner, an industrial collaborator at GSK. The complex Tb**L**^{6b} was the only complex formed using a mixture of regioisomers that was found to be separable by HPLC. It required two preparative HPLC runs where the first run isolated the mixture of regioisomers of Tb**L**^{6b}, and the second run was able to separate the two isomers (major and minor). It could be supposed that the major isomer is the γ-isomer and the minor isomer is the α-isomer, however due to the presence of the paramagnetic terbium they are indistinguishable by NMR spectroscopy so cannot be assigned with certainty so shall be referred to as the major and minor isomers.



Scheme 3.6. CuAAC reaction of Ln.pDO3A to FA-PEG$_n$-N$_3$ to produce Ln**L**^{6}. *Reagents and conditions: a) $(CuOTf)_2 \cdot C_6H_6$* (0.1 eq.), *MeOH/DMSO, 75 °C, 24 h or $CuSO_4 \cdot 5H_2O$ (0.1 eq.), sodium ascorbate (0.5 eq.), MeOH/DMSO/H_2O, 40 °C; Eu**L**^{6a} = 24%; Tb**L**^{6a} = 4%; Tb**L**^{6b} minor = 12%; Tb**L**^{6b} major = 18%.*

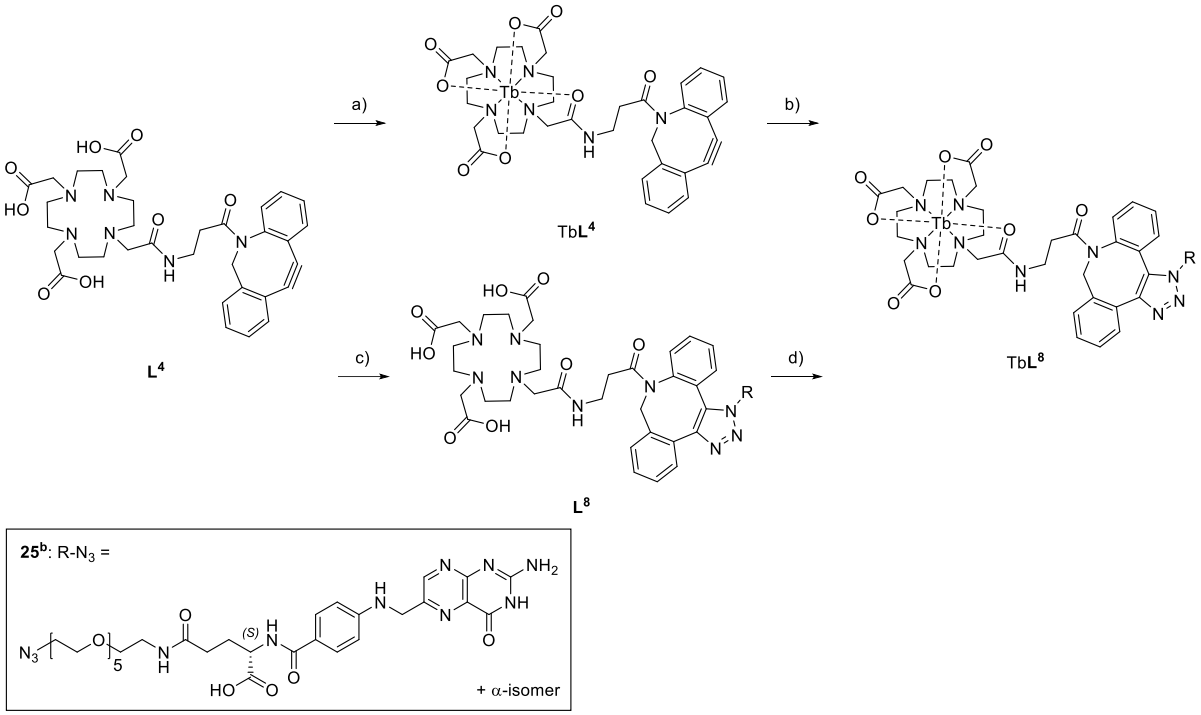
The propargyl-DO3A ligand requires direct metal excitation because of the lack of chromophore, therefore an additional alkyne-appended DO3A ligand, **L**^{2} was prepared in Section 2.2.1, to allow indirect metal excitation which is more favourable when using the compounds as luminescent probes in cell studies. Due to solubility issues with the shorter PEG chain in the folate-PEG_2-azide, **25**^{a}, CuAAC was only carried out with the folate-PEG_5-azide, **25**^{b}. Alkyne, **L**^{2} was used as a substrate for copper-catalysed cycloaddition with **25**^{b} to afford Ln**L**^{7} as a mixture of regioisomers.



*Scheme 3.7. CuAAC reaction of ethynylacetophenoneDO3A to FA-PEG$_5$-N$_3$ to produce Ln**L**^{7}. Reagents and conditions: a) CuSO$_4$·5H$_2$O (0.1 eq.), sodium ascorbate (0.5 eq.), MeOH/DMSO/H$_2$O, 40 °C; Eu**L**^{7} crude = 158%; Tb**L**^{7} = 39%.*

3.2.3.2 Copper-free click chemistry

The synthesis of the strain-promoted alkyne, DOTA-DBCO, **L**^{4} was outlined in Section 2.2.4. As the aim with these compounds was to be used in cell studies, due to its more emissive properties terbium was chosen for complexation. Two methods to synthesise Ln**L**^{8} are shown in Scheme 3.8. Method 1 (top) was the preferred method as it represents the archetypal copper-free click reaction, where the metal complexation is carried out first and then the azide-alkyne cycloaddition happened afterwards. The concern with this route was that the complexation reaction is heated for 48 hours and the strained dibenzocycloctyne may be susceptible to degradation, therefore the complexation was carried out at 50 °C, slightly lower than the normal 60 °C. The Tb**L**^{4} product was confirmed by MS (*m/z* 819 $[M+H]^+$) and the crude was carried forward for the cycloaddition. The click reaction proceeded quickly, as confirmed by LC-MS, but was allowed to react for 24 hours to ensure completion. The alternative route (Scheme 3.8, bottom) was carried out where the strain-promoted click reaction happened prior to complexation. This generated the stable triazole, **L**^{8}, before metal complexation took place. Both routes resulted in the desired product, Tb**L**^{8} as confirmed by LC-MS.



Scheme 3.8. Strain-promoted azide-alkyne cycloaddition. Reagents and conditions: a) $Tb(OTf)_3$ (1.05 eq.), 7 H_2O: 3 MeCN, 50 °C, 48 h, 154%; b) FA-PEG_5-N_3, **25^b**(0.95 eq.), 8 H_2O: 2 MeCN, r.t., 24 h, 44%; c) FA-PEG_5-N_3, **25^b** (1.0 eq.), 8 H_2O: 2 MeCN, r.t., 7 h, 97%; d) $Tb(OTf)_3$, (1.05 eq.), 7 H_2O: 3 MeCN, 60 °C, 48 h, 59%. *Excess mass attributed to salts; product used with salts.*

With the copper-free click reaction, it is possible to generate both the 1,4- and 1,5-triazoles; this is in addition to the two isomers of the folate-PEG_5-N_3, **25^b** used in the reaction, resulting in four possible isomers of the terbium complex, Tb**L**^{8}. Due to the difficulty in isolation of these isomers, the compounds were purified by HPLC at GSK, even so, the triazoles and the α- and γ-isomers were not possible to separate. The two strain-promoted click products were purified separately by RP-HPLC with the same retention times (Figure 3.5, t_R(ana) = 1.5 mins) supporting that both routes gave the desired compound.

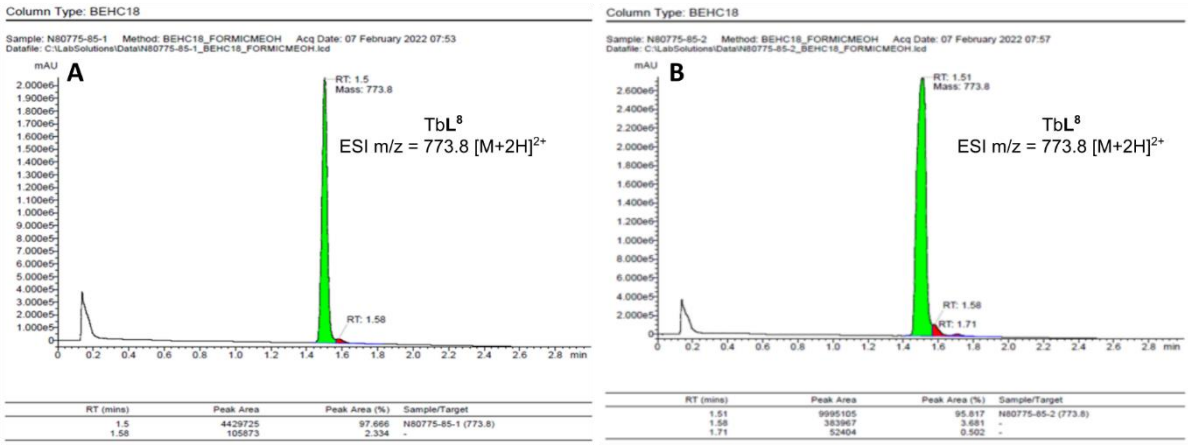


*Figure 3.5. Analytical HPLC traces of Tb**L**^{8} produced a) Scheme 3.8, top, t_R = 1.5 mins; b) Scheme 3.8, bottom, t_R = 1.51 mins.*

3.3 Paramagnetic ^{1}H NMR spectroscopy

The Tb-DOTA-PEG$_6$-FA, Tb**L**$^{5\gamma}$ and Tb**L**$^{5\alpha}$ complexes are indistinguishable by NMR spectroscopy, as shown in Figure 3.6. The ^{1}H NMR spectra shows that the complexes exist primarily in the SAP isomer, with the axial ring protons present in the 1:2:1 ratio with the neighbouring carboxylic acid arms residing in the same chemical environment. The ^{1}H NMR spectrum of Tb-DOTA-DBCO clicked to N_3-PEG$_5$-FA, Tb**L**^{8}, was also found to strongly resemble the Tb-DOTA-PEG$_6$-FA complexes, Tb**L**^{5}. This is reasonable as the three complexes have 3 acetic acid arms and the functionalised arm is joined by an amide linker group. The broadening of the lines in the case of Tb**L**^{8} is most likely as a result of the Tb-DOTA-DBCO complex being less soluble than the other two complexes.

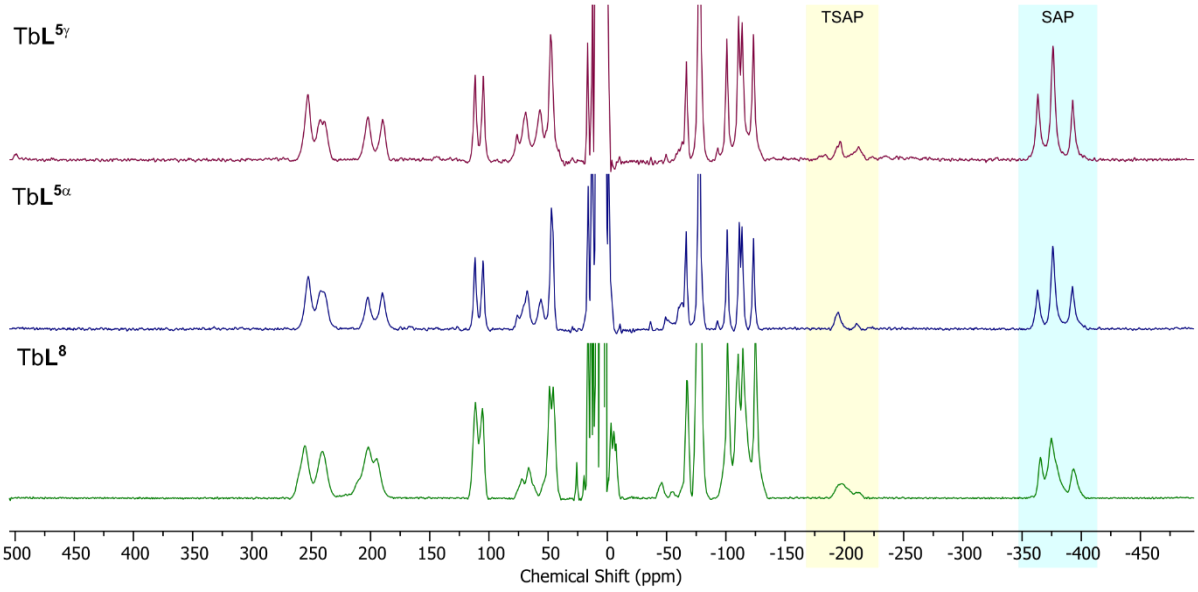


*Figure 3.6. ^{1}H NMR spectra of TbDOTA-PEG$_6$-FA (500 MHz, D_2O), showing the γ-isomer, Tb**L**$^{5\gamma}$ (top) and α-isomer, Tb**L**$^{5\alpha}$ (middle) and Tb-DOTADBCO click to N_3-PEG$_5$-FA, Tb**L**^{8} (bottom). Yellow region (TSAP isomer) and blue region (SAP isomer).*

Similarly, for the major and minor isomers of the TbpDO3A-N_3-PEG$_5$-FA, Tb**L**^{6b} and the shorter chain equivalent, Tb**L**^{6a}, the ^{1}H NMR spectra are practically identical (Figure 3.7) with only very minor differences in chemical shifts to suggest differences in the chemical structure. As the closest protons to the terbium centre are most greatly shifted by the paramagnetism, it is expected that the ^{1}H NMR spectra would look analogous as the terbium was coordinated by three acetate arms and a triazole linker.

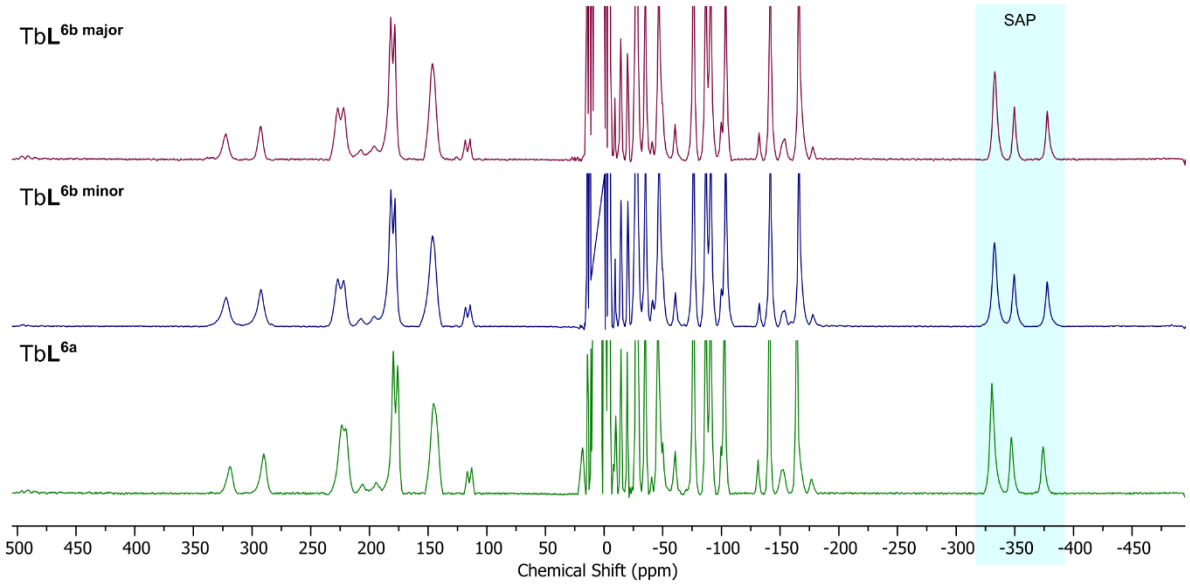


Figure 3.7. ^{1}H NMR spectra of TbpDO3A-N_3-PEG$_n$-FA (500 MHz, D_2O), showing the major isomer (top, n=5); minor isomer (middle, n=5) and bottom (n=2, mixture of regiosiomers). Blue region (SAP isomer).

The ^{1}H NMR spectra of the acetophenone based ligands before and after the click reaction are shown in Figure 3.8. Like the other terbium-folate conjugates the complexes exhibit a shift upfield with the coordinating arms in a 1:2:1 ratio which is more visible for the alkyne precursor, Tb**L**^{2}. The copper-click product, Tb**L**^{7}, displays similar peaks but with significant peak broadening; this could be attributed to poor solubility in the NMR solvent resulting in a viscous inhomogeneous NMR sample or a more concentrated sample.

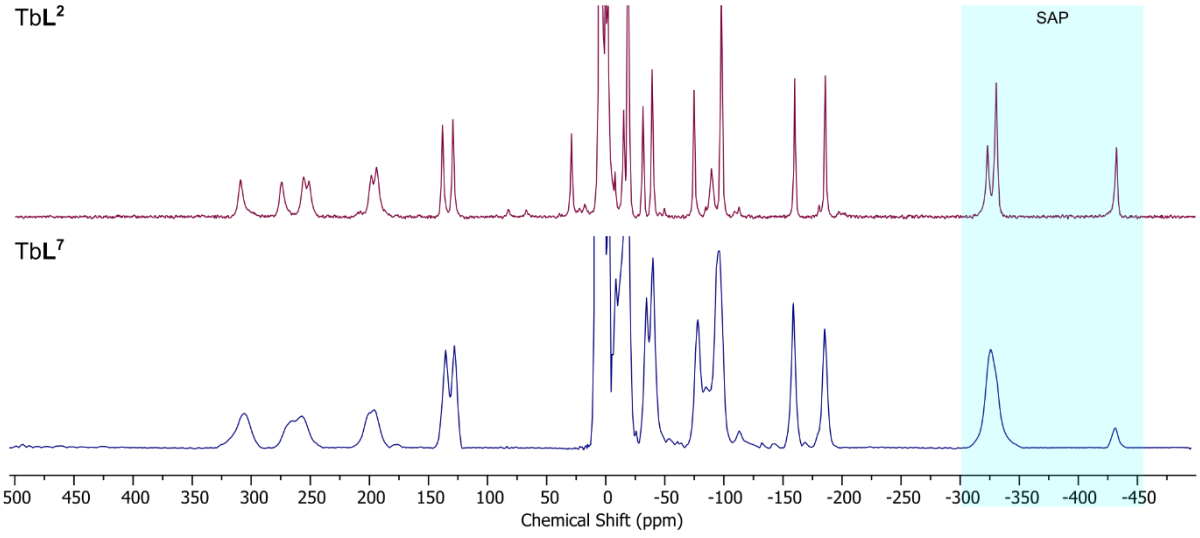


*Figure 3.8. ^{1}H NMR spectra showing the alkyne, Tb**L**^{2} ((400 MHz, D_2O), top) and the copper-click product, Tb**L**^{7} ((500 MHz, D_2O), bottom). Blue region (SAP isomer).*

3.4 Photophysical characterisation

3.4.1 UV-Visible spectroscopy

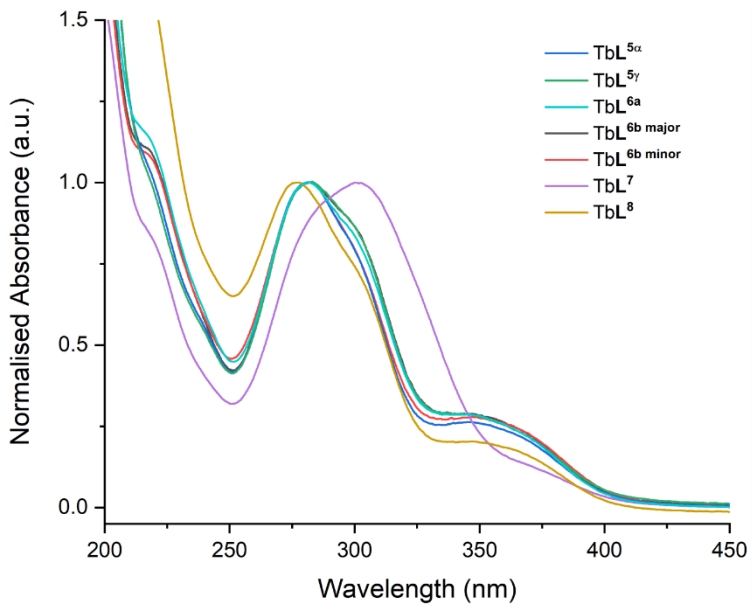


Figure 3.9. Absorption spectra of terbium-folate complexes in water solutions, normalised to dominant peak in 250-310 nm region.

The absorption spectra of the terbium folate complexes are shown in Figure 3.9. The absorption spectrum of folic acid is characterised by two absorption bands in the region of 250 - 300 nm and 300 - 400 nm, which correspond to the $\pi \rightarrow \pi^*$ transition for the pterin, and the $n \rightarrow \pi^*$ transition for the p-amino benzoyl acid moieties respectively.[24] All the terbium complexes exhibit these two distinct absorption characteristics of the folic acid moiety. Differences are observed for the acetophenone, Tb**L**^{7} which is red-shifted and broadened due to the overlap with the acetophenone moiety; similar absorbance spectra of acetophenone-folate complexes have been reported by Quici *et al.*[5] A small blue-shift was observed for the strain-promoted click Tb-DOTA-DBCO, Tb**L**^{8}, which is caused by the overlap with the dibenzocyclooctene-triazole absorption bands.

3.4.2 Fluorescence and Phosphorescence emission

The emission spectra of the terbium-folate complexes are shown in Figure 3.10. With the exception of the acetophenone-containing complex, all complexes were excited between 277-283 nm corresponding to the pterin absorption band. Therefore, weak indirect excitation was able to be performed using through space energy transfer (Förster) from the pterin moiety to terbium. For the acetophenone-containing complex, Tb**L**^{7}, indirect sensitisation through the chromophore (Dexter energy transfer) at 301 nm was possible. In Figure 3.10a and b, the complexes both display strong fluorescence from the folate moiety, with the peak at ~440 nm corresponding to the pterin emission, whilst the characteristic terbium emission peaks are just visible at 545, 588 and 621 nm corresponding to the $^{5}D_4 \rightarrow {}^{7}F_J$ (J=5-3) respectively. This indicates that the variations in the structure

with the α- and γ- folate regioisomers makes minimal difference in absorption or the terbium fluorescence emission spectra as shown for DOTA-PEG_6-FA, Tb**L**^{5} and TbpDO3A-N_3-PEG_5-FA, Tb**L**^{6}. Similarly, the length of PEG chain also makes no difference for the fluorescence emission, shown in Figure 3.10b, where Tb**L**^{6a} contains a PEG_2 chain and Tb**L**^{6b} contains PEG_5. The exception is for the emission peak at ~350 nm which is found to be more intense in the α-isomers (Tb**L**$^{5\alpha}$ and Tb**L**$^{6b\ minor}$), assuming that the minor isomer collected by HPLC was the α-isomer.

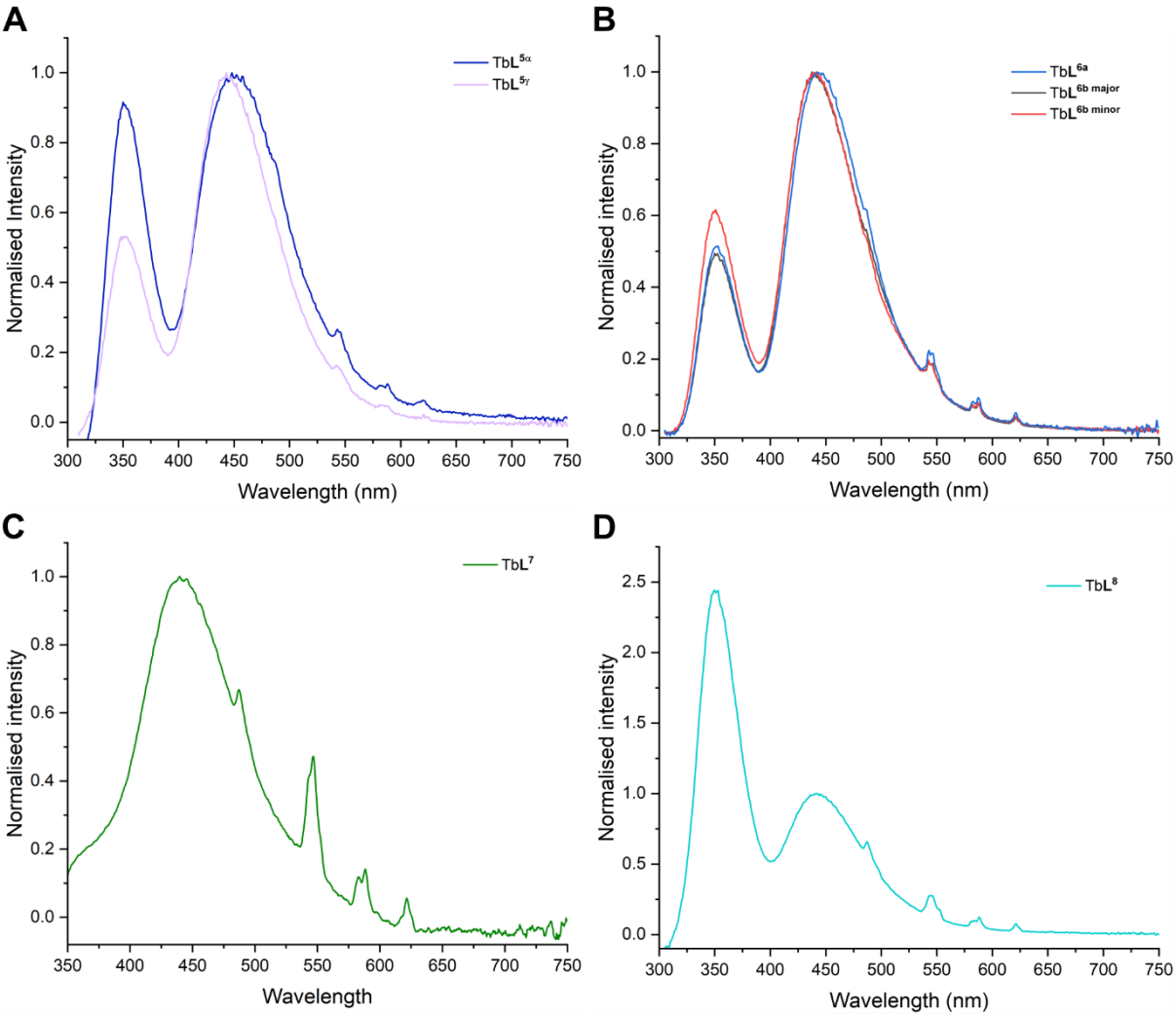


Figure 3.10. Fluorescence emission spectra of Tb-folate complexes a) α: λ_{ex} = 283 nm, γ: λ_{ex} = 277 nm; b) λ_{ex} = 282 nm; c) λ_{ex} = 301 nm; d) λ_{ex} = 277 nm.

The largest difference is observed for the acetophenone-containing complex (Figure 3.10c), where the indirect excitation *via* Dexter energy transfer increases the terbium fluorescence with the peak at 488 nm visible ($^5D_4 \rightarrow {}^7F_6$); nevertheless, the folate emission at ~440 nm still dominates the signal. Interestingly, Quici *et al.* report a folate-acetophenone-containing europium complex with significantly less folate fluorescence.[5] The strain-promoted click product also displays the folate emission at ~440 nm, yet the peak at ~350 nm is roughly 1.5 times the magnitude of this emission. This could correspond to the dibenzocyclooctene-triazole linker fluorescence as prior to the click

reaction, the alkyne was found to display very strong fluorescence at ~400 nm (Figure 2.15). This emission may have blue-shifted following the formation of the triazole; alternatively, it could be undergoing intramolecular charge transfer to the folate moiety thereby increasing its fluorescence due to the greater quantum efficiency of the folate.

These spectra support the conclusion that folate is a poor sensitiser, and difficulties with it acting as a chromophore stem from the pterin moiety being a long distance away from the metal centre, impeding Förster energy transfer, as well as the triplet state not aligning with the emissive levels of terbium. However, folate was never intended to adopt this role and its functionality as a targeting moiety remain. Given the significant residual fluorescence arising from the folate moiety, itself a consequence of inefficient energy transfer to the distant terbium ion, it is here where long-lived lanthanide emission is ideally suited to signal separation. Figure 3.11 shows the phosphorescence emission spectra of the terbium-folate complexes, normalised to the peak at 545 nm to reveal the differences in the relative intensity of the 488 nm peak. The peak at 488 nm corresponds to the $^5D_4 \rightarrow {}^7F_6$ transition which is an electric quadrupole transition sensitive to its local coordination environment. All terbium-folate complexes display the typical terbium bands. There are small changes in the quadrupolar transition intensity, which reveal structural differences in the solution state that were indetectable by NMR spectroscopy.

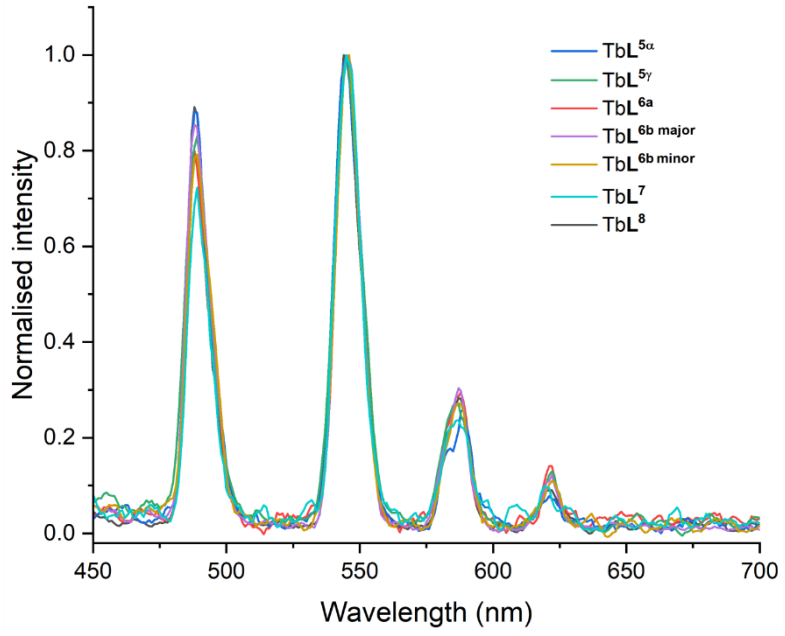


Figure 3.11. Phosphorescence emission spectra of Tb-folate complexes normalised to the peak at 545 nm.

3.4.3 Lifetimes and *q* values

The emission lifetimes of the complexes were measured to allow the hydration number, q (the number of metal-bound waters), to be quantified for each complex. This confirms the coordination environment around the metal centres. The inner sphere hydration number was calculated by measuring the excited state lifetimes of the terbium complexes in H_2O and D_2O and using the

difference in quenching between the O-H and O-D oscillators (Eq. 1.1). The results are shown in Table 3.1, with all the folate probes having a value of $q \sim 1$, indicating one water molecule is bound to the metal centre. This supports that all complexes bind as 8-coordinate, with the 8th coordination site either arising from the triazole N lone pair or a ketone O lone pair from the functionalised pendant arm.

Table 3.1. Terbium emission lifetimes of Tb-folate complexes in water.

Compound number	Compound name	λ_{ex} (nm)	λ_{em} (nm)	k_{H_2O} (ms^{-1})	k_{D_2O} (ms^{-1})	q
Tb**L**$^{5\alpha}$	Tb-DOTA-PEG_6-FA (α-isomer)	283	545	0.52	0.30	0.8
Tb**L**$^{5\gamma}$	Tb-DOTA-PEG_6-FA (γ-isomer)	277	545	0.55	0.35	0.7
Tb**L**^{6a}	Tb-pDO3A-N3-PEG_2-FA	282	545	0.52	0.31	0.7
Tb**L**$^{6b\ major}$	Tb-pDO3A-N_3-PEG_5-FA (major)	282	545	0.52	0.32	0.7
Tb**L**$^{6b\ minor}$	Tb-pDO3A-N_3-PEG_5-FA (minor)	282	545	0.54	0.32	0.7
Tb**L**^{7}	Tb-DOTA-ethynylacetophenone-N_3-PEG_5-FA	301	545	0.73*	0.41*	1.3*
Tb**L**^{8}	Tb-DOTA-DBCO-N_3-PEG5-N3	277	545	0.52	0.29	0.9

**biexponential decay fit y = A1*exp(-x/t1) + A2*exp(-x/t2) + y0. A1 (fast decay weighting) = 0.82, A2 (slow decay weighting) = 0.18 for H_2O and D_2O. $k_{H2Ofast}$ = 11.37 ms^{-1}; $k_{D2Ofast}$ = 11.22 ms^{-1}. k = 1/t2; Estimated error ± 10%.*

3.5 Conclusion

In this chapter, a range of terbium complexes with a folate-targeting moiety were designed and synthesised. The linkers were generated with different lengths of polyethylene glycol linkers and using solid-phase synthesis amide linkages, copper-click, and strain-promoted azide-alkyne cycloadditions to attach the targeting group. All terbium complexes are kinetically stable 8-coordinate complexes that exist primarily as the SAP isomer. The next step in this work is for these compounds to be tested in KB cells (cells with high FR-α expression) and a cell type transfected to allow high FR-β expression to test the binding affinity for the probes and to determine whether there is a difference in binding between the α- and γ-regioisomers. Moreover, it would be of interest to discover whether any of the methods of attachment alters internalisation as a result of changing the lipophilicity and sterics. Despite the large fluorescence from the folate moiety, it is anticipated that the long luminescence lifetime of the terbium will enable distinction using time-gated techniques such a FLIM.

3.6 References

1. D. Messeri, PhD thesis, University of Durham, 2001.
2. *World Pat.*, WO99/59640, 1999.
3. Z. L. Du, G. N. Borlace, R. D. Brooks, R. N. Butler, D. A. Brooks and S. E. Plush, *Inorg. Chim. Acta*, 2014, **410**, 11-19.
4. Z. L. Du, J. Sun, C. A. Bader, D. A. Brooks, M. Q. Li, X. Li and S. E. Plush, *J. Inorg. Biochem.*, 2018, **178**, 32-42.
5. S. Quici, A. Casoni, F. Foschi, L. Armelao, G. Bottaro, R. Seraglia, C. Bolzati, N. Salvarese, D. Carpanese and A. Rosato, *J. Med. Chem.*, 2015, **58**, 2003-2014.
6. *Lanthanide Luminescence: Photophysical, Analytical and Biological Aspects*, eds. P. Hänninen and H. Härmä, Springer Berlin Heidelberg, Berlin, Heidelberg, 2011.
7. A. S. Wibowo, M. Singh, K. M. Reeder, J. J. Carter, A. R. Kovach, W. Y. Meng, M. Ratnam, F. M. Zhang and C. E. Dann, *Proc. Natl. Acad. Sci. U.S.A.*, 2013, **110**, 15180-15188.
8. T. L. Kalber, N. Kamaly, P. W. So, J. A. Pugh, J. Bunch, C. W. McLeod, M. R. Jorgensen, A. D. Miller and J. D. Bell, *Mol. Imaging Biol.*, 2011, **13**, 653-662.
9. S. G. Konig and R. Kramer, *Chem. Eur. J.*, 2017, **23**, 9306-9312.
10. C. Corot, P. Robert, E. Lancelot, P. Prigent, S. Ballet, I. Guilbert, J. S. Raynaud, I. Raynal and M. Port, *Magn. Reson. Med.*, 2008, **60**, 1337-1346.
11. S. Wang, R. J. Lee, C. J. Mathias, M. A. Green and P. S. Low, *Bioconjugate Chem.*, 1996, **7**, 56-62.
12. Q. S. Chen, X. J. Meng, P. McQuade, D. Rubins, S. A. Lin, Z. Z. Zeng, H. Haley, P. Miller, D. G. Trotter and P. S. Low, *Mol. Pharmaceutics*, 2016, **13**, 1520-1527.
13. Q. S. Chen, X. J. Meng, P. McQuade, D. Rubins, S. A. Lin, Z. Z. Zeng, H. Haley, P. Miller, D. G. Trotter and P. S. Low, *Mol. Pharmaceutics*, 2017, **14**, 4353-4361.
14. Y. Y. J. Gent, K. Weijers, C. F. M. Molthoff, A. D. Windhorst, M. C. Huisman, D. E. C. Smith, S. A. Kularatne, G. Jansen, P. S. Low, A. A. Lammertsma and C. J. van der Laken, *Arthritis Res. Ther.*, 2013, **15**, R37.
15. S. A. Kularatne, M. J. Belanger, X. J. Meng, B. M. Connolly, A. Vanko, D. L. Suresch, I. Guenther, S. B. Wang, P. S. Low, P. McQuade and D. G. Trotter, *Mol. Pharmaceutics*, 2013, **10**, 3103-3111.
16. M. Rutnakornpituk, N. Puangsin, P. Theamdee, B. Rutnakornpituk and U. Wichai, *Polymer*, 2011, **52**, 987-995.
17. A. F. Trindade, R. F. M. Frade, E. M. S. Macoas, C. Graca, C. A. B. Rodrigues, J. M. G. Martinho and C. A. M. Afonso, *Org. Biomol. Chem.*, 2014, **12**, 3181-3190.

18. M. Dzwonek, D. Zalubiniak, P. Piatek, G. Cichowicz, S. Meczynska-Wielgosz, T. Stepkowski, M. Kruszewski, A. Wieckowska and R. Bilewicz, *RSC Adv.*, 2018, **8**, 14947-14957.
19. M. R. Ke, S. L. Yeung, D. K. P. Ng, W. P. Fong and P. C. Lo, *J. Med. Chem.*, 2013, **56**, 8475-8483.
20. J. M. Harris, N. E. Martin and M. Modi, *Clin. Pharmacokinet.*, 2001, **40**, 539-551.
21. Y. X. Dai, X. G. Cai, X. Z. Bi, C. X. Liu, N. Yue, Y. Zhu, J. Q. Zhou, M. A. Fu, W. L. Huang and H. Qian, *Eur. J. Med. Chem.*, 2019, **171**, 104-115.
22. A. Yamaguchi, Y. Anami, S. Y. Y. Ha, T. J. Roeder, W. Xiong, J. Lee, N. T. Ueno, N. Y. Zhang, Z. Q. An and K. Tsuchikama, *Bioorg. Med. Chem.*, 2021, **32**, DOI: 10.1016/j.bmc.2021.116013.
23. L. N. Goswami, Z. H. Houston, S. J. Sarma, S. S. Jalisatgi and M. F. Hawthorne, *Org. Biomol. Chem.*, 2013, **11**, 1116-1126.
24. M. Baibarac, I. Smaranda, A. Nila and C. Serbschi, *Sci. Rep.*, 2019, **9**, DOI: 10.1038/s41598-019-50721-z.

4 Tuftsin-derived imaging agents

4.1 Introduction

Tuftsin is a tetrapeptide that has been used previously as a targeting moiety for the imaging of macrophages. This work involves the development of previous work by the Faulkner group using tuftsin.[1-3] Earlier work involved optical imaging of tuftsin and a related pentapeptide using terbium complexes and a fluorescent fluorescein isothiocyanate tuftsin, as well as Gd-DOTA-labelled tuftsin derivatives for MR imaging.[2, 3] This has therefore has been expanded on in this work by attaching the tuftsin targeting moiety to a photoacoustic imaging modality component (see section 5.2.2.1), as well as exploring novel NMR characterisation methods using the gadolinium complexes.

4.1.1 INDIANA

INDIANA (IN cell DIffusion ANAlysis) is an NMR technique devised by Dr. Gogulan Karunanithy and Prof. Andrew Baldwin using fundamental NMR principles to distinguish between water molecules in two separate pools in a monocellular sample (intracellular and extracellular populations) to establish cell uptake and differentiate between complexes in the intra- and extra-cellular environments. The NMR technique involves varying the gradient strength, g, and the diffusion delays, Δ, in a stimulated echo diffusion experiment. The method includes a software package to model the NMR data as a two-pool model with exchange between the two pools, based upon the Kärger equations[4] to extract the cell specific parameters. More details of the method are described in Dr. Karunanithy's thesis.[5]

The water molecules found within the cells are diffusing at a slower rate than those found in the extracellular pool, so using pulsed field gradients and a sequence of increasing delay times to allow for relaxation enables differentiation between the two populations. The method can be used to determine cell density, cell radii, permeability, diffusion coefficients of the cell samples and intra- and extracellular relaxation rates of water.[6]

4.1.2 Design of tuftsin-labelled probes

Previous studies have shown that there are important components of the chemical structure of tuftsin for retaining its biological activity; minor alterations to these have been reported to reduce or inhibit its activity.[7-10] Earlier studies reported that modifications to the *N*-terminus of the peptide with fluorescent dyes did not affect the internalisation mechanism or the biological activity.[11, 12] This is in agreement with the crystal structure which shows the binding of tuftsin to the Nrp-1 receptor (Figure 1.16)[13] The *C*-terminal arginine binds to the N1b1b2 domain of the receptor, with aliphatic portions stacked between side chains of the first binding loop and the guanidine bridges to the second ligand binding loop.[13]

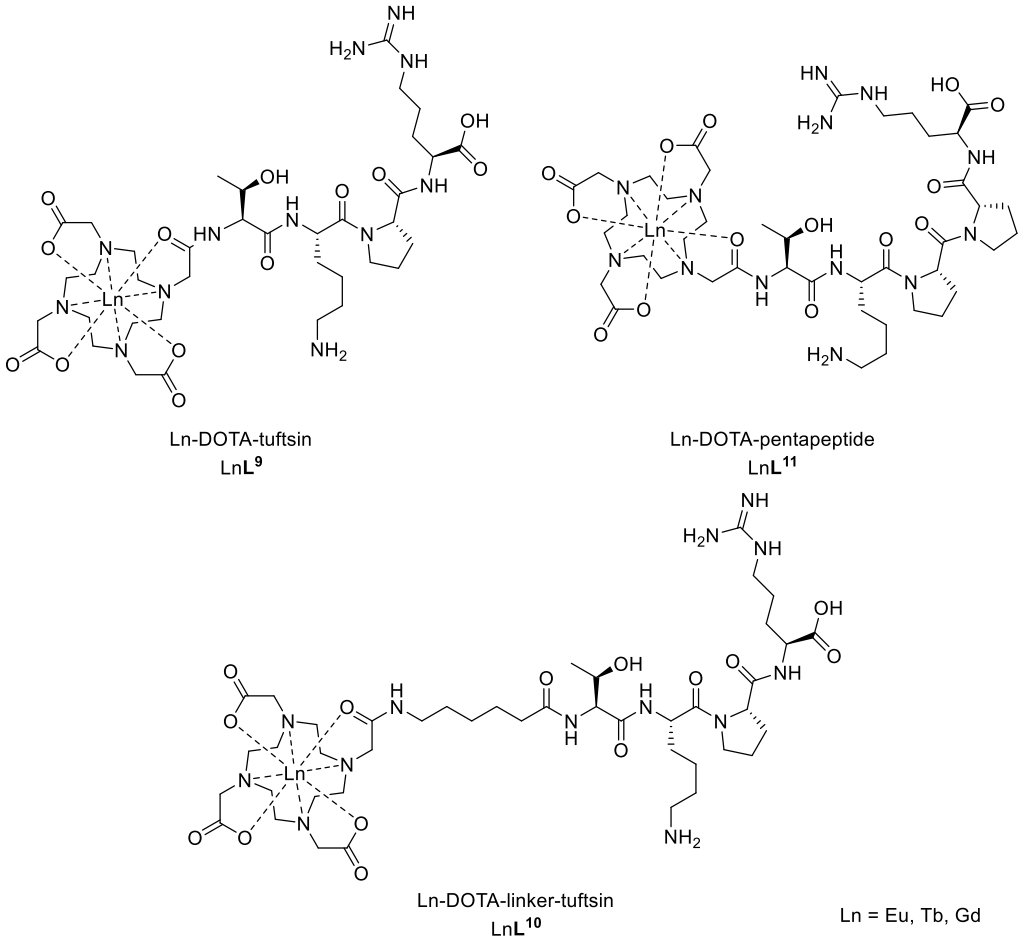


Figure 4.1. Peptide lanthanide complexes discussed in this chapter.

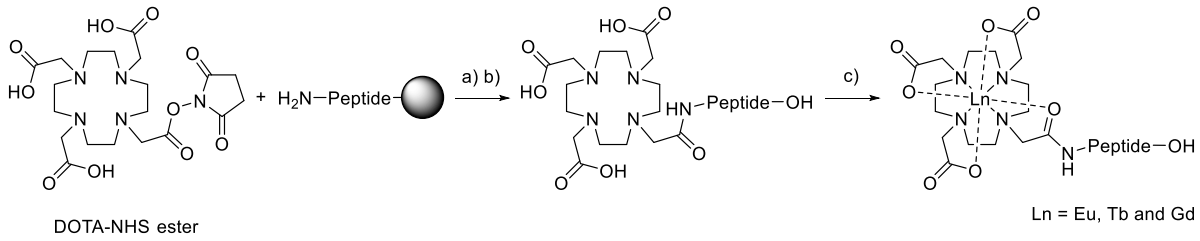
Given this and earlier work,[1-3] the DOTA monoamide was attached to tuftsin at the *N*-terminus of the peptide for the DOTA-labelled tuftsin complexes. The structures of the DOTA-labelled tuftsin complexes are shown in Figure 4.1. In addition to direct attachment of the peptide, **L**^{9}, a tuftsin attached via a hexanoic linker chain was made to determine whether distancing the steric bulk of the probe from the tuftsin moiety affects either the receptor binding or probe properties, **L**^{10}. The final DOTA-labelled tuftsin analogue was the pentapeptide, **L**^{11}, Thr-Lys-Pro-Pro-Arg (TKPPR), a tuftsin antagonist which is reported to have a fourfold greater receptor affinity than tuftsin;[14] therefore the difference in binding and downstream effects would be beneficial to compare with tuftsin.

4.2 Synthesis of complexes

Since the previous work done by the Faulkner group and collaborators to explore tuftsin, peptide synthesis has progressed to become more affordable and accessible. An outline of the synthesis is shown in Scheme 4.1. All resin-bound peptides were prepared using an automated peptide synthesis with a microwave reactor using preloaded N$^{\alpha}$-Fmoc-Arg(Pbf)-Wang resin and the following protected amino acids and linkers: N$^{\alpha}$-Fmoc-L-Thr(tBu)-OH, N$^{\alpha}$-Fmoc-Lys(Boc)-OH, N$^{\alpha}$-

Fmoc-L-Pro-OH and Fmoc-21-amino-4,7,10,13,16,19-hexaoxaheneicosanoic acid (CAS: 882847-34-9). The Fmoc-protecting group was cleaved using piperidine (20% piperidine in DMF) before each amide coupling reaction. Amide couplings were promoted using the coupling reagent, *N,N'*-diisopropylcarbodiimide (DIC) and Oxyma Pure, as a non-explosive alternative to 1-hydroxybenzotriazole (HOBt) to reduce racemisation. A final Fmoc-deprotection step was used in the synthesis to leave the peptide-bound resin with a free terminal amine for attachment to a suitable probe.

Peptide-loaded resin was transferred to a biotage isolute fritted column and swollen before the peptide was attached to the macrocycle via amide coupling using the activated NHS ester. Following completion of the reaction, the resin was washed and dried before the cleavage cocktail was added to the reaction vessel. The cleavage cocktail consisted of trifluoroacetic acid (TFA), triisopropylsilane (TIPS), H_2O and 1,3-dimethyoxybenzene (95:2.5:2.5:2.5), where all cations and free radicals would be quenched by the added scavengers. The DOTA-labelled tuftsin derivatives were then purified by preparative RP-HPLC to obtain the ligands in good purity before lanthanide complexation. The DOTA-labelled tuftsin derivatives were fully characterised by ^{1}H and ^{13}C NMR spectroscopy using standard techniques such as COSY, HSQC, HMBC and TOCSY.



Scheme 4.1. Reaction scheme for the synthesis of the peptide based DOTA complexes. Reagents and conditions: a) TEA, DMF, r.t., N_2 agitation, 3 days; b) TFA: TIPS: H_2O: 1,3-dimethoxybenzene (92.5:2.5:2.5:2.5), r.t., 3 h; c) $Ln(OTf)_3$, MeOH, 60 °C, 48 h.

Following lanthanide complexation, the compounds were dialysed using Float-A-Lyzer® dialysis chambers with the appropriate molecular weight cut off (MWCO) for the complex to remove any residual salts from the complexation mixture. Complexation was carried out with three lanthanides with each being chosen for a different purpose: europium complexes were used for luminescent studies and NMR structural characterisation; terbium complexes were made due to their stronger emission intensity for luminescent cell studies; and gadolinium complexes were made for relaxivity measurements. The structures of the DOTA-labelled tuftsin derivatives are shown in Figure 4.1.

4.3 Characterisation of the complexes

4.3.1 Paramagnetic ^{1}H NMR spectroscopy

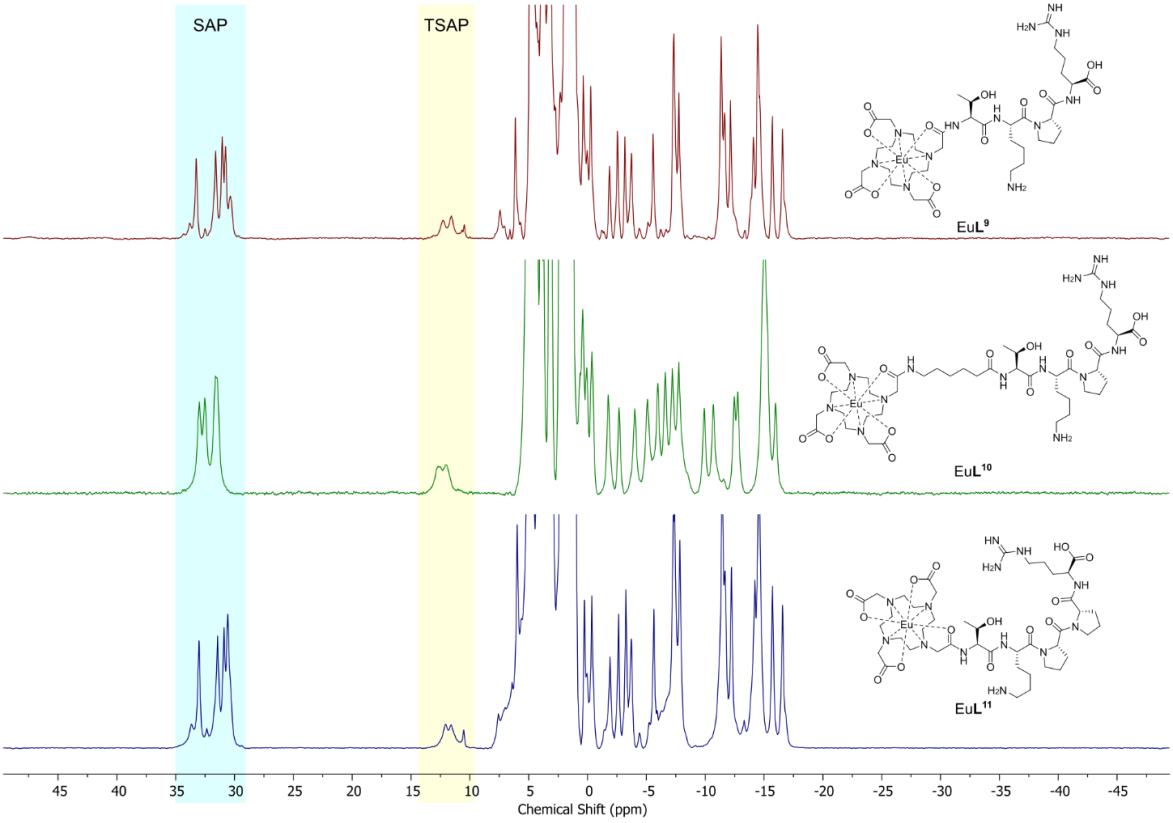


*Figure 4.2. Stacked ^{1}H NMR spectra (400 MHz, D_2O) of Eu-DOTA-tuftsin, Eu**L**^{9} (top), Eu-DOTA-linker-tuftsin, Eu**L**^{10} (middle) and Eu-DOTA-pentapeptide, Eu**L**^{11} (bottom) measured at r.t.*

Lanthanide complexes of cyclen-based ligands, such as DOTA, are found to undergo structural fluctuations in solution.[15] The square antiprismatic (SAP) and twisted SAP (TSAP) conformations are observable by ^{1}H NMR spectroscopy as they are in slow exchange. The fluxional nature of the tuftsin-based complexes are more easily studied using Eu(III) complexes than the more paramagnetic Tb(III). All complexes discussed in this chapter are neutrally charged 8-coordinate complexes which rigidifies the molecule, in comparison to 7-coordinate complexes which exhibit peak broadening due to the lower activation barrier for interconversion. For the tuftsin-based Eu(III) complexes the ^{1}H NMR spectra exhibit similar features (Figure 4.2). The most downfield resonances in the 30-35 ppm region, highlighted in blue, correspond to the axial ring protons on the macrocyclic backbone in the SAP geometry. The predominant coordination geometry of the europium complexes is SAP whilst the resonances at 10-15 ppm correspond to the minor isomer, in the TSAP geometry.

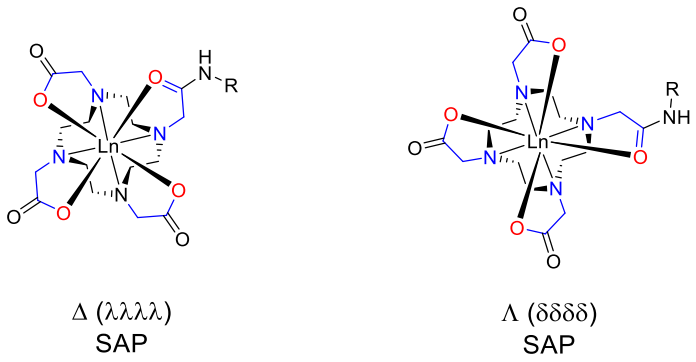


Figure 4.3. Enantiomers of the SAP isomer showing different helicity.

A difference in the SAP resonances is observable between the complexes where the peptide is bound directly to the macrocycle, Eu**L**^{9} and Eu**L**^{11}, compared to the complex containing the hexanoic linker, Eu**L**^{10}. All of the complexes explored here are unsymmetrical and therefore up to four signals can be expected for the psuedo-axial cyclen ring protons for the SAP conformation.[16] The Eu-DOTA-linker-tuftsin, Eu**L**^{10} exhibits this type of behaviour with the four signals (two distinct and two overlapping). However, the directly attached peptide complexes, Eu**L**^{9} and Eu**L**^{11} (Figure 4.2, top and bottom) display more than four peaks which indicates that there is more than one complex with SAP conformation (both forms of the SAP enantiomers, Figure 4.3).[16] This is likely because of the more closely bound peptide, which restricts rotation, while the linker chain distances the peptide from the metal-centre. This combines with the inherent chirality of the peptide chain to ensure that diastereoisomers of the macrocycles will exhibit different properties. On this basis and given that the peptides were prepared from homochiral amino acids, two distinguishable SAP isomers, and two distinguishable TSAP isomers, would be expected to be observed; this is supported by the observed spectra.

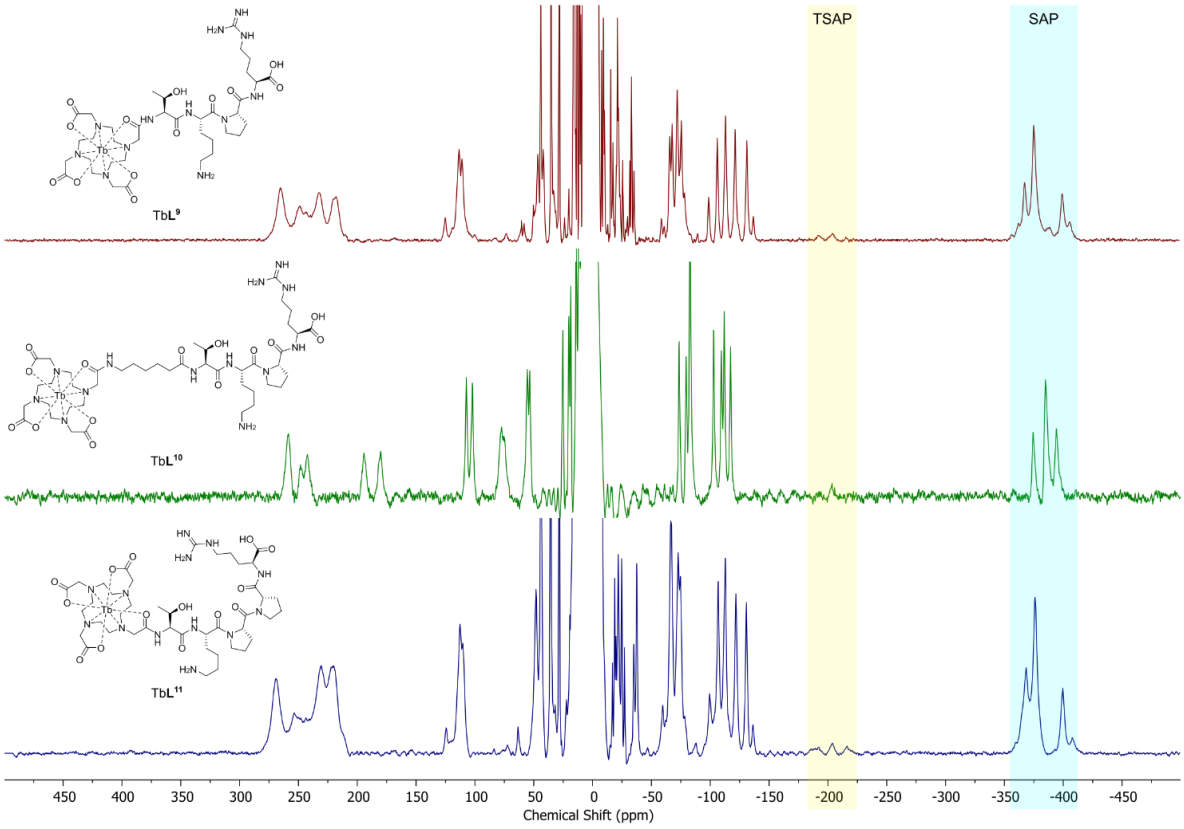


*Figure 4.4. Stacked ^{1}H NMR spectra (400 MHz, D_2O) of Tb-DOTA-tuftsin, Tb**L**^{9} (top), Tb-DOTA-linker-tuftsin, Tb**L**^{10} (middle) and Tb-DOTA-pentapeptide, Tb**L**^{11} (bottom) measured at r.t.*

The ^{1}H NMR spectra of the Tb(III) complexes of the peptide ligands are shown in Figure 4.4. The ground state of terbium has a different electron distribution from that of Eu(III): for Eu: $^{7}F_0$ (S = 3 ; L = 3 ; J = 0) and Tb(III): $^{7}F_6$ (S = 3; L = 3; J = 6). Terbium can be described as having an oblate electron distribution in its 3+ state (the ground state of europium is not paramagnetic, but thermal population of the low-lying $^{7}F_1$ state gives rise to a prolate distribution).[17] This results in an upfield shift of the SAP pseudo-axial protons on the macrocyclic ring. Terbium has a stronger magnetic field than europium and elicits greater pseudocontact shifts,[18] which can only be observed in the wider sweep width on conventional NMR instrument. It is reported that paramagnetic broadening can be reduced by using an NMR spectrometer with a lower magnetic field strength.[19] Given the paramagnetic broadening, it is harder to distinguish the TSAP isomer in the -175 to -225 ppm region; although it could be that with the slightly smaller ionic radii of terbium compared to europium that the SAP isomer is more favoured.

4.3.2 Photophysical characterisation

4.3.2.1 UV-visible spectroscopy

Generally, for the complexes the UV-visible spectra are superfluous as none of the complexes contain a chromophore and, at the concentrations used to record the luminescence spectra,

the metals are also not visible. At higher concentrations, 0.5 mM or higher, a very small peak corresponding to the metal excitation centre can be observed.

4.3.2.2 Luminescence

The steady-state excitation for the europium complexes was recorded at 300-550 nm for the $5D_0 \rightarrow {}^7F_1$ emission peak at 595 nm, which is one of the most intense emission peaks for uncorrected data. The luminescence spectra of europium complexes exhibited strong and characteristic Eu emission bands upon direct metal excitation at 397 nm; the characteristic europium peaks at 580, 592, 616, 653, 688 and 701 nm, arising respectively from the transitions ${}^5D_0 \rightarrow {}^7F_J$ (where J=0-4), are labelled in the europium emission spectra in Figure 4.5.

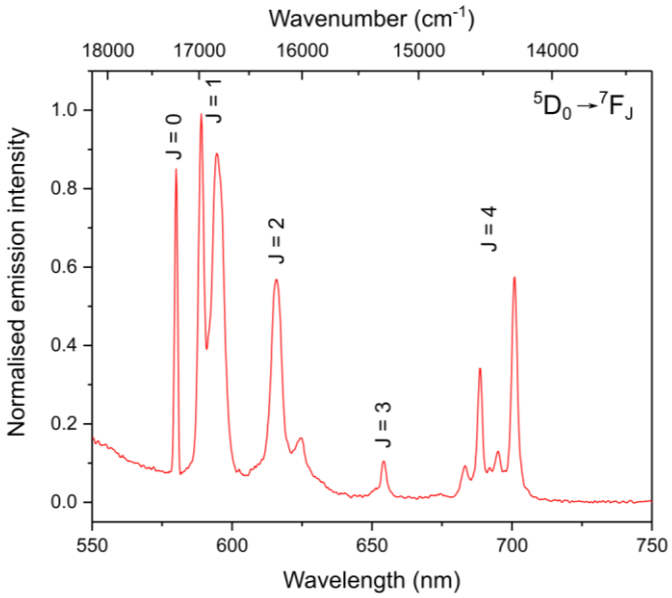


Figure 4.5. Uncorrected Eu-DOTA-tuftsin emission spectrum λ_{ex} = 397 nm showing the transitions from the ${}^5D_0$ emissive state.

The emission spectra for the three Eu-DOTA-tuftsin-based complexes are shown in Figure 4.6. As a result of the lack of chromophore, the complexes are all excited using direct metal excitation at 397 nm for Eu and using relatively high concentrations (> 1 mM). The emission peak at 616 nm corresponds to the ${}^5D_0 \rightarrow {}^7F_2$ transition and this is a quadrupolar transition which is hypersensitive to the symmetry of the complexes.[20] For all of the tuftsin-derived complexes, the peak at 616 nm exhibits the same intensity relative to the other emission peaks – this is as expected, as the coordination environment would be very similar for the complexes. Similarly, the phosphorescence emission spectra exhibit the same characteristic europium emission peaks for direct excitation of the metal complexes with no differences for the quadrupolar transition (Figure 4.6d).

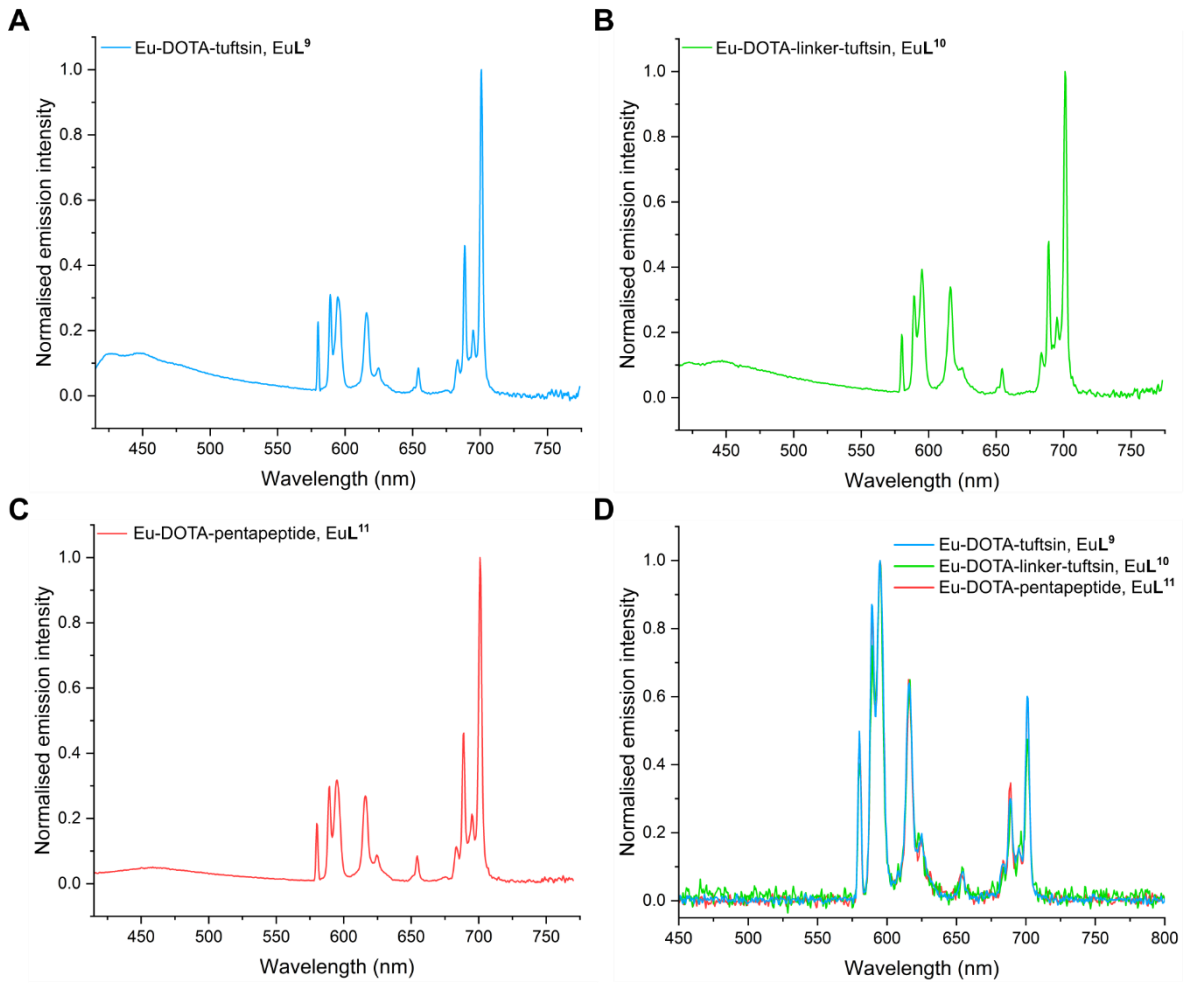


*Figure 4.6. Corrected normalised luminescence emission spectra for a) Eu-DOTA-tuftsin, [Eu**L**^{9}]= 1.5 mM in H_2O; b) Eu-DOTA-linker-tuftsin, [Eu**L**^{10}]=1.0 mM in H_2O; c) Eu-DOTA-pentapeptide, [Eu**L**^{11}]= 1.0 mM in H_2O. d) Uncorrected normalised phosphorescence emission spectra. λ_{ex} = 397 nm.*

The steady-state excitation for the terbium complexes was recorded from 270-450 nm for the $^5D_4 \rightarrow {}^7F_5$ emission peak at 545 nm, which is one of the most intense emission peaks for uncorrected data (Figure 4.7). The luminescence spectra of terbium complexes exhibited strong and characteristic Tb emission bands upon direct metal excitation at 366 or 371 nm; the characteristic terbium peaks at 490, 545, 580, 620, 650, 660, and 675 nm, arising from the transitions $^5D_4 \rightarrow {}^7F_J$ (where J=6-0), are labelled in the general terbium emission spectra in Figure 4.7.

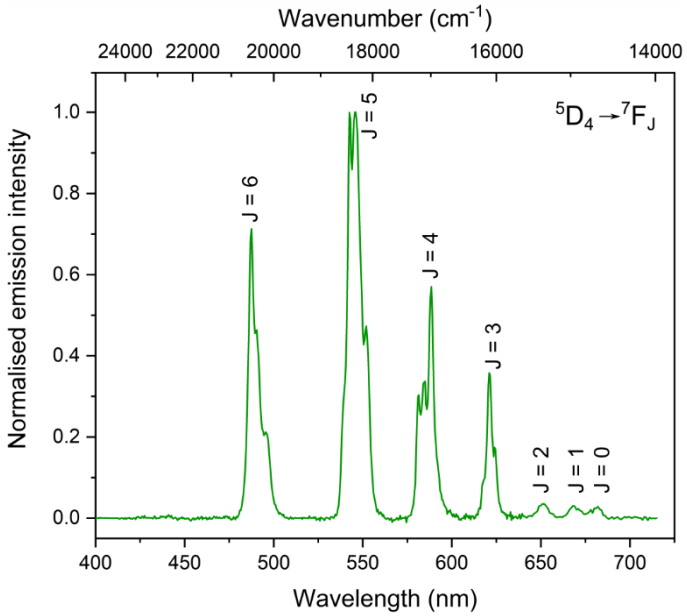


Figure 4.7. Uncorrected Tb-DOTA-tuftsin emission spectrum λ_{ex} = 366 nm showing the transitions from the $^5D_4$ emissive state.

The luminescence emission spectra for the three Tb-DOTA-tuftsin-based complexes are shown in Figure 4.8a-c. In Figure 4.8, some of the weaker emission peaks are visible in the 640-780 nm range (650 = $^7F_2$, 660 = $^7F_1$, 675 = $^7F_0$).[21] These can be difficult to observe without the presence of a chromophore, but it was found that at high enough concentrations of complex (> 0.1 mM) and wider slit widths they could be detected.

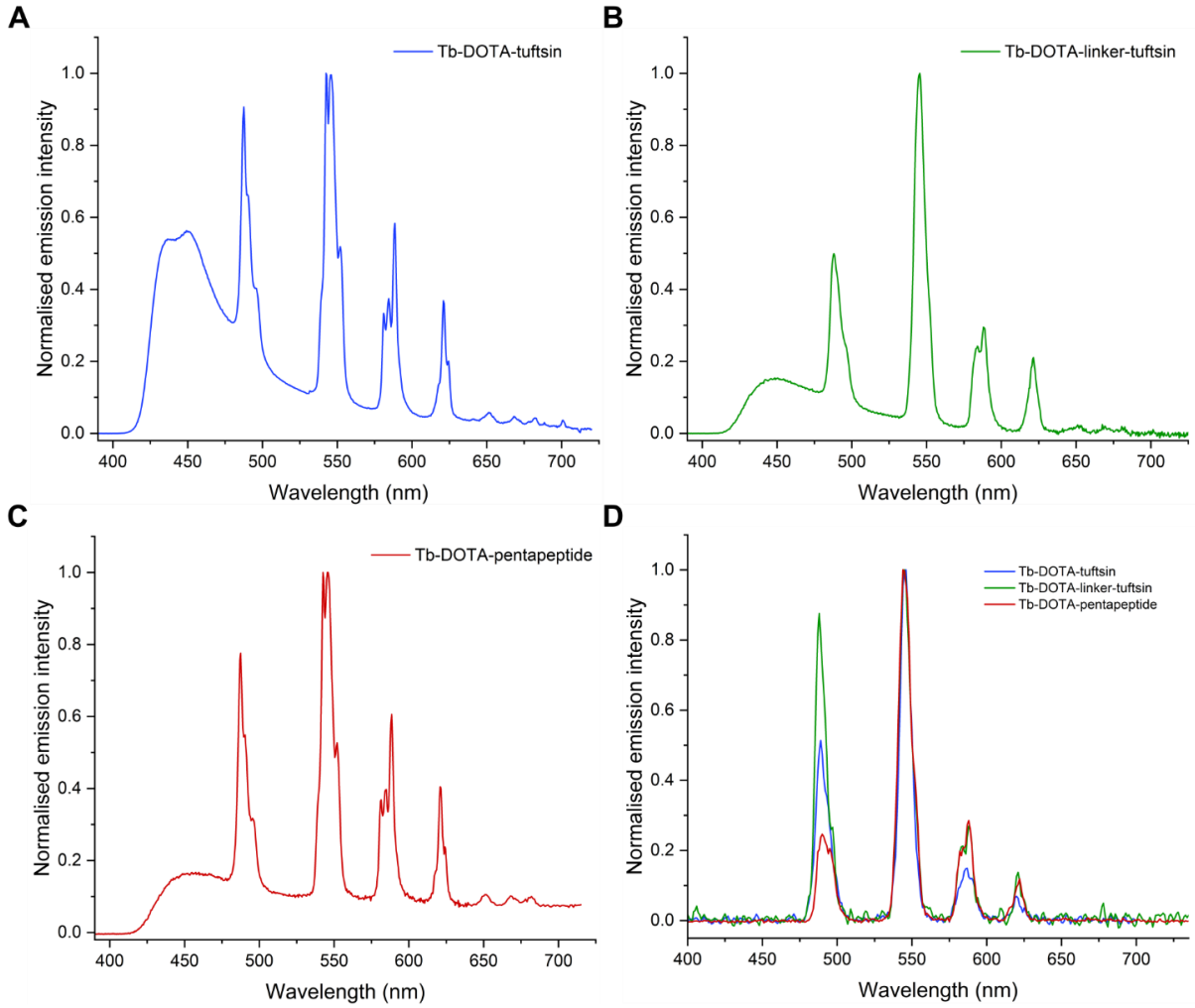


*Figure 4.8. Corrected normalised luminscence emission spectra for a) Tb-DOTA-tuftsin, [Tb**L**^{9}] = 1.0 mM in H_2O, λ_{ex} = 371 nm; b) Tb-DOTA-linker-tuftsin, [Tb**L**^{10}] = 0.1 mM in H_2O, λ_{ex} = 366 nm; c) Tb-DOTA-pentapeptide, [Tb**L**^{11}] = 0.25 mM in H_2O, λ_{ex} = 366 nm. d) Uncorrected normalised phosphorescence emission spectra, λ_{ex} = 366 nm.*

Similarly, the phosphorescence emission spectra are shown in Figure 4.8d and display the characteristic terbium transitions. The more pronounced difference for the terbium complexes is observed for the hypersensitive ΔJ =2 transition at 488 nm, which is most likely because of the smaller ionic radii of terbium compared to europium where no difference is seen for the 616 nm, ΔJ = 2 peak (Figure 4.6d).

The europium and terbium emission lifetimes of the excited state were measured in H_2O and D_2O to determine the hydration number (*q*) of the complex; the Eu results are shown in Table 4.1 and Tb results are shown in Table 4.2. The europium decay-by-delay spectra were fit to a monoexponential decay, and the terbium decay-by-delay were fit to a biexponential decay, and q was calculated from the component with the largest weighting. All the *q* values lie between 0.7 and 1.3, which indicates that the complexes generally have 1 water molecule bound to the metal centre. This is expected as the lanthanides can have a coordination number of 9 and the ligand occupies 8

of these sites, leaving one available for water binding. When comparing the equivalent complexes with europium and terbium, the hydration numbers are 0.2-0.4 greater for europium than terbium. As Eu has a larger ionic radius than Tb and was found to exist in a higher proportion of the TSAP conformation (Figure 4.2), it is expected that Eu would have a higher hydration number.

Table 4.1. Excited state emission lifetimes for Eu(III) peptide complexes in H_2O and D_2O and calculated hydration number (q).

Compound	Complex	τH_2O (ms)	τD_2O (ms)	*q*
Eu**L**[9]	Eu-DOTA-tuftsin	0.62	2.26	1.1
Eu**L**[10]	Eu-DOTA-linker-tuftsin	0.52	2.32	1.3
Eu**L**[11]	Eu-DOTA-pentapeptide	0.61	2.17	1.1

All were fit to a monoexponential decay. Estimated error ± 10%

Table 4.2. Excited state emission lifetimes for Tb(III) peptide complexes in H_2O and D_2O and calculated hydration number (q). All were fit to a biexponential decay†.

Compound	Complex	A1:A2	τ_1H_2O (ms)	τ_1D_2O (ms)	τ_2H_2O (ms)	τ_2D_2O (ms)	*q*
Tb**L**[9]	Tb-DOTA-tuftsin	3.22	1.93	3.22	0.14	0.16	0.7
Tb**L**[10]	Tb-DOTA-linker-tuftsin	0.13	1.33	2.13	0.12	0.12	-
Tb**L**[11]	Tb-DOTA-pentapeptide	2.92	1.82	3.29	0.17	0.2	0.9

*†biexponential decay, where y = A1*exp(-x/t1) + A2*exp(-x/t2) + y0. Estimated error ± 10%. t_1 (longer lifetime component) was used to calculate q due to being the most significant component, as measured by the weightings of the exponential. t_2 is likely to be an instrument artifact, defined by the flash lamp.*

4.3.3 ^{1}H Relaxivity

The ^{1}H water relaxation rate was measured with increasing concentrations of the tuftsin-labelled gadolinium DOTA complexes in phosphate buffered saline (PBS) (Figure 4.9, values in Table 4.3) with the standard inversion-recovery pulse sequence at 500 MHz (11.74 T). These relaxivities were compared to commercially available DOTAREM®, $[Gd\text{-}DOTA]^-$ with the meglumine salt, which is a non-targeting 8-coordinate macrocyclic complex for comparison of the tuftsin-derived moieties. The Gd-tuftsin conjugates are monoamide derivatives of DOTA, and it has been demonstrated that replacement of a strongly ligating carboxylate group by an amide reduces the water exchange rate of Gd complexes by 3-4 times.[22, 23] Therefore it might be expected that the Gd-tuftsin conjugates have lower relaxivity values than $[Gd\text{-}DOTA]^-$ due to a longer water residency time (τ_m) of the monoamide. Outer-sphere relaxation occurs through space and, through dipole intereactions with neighbouring molecules, increases r_1. It has been reported that outer-sphere relaxation is comparable for molecules with similar molecular weight as diffusion is the main

contributor,[24] therefore given the similarities in the gadolinium-tuftsin conjugates outer-sphere relaxation is likely to be significant for these complexes.

However, the proton relaxivity of the complexes was found to be similar to that of other conventional MRI contrast agents with an inner-sphere hydration number, *q*, roughly equal to 1, as shown by the similarity of Gd-DOTAREM, Gd-DOTA-tuftsin and Gd-DOTA-linker-tuftsin: 3.38, 3.26 and 3.37 s^{-1} mM^{-1} respectively. Previously the relaxivity of Gd-DOTA-tuftsin in PBS was reported to be 2.52 s^{-1} mM^{-1} recorded on a 400 MHz NMR spectrometer; this is more similar to a Gd-DOTA-tuftsin control (2.23 s^{-1} mM^{-1}) that was characterised by INDIANA at 600 MHz.[3] Slight differences in values could be due to excess lanthanides salts which can lead to errors in masses, but also the difference in field strength also results in variations in relaxivity, r_1 values. These errors could also be the reason for the difference with the Gd-DOTA-pentapeptide which has a relaxivity of 2.67 s^{-1} mM^{-1}.

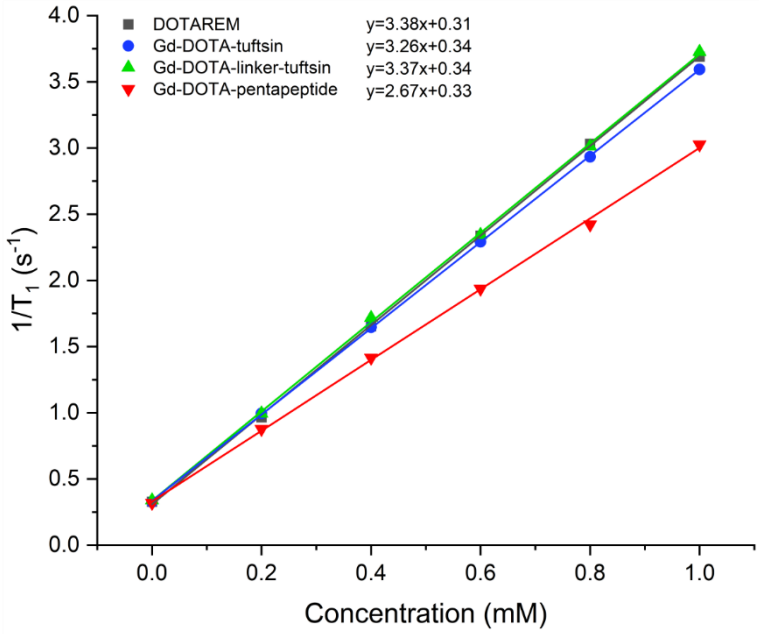


Figure 4.9. ^1H relaxation rate (R1) versus concentration of Gd complexes, 0.01M PBS, pH 7, 500 MHz, 298 K.

Table 4.3. H_2O ^1H relaxivity with Gd complexes at 500 MHz (11.7 T), pH 7, 298 K in 0.01M PBS solution.

	r_1 (mM Gd^{-1} s^{-1})		
Complex	**400 MHz (9.4 T)[a]**	**500 MHz (11.7 T)[b]**	**600 MHz (14.1 T)[c]**
DOTAREM	-	3.38	-
Gd-DOTA-tuftsin, Gd**L**[9]	2.52	3.26	2.23
Gd-DOTA-linker-tuftsin, Gd**L**[10]	-	3.37	-
Gd-DOTA-pentapeptide, Gd**L**[11]	-	2.67	-

[a]Feng et al. study[3, 25]; [b]inversion recovery pulse sequence; [c]INDIANA pulse sequence with 1-pool fit.

It is worth noting that water exchange kinetics vary between SAP and TSAP isomers, which influences the relaxivity of the complexes. Compared to the SAP isomer, TSAP exhibits faster water exchange at the Gd centre, meaning that the relaxation can be transferred more rapidly to the bulk water.[15] For the europium and terbium complexes of the peptide conjugates, the SAP isomer was the major isomer. As gadolinium is situated between europium and terbium in the periodic table, its ionic radius is between Eu and Tb, therefore it is expected that the Gd-complexes will also predominantly exist as the SAP isomer. Likewise, $[Gd\text{-}DOTA]^-$ primarily adopts a SAP structure so it is not the most optimised contrast agent.[15, 26] However, as it is routinely used in clinical settings and these Gd-DOTA-tuftsin based complexes exhibit similar r_1 values, it is anticipated that these would be usable in an MRI context.

4.4 NMR techniques

4.4.1 INDIANA

Recent collaboration with the Baldwin group at Oxford has developed a method to model the result of NMR diffusion experiments in a way that the different proton relaxation rates can be used to distinguish between outer and intracellular population and the exchange rates between the two.[6] The existing method was designed to model the behaviour and properties of two pools of fluid with different rates of diffusion. The core principle of INDIANA is that the size of the cell defines the diffusion rate rather than the voxel size for MRI; the cell size is significantly smaller than that of a voxel meaning that on a cellular level more information can be obtained from INDIANA than MRI.

Initial work applied the INDIANA model as a one pool system on human blood plasma only – the results are shown in Figure 4.10 and values given in Table 4.4. A one-pool INDIANA method is analogous to the inversion-recovery experiment and so was used to obtain the r_1, relaxivity rates in human blood plasma. This bridges between the relaxivity measurements in PBS and whole blood as there are proteins present in blood such as blood serum albumin (BSA) that can bind to and alter the relaxation rate of contrast agents.[27, 28] If BSA binds too strongly to a contrast agent, it has been found that the contrast agent bound to BSA is retained in the blood;[27, 29] this is undesirable for a cell targeting probe like the tuftsin-conjugates.

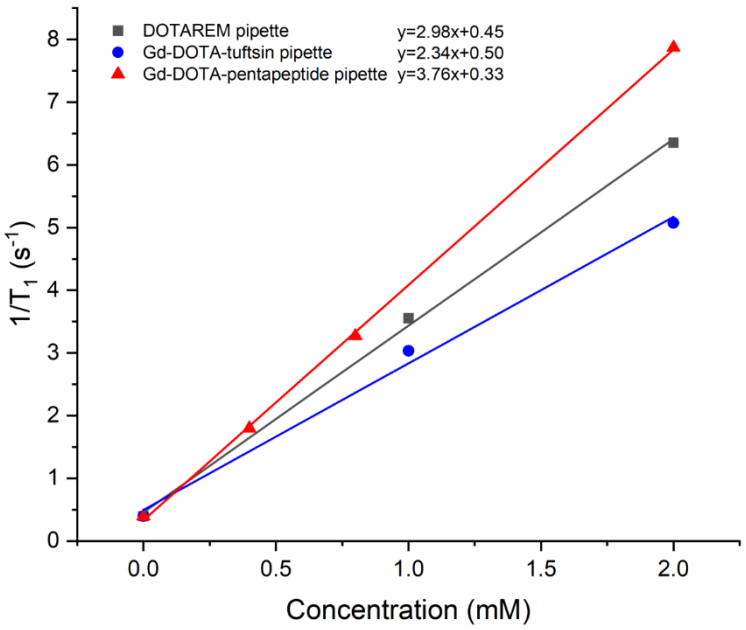


Figure 4.10. ^{1}H relaxation rate (R1) versus concentration of Gd complexes, human blood plasma, 600 MHz, 298 K.

The relaxivity of $[GdDOTA]^-$ in human blood plasma, was found to be comparable with values reported in the literature[30] when accounting for differences in temperature and the proton Larmor frequency at different field strengths. Even when considering the differences arising from the field strengths, the r_1 value for Gd-DOTA-tuftsin in blood plasma decreased. This contrasted with earlier findings by Feng *et al.*, who reported an increase in relaxivity between Gd-DOTA-tuftsin in PBS solution compared to Gd-DOTA-tuftsin in PBS with 8% BSA solution (2.52 mM^{-1} s^{-1} vs 2.64 mM^{-1} s^{-1}).[3, 25] Feng reasoned that a low proportion of the Gd-DOTA-tuftsin complex binds non-covalently with the BSA, hence resulting in only a small increase. Although human blood plasma is comprised of 6-7% proteins, where ~60% of those correspond to serum albumin, there are also other lipids, hormones, and proteins such as immunoglobulins that can alter the relaxivity of Gd contrast agents.

Table 4.4. Comparison of H_2O ^1H relaxivity with Gd complexes at 600 MHz (14.1 T), 298 K in human blood plasma from this study compared with literature reported values.

Solution	**Human blood plasma**	**PBS + 8% BSA solution**	**Human blood plasma**
Field strength (Tesla)	7	9.4	14.1
Temperature (K)	310	298	298
Complex	**r_1 (mM Gd^{-1} s^{-1})**		
DOTAREM	3.2		2.98
Gd-DOTA-tuftsin		2.64	2.34
Gd-DOTA-pentapeptide			3.76
Reference	[30]	[3, 25]	Present work

The opposite effect seemed to occur for the Gd-DOTA-pentapeptide where the r_1 value increased in human blood plasma (comparing values in Table 4.3 to Table 4.4). Given that the results are inconsistent and were only carried out once, it would be necessary to repeat to have more confidence in this conclusion.

Following this, Gd-tuftsin conjugates were tested in whole blood. As mentioned earlier, the original INDIANA model was created to model a two-pool system (one cell type in solution). However, given the diversity of sizes of different cell types within whole blood, preliminary work with Prof. Baldwin and Virginia Casablancas-Antras investigated whether it would be beneficial to extend the model to a three-pool system, with two intracellular compartments and one external fluid pool. This aimed to capture the heterogeneity of the cell types within whole blood to try to model the system more accurately.

With repeat simulations and sample distributions for the parameters using the bootstrapping method, it was found that the parameters were not always normally distributed as expected and occasionally the model fitting became trapped in a local energy minimum rather than a global energy minimum. Even with the introduction of a Levenberg-Marquadt with basin hopping optimising algorithm to randomly probe the wider energy landscape, it was concluded that there were too many parameters to have confidence of the fit produced from the model without further optimisation and verification against experimental data. Therefore, given the scope of this work, it was concluded that using the original two-pool model was most appropriate.

The INDIANA study on whole blood treated with different concentrations of Gd-DOTA-tuftsin is shown in Figure 4.11 and the cell counts from the blood sample are given in Table 4.5. For whole blood only, the INDIANA technique found an average cell radius of ~11.30 μm (Figure 4.11a).

Given that the majority of blood is comprised of red blood cells which have a small intracellular space, it is likely that most of the "intracellular" pool is made up of white blood cells that have larger cell radii, which more closely aligned with the average cell radius found in our experiments. When comparing the p_{out}, it is observed that with increasing concentrations of gadolinium complex there is increasing number of mole fractions of the particles inside the cell at equilibrium, which supports the hypothesis that the gadolinium complexes are entering into one or more cell types in whole blood. However, due to the complexity of the blood, there is currently not enough evidence to confirm which cell type(s) in the whole blood the Gd-DOTA-tuftsin is entering.

Table 4.5. Cell counts from the blood sample used in the INDIANA study purchased from Research Donors. WBC (white blood cell).

Cell type	**Cell count (/L)**	**% of total number of cells**	**Type of WBC**	**Cell count (/L)**	**% of total number of WBCs**	**Cell radius (µm)[31]**
WBC	7.43×10^9	0.14	Neutrophils	3.55×10^9	47.78	6-7
			Lymphocytes	2.70×10^9	36.34	3-4.5
			Monocytes	8.60×10^8	11.57	<10
			Eosinophils	2.70×10^8	3.63	6-8.5
			Basophils	5.00×10^7	0.67	7-8
Red blood cells	4.96×10^{12}	93.97	-	-	-	3.5
Platelets	3.14×10^{11}	5.95	-	-	-	0.85

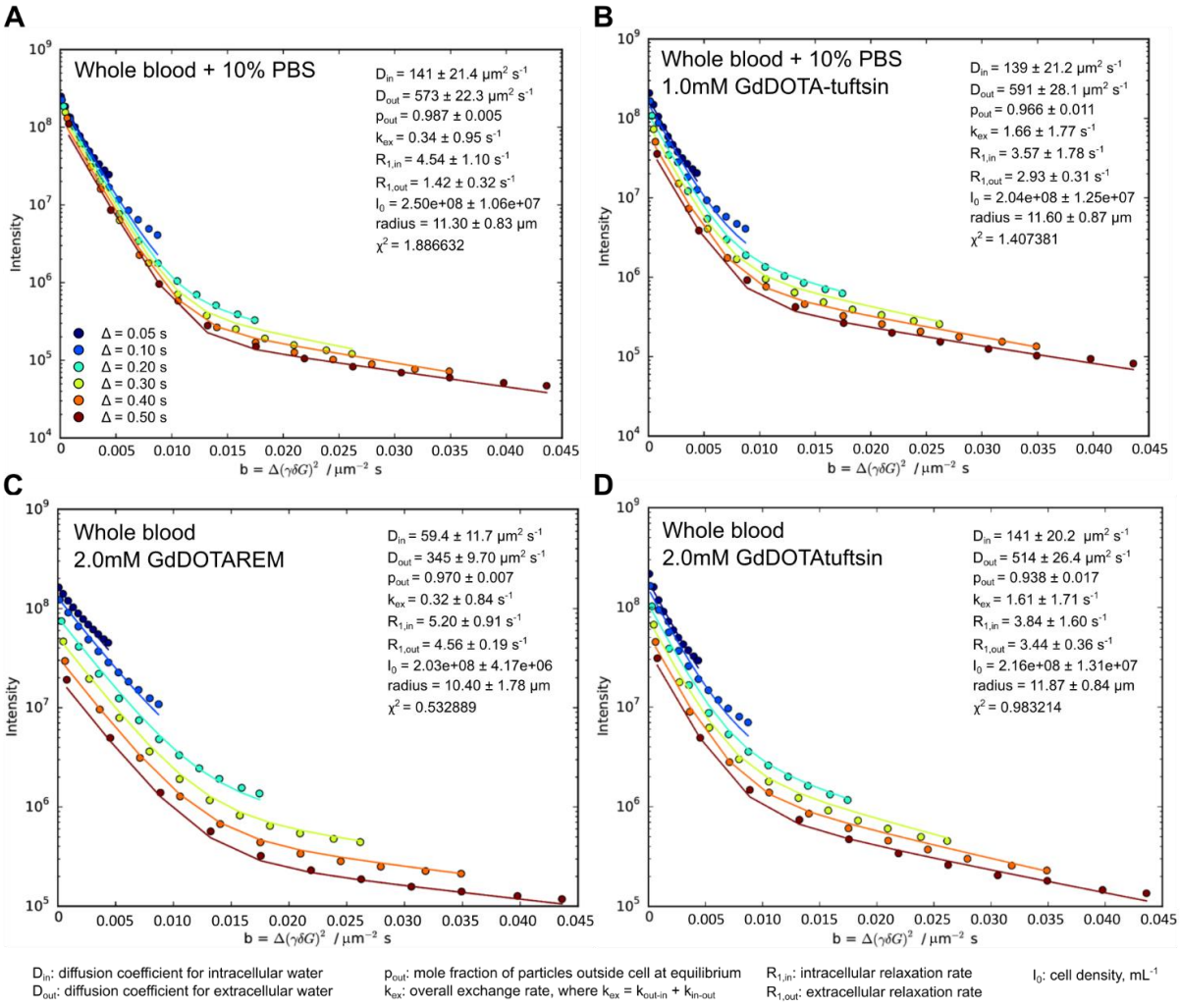


Figure 4.11. NMR data collected from human blood samples a) whole blood + 10% PBS; b) whole blood + 10% PBS, 1.0 mM Gd-DOTA-tuftsin; c) whole blood, 2.0 mM Gd-DOTAREM and d) whole blood, 1.0 mM Gd-DOTA-tuftsin. Each point in the graph is the integration of a water peak from one ^1H NMR spectrum. The coloured lines correspond to increasing diffusion times, Δ, between the encoding and decoding pulses in the stimulated echo experiment.

Figure 4.11b shows the results when 1.0 mM Gd-DOTA-tuftsin was added to the whole human blood with 10% PBS. The diffusion coefficient for bulk extracellular water, D_{out} = 591 μm^2 s^{-1}, is slower than those previously reported for a single cell type (D_{out} ~ 1250 - 1980 μm^2 s^{-1})[6] and for the apparent diffusion coefficient of water in blood plasma (1470 μm^2 s^{-1})[32]. Given that it is 2-3 times lower than the expected diffusion coefficient, this indicates that our model is not fitting the data well. Another indicator of the poor fit is the χ^2 is large, as ideally a value less than 0.5 would represent a better fit. This is also highlighted by the mid-blue fit (Δ = 0.10 s) where the model diverges from the data points.

GdDOTAREM was used to compare whether a non-targeting Gd-complex was entering cells. From the p_{out} values, initial results suggest that DOTAREM, like Gd-DOTA-tuftsin, is entering cells, although there is insufficient evidence to suggest which cell types within the whole blood it is

entering (Figure 4.11c). The original INDIANA model was created to model a two-pool system (one cell type in solution); therefore, given the diversity of cell types within whole blood it would be recommended for future work to narrow the cell types in solution further by centrifugation. Centrifugation would allow the separation of the peripheral blood mononuclear cells (predominantly white blood cells) from whole blood; it would then be expected that the tuftsin-labelled complex would be taken up more than the non-targeting complex by these cells.

The INDIANA method holds potential for further studies with blood products to determine whether targeted contrast agents are entering into cells, as well as provide new information on commercially available contrast agents.

4.4.2 diffCEST

In addition to INDIANA, diffCEST (diffusion Chemical Exchange Saturation Transfer) experiments were carried out on the blood samples. CEST experiments can be used to detect the presence of a species in a very low concentration through its interaction with a highly concentrated species by the transfer of magnetisation between the two species.[33] In water CEST, these solute molecules contain hydrogens that are able to chemically exchange with the hydrogens of bulk water.[23] A radiofrequency (RF) pulse is used to selectively saturate the exchange solute protons, and through chemical exchange of the protons with the bulk water the protons transfer their saturation onto the bulk water protons, and reduce the signal intensity of the bulk water (Figure 4.12).[23] In an analogous way to INDIANA, the difference in the diffusion coefficient between sub-compartments is exploited to differentiate between the intracellular and extracellular pools.[34]

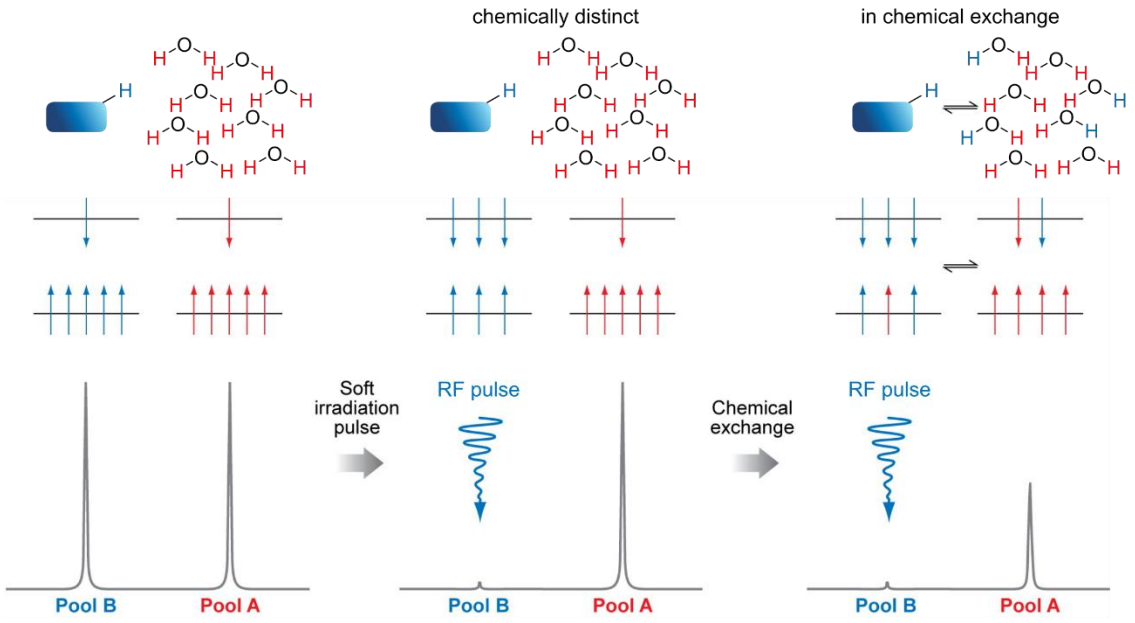


Figure 4.12. Schematic representation of an NMR CEST experiment. with two chemically distinct pools (left), two distinct pools where an RF pulse is applied to pool B and there is no chemical exchange (middle), and two pools under chemical exchange after a RF pulse is applied to pool B. Adapted from Sherry et al. with permission.[35]

The diffCEST experiment was carried out with Gd-DOTA-tuftsin in whole human blood, with results shown in Figure 4.13. The large dip at ~4.7 ppm corresponds to the water peak when saturated at the specific radiofrequency, and the features in the aliphatic (0.5-3.0 ppm) and aromatic (6.5-8.5 ppm) regions correspond to CEST effects. As observed in Figure 4.13a, there is a stark difference between the intracellular and extracellular pools without a contrast agent. The diffusion rate for intracellular fluid is slow compared to extracellular, and there is chemical exchange between the bulk water and intracellular proteins. The extracellular pools show that there is no chemical exchange or cross-relaxation between the extracellular bulk water.

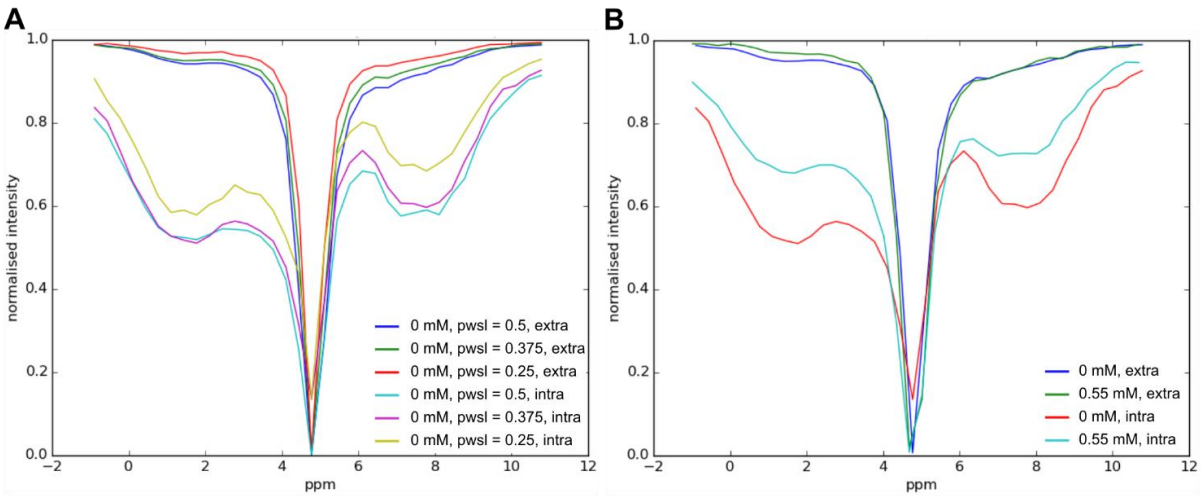


Figure 4.13. diffCEST results for whole human blood with a) no Gd-complex, different pwsl for intracellular (intra) and extracellular (extra) pools; b) [Gd-DOTA-tuftsin] = 0.55 mM for pwsl (pulse length) = 0.375 μs. x-axis corresponds to the ppm frequency of the RF pulse.

When the blood was treated with Gd-DOTA-tuftsin (Figure 4.13b), for the intracellular compartment there is a difference between the 0 mM and 0.55 mM Gd-DOTA-tuftsin. The addition of 0.55 mM gadolinium conjugate has resulted in faster relaxation of the water protons, compared to no gadolinium, illustrated by the reduction in the profile between 0-3 ppm and 6-9 ppm. Overall, like INDIANA, diffCEST is a useful NMR tool for probing the intracellular and extracellular environments and has demonstrated promising results for future research.

4.5 Conclusions

In this work an improved synthesis of tuftsin-conjugated DOTA-amide complexes has been used to produce sufficient quantities of the ligands to make europium, terbium and gadolinium complexes. The paramagnetic NMR spectra of the europium and terbium complexes show that the tuftsin-conjugated DOTA-amide complexes preferentially adopt a SAP conformation. Luminescence studies were possible with higher concentration of the complexes, and a future step for the development of these as optical imaging probes would be to incorporate a chromophore to allow for indirect excitation. As expected, all of the probes were found to bind to one water molecule;

relaxivities were reported for the gadolinium complexes, in PBS and human blood plasma, in the region of others in literature.

NMR techniques such as INDIANA and diffCEST for studying contrast agents in whole blood present many opportunities for development and expansion on the existing models. More work needs to be done to progress beyond the two-pool model to better describe the heterogeneity of the blood environment, which would require validation with cell counting and measurements. For future work, repeats of the NMR studies in PBS, PBS and BSA, and blood plasma would provide foundational values to gain basic understanding of the gadolinium contrast agents. Moreover, to understand the internalisation of the gadolinium-tuftsin conjugates, INDIANA could be applied to a single cell population of macrophages and lipopolysaccharide-activated macrophages (to stimulate macrophage activation) which is more easily modelled. An extension of this would be to treat isolated peripheral blood mononuclear cells with gadolinium-tuftsin conjugates so that macrophages make up a larger proportion of the blood solution. Finally, the INDIANA experiments could be repeated in whole blood which would allow for a greater understanding of the processes governing the observations found in this work.

4.6 References

1. R. Aarons, PhD thesis, University of Manchester, 2004.
2. R. J. Aarons, J. K. Notta, M. M. Meloni, J. H. Feng, R. Vidyasagar, J. Narvainen, S. Allan, N. Spencer, R. A. Kauppinen, J. S. Snaith and S. Faulkner, *Chem. Commun.*, 2006, 909-911.
3. J. H. Feng, M. M. Meloni, S. M. Allan, S. Faulkner, J. Narvainen, R. Vidyasagar and R. Kauppinen, *Contrast Media Mol. Imaging*, 2010, **5**, 223-230.
4. J. Karger, *Adv. Colloid Interface Sci.*, 1985, **23**, 129-148.
5. G. Karunanithy, PhD thesis, University of Oxford, 2019.
6. G. Karunanithy, R. J. Wheeler, L. R. Tear, N. J. Farrer, S. Faulkner and A. J. Baldwin, *J. Magn. Reson.*, 2019, **302**, 1-13.
7. P. Gottlieb, A. Beretz and M. Fridkin, *Eur. J. Biochem.*, 1982, **125**, 631-638.
8. M. Fridkin and V. A. Najjar, *Crit. Rev. Biochem. Mol. Biol.*, 1989, **24**, 1-40.
9. J. Martinez and F. Winternitz, *Ann. N.Y. Acad. Sci.*, 1983, **419**, 23-34.
10. K. Nishioka, J. McMurray, F. Al Obeidi and B. M. Pettitt, *Curr. Med. Chem.*, 1996, **3**, 153-166.
11. A. A. Amoscato, P. J. A. Davies, G. F. Babcock and K. Nishioka, *Ann. N.Y. Acad. Sci.*, 1983, **419**, 114-134.
12. P. Gottlieb, E. Hazum, E. Tzehoval, M. Feldman, S. Segal and M. Fridkin, *Biochem. Biophys. Res. Commun.*, 1984, **119**, 203-211.
13. C. W. Vander Kooi, M. A. Jusino, B. Perman, D. B. Neau, H. D. Bellamy and D. J. Leahy, *Proc. Natl. Acad. Sci. U.S.A.*, 2007, **104**, 6152-6157.
14. M. K. Chaudhuri, D. Konopinska, N. J. Bump and V. A. Najjar, *Ann. N.Y. Acad. Sci.*, 1983, **419**, 135-142.
15. L. G. Nielsen and T. J. Sorensen, *Inorg. Chem.*, 2020, **59**, 94-105.
16. S. R. Kiraev, E. Mathieu, F. Siemens, D. Kovacs, E. Demeyere and K. E. Borbas, *Molecules*, 2020, **25**, DOI: 10.3390/molecules25225282.
17. J. D. Rinehart and J. R. Long, *Chem. Sci.*, 2011, **2**, 2078-2085.
18. W. D. Horrocks and J. P. Sipe, *Science*, 1972, **177**, 994-996.
19. S. Aime, M. Botta and G. Ermondi, *Inorg. Chem.*, 1992, **31**, 4291-4299.
20. K. Binnemans, *Coord. Chem. Rev.*, 2015, **295**, 1-45.
21. *Lanthanide Luminescence: Photophysical, Analytical and Biological Aspects*, eds. P. Hänninen and H. Härmä, Springer Berlin Heidelberg, Berlin, Heidelberg, 2011.
22. D. H. Powell, O. M. NiDhubhghaill, D. Pubanz, L. Helm, Y. S. Lebedev, W. Schlaepfer and A. E. Merbach, *J. Am. Chem. Soc.*, 1996, **118**, 9333-9346.
23. A. E. Merbach, L. Helm and É. Tóth, *The chemistry of contrast agents in medical magnetic resonance imaging*, Wiley, Chichester, 2nd edn., 2013.

24. P. Caravan and Z. D. Zhang, *Eur. J. Inorg. Chem.*, 2012, **2012**, 1916-1923.
25. J. Feng, M. M. Meloni, S. M. Allan, J. Narvainen, S. Faulkner and R. Kauppinen, *Proc. Intl. Soc. Mag. Reson. Med.*, 2006, **14**, 1885.
26. S. Aime, A. Barge, J. I. Bruce, M. Botta, J. A. K. Howard, J. M. Moloney, D. Parker, A. S. de Sousa and M. Woods, *J. Am. Chem. Soc.*, 1999, **121**, 5762-5771.
27. F. M. Cavagna, F. Maggioni, P. M. Castelli, M. Dapra, L. G. Imperatori, V. Lorusso and B. G. Jenkins, *Invest. Radiol.*, 1997, **32**, 780-796.
28. S. Goetschi, J. M. Froehlich, N. C. Chuck, R. Curcio, V. M. Runge, G. Andreisek, D. Nanz and A. Boss, *Invest. Radiol.*, 2014, **49**, 608-619.
29. P. Caravan, N. J. Cloutier, M. T. Greenfield, S. A. McDermid, S. U. Dunham, J. W. M. Bulte, J. C. Amedio, R. J. Looby, R. M. Supkowski, W. D. Horrocks, T. J. McMurry and R. B. Lauffer, *J. Am. Chem. Soc.*, 2002, **124**, 3152-3162.
30. I. M. Noebauer-Huhmann, P. Szomolanyi, V. Juras, O. Kraff, M. E. Ladd and S. Trattnig, *Invest. Radiol.*, 2010, **45**, 554-558.
31. M. Peckham, A. Knibbs and S. Paxton, The Histology guide, https://www.histology.leeds.ac.uk/blood/index.php, (accessed 27/04/2022).
32. J. G. Li, G. J. Stanisz and R. M. Henkelman, *Magn. Reson. Med.*, 1998, **40**, 79-88.
33. P. C. M. van Zijl and N. N. Yadav, *Magn. Reson. Med.*, 2011, **65**, 927-948.
34. G. Karunanithy, K. J. Ray, R. J. Wheeler, V. Pereno, L. Bau, E. Stride, M. A. Chappel, N. Sibson and A. J. Baldwin, unpublished work.
35. A. D. Sherry and M. Woods, *Annu. Rev. Biomed. Eng.*, 2008, **10**, 391-411.

5 Macrophage targeted photoacoustic contrast agents

5.1 Introduction

5.1.1 Principles of PA imaging

Another imaging modality explored in this research is photoacoustic (PA - also known as optoacoustic) imaging. Even the more advanced microscopy techniques such as two-photon and multiphoton microscopy can only penetrate to depths of 300-500 μm *in vivo*, as techniques relying on optical detection are limited by light scattering in tissues.1 The benefit of PA imaging is that it can image to greater depths in the body than optical microscopy, with penetration of up to several cm *in vivo*,[2] as acoustic waves are less scattered by tissue than light.[3]

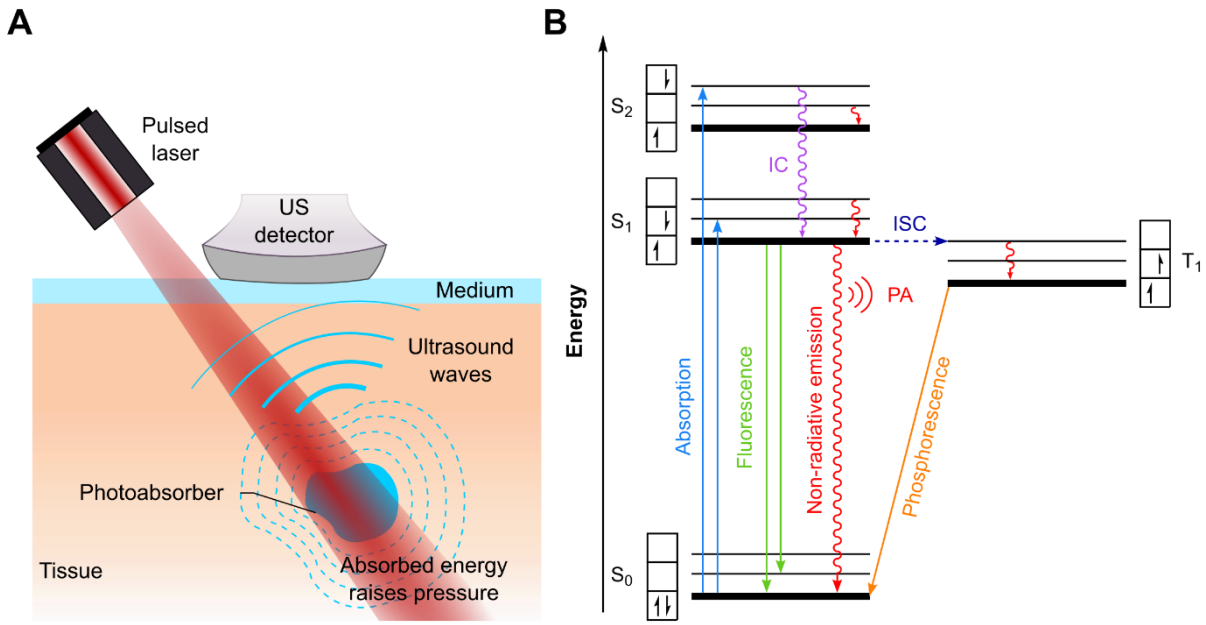


Figure 5.1. a) Schematic representation of the photoacoustic effect in tissue; b) Jablonkski diagram showing excitation of a NIR dye and its radiative and non-radiative decay processes. (PA: photoacoustic, IC: internal conversion, ISC: Intersystem Crossing).

Photoacoustic imaging exploits the "photoacoustic effect", whereby light is absorbed by a chromophore and converted into heat, which generates measurable acoustic waves[4] as outlined in Figure 5.1a. A pulsed laser is directed at the tissue and photons are absorbed by the chromophore, then the absorbed energy is able to decay via either radiative pathways (fluorescence or phosphorescence) or non-radiative emission, as outlined in Figure 5.1b.[5] Ideally, energy absorbed by chromophores will decay via non-radiative pathways, shown in Figure 5.1b as wavy lines. These denote vibrations which result in the emission of heat[5] leading to an increase in pressure.[4] Thermoelastic expansion that occurs as a result of the increased pressure then transmits as an acoustic wave because of the elasticity of the tissue, which can be recorded by an ultrasound detector.[2, 4]

Different imaging modalities can span different penetration depths; for modalities involving light, such as microscopy and photoacoustic, these are limited by the optical and acoustic attenuation

(loss of signal) by the medium.[6] However, generally it is the optical attenuation that is the largest contributor to the loss of signal in soft tissues, which depends on the absorption and scattering coefficients of the tissue.[6] The scattering by cellular structures in tissues arises from the absorption and re-emission of photons without losing energy but can result in a change in direction of the photon.[7] Despite a high probability of being absorbed and reemitted in the same forward direction (ballistic photons), accumulation of many scattering events leads to gradual divergence from the original direction.[6, 7] As a result, there will be a great number of scattering events in solely optical imaging techniques as the signal needs to reach the target and return. Whilst to a degree, photoacoustic imaging can be restricted by the optical attenuation of tissues, it benefits from the higher spatial resolution resulting from ultrasound propagation, therefore penetration depth of several centimetres can be achieved.[6]

The body contains several endogenous photoabsorbers such as oxyhaemoglobin and deoxyhaemoglobin, lipids, water, and melanin (Figure 5.2).[8, 9] Studies of haemoglobin captured by PA imaging have resulted in the visualisation of vasculature whilst imaging of melanin has enabled detailed characterisation of melanomas,[8] but endogenous photoabsorbers are limited in the number of biological processes that they can help to illuminate. This presents a challenge to the design of exogenous contrast agents as they must absorb outside the range where endogenous photoabsorbers absorb.

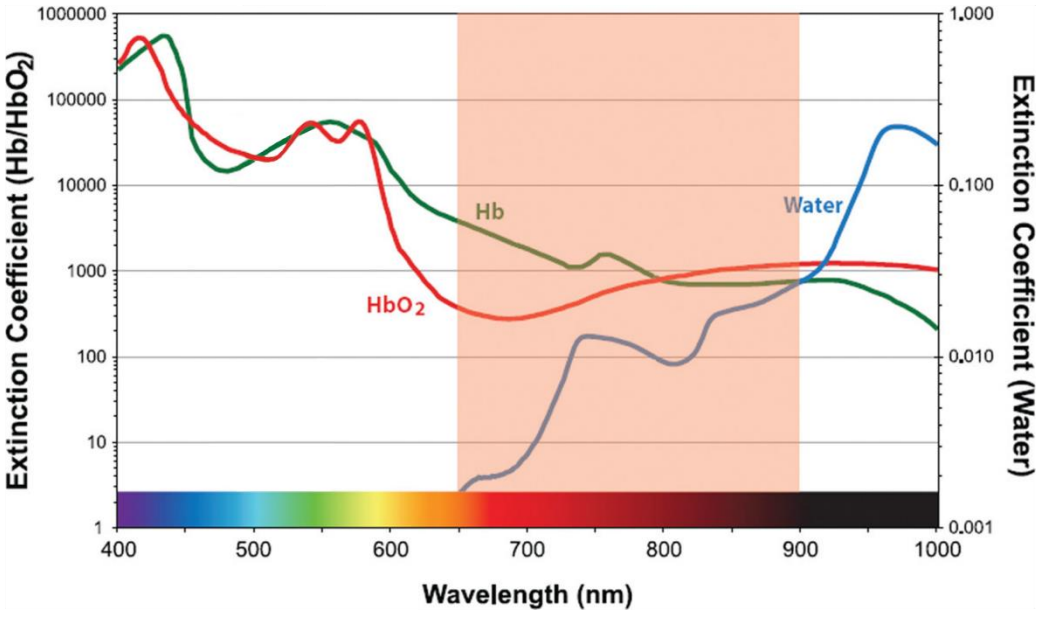


Figure 5.2. Absorption coefficient spectra of endogenous tissue chromophores, including oxyhaemoglobin (HbO_2) and deoxyhaemoglobin (Hb). Highlighted region represents the NIR optical window with lower levels of absorption from endogenous chromophores. Reprinted (adapted) with permission from Chem. Rev. 2010, 110, 5, 2620-2640. Copyright 2010 American Chemical Society.[10]

It is therefore desirable for contrast agents to have their peak absorption in the near infrared (NIR) optical window (650-900 nm), demonstrated in Figure 5.2.[1, 9] In this region, endogenous

photoabsorbers do not absorb light well, meaning the light can penetrate further and reach the desired exogenous contrast agent. Further characteristics required are a large molar extinction coefficient for strong absorption of light, photostability to avoid degradation, and a low quantum yield.[8] Quantum yield is a key indicator of the conversion of light energy into photoacoustic signal; a low quantum yield corresponds to a poor fluorescent agent as energy is dissipated by non-radiative emission instead of light.

A wide variety of contrast agents have been developed for PA imaging including inorganic nanomaterials (gold and carbon nanoparticles), organic nanostructures (polymer nanoparticles, carbon nanotubes), small-molecule NIR dyes and genetically engineered chromophores – some examples are shown in Figure 5.3.[3, 8] Inorganic nanoparticles are the most common category of PA contrast agents because they have very large molar extinction coefficients ($\varepsilon \sim 10^7 - 10^{11}\ M^{-1}\ cm^{-1}$)[8] in the NIR range and exist broadly in two categories – gold and carbon nanoparticles. Gold nanoparticles exploit surface plasmon resonances to enhance the photoacoustic signal.[8] Carbon nanoparticles are primarily based on either graphene-based structures or single-walled carbon nanotubes (SWNT) owing their properties to their extended π-conjugation through the sp^2 carbon structure and the potential for surface functionalisation.[3] These offer high molar extinction coefficients and good photostability; however they remain challenging due to their large MWs leading to poor biocompatibility, as well as difficulty in reproducible synthesis.[8]

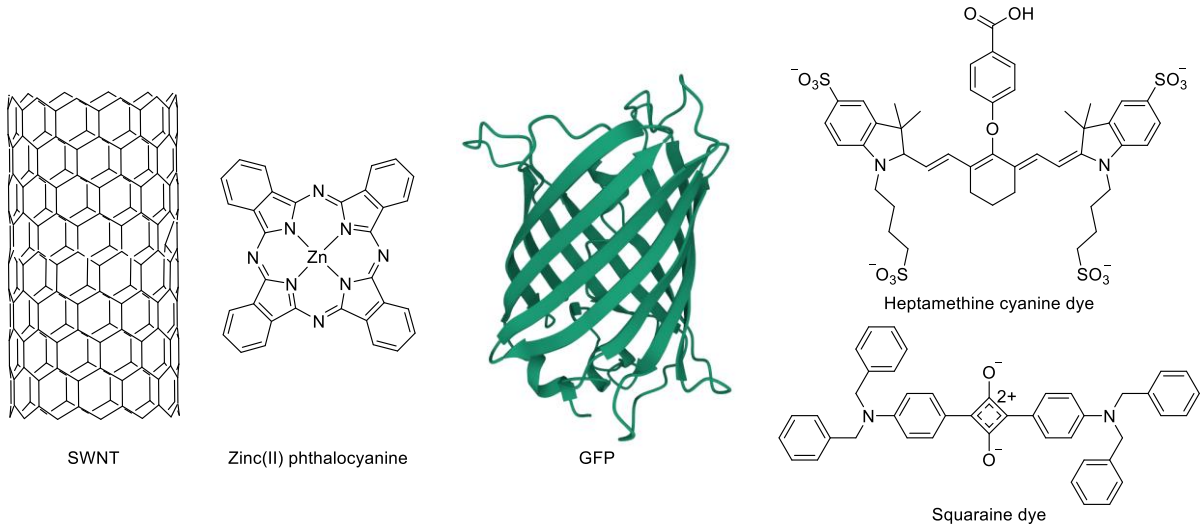


Figure 5.3. Examples of photoacoustic imaging agents. From left to right: Single wall nanotubes (SWNT) can be functionalised with targeting ligands;[11] zinc(II) phthalocyanine;[12] green fluorescent protein (GFP) image of 1EMA (10.2210/pdb1EMA/pdb) created with Mol Viewer;[13, 14] heptamethine cyanine dyes[15] and squaraine dyes have been loaded in albumin nanoparticles for administration.[16]*

Common organic nanostructures are based on conjugated polymers or porphyrins.[8, 17] Typically, polymers will be used that have a delocalised conjugated backbone extended through the system that can then be formed into nanoparticles, producing higher molar extinction coefficients than small molecule dyes and with good photostability. A limitation of the conjugated polymers is that they can

have a broad absorption spectra which makes differentiating between the contrast agent and the background fluorescence more difficult.[8] Porphyrin-based dyes such as phthalocyanine (Figure 5.3) and naphthalocyanine have been used due to their strong extinction coefficients, narrow absorption peak in the NIR window and good photostability.[17] As with conjugated polymers, porphyrin-based dyes are insoluble in aqueous solutions and need to be incorporated into self-assembled macroscopic structures with solubilising moieties.[8]

Relative to nanoparticles, NIR dyes have smaller molar extinction coefficients, however their use remains popular - especially those based on cyanine dyes (Figure 5.3) - due to their favourable biocompatibility. Enhancement of the photoacoustic signal generally arises from a series of conjugated π-bonds and aromatic ring structures. Cyanine dyes can be modified by adding hydrophilic groups, electron-donating or electron-withdrawing groups, or lengthening the chain to adjust the solubility, stability and photophysical properties of the compound. Others in this class include squaraine, rhodamine and azo dyes but these are less commonly used due to insolubility, aggregation and chemical reactivity.[3, 8]

5.1.2 Design of a macrophage-targeted PA contrast agent

There are several factors that are important to consider when designing a photoacoustic agent. Like all imaging agents, it is important that the probe is non-toxic, has an appropriate half-life *in vivo*, and will be cleared intact from the body. Next, given that the NIR optical window has been identified as having the lowest levels of background photoabsorbers, a probe with a high molar extinction coefficient within the NIR optical window of 650 - 900 nm would maximise depth penetration.[8] Furthermore, a sharp characteristic absorption spectrum is favourable as this allows more accurate spectral unmixing to distinguish the signal from background photoabsorbers.[3] Moreover, a low fluorescent quantum yield is desirable to result in the greatest number of photons relaxing by non-radiative decay.[3] Finally, probes should have high photostability to ensure that the spectral profile is unchanged over the course of imaging.[3, 8]

For this work, small-molecule NIR dyes were chosen with a heptamethine cyanine (Cy7) backbone. Cyanine dyes are organic dyes with an odd number of methine carbons in a conjugated π-system connecting a neutral and positively charged nitrogen centre.[18] Indocyanine green (ICG, Figure 5.4) is an FDA-approved probe used in medical diagnostics such as ophthalmic angiography, measuring cardiac output and hepatic function.[43] Given that it has an absorption maxima in the NIR optical window, around 780 nm, it has spurred on a lot of research in the development of heptamethine cyanine dyes for use in both fluorescent and photoacoustic imaging.[19-22] However the cyanine dyes are limited in their use by their propensity to photobleach[23] and their susceptibility to aggregate in solution.[24] Therefore, these limitations were considered when designing the PA probe for this work - an overview is given in Figure 5.4.

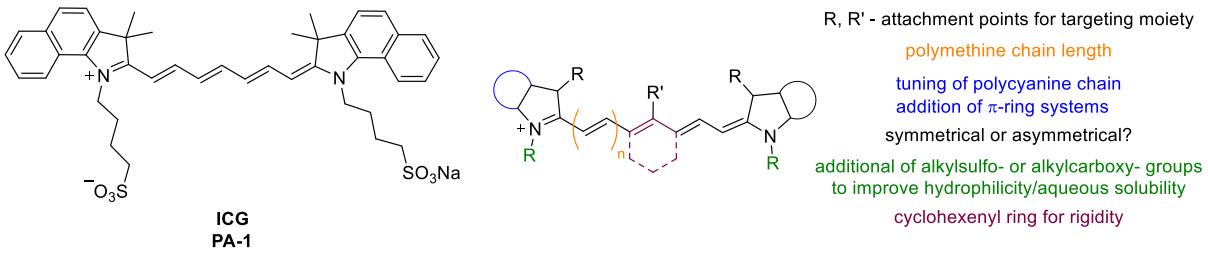


Figure 5.4. Indocyanine green, ICG, and general structure of polymethine cyanine dye with molecular design considerations.

The length of the polymethine cyanine chain was chosen to be 7 as Cy7 dyes exhibit a λ_{max} in the NIR region 756 nm, rather than Cy5 which has a λ_{max} of 649 nm, outside of the NIR optical window. Hydrophilic groups such as carboxylic or sulfonic acid groups can be incorporated (Figure 5.4, green R) to enhance solubility and reduce off-target binding to proteins in the blood and lessen their tendency to aggregate.[9, 25] A cyclohexenyl ring was chosen for the centre to increase rigidity and, as a result, photostability.[26, 27] A symmetrical dye was selected to allow for simple synthesis and purification by reducing the number of side products. One fewer phenyl ring than ICG was attached onto the pyrrole ring with the aim to reduce the hydrophobicity of the probe.

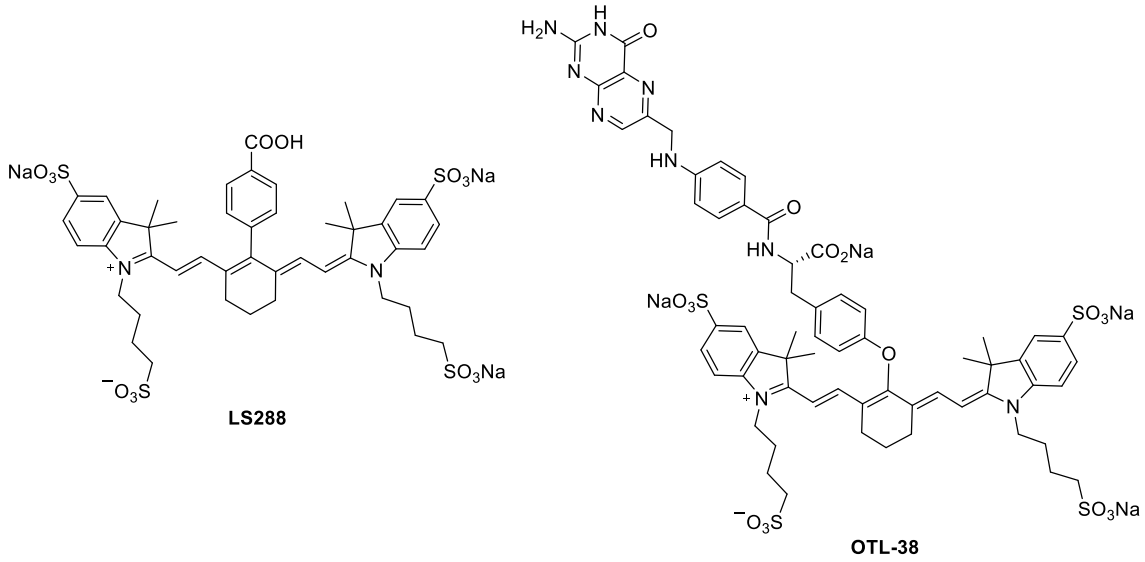


Figure 5.5. Structures of NIR dyes: LS288 and OTL-38.

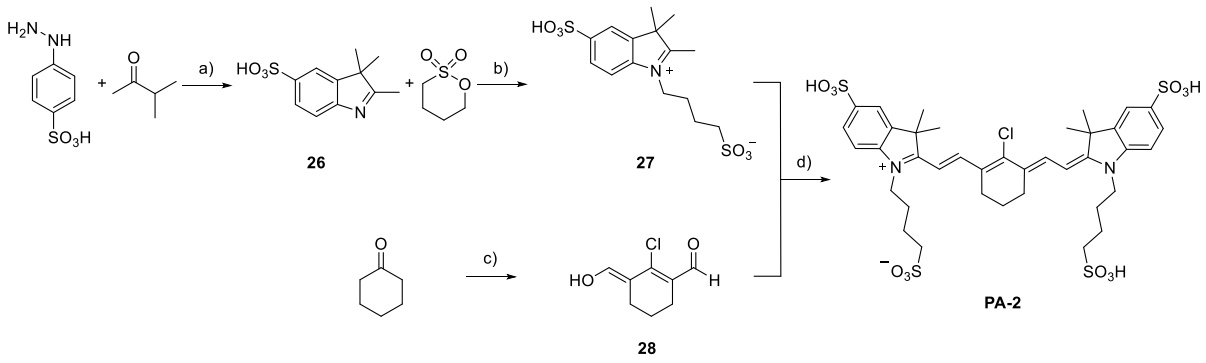
Applying the toolkit approach, the targeting peptide, tuftsin, can be incorporated into the photoacoustic agents outlined in this chapter. Peptides are often reported as targeting strategies, with dye-peptide conjugates that were initially used for fluorescent imaging being repurposed as contrast agents for use in PA imaging. Previously, dye-peptide PA conjugates have been used to successfully target integrin αvβ3 which is associated with tumour progression and angiogenesis,[29, 30] as well as caspase-9 for monitoring cell apoptosis, with the addition of the dye not limiting the targeting ability.[31, 32] Therefore, this lends confidence that the tetrapeptide tuftsin should function suitably as a targeting moiety.

Previous NIR fluorescent dyes conjugated to folate have been reported but could potentially be repurposed as photoacoustic probes depending on their photophysical properties. The earliest report of folate conjugated to a dye was by Tung *et al.* in 2002 where an asymmetrical cyanine-5 dye was attached to folate via a hydrophilic spacer on a terminal position of the chain.[34] Extensive work has been carried out by Kularatne *et al.* from On Target Laboratories to develop a fluorescent heptamethine cyanine dye conjugated to folate, which is detailed in their patent.[35] Their lead compound, OTL-38 (Figure 5.5), is an imaging agent developed for use in fluorescent intraoperative molecular imaging of various human carcinomas.[36] It is comprised of a pteroyl targeting vector conjugated to a heptamethine cynanine dye (IRDye®-800CW) and currently it is in phase III clinical trials.[36] Similar compounds to those in this work are mentioned in the patent with an LS288 dye (Figure 5.5), attached by a diamine PEG linker to folate.[35] It was dismissed from further development as a fluorescent probe as it had shown lower levels of fluorescence compared to other second generation derivatives; however this positions it as an ideal candidate for photoacoustic imaging as a lower fluorescence quantum yield means an increase in non-radiative decay.[9, 35] More recent work by König and Krämer investigated a wide range of heptamethine indotricarbocyanine chromophores for stability and tuning of optical properties with folate targeting moieties.[29] Given the range of previous work combining folate with dye it was expected that this would be achievable.

5.2 Synthesis

5.2.1 Synthesis of the heptamethine cyanine dye

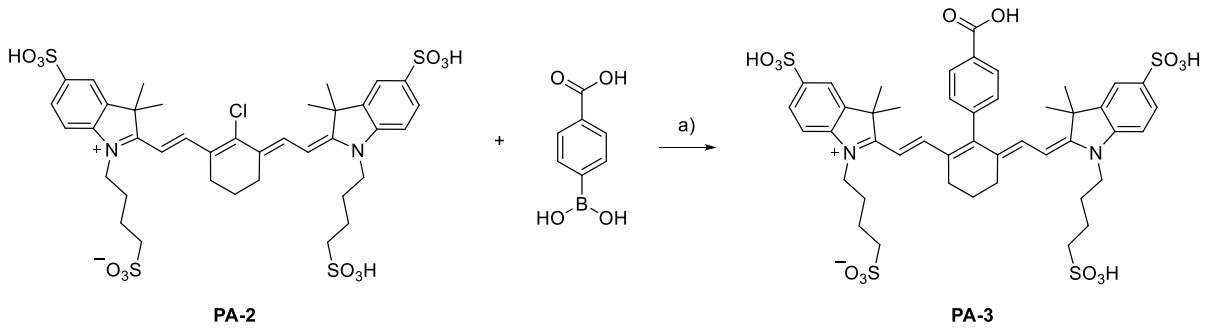
For synthetic simplicity a symmetrical dye was chosen: the chloro-substituted heptamethine cyanine dye, **PA-2**, was prepared by combining two equivalents of the identical indolenine nuclei, **27**, with the bis-aldehyde, **28**, through the conjugated chain of seven methine carbons.[37] An aldol-like condensation reaction between 2.1 equivalents of **27** and one equivalent of **28** was achieved by heating in methanol to 80 °C for 3 hours in the presence of sodium acetate and acetic anhydride. Once cooled, a fine green precipitate was formed upon addition of diethyl ether and collected by centrifugation. The green powder was triturated with propan-2-ol from minimal water and obtained by centrifugation to yield a static green powder, **PA-2**, at 66 % yield.



*Scheme 5.1. Schematic overview of the synthesis of heptamethine cyanine dye, **PA-2**. Reagents and conditions: a) NaOAc (2.0 eq.), acetic acid, 130 °C, 5 h, N_2, crude 166%; b)1,2-dichlorobenzene, 110 °C, 16 h, Ar, 48%; c) $POCl_3$ (3.6 eq.), DMF, DCM, 0 °C for 30 mins → 50 °C for 6 h, 66%; d) NaOAc (2.0 eq.), acetic anhydride, MeOH, 80 °C, 3 h, 56%.*

Typically, the chlorine at the *meso*-position of the central cyclohexenyl ring of the dye is susceptible to nucleophilic substitution and has been used as a way to introduce moieties that target biomolecules[38] such as via an ether linkage, as in OTL38 (Figure 5.5).[39] However, such ether and thioether bonds have been reported as being vulnerable to cleavage, resulting in loss of the fluorescence signal.[28, 40]

Given this, it was decided to introduce the robust C-C bond reported by Lee *et al*. to further functionalise the dye (Scheme 5.2).[28] A palladium-catalysed Suzuki cross-coupling was carried out between the dye, **PA-2**, and 4-carboxyphenylboronic acid; unusually for a Suzuki coupling it was carried out without a base. The reaction was found to be able to proceed both in the presence and absence of a base, however the base-promoted reaction required work-up by column chromatography whereas purification was simpler in the absence of base. The compound was triturated with methanol and acetone to afford a green powder, **PA-3**, in 85 % yield.[29] With the available carboxylic acid, the heptamethine cyanine dye can be easily attached to either folate or tuftsin via an amide linkage.

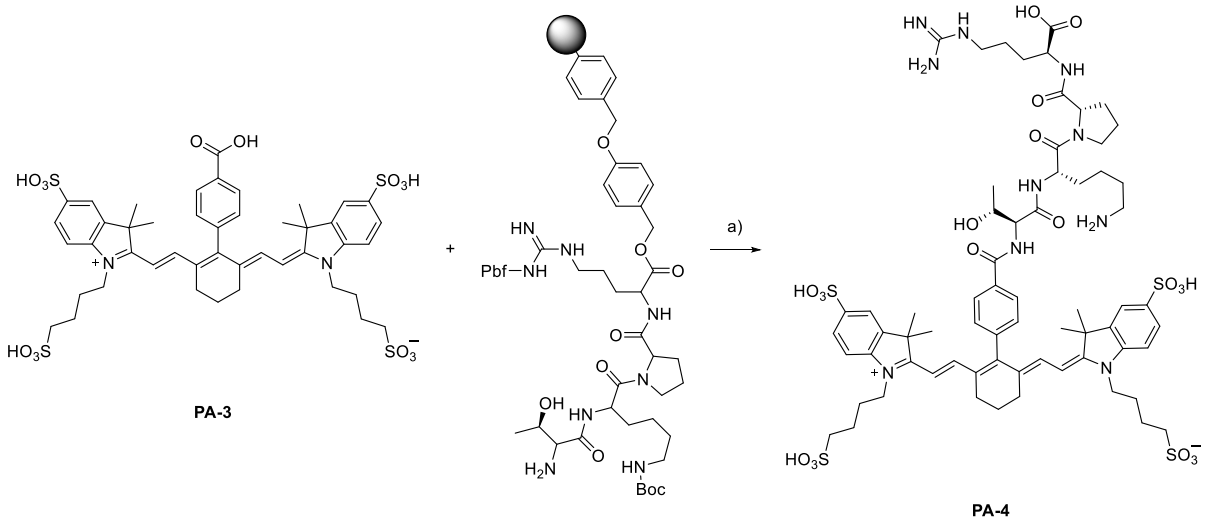


Scheme 5.2. Schematic overview of palladium-catalysed Suzuki cross-coupling. Reagents and conditions: $Pd(PPh_3)_4$, degassed H_2O, 100 °C, 24 h, Ar, dark, 85%.

5.2.2 Synthesis of the macrophage binding moieties

5.2.2.1 Synthesis of tuftsin-functionalised probe, [PA-4]

For the synthesis of the final photoacoustic probes, solid-phase synthesis was carried out to attach the heptamethine cyanine dye to the targeting vector, tuftsin, as outlined in Scheme 5.3. Tuftsin was attached to the solid support and the dye conjugated via an amide coupling reaction using the coupling agent, 1-[bis(dimethylamino)methylene]-1*H*-1,2,3-triazolo[4,5-*b*]pyridinium 3-oxide hexafluorophosphate (HATU). The final probe was cleaved from the solid support using a cleavage mixture (Figure 5.3), which also removed the protecting groups on the peptide.



*Scheme 5.3. Schematic overview of tuftsin functionalisation of the heptamethine cyanine dye to give **PA-4**. Reagents and conditions: a)i) HATU (1.5 eq.), DIPEA (2.0 eq.), DMF, N_2 agitation, 3 days; a)ii) TFA: H_2O: TIPS: 1,2-dimethyoxybenzene (92.5:2.5:2.5:2.5), 3 h, r.t, crude 89%.*

The crude compound was isolated by trituration with diethyl ether before purification by wavelength-directed RP-HPLC using acidic conditions collected using λ = 600 nm to yield the desired product as a green powder. The correct fractions were confirmed using mass spectrometry. The purity of the compound (96%) was confirmed using LC-MS (Figure 5.6).

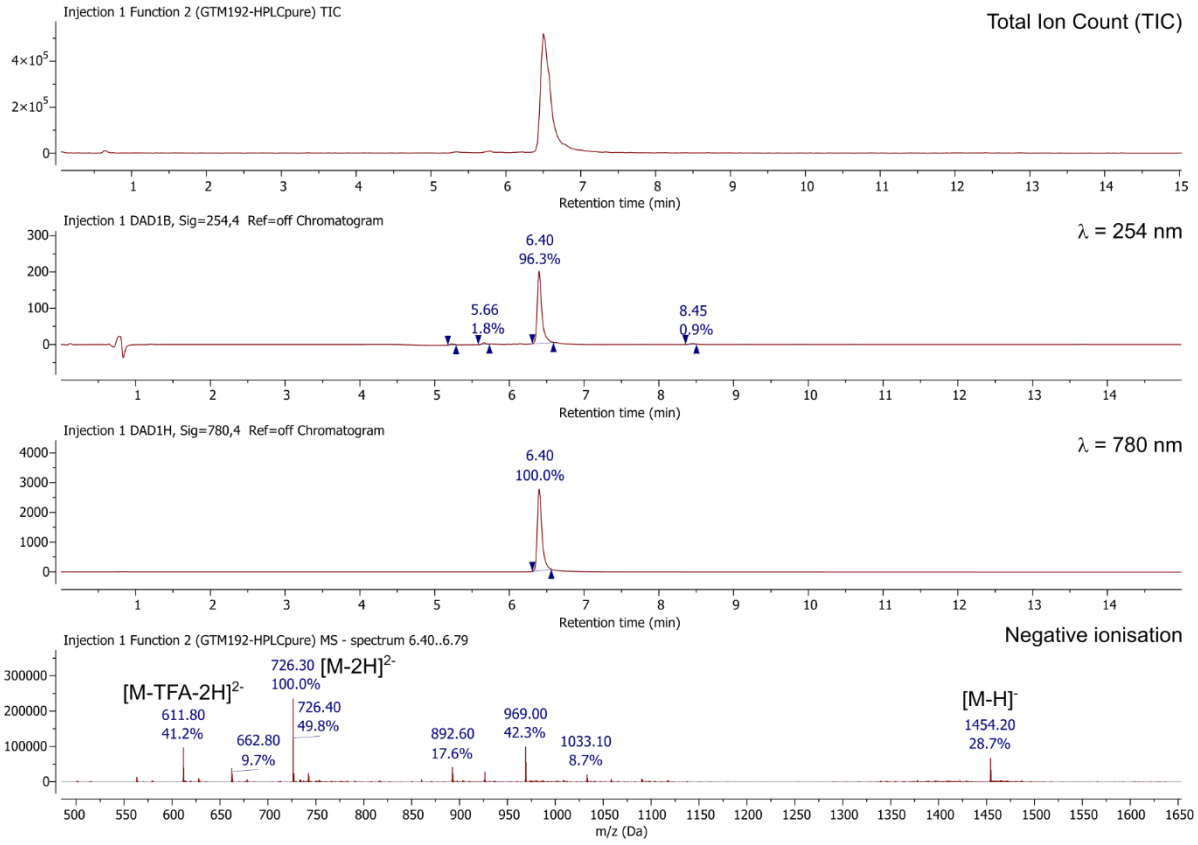
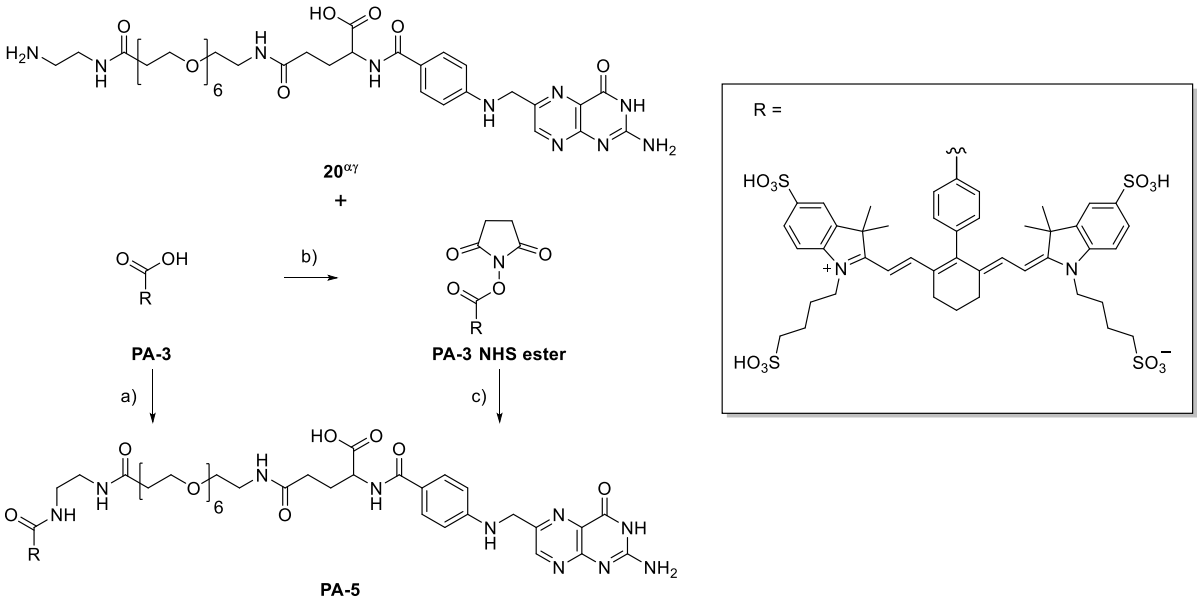


*Figure 5.6. LC-MS (negative ionisation) trace of reinjected compound **PA-4** for purity testing. t_R = 6.4 mins, 96% purity. Relative intensities are calculated by relative UV-Vis spectral absorbance integrated for the absorptions at 254 and 780 nm.*

Due to the compounds high MW and its propensity to aggregate in solution, obtaining an NMR spectrum proved challenging. Even when ~5 mg of compound was run on a high field NMR spectrometer (700 MHz), the peaks were too broad to identify accurately.

5.2.2.2 Synthesis of [PA-5]

Having previously synthesised folate-PEG_6-ethylene diamine, **20**$^{\alpha\gamma}$ (Section 3.2.2), the aim was to combine the folate targeting moiety with the dye. Further, it has been reported in literature that coupling of the dye with folate or peptides with TBTU[29] and PyBop[41] has been successful. Scheme 5.4 provides an overview of the reactions attempted to conjugate the dye to the folate moiety. Initially the amide coupling using HATU was attempted, as these conditions worked well for tuftsin. The reaction was followed by TLC on neutral alumina (7 MeCN: 3 H_2O + 1 drop NH_4OH). After 23 hours, the reaction mixture showed a different retention to the dye starting material. The reaction mixture was worked up with triturations in methanol and diethyl ether to remove DMF and DMSO before undergoing RP-HPLC using acidic conditions.



*Scheme 5.4. Schematic overview of folate functionalisation of the heptamethine cyanine dye, **PA-5**. Reagents and conditions: a)i) HATU (1.5 eq.), DIPEA (2.0 eq.), DMF/DMSO, r.t, 3 days; b) N-hydroxysuccinimide (3 eq.), EDC (3 eq.), DMSO, r.t., Ar, 6 hours; c) DMSO, TEA (2.0 eq.), Ar, r.t, dark.*

The main isolated fractions from HPLC were the dye starting material (confirmed by NMR spectroscopy) and an unknown compound that appeared to be missing some of the characteristic dye peaks in the aromatic region and did not have the large PEG chain which is indicative of the folate moiety. By LC-MS the *m/z* showed peaks of 973 $[M+H]^+$ (dye starting material, t_R = 6.12 mins) and 1056 $[M+H]^+$ (unknown, t_R=6. 37 mins). Other difficulties stemmed from the PEG chain being difficult to ionise in the mass spectrometry, which limited monitoring to mainly using the negative ionisation mode. Moreover, because of the high likelihood of multiple charge states and the addition of sodium ions on the dye, it was difficult to identify any peaks that may clearly correspond to the desired compound. In addition, the LC-MS was limited in the range with molecular weight up to 1650 Da, and the RP-HPLC was wavelength-directed but the maximum in this range was 600 nm, both of which were unsuited to the compounds. This reaction was repeated 3 times: as described with different ratios of DMF and DMSO and in anhydrous conditions using only DMSO – the reactions were unsuccessful.

Hence an alternative synthetic route was attempted to make the NHS-activated ester of the dye to then promote the amide coupling[40] with the folate moiety (Scheme 5.4). The formation of the activated NHS ester dye was monitored by TLC on neutral alumina (7 MeCN: 3 H_2O + 1 drop NH_4OH) and went to completion after 6 hours, product confirmed by LC-MS (*m/z* 1067 $[M+H]^+$). This was then immediately used in the amide coupling reaction with the folate moiety, but no product was observable by mass spectrometry. It is hypothesised that due to the flexibility of the PEG chain in the folate moiety, the coupling reaction was made more difficult; a future alternative would be to repeat the reaction with either a reduced PEG chain length or no PEG chain.

5.2.3 Scope of probes

Therefore, the four probes shown in Figure 5.7 were used for photophysical and photoacoustic characterisation. Commercially available indocyanine green, **PA-1**, was chosen as a reference. The meso-chloro dye, **PA-2**, was chosen to allow for a comparison between the base ICG structure and the theoretically more stable compound **PA-3** with the C-C central bond. Finally, **PA-4** is the probe of interest and it was important to establish whether the incorporation of the targeting moiety, tuftsin, affected the photophysical or photoacoustic properties.

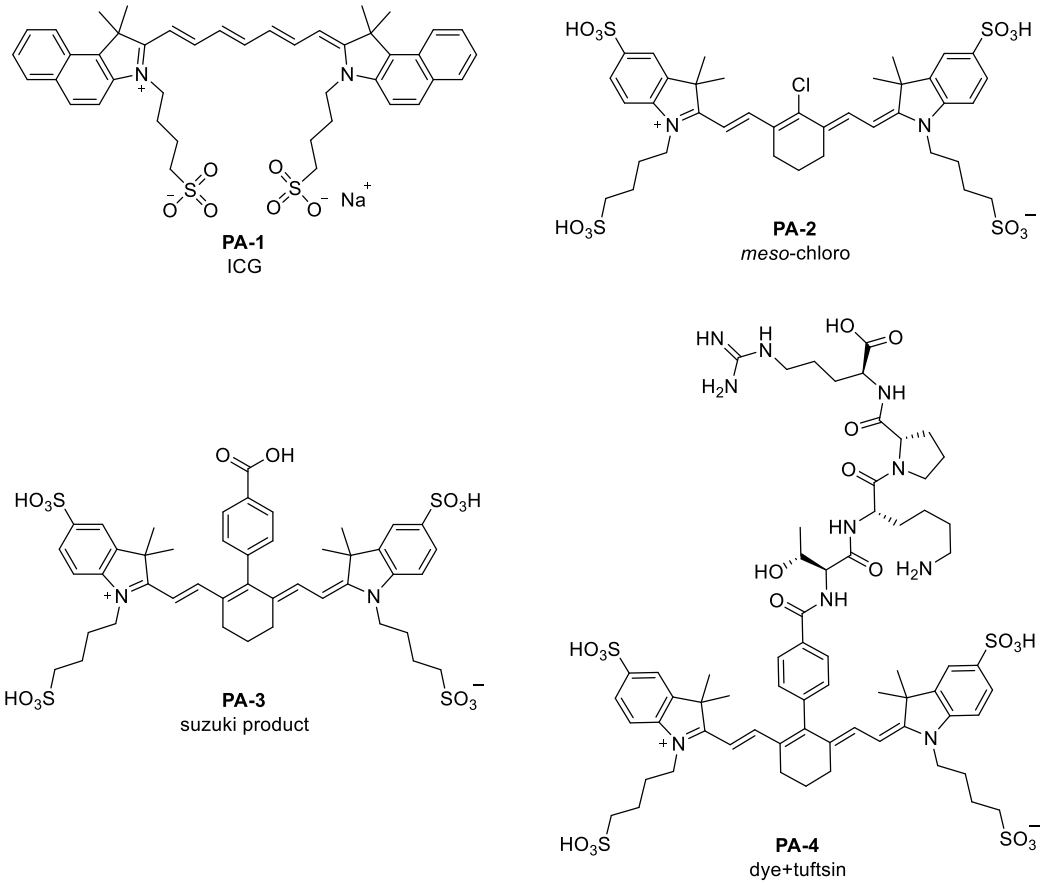


Figure 5.7. Structure of the probes used for photophysical and photoacoustic characterisation.

5.3 Photophysical characterisation

5.3.1 Photophysical properties

The absorption and fluorescence emission spectra of probes **PA-1 to PA-4** were recorded in water and are shown in Figure 5.8. An overview of the photophysical properties of the PA probes and their precursors are given in Table 5.1. The extinction coefficient of the synthesised probes **PA-2 to PA-4** are slightly lower than the purchased ICG, **PA-1** (Table 5.1); however, they are within the same order of magnitude so are all strong absorbers of photons. The absorption at 760-780 nm is indicative of an extended π-conjugated system, which leads to a smaller energy transition between the HOMO and the LUMO in the molecule, and corresponds to the singlet ($S_0 \rightarrow S_1$) absorption in

agreement with a π-π* transition.[43, 44] All the absorption maxima for the developed probes fall within the NIR optical window of 650-900 nm where the endogenous photoabsorbers are found to be weakly absorbing, thus demonstrating their potential suitability as photoacoustic probes.

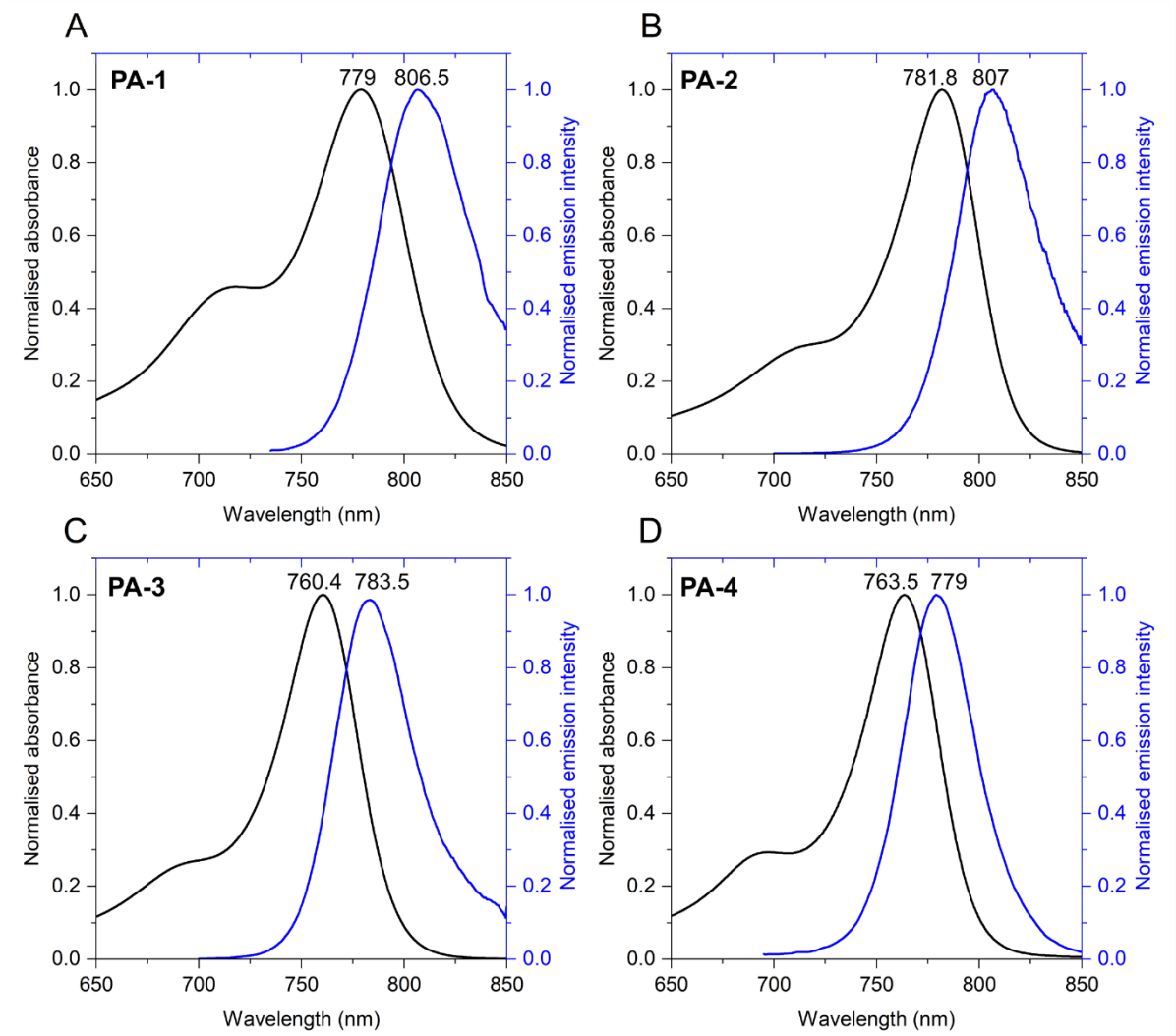


*Figure 5.8. Normalised absorption (black) and fluorescence emission (blue) spectra of probes a) **PA-1**, ICG; b) **PA-2**, meso-chloro; c) **PA-3**, suzuki product; d) **PA-4**, dye + tuftsin.*

Table 5.1. Photophysical properties of the photoacoustic probes and their precursor moieties compared with commercially available indocyanine green in water.

Compound	$\lambda_{max(Abs)}$ (nm)	$\lambda_{max(Em)}$ (nm)	Stokes shift (nm)	ε (M^{-1} cm^{-1})
PA-1	779	806.5	27.5	192 900
PA-2	781.8	807	25.2	168 200
PA-3	761	783.5	22.5	171 500
PA-4	763.5	779	15.5	158 200

The emission spectra of probes were recorded following excitation below their maximum absorption (λ_{ex} ~ 680 nm) to capture the whole fluorescence peak, adhering to Kasha's rule whereby generally the same emission spectrum is observed irrespective of the excitation wavelength.[25] To

maximise emission intensity, excitation would need to occur at the λ_{max} of absorption. The emission spectra displayed a similar broad peak to the absorbance spectra with one main emission band centred around 804 nm which is the mirror image of the main $S_0 \rightarrow S_1$ absorption, indicating it is the relaxation from the excited S_1 state back down to the S_0 energy level. Like **PA-1**, probes **PA-2** and **PA-3** exhibit a small Stokes shift of between 22-28 nm. As mentioned earlier, heptamethine cyanine dyes are sensitive to concentration effects and a consequence of their small Stokes' shift is their susceptibility to concentration quenching.[25] The targeted photoacoustic probe, **PA-4** shows a smaller Stokes' shift than the precursor probes of 15.5 nm.

5.3.2 Photostability

As mentioned earlier, an important property of the probes for biological imaging is the photostability of the fluorophores. Therefore, a comparative study of the probes was carried out by irradiating 5 μM solutions in water using a 625 nm LED lamp, the results of which are shown in Figure 5.9. This concentration was selected as all dyes had an absorption of less than 1 and so the greatest deterioration could be observed. The decrease in the fluorescence intensity of all the probes was able to be fit to a monoexponential decay curve. Of the probes studied, the greatest photodegradation was observed for **PA-2**, while the least was observed for **PA-3** – this supports the incorporation of the C-C bond for increased stability of the probes.

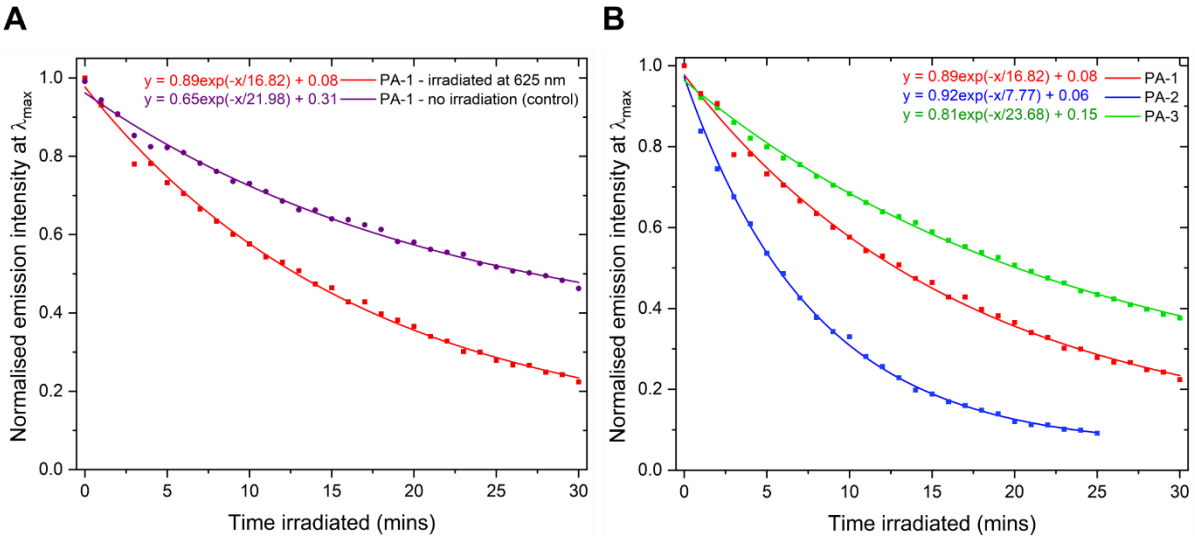


*Figure 5.9. Deterioration of fluorescence emission intensity following irradiation with a 625 nm LED lamp. a) Irradiation of **PA-1** using 625 nm LED compared to control with no irradiation; b) **PA-1** to **PA-3** irradiated with 625 nm LED lamp. Data was fit to a monoexponential decay curve and all fits were $r^2>0.99$.*

5.4 Photoacoustic characterisation

5.4.1 Pre-clinical iThera photoacoustic imaging

Multispectral Optoacoustic Tomography (MSOT) is an imaging technology that uses pulsed light across a range of different wavelengths on the probe in water and a water only control to differentiate between the synthetic photoacoustic probe and background tissue absorption.[3, 45]

"Spectral unmixing" is a computational technique that is applied afterwards to deconvolute the signals emitted by the different absorbers based on their PA spectra.[3] Typical spectral unmixing compares the difference in signal with and without the contrast agent and applies multivariate statistical methods such as linear regression to distinguish the probe signal from the background – this is particularly important for heterogeneous mediums like *in vivo* studies.[45]

These experiments were undertaken in collaboration with the National Physical Laboratory. Dr. Anant Shah carried out the measurements using multispectral optoacoustic imaging performed on the iThera Medical inVision-256TF at the Institute of Cancer Research. The setup included a pre-made phantom composed of polyurethane with titanium dioxide to adjust the light scattering. The phantom contained hollow inserts, where the aqueous samples were inserted for imaging (Figure 5.10). The samples were prepared by dissolving the dried compounds in deionised water to concentrations of 5 µM or lower with an optical density value of less than 1 to avoid staining the phantom. Even though the incorporation of the titanium dioxide alters the light scattering of the phantom, it does not mimic tissue with respect to the optical absorption or acoustic properties. The speed of sound through the phantom is different from that of biological tissue so this was corrected prior to reconstruction. Images of the phantoms were obtained at 10 nm intervals between 680 and 980 nm, using the average of 3 scans per wavelength – Figure 5.10 shows the image recorded at 770 nm. The mean pixel intensity of the region of interest from the images was plotted to record the photoacoustic spectrum. The acquired raw data was reconstructed using the model-based software provided by the manufacturer and accounts for the geometry of the transducer. More details on the reconstruction algorithm can be found in the paper by Razansky *et al.*[46]

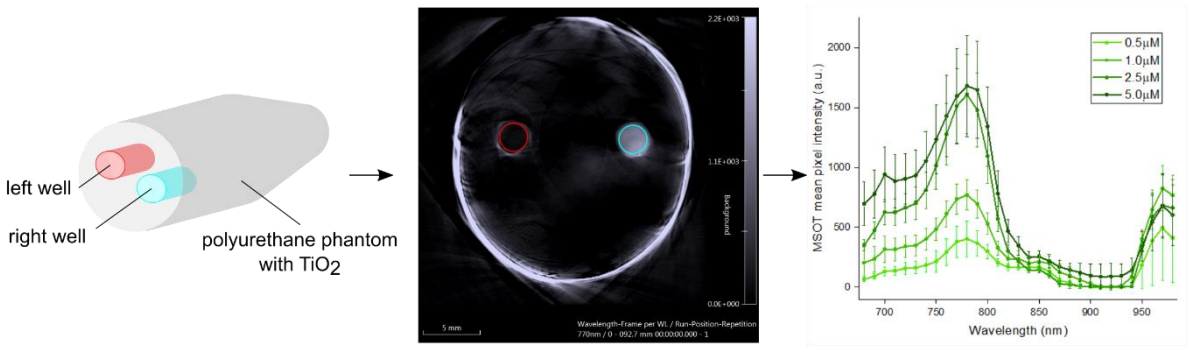


Figure 5.10. Schematic of the experimental set up in the phantom (left) containing hollow inserts where the probes in aqueous solution were filled. An image obtained of the phantom (middle) with the selected regions of interest for the reference, H_2O (red) and probe well (cyan) and a resultant photoacoustic spectrum obtained from the phantoms is shown (right).

5.4.2 Optimal transmit parameters

The PA spectra obtained in H_2O largely resembles the absorption spectra (Figure 5.11) with the λ_{max} values similar for all probes (Table 5.2). A slight broadening of the signal for probes **PA-2** to **PA-4** was exhibited but it was difficult to distinguish whether this was because of the PA effect,

or the 10 nm intervals used to record the spectra. The exception was for **PA-1**, ICG, which exhibited greater broadening of the PA peak and the peak was slightly red shifted from an absorption maximum of 779 nm to a maximum MSOT intensity of 800 nm. It was also observed for **PA-1** that there were signs of aggregation of the probe on the well boundary which was visible in the MSOT images. This was not observed for the rest of the probes.

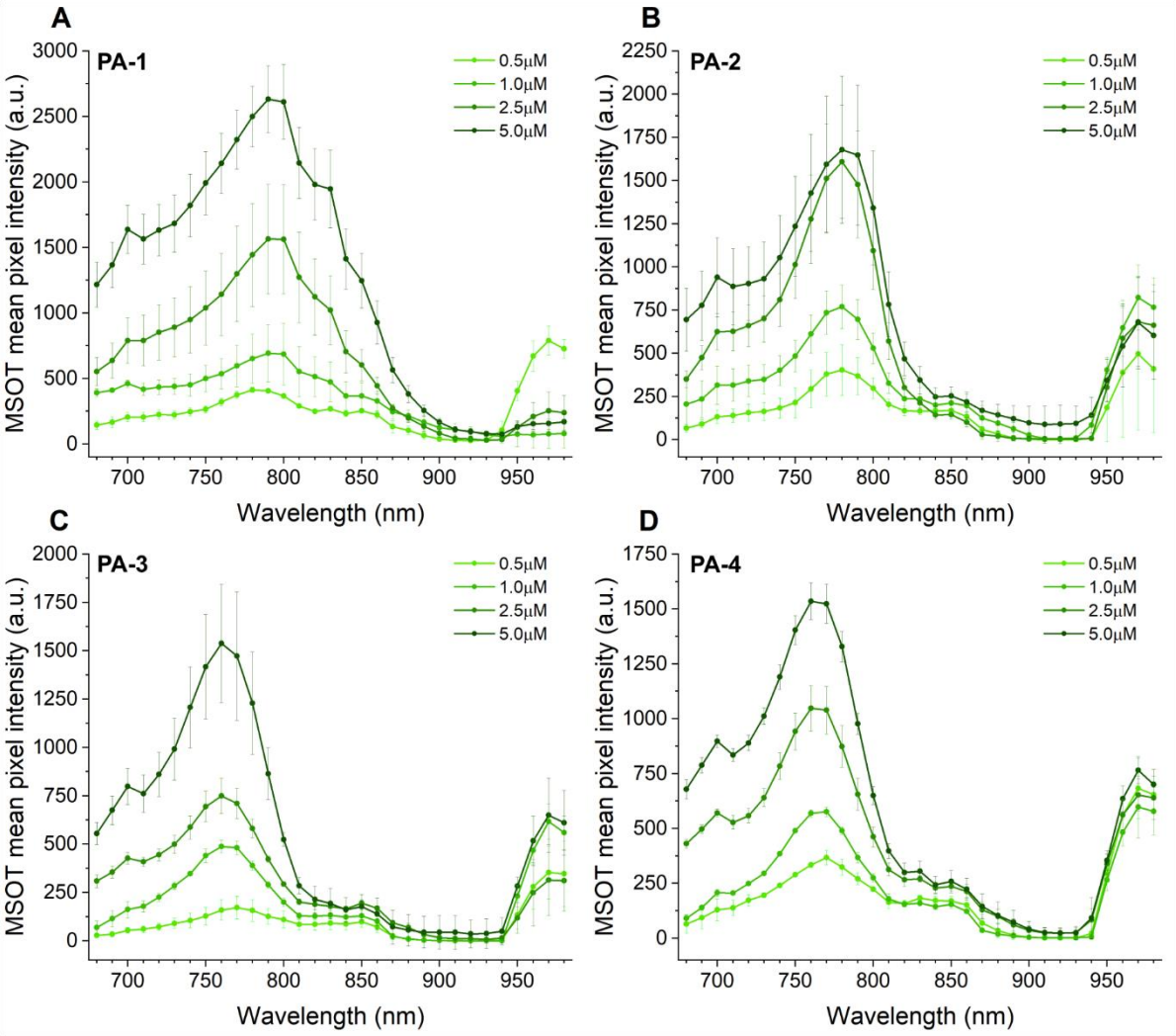


Figure 5.11. Mean PA intensity for probes 1-4 represented by graphs a-d respectively at 4 different concentrations in H_2O from 680-980 nm with λ_{max} being 790, 780, 760, and 760 nm.

Table 5.2. Comparison between optical and photoacoustic properties recorded in H_2O.

Compound	Optical λ_{max} (nm)	Molar Extinction Coefficient (L^{-1} mol^{-1} cm^{-1})	PA λ_{max} (nm) for 5 μM solutions
PA-1	779	192 900	800
PA-2	782	168 200	780
PA-3	761	171 500	760
PA-4	763.5	158 200	760

5.4.3 Linearity

Figure 5.12 shows the MSOT mean intensity at λ_{max} plotted against the concentration of the probes. All probes except for **PA-2** (*meso*-chloro dye) show a strong linear correlation between the probe concentration and the signal intensity with R^2 value greater than 0.97. **PA-2** appears to fit a sigmoidal curve - this could be due to aggregation of the dye at higher concentrations although that is unlikely as a linear correlation was observed for the dye for the UV-vis at similar concentrations. On the other hand, given the broadening of the PA spectra observed for **PA-1** in Figure 5.11 and the accumulation of the dye on the well boundary, it was unexpected to observe the linear concentration-dependent PA signal seen in Figure 5.12.

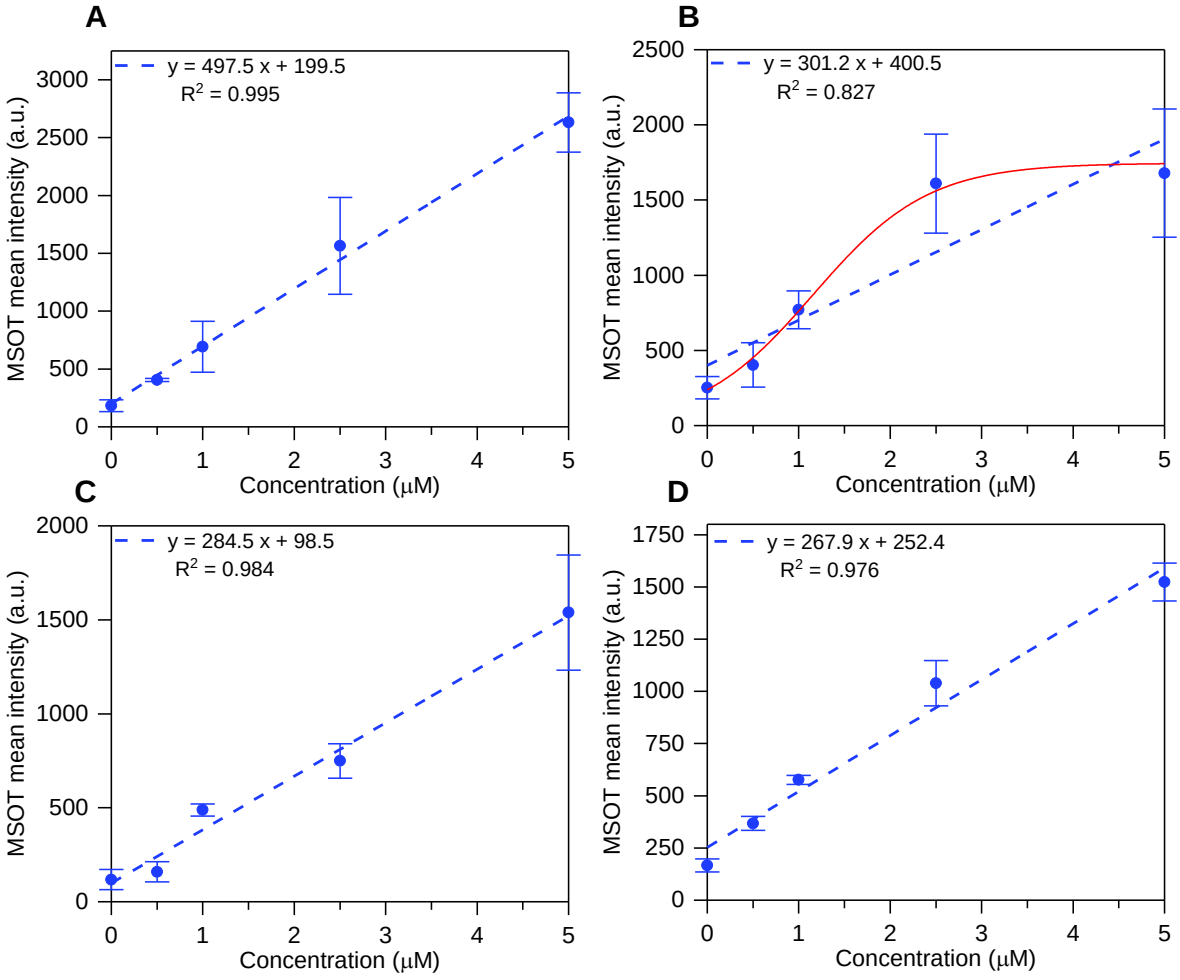


*Figure 5.12. Mean MSOT intensity at λ_{max} against probe concentration: a) **PA-1**, ICG; b) **PA-2**, meso-chloro dye; d) **PA- 3**, Suzuki product; d) **PA-4**, dye+tuftsin.*

5.4.4 Sensitivity of the PA probes

The contrast to noise ratio (sensitivity) of the probes was calculated from equation (5.1) and the results are shown in Figure 5.13. For the set up used, the sensitivity was defined as the minimum detectable concentration that has a contrast to noise ratio (CNR) of 2 dB. All probes display linearity

within the range of error of the measurement. From this it was determined that the sensitivity of all of the probes is 0.45 µM or less.

$$CNR = \frac{mean\ signal\ (probe) - mean\ signal\ (water)}{standard\ deviation\ (water)} \quad (5.1)$$

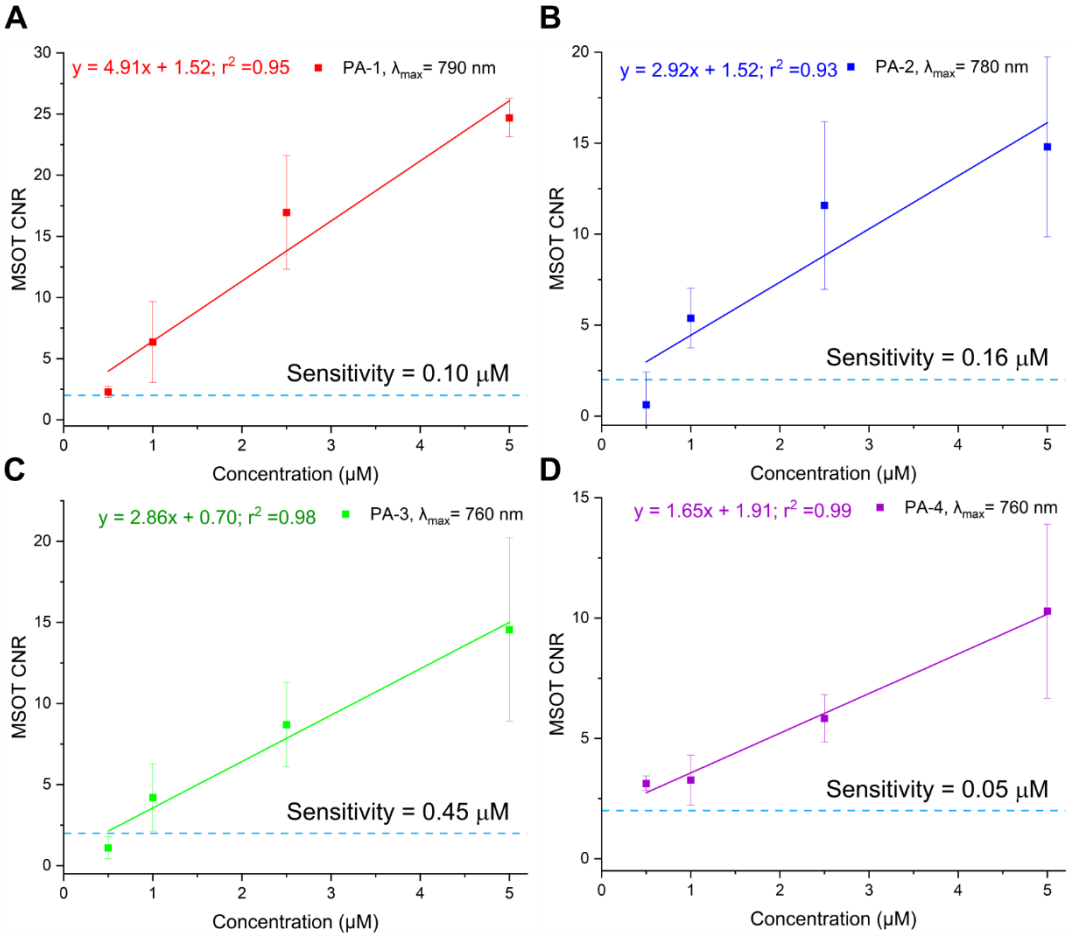


Figure 5.13. Contrast to noise ratio graphs for a-d) PA-1-4. The sensitivity is calculated for the minimum detectable concentration when the CNR is equal to 2 dB (blue horizontal line).

5.4.5 Photostability

The photostability of **PA-1** to **PA-4** was assessed on the iThera Medical inVision-256TF by monitoring the decay of the PA response as a function of the number of pulses at a set energy output (maximum permissible) with a pulsed laser at the probes' maximum absorption over the course of 1000 pulses; the results are shown in Figure 5.14. The high number of pulses with the laser was chosen as this was intended to be a higher number of pulses than would be required for photoacoustic imaging in a clinical setting. The MSOT system does not provide pulse energies of the system in real time.

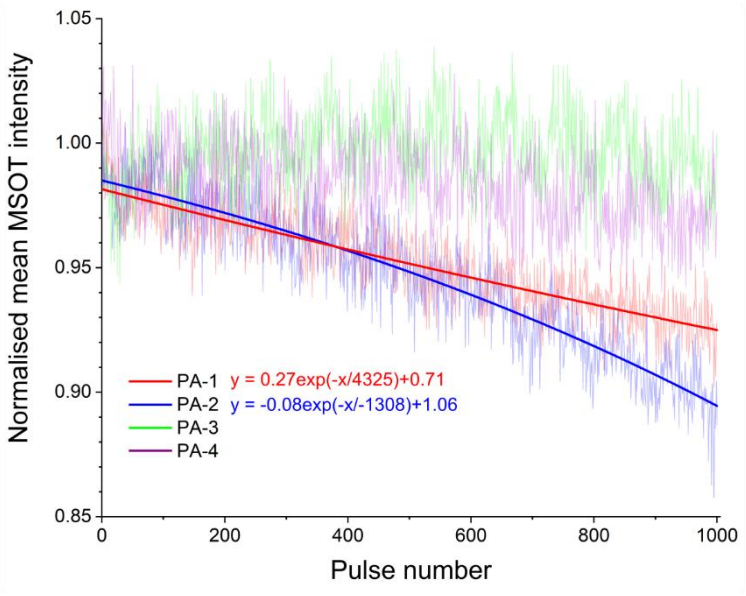


*Figure 5.14. Normalised mean MSOT intensity measured for 1000 pulses of laser, where the energy of the laser at λ_{max} was 68-71 mJ and the surface fluence was approximately 20 mJ cm^{-2}. **PA-1** and **PA-2** were fitted as monoexponential decay curves, **PA-3** and **PA-4** did not fit linear or monoexponential decay.[PA] = 2.5 μM in H_2O.*

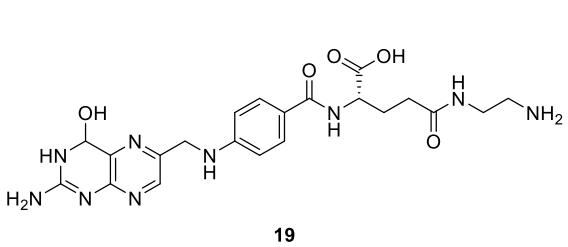
Probes **PA-1** and **PA-2** were fit as monoexponential decay curves, but **PA-3** and **PA-4** were unable to be fit as linear or monoexponential decay. As expected, **PA-1** and **PA-2** show the largest decrease in signal corresponding to the largest instability under pulsed laser (Figure 5.14). Neither **PA-3** nor the **PA-4** show a linear decrease of the signal. **PA-3** displays a minor increase in signal over 1000 pulses although there is a repeated oscillation over the duration, and as there is no decrease in signal it supports the hypothesis of incorporation of the central C-C bond to improve the stability of the probes. All probes exhibit an oscillation of the signal. It then followed that the tuftsin-functionalised probe, **PA-4**, also showed only a small decline in the signal to 97% of the initial intensity demonstrating that the addition of the peptide did not lead to a reduction in stability. Overall, **PA-1** experienced the greatest photobleaching with a reduction to 88% of its original signal intensity after 1000 pulses; however, given that **PA-1** had the strongest PA signal initially (Figure 5.11), its signal remained the largest even after the photodamage. Significantly, there is agreement between the photostability studies carried out using fluorescence and PA signal.

5.5 Conclusions

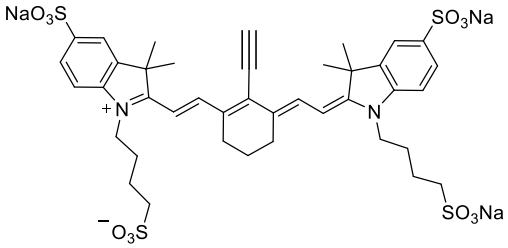
In this work a macrophage-targeted photoacoustic contrast agent using the tuftsin targeting approach was synthesised. The photophysical characterisation of this and the heptamethine dye precursors **PA-2 to PA-4** were recorded and compared to the commercially available indocyanine green, **PA-1**. All the probes displayed an absorbance and emission within the NIR optical window which makes them well placed to act as photoacoustic probes. All dyes were prone to damage by

photobleaching, as shown in fluorescence stability studies, with the greatest damage observed for the **PA-1** and *meso*-chloro precursor, **PA-2** over the course of the photostability studies carried out.

The folate analogue of the photoacoustic probe was unable to be synthesised during this work and future recommendations include complete removal or shortening of the long PEG chain linker by attaching folic acid directly or with an ethylene-diamine linker (**19**, Figure 5.15). In addition, the amide coupling could be attempted with other amide coupling reagents such as DCC, TBTU and PyBop to understand whether HATU was ineffective in this case. An alternative could be to attach an alkyne on the central position of the heptamethine cyanine dye (**29**, Figure 5.15) to allow for attachment of an azide-functionalised folate moiety using copper click chemistry, explored in other chapters of this work.



19



29

*Figure 5.15. Structures for future work. Folate-ethylene diamine, **19** and heptamethine dye with a terminal alkyne for CuAAC, **29**.*

Extension of this work would include cell testing to check the toxicity, binding, and functionality of these probes *in vitro*. Further work could then explore second-generation photoacoustic probes to optimise the photophysical properties to improve their suitability as photoacoustic contrast agents, as well as improving stability. In addition, it could be anticipated that this work would be extended to bimodal imaging, similar to work that has carried out by the Laurent group combining a photoacoustic probe with an MR imaging group.[47]

5.6 References

1. V. Ntziachristos and D. Razansky, *Chem. Rev.*, 2010, **110**, 2783-2794.
2. L. H. V. Wang and S. Hu, *Science*, 2012, **335**, 1458-1462.
3. V. Gujrati, A. Mishra and V. Ntziachristos, *Chem. Commun.*, 2017, **53**, 4653-4672.
4. B. Cox, J. G. Laufer, S. R. Arridge and P. C. Beard, *J. Biomed. Opt.*, 2012, **17**, 061202-1-061202-22.
5. M. Pope and C. E. Swenberg, in *Electronic processes in organic crystals and polymers*, Oxford University Press, Oxford, 2nd edn., 1999.
6. P. Beard, *Interface Focus*, 2011, **1**, 602-631.
7. V. Ntziachristos, *Nat. Methods*, 2010, **7**, 603-614.
8. J. Weber, P. C. Beard and S. E. Bohndiek, *Nat. Methods*, 2016, **13**, 639-650.
9. M. Y. Berezin, K. Guo, W. Akers, J. Livingston, M. Solomon, H. Lee, K. Liang, A. Agee and S. Achilefu, *Biochemistry*, 2011, **50**, 2691-2700.
10. H. Kobayashi, M. Ogawa, R. Alford, P. L. Choyke and Y. Urano, *Chem. Rev.*, 2010, **110**, 2620-2640.
11. A. De La Zerda, C. Zavaleta, S. Keren, S. Vaithilingam, S. Bodapati, Z. Liu, J. Levi, B. R. Smith, T. J. Ma, O. Oralkan, Z. Cheng, X. Y. Chen, H. J. Dai, B. T. Khuri-Yakub and S. S. Gambhir, *Nat. Nanotechnol.*, 2008, **3**, 557-562.
12. C. J. H. Ho, G. Balasundaram, W. Driessen, R. McLaren, C. L. Wong, U. S. Dinish, A. B. E. Attia, V. Ntziachristos and M. Olivo, *Sci. Rep.*, 2014, **4**, DOI: 10.1038/srep05342.
13. D. Sehnal, S. Bittrich, M. Deshpande, R. Svobodova, K. Berka, V. Bazgier, S. Velankar, S. K. Burley, J. Koca and A. S. Rose, *Nucleic Acids Res.*, 2021, **49**, W431-W437.
14. M. Ormo, A. B. Cubitt, K. Kallio, L. A. Gross, R. Y. Tsien and S. J. Remington, *Science*, 1996, **273**, 1392-1395.
15. N. Sim, S. Gottschalk, R. Pal, M. Delbianco, O. Degtyaruk, D. Razansky, G. G. Westmeyer, V. Ntziachristos, D. Parker and A. Mishra, *Chem. Commun.*, 2015, **51**, 15149-15152.
16. F. F. An, Z. J. Deng, J. Ye, J. F. Zhang, Y. L. Yang, C. H. Li, C. J. Zheng and X. H. Zhang, *ACS Appl. Mater. Interfaces*, 2014, **6**, 17985-17992.
17. E. Y. Park, D. Oh, S. Park, W. Kim and C. Kim, *APL Bioeng.*, 2021, **5**, 031510-1- 031510-15.
18. L. Yuan, W. Y. Lin, K. B. Zheng, L. W. He and W. M. Huang, *Chem. Soc. Rev.*, 2013, **42**, 622-661.
19. R. E. Borg and J. Rochford, *Photochem. Photobiol.*, 2018, **94**, 1175-1209.
20. S. M. Mahalingam, S. A. Kularatne, C. H. Myers, P. Gagare, M. Norshi, X. Liu, S. Singhal and P. S. Low, *J. Med. Chem.*, 2018, **61**, 9637-9646.

21. S. Roberts, A. Strome, C. Choi, C. Andreow, S. Kossatz, C. Brand, T. Williams, M. Bradbury, M. F. Kircher, Y. K. Reshetnyak, J. Grimm, J. S. Lewis and T. Reiner, *Sci. Rep.*, 2019, **9**, DOI: 10.1038/s41598-019-44873-1.
22. A. Mishra, Y. Y. Jiang, S. Roberts, V. Ntziachristos and G. G. Westmeyer, *Anal. Chem.*, 2016, **88**, 10785-10789.
23. H. Hyun, E. A. Owens, L. Narayana, H. Wada, J. Gravier, K. Bao, J. V. Frangioni, H. S. Choi and M. Henary, *RSC Adv.*, 2014, **4**, 58762-58768.
24. F. Wurthner, T. E. Kaiser and C. R. Saha-Moller, *Angew. Chem. Int. Ed.*, 2011, **50**, 3376-3410.
25. J. R. Lakowicz, *Principles of fluorescence spectroscopy*, Springer Science Business Media, New York, 2nd edn., 1999.
26. W. Pham, Z. Medarova and A. Moore, *Bioconjugate Chem.*, 2005, **16**, 735-740.
27. G. A. Reynolds and K. H. Drexhage, *J. Org. Chem.*, 1977, **42**, 885-888.
28. H. Lee, J. C. Mason and S. Achilefu, *J. Org. Chem.*, 2006, **71**, 7862-7865.
29. S. G. Konig and R. Kramer, *Chem. Eur. J.*, 2017, **23**, 9306-9312.
30. W. Wang, S. Ke, Q. Wu, C. Charnsangavej, M. Gurfinkel, J. G. Gelovani, J. L. Abbruzzese, E. M. Sevick-Muraca and C. Li, *Mol. Imaging*, 2004, **3**, 343-351.
31. M. L. Li, J. T. Oh, X. Y. Xie, G. Ku, W. Wang, C. Li, G. Lungu, G. Stoica and L. V. Wang, *Proc. IEEE*, 2008, **96**, 481-489.
32. Y. Luan, Q. Yang, Y. Xie, S. Duan, S. Cai and M. L. Forrest, *Drug Discoveries Ther.*, 2011, **5**, 220-226.
33. Q. H. Yang, H. Z. Cui, S. Cai, X. M. Yang and M. L. Forrest, *J. Biomed. Opt.*, 2011, **16**, 116026-1-116026-4.
34. C. H. Tung, Y. H. Lin, W. K. Moon and R. Weissleder, *ChemBioChem*, 2002, **3**, 784-786.
35. *World Pat.*, WO 2014149073, 2014.
36. E. De Jesus, J. J. Keating, S. A. Kularatne, J. Jiang, R. Judy, J. Predina, S. Nie, P. Low and S. Singhal, *Int. J. Mol. Imaging*, 2015, **2015**, DOI: 10.1155/2015/469047.
37. R. B. Mujumdar, L. A. Ernst, S. R. Mujumdar, C. J. Lewis and A. S. Waggoner, *Bioconjugate Chem.*, 1993, **4**, 105-111.
38. L. Strekowski, M. Lipowska and G. Patonay, *J. Org. Chem.*, 1992, **57**, 4578-4580.
39. N. Sim and D. Parker, *Chem. Soc. Rev.*, 2015, **44**, 2122-2134.
40. D. D. Su, C. L. Teoh, A. Samanta, N. Y. Kang, S. J. Parka and Y. T. Chang, *Chem. Commun.*, 2015, **51**, 3989-3992.
41. V. von Kiedrowski, R. Hubner, D. Kail, X. Cheng, R. Schirrmacher, C. Wanglerb and B. Wangle, *J. Mater. Chem. B*, 2020, **8**, 10602-10608.
42. J. T. Alander, I. Kaartinen, A. Laakso, T. Patila, T. Spillmann, V. V. Tuchin, M. Venermo and P. Valisuo, *Int. J. Biomed. Imaging*, 2012, **2012**, DOI: 10.1155/2012/940585.

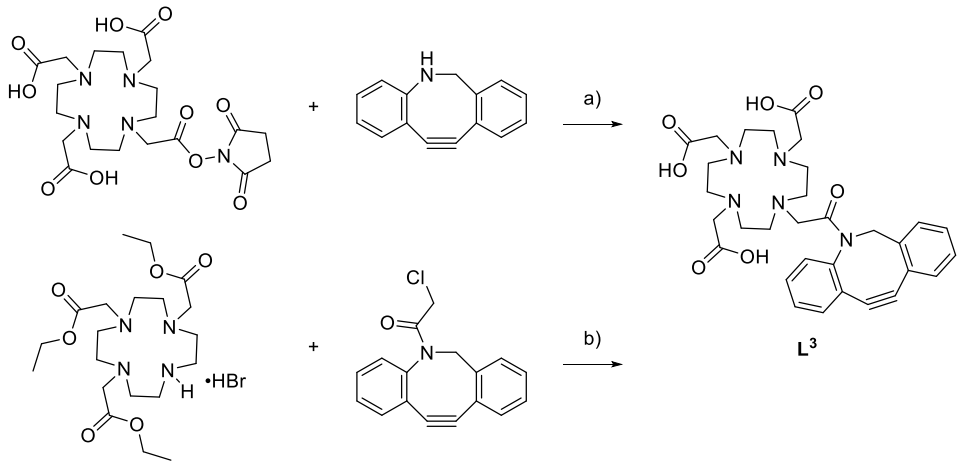
43. K. Makhal, S. Maurya and D. Goswami, *Phys. Scr.*, 2019, **94**, DOI: 10.1088/1402-4896/ab0064.
44. D. S. Pisoni, L. Todeschini, A. C. A. Borges, C. L. Petzhold, F. S. Rodembusch and L. F. Campo, *J. Org. Chem.*, 2014, **79**, 5511-5520.
45. D. Razansky, C. Vinegoni and V. Ntziachristos, *Opt. Lett.*, 2007, **32**, 2891-2893.
46. X. L. Dean-Ben, A. Buehler, V. Ntziachristos and D. Razansky, *IEEE Trans. Med. Imaging*, 2012, **31**, 1922-1928.
47. M. Devreux, C. Henoumont, F. Dioury, D. Stanicki, S. Boutry, L. Larbanoix, C. Ferroud, R. N. Muller and S. Laurent, *Eur. J. Inorg. Chem.*, 2019, **2019**, 3354-3365.

6 Conclusions

The principal aim of this project was to design, synthesise and evaluate series of probes suitable for multiple different imaging modalities that specifically target macrophages.

Chapter 2 of this work outlines the synthesis and characterisation of a set of three alkyne appended-DO3A complexes that are capable of CuAAC and SPAAC. The acetophenone-derived DO3A, Ln**L**^{2} allowed for efficient sensitisation of the metal centre, and in theory, provided a more stable 8-coordinate complex than the 7-coordinate pDO3A**,** Ln**L**^{1}. It was found that the Ln-DOTA-DBCO is highly fluorescent but unstable complex. Early work suggests that the DBCO can sensitise the lanthanide metal centre, but its signal is quenched by oxygen, or the strained alkyne is destroyed by oxidative photodamage.

For further work, several routes can be suggested, the first would be to further investigate the DBCO-based structures. Although initial strategies to synthesise ligand **L**^{3} were unsuccessful, a shorter distance between the metal centre and DBCO may allow for improved Dexter energy transfer when used for luminescent lanthanide probes. Therefore, two potential synthetic routes for generating **L**^{3} are proposed in Scheme 6.1: DOTA-NHS ester could react with the amine of the DBCO or DO3A could be alternatively protected using an ethyl ester. Secondly to investigate the utility of the DBCO-triazole, the DOTA-DBCO, Ln**L**^{4} should be reacted with a simpler azide, such as sodium azide or benzyl azide, to determine whether the triazole improves lanthanide sensitisation. Moreover, as the DBCO moiety is very hydrophobic it is likely to alter the pharmacokinetics of the imaging agents possibly resulting in undesirable hepatobiliary clearance or non-specific protein binding. Therefore, it may be necessary to use a strained alkyne with less aromaticity such as difluorocyclooctyne or bicyclo[6.1.0]non-4-yne (Figure 6.1).



*Scheme 6.1. Alternative synthetic routes for synthesising **L**^{3}. Reagents and conditions: a) Anhydrous DMF, TEA, r.t.; b)i) MeCN, Na_2CO_3, 50 °C, ii) 1 M NaOH, 0 °C.*

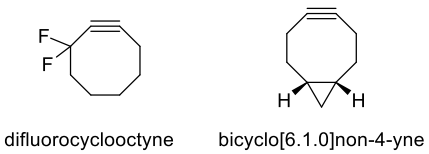


Figure 6.1. Alternative strained cyclooctynes to dibenzocyclooctyne.

Chapter 3 details the synthesis of a range of folate-derived terbium complexes using solid phase synthesis, copper- and strained promoted azide alkyne cycloaddition and the characterisation of their structure by NMR spectroscopy and photophysical properties. Future work should explore the stability of the folate complexes in solutions at varying pH and the photophysical properties to determine their suitability as macrophage optical imaging agents. This would imitate the different environments that the folate-based imaging agents are found to reside upon cell internalisation and determine whether the probes are suitable for *in vitro* luminescent imaging. The final validation of these probes would be for them to be tested *in vitro* on cells that have high expression of FR-α (KB cells – human cancer cell line) and FR-β (CHO cells transfected with FR-β) to determine the cell binding affinity relative to free folic acid and whether the modifications (PEG chain, click chemistry) affect cell binding or alter internalisation. For *in vitro* studies, fluorescence-lifetime imaging microscopy (FLIM) would be suitable to distinguish between the long-lived terbium emission from the short-lived folate and autofluorescence – this may inform on cell internalisation and localisation. Moreover, given the dominance of the folate fluorescence, it would be recommended to develop second-generation optical probes incorporating a chromophore close to the lanthanide binding site to improve the indirect excitation of the lanthanide, before progressing to *in vivo* testing.

Another extension of the folate work would be to substitute the terbium metal centre for gadolinium and investigate the use of the folate conjugates as MR contrast agents. Initial work would entail measuring the relaxivity of the probes in PBS, at different pHs and in the presence of blood serum albumin, before proceeding to test the compounds *in vitro*.

In addition, a range of lanthanide-tuftsin conjugates were synthesised for use in different imaging modalities (optical and MR). To extend the optical probes, incorporation of a chromophore, such as an acetophenone or a carbostyril moiety, would significantly improve the lanthanide fluorescence (Figure 6.2). As for the folate probes, final validation would be for *in vitro* cell studies in macrophages (resident and activated) to determine binding affinity and internalisation, as tuftsin is reported to be mainly targeted to activated macrophages.

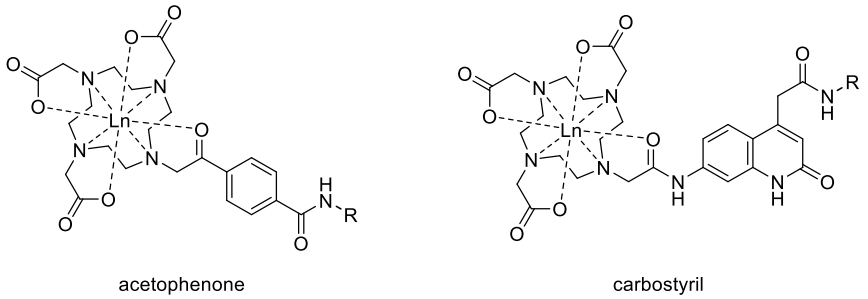


Figure 6.2. DO3A functionalised with a chromophore to allow for indirect lanthanide excitation with an R group showing the point for tuftsin conjugation.

Preliminary work using novel diffusion NMR techniques, INDIANA and diffCEST, show potential for use in determining GBCA internalisation in whole blood. Possible extension of the INDIANA model to be a three-pool system could potentially capture more of the heterogeneity of complex systems, such as blood, but more work is required to validate these models. With respect to the tuftsin probes, it would be desirable to test the GBCAs in a two-pool system – a single macrophage cell type – to understand internalisation using INDIANA and validate the results with cell counting and measuring cell sizes to confirm findings using the NMR technique. For further probe development, the DOTA-tuftsin based probes adopt mainly the SAP isomer, so structural alterations could be carried out to improve the longitudinal relaxivity; this could include adding bulky groups close to the macrocyclic ring to force the TSAP conformation.

The final area of this work involved the synthesis of macrophage targeted photoacoustic contrast agents – their photophysical and photoacoustic properties were characterised. Synthesis of the FR-targeted PA probe was not achieved during this work, however conjugation with folate using an alkyne-appended heptamethine dye or by using folate with a shorter PEG linker may result in more success. The developed probes, **PA-2** to **PA-4**, had similar molar extinction coefficients to the commercially available ICG. The advantage of probes **PA-3** and **PA-4** over ICG was the improved photostability as well as a narrower PA signal which allows for easier distinction between the PA probe and the background signal *in vivo*. The heptamethine cyanine dyes are plagued by problems of photostability, and so these may not be the most suitable structures for further development as PA probes.

Overall, this work demonstrates a toolkit of molecular probes suitable for imaging using optical, MR and photoacoustic with many recommendations for avenues for future work to explore.

7 Experimental Procedures

7.1 General Procedures

Commercially available solvents and reagents were used without further purification unless otherwise stated. Reagents were laboratory grade and obtained from standard commercial sources including Sigma-Aldrich, Fisher Scientific, Alfa Aesar, Fluorochem, CheMatech, ChemicalPoint, and Insight Biotechnology. Anhydrous solvents used were obtained by passing through a *MBraun MPSP-800* column (degassed with N_2) and then used immediately. Deionised water was obtained using an Elix® Essential water purification system. Propargyl bromide was used as 80 wt% solution in toluene (Sigma-Aldrich). Neutral alumina for column chromatography was purchased from Alfa Aesar (aluminium oxide activated, neutral Brockmann Grade I, pore size 58 Å, 60 mesh). Silica gel for column chromatography was purchased from Merck (Geduran®, pore size 60 Å, 230-400 mesh, 40-63 μm. Aluminium oxide neutral TLC plates and silica TLC plates were TLC gel 60 purchased from Merck. Brine is a saturated sodium chloride solution.

Float-A-Lyzer® G2 dialysis tubes (500, 1000MWCO) equipped with regenerated cellulose were purchased from Spectrum and used to purify the lanthanide complexes. The dialysis tube was activated by 10 % ethanol or isopropanol solution in deionised water followed by deionised water before being used. The corresponding complexes were dissolved in water and transferred into dialysis tube. The dialysis tube was placed in a 5 L-beaker filled with deionised water. The dialysis lasts for at least two days under stirring and the deionised water was replaced with fresh deionised water more than three times during dialysis.

NMR spectroscopy: NMR spectra were recorded at 298 K unless otherwise stated. 600 MHz ^{1}H-NMR and 151 MHz ^{13}C-NMR were obtained using a Bruker NEO 600 with broadband helium cryoprobe equipped with a 14 T magnet. 500 MHz ^{1}H-NMR, 126 MHz ^{13}C-NMR were recorded on a Bruker Avance III NMR equipped with a 11.75 T magnet. 400 MHz ^{1}H-NMR and 101 MHz ^{13}C-NMR were obtained using a Bruker Avance III nanobay 400 NMR equipped with a 9.4 T magnet. All coupling constants are quoted in Hz with all chemical shifts quoted in parts per million (ppm) and referenced to the residual solvent peak. Abbreviations when quoting NMR data are as follows: singlet (s), doublet (d), triplet (t), quartet (q), multiplet (m) and broad (br).

NMR Spectroscopy (Diffusion Experiments): All diffusion NMR experiments were acquired at 298 K on a 14.1 T (600 MHz) Agilent DD2 NMR spectrometer equipped with a 5 mm z-axis gradient triple resonance room temperature probe. Gradients were calibrated using the known diffusion coefficient of residual HDO (1902 $\mu m^2 s^{-1}$) in a sample of D_2O at 298 K. The spectrometer temperature was calibrated with *d*$_4$-methanol. A stimulated echo pulse sequence with six variable diffusion delays (Δ = 50, 100, 200, 300, 400 and 500 ms) was used in all diffusion experiments. In

all experiments δ = 2 ms, $\tau 2$, the time for which the magnetisation is transverse, was always set to 10 ms and eleven quadratically spaced gradient field strengths between 8 and 60 $G \cdot cm^{-1}$ were employed.

All spectra were Fourier transformed and phased using NMRPipe. Data were analysed in phase-sensitive mode, with the lowest gradient field strength and diffusion delay spectrum used to determine the phase parameters that are then applied to all other spectra. The water peak intensity in each spectrum was integrated and analysed using the INDIANA method to determine the intra-cellular water mole fraction, cell radius, water exchange rate over the membrane and diffusion coefficients and longitudinal relaxation rates in both the intra- and extra-cellular spaces. Previous simulations have shown that while the INDIANA method is relatively insensitive to small changes in the intra-cellular longitudinal relaxation rate it is sensitive to when this rate exceeds approximately 0.5 s^{-1}.

Blood samples: The human biological samples were sourced ethically, and their research use was in accord with the terms of the informed consents under an IRB/EC approved protocol. Chilled fresh whole human blood and blood plasma in lithium heparin were purchased from Research Donors and received by chilled overnight delivery. The blood was from healthy donors aged between 18-60, screened and tested negative for HIV, Hepatitis B and C.

NMR Relaxivity Experiments: Contrast agent measurements were performed using a Bruker Avance III HD nanobay NMR equipped with 5 mm z-gradient broadband X-19F/1H BBFO SMART probe, and a 9.4 T magnet at 25°C. T_1 data was analysed using Bruker TopSpin 3.5 NMR software. Samples were prepared between 0-1 mM, (200 µL, PBS) and placed into a melting point tube (50 µL) and transferred to a 5 mm NMR tube. No lock solvent was required.

Mass Spectrometry: Low-resolution mass spectra were obtained using either an Agilent Technology 1260 Infinity or a Waters LCT Premier XE spectrometer. LC-MS were measured by a Waters LCT Premier bench-top orthogonal acceleration time-of-flight LC-MS system. High-resolution accurate mass spectra were performed by the staff of the Chemistry Research Laboratory, University of Oxford using Bruker µTOF or Waters Micromass® GCT spectrometers and recorded to 4 decimal places.

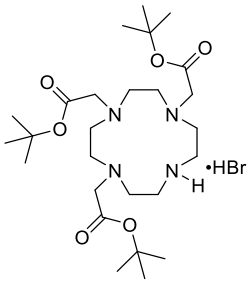
UV-Vis spectroscopy: UV-vis spectra were recorded on a Cary60 UV-vis spectrophotometer fitted with a xenon source lamp or on a Jasco V-770 UV-visible/NIR spectrophotometer.

Luminescence spectroscopy: HORIBA Jobin Yvon FluoroLog3-12 fluorimeter (Hamamatsu R928 detector and a double-grating emission monochromator) was used to acquire the luminescence spectra operated under FluorEssence software. The standard conditions for acquiring emission and excitation spectra are room temperature and steady-stated mode unless otherwise stated. HORIBA

Jobin Yvon FluoroLog3 fluorimeter system equipped with a Xenon flash lamp was used to acquire emission lifetimes. Luminescence lifetimes were obtained by tail fit for Eu(III) complexes using Origin software.

Multispectral Optoacoustic Imaging: These experiments were undertaken in collaboration with the National Physical Laboratory. Dr. Anant Shah carried out the measurements using multispectral optoacoustic imaging performed on the iThera Medical inVision-256TF at the Institute of Cancer Research. The samples were prepared by dissolving the dried compounds in deionised water to concentrations of 5 μM or lower with an optical density value of less than 1. The setup included a pre-made phantom, consisting of hollow inserts, where the aqueous probes were inserted for imaging. The phantom is composed of polyurethane and uses titanium dioxide to adjust the light scattering. Even though the incorporation of the titanium dioxide alters the light scattering of the phantom, it does not mimic tissue with respect to the optical absorption or acoustic properties. The speed of sound through the phantom is different from that of biological tissue so was adjusted for prior to reconstruction. The images were obtained of the phantoms where the two wells were defined as the regions of interest (control and probe), scanning the wavelengths between 680-980 nm, using 10 nm intervals and 3 independent averages per wavelength. The acquired raw data was reconstructed using the model-based software provided by the manufacturer and accounts for the geometry of the transducer. More details on the reconstruction algorithm can be found in the paper by Razansky *et al.*[1] Photoacoustic signals were acquired with a laser where the energy of the laser was 68-71 mJ.

tBuDO3AH: 1,4,7-Tris(*tert*-butoxycarbonylmethyl)-1,4,7,10-tetraazacyclododecane hydrobromide salt[2] (1)



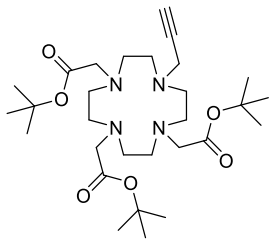
1,4,7,10-Tetrazacyclododecane (cyclen) (6.00 g, 34.8 mmol, 1.00 eq.) was dissolved in anhydrous acetonitrile (120 mL) with sodium hydrogen carbonate (9.66 g, 115 mmol, 3.30 eq.) and stirred for 20 minutes in an ice bath. *Tert*-butyl bromoacetate (17.0 mL, 115 mmol, 3.30 eq.) was dissolved in anhydrous acetonitrile (80 mL) and added dropwise to the stirred solution over 1 hour. The reaction mixture was then allowed to warm to room temperature and was stirred for 48 hours. The inorganic solids were removed by filtration through a celite pad, and the solvent was removed under reduced

pressure. The off-white solid was stirred in cold toluene for 24 hours and filtered. The solid was recrystallised from hot toluene to give the final product, **1** as a white solid (9.09 g, 44%).

^{1}H NMR (400MHz, $CDCl_3$): δ 10.05-9.87 (br s, 2H, N***H***·***H***Br), 3.31 (s, 4H, COC***H*****$_2$**N), 3.23 (s, 2H, COC***H*****$_2$**N), 3.04 (br t, 4H, NC***H*****$_2$**), 2.87 (br t, 8H, NC***H*****$_2$**), 2.82 (br t, 4H, NC***H*****$_2$**), 1.40 (s, 18H, 2 × C(C***H*****$_3$**)$_3$), 1.39 (s, 9H, C(C***H*****$_3$**)$_3$) ppm. The ^{1}H NMR data corresponds to reported literature values.[2]

ES-MS (MeOH): *m/z* 515.4 $[M + H]^+$.

Propargyl-tBu$_3$DO3A: 1,4,7-tri(tert-butoxycarbonylmethyl)-10-(prop-2-ynyl)-1,4,7,10-tetraazacyclododecane (2)



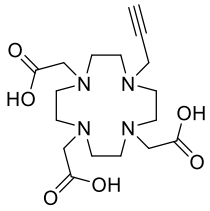
Prepared with minor adaptation from the procedure described by Jauregui *et al.*[3, 4] Triester, **1** (4.00 g, 6.72 mmol, 1.00 eq.) was added to dry MeCN (60 mL) with potassium carbonate (2.32g, 16.8 mmol, 2.50 eq.) and stirred for 20 minutes. The flask was cooled on ice, propargyl bromide (80% wt in toluene) (0.75 mL, 5.83 mmol, 1.00 eq.) was added dropwise and the reaction was left stirring overnight at room temperature under N_2. Inorganic solids were removed by filtration and the solvent was removed under reduced pressure. The resulting oil was dissolved in toluene (75 mL) and washed with water (60 mL × 2). The organic layer was dried over $MgSO_4$, filtered through celite pad and the solvent removed to give **2** as a clear golden oil (2.61 g, 4.72 mmol, 70%).

^{1}H NMR (500 MHz, $CDCl_3$) δ 3.42 (s, 2H, C***H*****$_2$**C≡C), 3.27 (s, 6H, arm C***H*****$_2$**CO_2), 2.82 (s, 12H, ring C***H*****$_2$**), 2.68 (m, 4H, ring C***H*****$_2$**), 2.14 (s or t, *J* = 2.4 Hz, 1H, C≡C***H***), 1.45 (s, 27H, ^{t}Bu) ppm.

^{13}C NMR (126 MHz, $CDCl_3$) δ 171.3 (***C***OO), 80.9 (***C***$(CH_3)_3$), 79.4(***C***≡CH), 72.6(C≡***C***H), 56.9 (***C***H_2CO (arm)), 52.3(N***C***H_2 (ring)), 52.0 (N***C***H_2 (ring)), 51.2 (N***C***H_2 (ring)), 43.2 (***C***H_2C≡CH), 28.37(C(***C***$H_3)_3$), 21.59 ppm.

ES-MS(MeOH): *m/z* 553.4 $[M + H]^+$, 575.4 $[M + Na]^+$; HRMS (ES^+), found (*m/z*): 553.3944 $[M+H^+]$; $C_{29}H_{53}O_6N_4$ requires 553.3960 ($|\Delta$ *m/z*$|$ = 2.81 ppm).

pDO3A:1,4,7-tris(carboxymethyl)-10-(prop-2-ynyl)-1,4,7,10-tetraazacyclododecane (L^1)



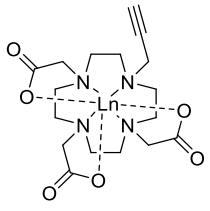
Prepared with minor adaptation from the procedure described by Jauregui *et al.*[3, 4] Propargyl-tBu_3DO3A, **2** (0.50 g, 0.90 mmol) was dissolved in DCM (6.25 mL) and TFA (6.25 mL) was added dropwise and the reaction stirred for 24 hours at room temperature. Extra DCM (~120 mL) was added, and the solvent was removed under reduced pressure; this was repeated with DCM (~120 mL) and then twice with MeOH (~120 mL). The orange residue was dissolved in a minimum amount of MeOH and triturated with diethyl ether, centrifuged and the supernatant was discarded to yield a pale brown solid and repeated. The brown solid was dissolved in minimal MeOH (~8 mL) and precipitated upon addition of DCM (~2 mL), centrifuged and the supernatant discarded to afford the product, $\mathbf{L^1}$ as the colourless trifluoroacetate salt (0.178 g, 0.462 mmol, 64%).

^{1}H NMR (500 MHz, D_2O) δ 3.94 – 3.71 (m, 6H, C***H*₂** arm), 3.62 (s, 2H, C***H*₂**C≡C), 3.51 – 3.25 (m, 8H, C***H*₂** ring), 3.25 – 3.05 (m, 8H, C***H*₂** ring), 2.78 (br. s, 1H, C≡C***H***) ppm.

^{13}C NMR (126 MHz, D_2O) δ 173.1 (br. s, ***C***=O), 171.0 (br. s, ***C***=O), 76.4 (br. s, ***C***≡CH), 55.5 (br. s), 53.8 (br. s), 50.6 (br. s), 50.3 (br. s), 48.9 (br. s), 48.0 (br. s), 43.0 (br. s) ppm.

ES-MS(MeOH): *m/z* 385.2 $[M + H]^+$; HRMS (ES^+), found (*m/z*): 385.2080 $[M+H^+]$; $C_{17}H_{29}O_6N_4$ requires 3585.2082 ($|\Delta\ m/z|$ = 0.48 ppm).

General method for Ln.pDO3A complexes (Ln$\mathbf{L^1}$)



Ln = Eu, Tb

pDO3A, $\mathbf{L^1}$ (1.00 eq.) was dissolved in 3 mL MeOH and the appropriate lanthanide triflate salt added (1.00 eq.). The reaction was stirred at 60 °C for 30 minutes and the pH adjusted to pH 4-5 with 1M NaOH (aq.) and then stirred for a further 48 hours at 60 °C maintaining the solution at pH 5. The solvent was removed under reduced pressure and the solid dissolved in 2 mL water. The pH was adjusted to pH 14 to precipitate out excess lanthanide as lanthanide hydroxide. The solution was centrifuged. The supernatant was kept, and the pH was adjusted to pH 7, before removing the solvent. The complexes were dialysed with Float-a-lyzer with MWCO 500 Da.

(Ln = Eu) From pDO3A (0.1 g, 0.26 mmol, 1.00 eq.) yielded a colourless powder (0.12 g, 0.22 mmol, 86%).

^{1}H NMR (400 MHz, D_2O) δ 25.9, 24.9, 18.5, 17.0, 15.3, -1.5, -5.7, -8.9, -10.0, -11.9, -14.7, -15.8, -18.6 ppm.

ES-MS (MeOH): *m/z* 535.2 $[M+H]^+$, 1067.5 $[2M+ H]^+$; HRMS (ES^+) found 533.1044 $[M+H^+]$; $C_{17}H_{26}O_6N_4Eu$ requires 533.1045 ($|\Delta\ m/z|$ = 0.19 ppm).

Luminescence lifetimes: H_2O: 0.38 ms, D_2O: 1.90 ms, q = 2.2.

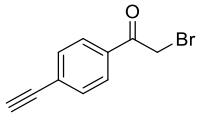
(Ln = Tb) From pDO3A (0.2 g, 0.4 mmol, 1.00 eq.) yielded a colourless powder (0.24 g, 0.45 mmol, 86%)

^{1}H NMR (400 MHz, D_2O) δ 414.6, 241.1, 225.5, 186.3, 82.7, 62.1, 51.5, 34.4, -13.0, -30.0, -45.2, -69.0, -88.1, -115.4, -167.8, -181.7, -344.6, -373.7, -384.7, -410.8 ppm.

ES-MS (MeOH): *m/z* 541.2 $[M+H]^+$; HRMS (ES^+) found 541.1105 $[M+H^+]$; $C_{17}H_{26}O_6N_4{}^{159}Tb$ requires 541.1100 ($|\Delta\ m/z|$ = 0.89 ppm).

Luminescence lifetimes: H_2O: 1.25 ms, D_2O: 2.90 ms, q = 2.0.

2-bromo-1-(4-ethynylphenyl)ethan-1-one/4'-ethynyl-2-bromoacetophenone[5] (3)



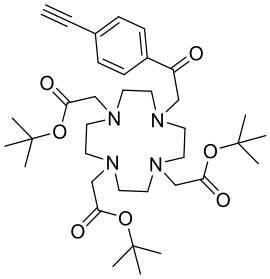
Prepared with minor adaptation from the procedure described by Wu *et al.*[5] 1,4-Diethynylbenzene (2.50 g, 19.8 mmol, 1.00 eq.), 1,3-dibromo-5,5-dimethylhydantoin (6.80 g, 23.8 mmol, 1.20 eq.) and *N,N'*-ethylenethiourea (0.304 g, 2.97 mmol, 0.15 eq.) were dissolved in 75 mL aqueous acetone ($V_{acetone}$:V_{water} = 100:1). The reaction was stirred at 45 °C and monitored by TLC (4-7 hours). Upon completion, the reaction mixture was cooled to room temperature and concentrated under vacuum. The residue was purified by column chromatography on short silica gel (pentane/ethyl acetate, 100:0 to 95:5), followed by a second column (pentane/Et_2O, 95:5 to 88:12) to afford the product **3** as a yellow oil/solid (0.848 g, 3.8 mmol, 19%). R_f = 0.36 (pentane/EtOAc, 9:1).

^{1}H NMR (500 MHz, $CDCl_3$) δ 7.94 (m, 2H, Ar***H***), 7.59 (m, 2H, Ar***H***), 4.43 (s, 2H, C***H***$_2$Br), 3.29 (s, 1H, C≡C***H***) ppm.

^{13}C NMR (126 MHz, $CDCl_3$) δ 190.7 (***C***=O), 133.7 (Ar***C***), 132.6 (2 × Ar***C***), 129.0 (2 × Ar***C***), 128.0 (Ar***C***), 82.6 (***C***≡CH), 81.2 (C≡***C***H), 30.7 (***C***H_2Br) ppm.

GC EI$^+$ MS found 221.96803 $C_{10}H_7BrO$ requires 221.96748 ($|\Delta\ m/z|$ = 9.46 ppm).

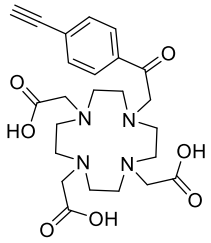
1-(4'-ethynyl-2-acetophenone)-4,7,10-tris(*tert*-butoxycarboxymethyl)-1,4,7,10-tetraazacyclododecane (4)



Triester, **1** (1.54 g, 2.99 mmol, 1.00 eq) was added to dry MeCN (15 mL) with potassium carbonate (1.03 g, 7.47 mmol, 2.50 eq.) and stirred for 30 minutes at room temperature. To this, **3** (0.73 g, 3.29 mmol, 1.10 eq.) in dry MeCN (5 mL) was added dropwise. The reaction was left stirring overnight for 16 hours at 60 °C under a positive pressure of N_2. Inorganic solids were removed by filtration and the solvent was removed under reduced pressure. The resulting residue was purified by column chromatography (DCM/MeOH, 100 % to 9:1 using 1% increments to yield **4** as a light brown crystalline powder (0.78 g, 35%) R_f = 0.1 (DCM/iPrOH, 9:1)

^{1}H NMR (400 MHz, $CDCl_3$) δ 7.85 (m, Ar***H***), 7.54 (m, 2H, Ar***H***), 4.00 (s, 2H, C$\boldsymbol{H_{2\text{-arm}}}$/C$\boldsymbol{H_{2\text{-ring}}}$), 3.72 – 1.79 (m, 23H, C$\boldsymbol{H_{2\text{-arm}}}$/C$\boldsymbol{H_{2\text{-ring}}}$, C≡C***H***), 1.43 (s, 27H, (C$\boldsymbol{H}_3$)$_3$) ppm.
^{13}C NMR (126 MHz, $CDCl_3$) δ 199.2 (***C***=O_{ketone}), 173.2 (2 × ***C***=O_{ester}), 173.0 (***C***=O_{ester}), 135.4 ($\boldsymbol{C}_{aryl}$), 132.5 (2 × ***C***H_{aryl}), 127.7 (2 × ***C***H_{aryl}), 127.6 ($\boldsymbol{C}_{aryl}$), 82.7 (***C***≡CH), 82.1, 82.0, 80.9 (C≡***C***H), 60.5, 56.0, 55.7, 53.6, 52.9, 48.8, 28.3 (**C**H_3), 28.21 (**C**H_3), 28.15 (**C**H_3), 28.0 (**C**H_3), 27.9 (**C**H_3) ppm.
ES-MS(MeOH): *m/z* 657.4 [M+H$^+$] LC-MS (MeOH) *m/z*: 657.09 [M+H$^+$]; HRMS (ES$^+$) found 657.4217 [M+H$^+$]; $C_{36}H_{56}O_7N_4$ requires 657.4222 (|Δ *m/z*| = 0.67 ppm).

1-(4'-ethynyl-2-acetophenone)-4,7,10-tris(carboxymethyl)-1,4,7,10-tetraazacyclododecane triflate salt/·xTFA (L^2)



4 (0.20 g, 0.304 mmol, 1.00 eq.) was dissolved in DCM (2.5 mL) before TFA (2.5 mL) was added dropwise, and the reaction stirred for at least 16 hours at room temperature, completion confirmed by mass spectrometry. Extra DCM was added (~120 mL) and was removed under reduced pressure; this was carried out a further three times with MeOH (~120 mL). The solid was isolated by tritration with minimal MeOH (2 mL) and diethyl ether (~110 mL) and centrifuged. The trituration was

repeated (total twice). The resulting solid was dried under high vacuum to yield the product $\mathbf{L^2}$ as a dark yellow powder (0.134 g, 0.274 mmol, 90%).

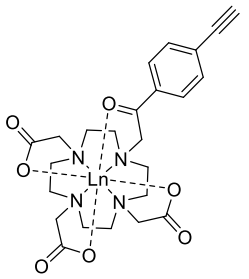
^{1}H NMR (600 MHz, D_2O/CD_3OD (1:1)) δ 7.96 (m, 2H, Ar***H***), 7.62 (m, 2H, Ar***H***), 4.52 (br s, 1H), 3.88 – 3.69 (m, 8H, C$\boldsymbol{H_2}$-arm, C$\boldsymbol{H_2}$-ring, C≡C***H***), 3.59-3.32 (s, 9H, C$\boldsymbol{H_2}$-arm, C$\boldsymbol{H_2}$-ring,), 3.27 – 3.02 (m, 8H, C$\boldsymbol{H_2}$-arm, C$\boldsymbol{H_2}$-ring,) ppm.

^{13}C NMR (151 MHz, D_2O/CD_3OD (1:1)) δ 163.4 (q, $^2J_{C\text{-}F}$ = 35.0 Hz), 133.3 (***C***H_{aryl}), 129.1 (***C***H_{aryl}), 117.6 (q, $^1J_{C\text{-}F}$ = 292.0 Hz), 83.6 (***C***≡***C***H), 82.6 (***C***≡***C***H), 59.3, 57.2, 55.1, 54.3, 52.1 ppm.

^{19}F NMR (565 MHz, D_2O/CD_3OD (1:1)) δ -77.5 ppm.

ES-MS(MeOH): *m/z* 489.3 $[M+H]^+$, 511.3 $[M+Na]^+$ LC-MS (MeOH) *m/z*: 489.0 $[M+H^+]$, 976.9 $[M+2H]^{2+}$; HRMS (ES^+) found 489.2344 $[M+H^+]$; $C_{24}H_{33}O_7N_4$ requires 489.2344 (|Δ *m/z*| = 0.02 ppm).

Lanthanide complexation of 1-(4'-ethynyl-2-acetophenone)-4,7,10-tris(carboxymethyl)-1,4,7,10-tetraazacyclododecane·xTFA (Ln$\mathbf{L^2}$)



Ln = Eu, Tb

To a solution of ligand, $\mathbf{L^2}$ in MeOH the appropriate $Ln(OTf)_3$ was added (1.05 eq.) and the reaction mixture was stirred at 60 °C for 30 minutes. The pH was adjusted to 4 by dropwise addition of an aqueous 1 M NaOH solution. The reaction was then allowed to stir at 60 °C for 48 hours. The MeOH was removed under reduced pressure and the residue suspended in water. The pH of this solution was adjusted to 7 by addition of aqueous 1 M NaOH and the solvent was removed under reduced pressure. The crude was purified by column chromatography on neutral alumina ($MeCN/H_2O$, 8:2 to 7:3) to yield the product as a powder.

(Ln = Eu) From $\mathbf{L^2}$ (0.10 g, 0.21 mmol, 1.00 eq.) yielded a pale beige-pink powder (0.040 g, 0.063 mmol, 31%). R_f = 0.13 ($MeCN/H_2O$, 7:3)

^{1}H NMR (400 MHz, MeOD) δ 40.3, 31.4, 29.8, 27.7, 23.7, 16.2, 15.4, 14.4, 10.2, 0.1, -0.9, -1.0, -2.3, -3.3, -4.3, -5.3, -6.2, -6.4, -8.1, -9.2, -10.6, -11.8, -12.9, -14.5, -15.1, -15.6, -17.5, -19.5, -20.3, -21.3 ppm. Only major resolved peaks outside the +10 to 0 ppm range are reported.

ES-MS (MeOH): *m/z* 639.2 $[M+H]^+$, 661.2 $[M+ Na]^+$; LC-MS (MeOH) *m/z*: 638.7 $[M+H^+]$; HRMS (ES^+), found (*m/z*): 637.1305 $[M-H]^+$; $C_{24}H_{30}N_4O_7Eu$ requires 637.1307 (|Δ *m/z*| = 0.40 ppm).

UV-Vis (H_2O): λ_{max} 291 nm.

Luminescence lifetimes: H_2O: 0.59 ms, D_2O: 2.19 ms, q = 1.2.

(Ln = Tb) From **L²** (0.15 g, 0.31 mmol, 1.00 eq.) yielded a pale beige-pink powder (0.108 g, 0.17 mmol, 79%). R_f = 0.13 (MeCN/H_2O, 7:3)

^{1}H NMR (400 MHz, MeOD) δ 354.9, 316.5, 291.3, 264.8, 228.3, 215.9, 164.6, 154.7, 106.0, 93.5, 23.9, 17.5, -10.9, -13.2, -24.6, -26.3, -31.4, -36.4, -48.9, -51.0, -58.5, -78.3, -101.8, -105.5, -125.7, -133.5, -157.8, -180.1, -213.8, -241.9, -249.3, -256.3, -352.2, -360.3, -477.3 ppm. Only major resolved peaks outside the +10 to -10 ppm range are reported.

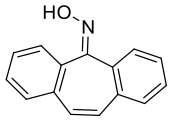
^{19}F NMR (377 MHz, MeOD) δ -77.7, -82.0 ppm.

ES-MS (MeOH) *m/z* 645.2 $[M+H]^+$, 667.2 $[M+Na]^+$; LC-MS (MeOH) *m/z*: 645.736 $[M+H^+]$; HRMS (ES^+), found (*m/z*): 645.1359 $[M+H]^+$; $C_{24}H_{30}N_4O_7{}^{159}Tb$ requires 645.1362 ($|\Delta\ m/z|$ = 0.51 ppm).

UV-Vis (H_2O): λ_{max} 292 nm.

Luminescence lifetimes: H_2O: 1.42 ms, D_2O: 2.27 ms, q = 1.0.

5*H*-dibenzo[*a,d*]cycloheptene-5-one oxime[6] (5)



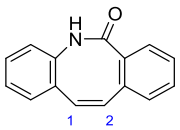
Prepared according to a procedure by Chadwick *et al.*[6] To a round-bottomed flask, 5-dibenzosuberenone (12.0 g, 58.2 mmol, 1.00 eq.), hydroxylamine hydrochloride (5.41 g, 77.9 mmol, 1.34 eq.), pyridine (18.6 mL) and ethanol (86 mL) was added, and the reaction mixture was heated under reflux for 22 hours. A further portion of hydroxylamine hydrochloride (1.01 g, 14.5 mmol, 0.25 eq.) was added to the reaction mixture and stirred for 16 hours. The reaction was cooled and diluted with DCM (70 mL) and washed with 1 M HCl (50 mL × 3) and brine (50 mL × 1). The organic layer was dried over Na_2SO_4, filtered and the solvent was removed *in vacuo*. The crude product was purified by column chromatography (100 DCM → 98 DCM: 2 MeOH) to yield the product, **5** as a pale beige powder (11.97 g, 93%). R_f = 0.21 (98 DCM/2 MeOH).

^{1}H NMR (600 MHz, $CDCl_3$) δ 8.54 (s, 1H, O***H***), 7.67 (dd, $^3J_{H\text{-}H}$ = 7.5, $^4J_{H\text{-}H}$ = 1.6 Hz, 1H, Ar***H***), 7.61 – 7.57 (m, 1H, Ar***H***), 7.46 – 7.34 (m, 6H), 6.92 (overlapping d, $^3J_{H\text{-}H}$ = 12.0 Hz, 2H, $\boldsymbol{H}_{7\text{-ring}}$) ppm. The ^{1}H NMR data corresponds to reported literature values.[6]

^{13}C NMR (151 MHz, $CDCl_3$) δ 156.9 (***C***≡N), 135.5 ($\boldsymbol{C}_{7\text{-ring}}$), 134.6 ($\boldsymbol{C}_{7\text{-ring}}$), 133.8, 130.8, 130.7, 130.6, 129.5, 129.2, 129.1, 129.0, 128.9, 127.9, 127.7 ppm.

ES-MS (MeOH): *m/z* 222.0 $[M+H]^+$.

Dibenzo[*b,f*][azocine-6(5*H*)-one[6, 7] (6)



Method 1:

Prepared according to a procedure by Cruchter *et al.*[7] Polyphosphoric acid (156 mL) was added to a 250 mL flask with a strong magnetic stir bar. The polyphosphoric acid was heated to 125 °C and 5H-dibenzo[*a,d*]cycloheptene-5-one oxime, **5** (10.0 g, 45.2 mmol, 1.00 eq.) was gradually added and stirred into the highly viscous polyphosphoric acid with a spatula. The resulting mixture was stirred at 125 °C for 1 hour, to obtain a viscous solution. The mixture was left to cool to ~50-60 °C and then slowly poured into ice water (~ 400 mL) and stirred for a further 30 minutes, where a grey suspension was obtained. The grey precipitate was filtered and dried *in vacuo* to obtain the crude product, **6** as a fine grey powder (8.05 g, 81%).

^{1}H NMR (400MHz, $CDCl_3$): δ 7.56 (br s, 1H, N***H***), 7.45 (dd, $^3J_{H\text{-}H}$ = 7.6, $^4J_{H\text{-}H}$ = 1.5 Hz, 1H, Ar***H***), 7.28 (td, $^3J_{H\text{-}H}$ = 7.5, $^4J_{H\text{-}H}$ = 1.6 Hz, 1H, Ar***H***), 7.09-7.25 (m, 5H, Ar***H***), 7.03 (m, 1H, Ar***H***), 6.94 (d, $^3J_{H\text{-}H}$ = 11.6 Hz, 1H, ***H1***), 6.82 (d, $^3J_{H\text{-}H}$ = 11.6 Hz, 1H, ***H2***) ppm.

ES-MS (MeOH) found *m/z* 222.0 for $[M+H]^+$ and 244.0 for $[M+Na]^+$.

Method 2:

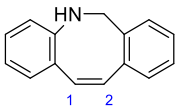
Prepared according to a procedure by Chadwick *et al.*[6] with minor modifications. To a flame dried flask, 5H-dibenzo[*a,d*]cycloheptene-5-one oxime, **5** (4.0 g, 18.1 mmol) was added and flushed with Ar. Eaton's reagent (ca. 7.5 wt % P_2O_5 in methanesulfonic acid) was added (24 mL) and the reaction stirred at 100 °C. After 30 min, a TLC (95 DCM: 5 MeOH) showed complete conversion. The reaction was quenched with H_2O (100 mL). The product was collected by extraction with multiple volumes of hot EtOAc (3 × ~ 350 mL). The organic layers were combined and concentrated to ca. 10 mL and allowed to cool to room temperature. The concentrated mixture was centrifuged, and the supernatant was discarded. Another portion of EtOAc (10 mL) was added and sonicated, and the mixture was centrifuged, and the supernatant was discarded. The precipitate was sonicated with ca. 4 mL MeOH, before addition of Et_2O (100 mL) and centrifuged. The supernatant was discarded, and the precipitate was dried under vacuum to yield a beige powder (3.73 g, 93%).

^{1}H NMR (400 MHz, $CDCl_3$) δ 7.53 (br s, 1H, N***H***), 7.47 (dd, $^3J_{H\text{-}H}$ = 7.6 Hz, $^4J_{H\text{-}H}$ = 1.6 Hz, 1H, Ar***H***), 7.31 (td, $^3J_{H\text{-}H}$ = 7.5 Hz, $^4J_{H\text{-}H}$ = 1.6 Hz, 1H, Ar***H***), 7.28 – 7.11 (m, 5H, Ar***H***), 7.05 (dt, $^3J_{H\text{-}H}$ = 7.7 Hz, $^4J_{H\text{-}H}$ = 0.6 Hz, 2H), 6.96 (d, $^3J_{H\text{-}H}$ = 11.7 Hz, 1H, ***H1***), 6.85 (d, $^3J_{H\text{-}H}$ = 11.8 Hz, 1H, ***H2***) ppm.

The ^{1}H NMR data corresponds to reported literature values.[8]

ES-MS (MeOH): *m/z* 222.0 $[M+H]^+$ and 244.0 $[M+Na]^+$.

5,6-dihydrodibenzo[*b,f*]azocine[7] (7)



Prepared according to a procedure by Cruchter *et al*.[7] Under inert conditions, dibenzo[*b,f*]azocin-6(5*H*)-one, **6** (3.90 g, 17.6 mmol, 1.00 eq.) was dissolved in anhydrous diethyl ether (~200 mL) and $LiAlH_4$ (8.14 g, 39.5 mmol, 2.24 eq.) was added to a flame dried flask and the reaction mixture was heated under reflux for 45 hours under Ar (completion confirmed by TLC). The reaction mixture was cooled to 0 °C before ice-cold water was carefully added (~300 mL) and stirred for 30 minutes to ensure the $LiAlH_4$ was completely quenched. The reaction mixture was filtered, and the organic layer of the filtrate was separated, and the aqueous layer was extracted with Et_2O (3 × 100 mL). The filter cake was crushed and vigorously stirred in Et_2O (~100 mL) for 15 minutes, then filtered and the filtrate was separated, this was carried out three times. All organic layers were combined dried over $MgSO_4$, filtered, and reduced *in vacuo*. The crude product was purified by flash chromatography (pentane/EtOAc 2:1). After drying the product, **7** was obtained as a bright greenish yellow solid (3.27 g, 15.8 mmol, 89%) R_f = 0.82 (pentane/EtOAc, 2:1).

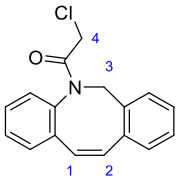
^{1}H NMR (400 MHz, $CDCl_3$) δ 7.28 – 7.23 (m, 1H, Ar***H***), 7.23 – 7.14 (m, 3H, Ar***H***), 6.98 (dd, $^3J_{H\text{-}H}$ = 7.8 Hz, $^4J_{H\text{-}H}$ = 1.6 Hz, 1H, Ar***H***), 6.93-6.85 (m, 1H Ar***H***), 6.65–6.58 (m, 1H, Ar***H***), 6.55 (d, $^3J_{H\text{-}H}$ = 13.1 Hz, 1H, ***H2***), 6.49 (dd, $^3J_{H\text{-}H}$ = 8.1 Hz, $^4J_{H\text{-}H}$ = 1.2 Hz, 1H, Ar***H***), 6.37 (d, $^3J_{H\text{-}H}$ = 13.1 Hz, 1H, ***H1***), 4.59 (s, 2H, C***H***$_2$NH) ppm. NH peak not observed.

^{13}C NMR (101 MHz, $CDCl_3$) δ 147.0, 139.4, 138.2, 134.8, 132.9, 130.3, 129.0, 128.1, 127.8, 127.6, 127.5, 122.0, 118.1, 118.0, 49.7 (s, 2H, ***C***H_2NH) ppm.

The ^{1}H and ^{13}C NMR data corresponds to reported literature values.[7]

ES-MS (MeOH): *m/z* 208.0 $[M+H]^+$.

(Z)-2-chloro-1-(dibenzo[*b,f*]azocin-5(6H)-yl)ethan-1-one (8)

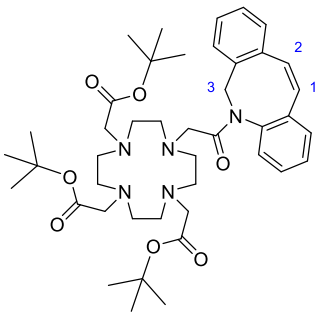


To 5,6-dihydrodibenzo[b,f]azocine (1.86 g, 9.0 mmol, 1.00 eq.) in dichloromethane (90 mL), $CsCO_3$ (7.03 g, 21.5 mmol, 2.40 eq.) was added. The reaction mixture was cooled to 0 °C and chloroacetyl chloride (0.86 mL, 10.8 mmol, 1.20 eq.) was added dropwise and the solution warmed to room temperature and stirred overnight. The solution was filtered, and the filtrate washed with deionised water (3 × 100 mL) and the aqueous layer washed with DCM (100 mL), the organic layers were

dried with $MgSO_4$, filtered and the solvent removed under reduced pressure to yield a viscous brown oil, **8** (2.40 g, 93%).

^{1}H NMR (400 MHz, acetone-d_6) δ 7.44 (m, 1H, Ar***H***), 7.35 (s, 3H, Ar***H***), 7.30 (d, $^3J_{H\text{-}H}$ = 7.2 Hz, 1H, Ar***H***), 7.22-7.12 (m, 3H, Ar***H***), 6.87 (d, $^3J_{H\text{-}H}$ = 12.9 Hz, 1H, ***H1***), 6.74 (d, $^3J_{H\text{-}H}$ = 12.8 Hz, 1H, ***H2***), 5.43 (d, $^2J_{H\text{-}H}$ = 15.1 Hz, 1H, ***H3***), 4.32 (d, $^2J_{H\text{-}H}$ = 15.2 Hz, 1H, ***H3***), 3.85 (d, $^2J_{H\text{-}H}$ = 13.4 Hz, 1H, ***H4***), 3.73 (d, $^2J_{H\text{-}H}$ = 13.4 Hz, 1H, ***H4***) ppm.
ES-MS (MeOH) found *m/z* 306 for $[M+Na]^+$.

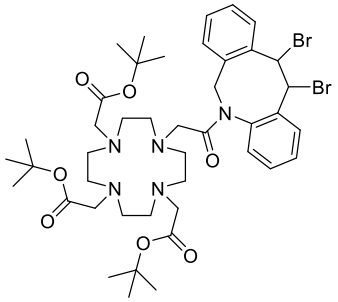
tri-*tert*-butyl 2,2',2''-(10-(2-(dibenzo[*b*,*f*]azocin-5(6*H*)-yl)-2-oxoethyl)-1,4,7,10-tetraazacyclododecane-1,4,7-triyl)(*Z*)-triacetate (9)



Triester **1** (2.70 g, 5.25 mmol, 1.00 eq.), **8** (2.23 g, 7.87 mmol, 1.50 eq.) and potassium carbonate (5.65 g, 40.9 mmol, 7.80 eq.) in acetonitrile (70 mL) were heated under reflux for 48 hours. The solvent was removed under reduced pressure and the residue was dissolved in DCM, filtered and the solvent was removed under reduced pressure to give a brown solid. The residue was purified by column chromatography (DCM/MeOH, 9:1) to yield the product as a golden oil (0.84 g, 21%). R_f = 0.43 (DCM/MeOH, 9:1).

^{1}H NMR (400 MHz, $CDCl_3$) δ 7.41 – 7.12 (m, 7H, Ar***H***), 7.04 (br s, 1H, Ar***H***), 6.79 (d, $^3J_{H\text{-}H}$ = 13.6 Hz, 1H, ***H1/H2***), 6.59 (d, $^3J_{H\text{-}H}$ = 13.3 Hz, 1H, H, ***H1/H2***), 5.41 (d, $^2J_{H\text{-}H}$ = 15.1 Hz, 1H, ***H3***), 4.16 (d, $^2J_{H\text{-}H}$ = 14.9 Hz, 1H, ***H3***), 3.51-1.66 (m, 24H, C***H***$_{2\text{-}arm}$/C***H***$_{2\text{-}ring}$), 1.56 (s, 9H, 1 × (C***H***$_3$)$_3$), 1.47 (s, 18H, 2 ×(C***H***$_3$)$_3$) ppm.
ES-MS (MeOH): *m/z* 762.4 for $[M+H]^+$; 784.4 for $[M+Na]^+$.

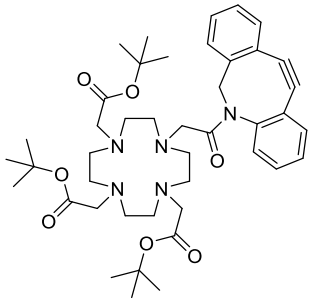
Tri-*tert*-butyl 2,2',2''-(10-(2-(11,12-dibromo-11,12-dihydrodibenzo[*b,f*]azocin-5(6*H*)-yl)-2-oxoethyl)-1,4,7,10-tetraazacyclododecane-1,4,7-triyl)triacetate (10)



9 (1.90 g, 2.50 mmol, 1.00 eq.) and pyridinium tribromide (0.88 g, 2.75 mmol, 1.10 eq.) were dissolved in DCM (10 mL) and stirred at room temperature for 18 hours. The solution was diluted with DCM (15 mL), washed with 5 % aqueous HCl (3 × 20 mL), and the aqueous layer washed with DCM (3 × 20 mL). The organic layers were combined and dried over $MgSO_4$, filtered, and the solvent removed under reduced pressure to yield an orange-brown crystalline solid. (2.16 g, 94%)

ES-MS (MeOH): 922 for $[M+H]^+$; 944 for $[M+Na]^+$.

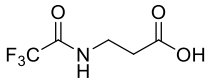
Tri-*tert*-butyl 2, 2', 2''-(10-(2-(didehydrodibenzo[*b,f*]azocin-5(6*H*)-yl)-2-oxoethyl)-1,4,7,10-tetraazacyclododecane-1,4,7-triyl)(*Z*)-triacetate (11)



10 (0.50 g, 0.54 mmol, 1.00 eq.) was dissolved in anhydrous THF (8 mL) and cooled to 0 °C. A 1 M solution of potassium *t*-butoxide in THF (1.65 mL, 1.65 mmol, 3.00 eq.) was added dropwise and the solution was warmed to room temperature and stirred for 45 hours under N_2. A further portion of potassium *t*-butoxide solution (0.85 mL, 0.85 mmol, 1.60 eq.) was added dropwise and the mixture was heated to 45 °C and stirred for a further 24 hours. The reaction mixture was then diluted with EtOAC (15 mL), washed with 5% HCl (3 × 20 mL) and brine (3 × 25 mL). The organic layer was dried over Na_2SO_4, filtered, and the solvent removed *in vacuo* to yield the crude as a reddy brown solid (0.12 g, 29%).

ES-MS (MeOH): 760.4 $[M+H]^+$, 784.4 $[M+H+Na]^{2+}$.

N-Trifluoroacetyl-*β*-alanine[9] (12)



Prepared according to a procedure by Naturale *et al*.[9] In a flame dried flask, triethylamine (5.48 mL, 39.3 mmol, 1.00 eq.) was added to 4-aminopropanoic acid/ β-alanine (3.5 g, 39.3 mmol, 1.00 eq.) in anhydrous MeOH (25 mL). After 5 minutes, ethyl trifluoroacetate (5.84 mL, 49.0 mmol, 1.25 eq.) was added dropwise and the reaction was allowed to stir for 24 hours under N_2. The mixture was concentrated under reduced pressure, co-evaporating with EtOH (50 mL × 3). The residue was dissolved in H_2O (ca. 75 mL) and acidified to pH 2/3 with concentrated HCl. After stirring for 30 minutes, the mixture was extracted with ethyl acetate (75 mL × 3) and the combined organic layer was washed with brine (150 mL), dried over $MgSO_4$, filtered, and concentrated by rotary evaporation to yield a white crystalline solid (6.35 g, 87%).

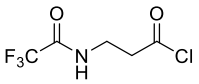
^{1}H NMR (600 MHz, MeOD) δ 4.85 (s, 1H, CON***H***), 3.53 (t, $^3J_{H\text{-}H}$ = 6.9 Hz, 2H, NHC***H*₂**), 2.58 (t, $^3J_{H\text{-}H}$ = 6.9 Hz, 2H, C***H*₂**COOH) ppm.

^{13}C NMR (151 MHz, MeOD) δ 174.6 (***C***OOH), 159.0 (***C***ON, q, $^2J_{F\text{-}C}$ = 36.9 Hz), 117.5 (***C***F_3, q, $^1J_{F\text{-}C}$ = 286.5 Hz), 36.8 (***C***H_2), 33.8 (***C***H_2) ppm.

^{19}F NMR (377 MHz, MeOD) δ -77.5 (C***F***$_3$) ppm.

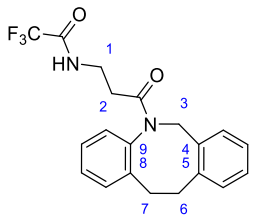
ES-MS (MeOH): *m/z* 184.0 $[M\text{-}H]^-$. HRMS(ES^-) found (m/z): 184.0215 $[M\text{-}H]^-$; $C_5H_5O_3NF_3$ requires 184.0227 ($|\Delta m/z|$ = 6.32 ppm).

N-trifluoroacetyl-*β*-alanyl chloride[10] (13)



Prepared according to a procedure by Cherevin *et al*.[10] with minor modifications. *N*-trifluoroacetyl-*β*-alanine, **12** (3.00 g, 16.2 mmol, 1.00 eq.) was added to a flame-dried flask and dissolved in thionyl chloride (40.2 mL, 0.55 mol, ~32.0 eq.). The solution was heated to reflux for 5 hours under Ar. The solvent was removed under reduced pressure, and then dried under high vacuum for at least 30 minutes before using immediately in the next reaction without characterisation. The acid chloride was a pale-yellow oil (3.17 g, 96%).

_N_-(6-dibenzo[b,f]azocin-5(6H)-yl)-6-oxopropyl)trifluoroacetamide[11] (14)



Prepared according to a procedure by Kuzmin *et al.*[11] with minor modifications. *N*-trifluoroacetyl-β-alanyl chloride, **13** (3.30 g, 16.2 mmol, 1.25 eq.) was added to a solution of 5,6-dihydrodibenzo[*b*,*f*]azocine, **7** (2.69 g, 13.0 mmol, 1.00 eq.) and pyridine (3.15 mL, 38.9 mmol, 3.00 eq.) in CH_2Cl_2 (40 mL) at room temperature and stirred overnight under Ar. The reaction mixture was diluted with CH_2Cl_2 (140 mL), washed with water (2 × 200 mL), and dried over anhydrous $MgSO_4$, filtered and the solvent was removed under reduced pressure. The residue was purified by column chromatography (7:3 pentane: EtOAc to 6:4 gradient) to provide the product as a yellowish oil/solid (4.33 g, 89%). R_f = 0.50 (pentane/EtOAc, 2:3).

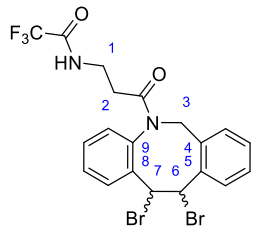
^{1}H NMR (600 MHz, $CDCl_3$) δ 7.37 (s, 1H, N***H***), 7.33 – 7.24 (m, 4H, Ar***H***), 7.22 – 7.13 (m, 4H, Ar***H***), 6.80 (d, $^3J_{H\text{-}H}$ = 12.9 Hz, 1H, ***H6*** or ***H7***), 6.58 (d, $^3J_{H\text{-}H}$ = 12.9 Hz, 1H, , ***H6*** or ***H7***), 5.55 (d, $^2J_{H\text{-}H}$ = 15.2 Hz, 1H, ***H3***), 4.30 (d, $^2J_{H\text{-}H}$ = 15.2 Hz, 1H, ***H3***), 3.55 – 3.43 (m, 2H, ***H1***), 2.29 (ddd, $^2J_{H\text{-}H}$ = 17.2 Hz, $^3J_{H\text{-}H}$ = 7.4, 3.7 Hz, 1H, ***H2***), 2.03 (ddd, $^2J_{H\text{-}H}$ = 17.2 Hz, $^3J_{H\text{-}H}$ = 7.8, 3.6 Hz, 1H, ***H2***) ppm.

^{13}C NMR (151 MHz, $CDCl_3$) δ 171.1 (***C***=O), 157.1 (q, $^2J_{C\text{-}F}$ = 37.0 Hz, ***C***OCF_3), 140.0 (***C4/5/8/9***), 136.4 (***C4/5/8/9***), 135.6 (***C4/5/8/9***), 134.2(***C4/5/8/9***), 133.0 (***C6*** or C***7***), 132.3 (Ar***C***), 131.2 (Ar***C***), 130.1 (Ar***C***), 129.0 (Ar***C***), 128.7 (Ar***C***), 128.0 (Ar***C***), 127.7 (Ar***C***), 127.3 (Ar***C***), 127.0 (***C6*** or C***7***), 116.0 (q, $^1J_{C\text{-}F}$ = 287.7 Hz, ***C***F_3), 54.6 (***C3***), 35.7 (***C1***), 33.7 (***C2***) ppm.

^{19}F NMR (561 MHz, $CDCl_3$) δ -76.1 (C***F***$_3$CONH) ppm.

ES-MS (MeOH): *m/z* 375.2 $[M+H]^+$, 397.1 $[M+Na]^+$; HRMS (ES^+): found (m/z) 375.1314 $[M+H]^+$ $C_{20}H_{18}O_2N_2F_3$ requires 375.1315 ($\left|\Delta m/z\right|$ = 0.13 ppm).

_N_-(trifluoroacetamidopropanoyl)-5,6,11,12-tetrahydro-11,12-dibromodibenzo[*b,f*]azocine[11] (15)



Prepared according to a procedure by Kuzmin *et al.*[11] with minor modifications. Pyridinium tribromide (3.76 g, 11.8 mmol, 1.10 eq.) was added to a solution of **14** (4.00 g, 10.7 mmol, 1.00 eq.) in DCM (16 mL) at room temperature, and the reaction mixture was stirred for 48 hours. The reaction mixture was diluted with DCM (80 mL), washed with 5% aqueous HCl (80 mL), dried over $MgSO_4$, and solvent removed under vacuum. The residue was purified under a short silica column (100% DCM) to give as the desired as a pale khaki green solid (4.66 g, 82%). R_f = 0.16 (100% DCM).

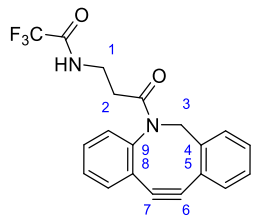
^{1}H NMR (600 MHz, $CDCl_3$) δ 7.73 (d, *J* = 7.8 Hz, 1H, Ar-***H***), 7.60 (s, 1H, N***H***), 7.24 (dd, *J* = 7.7, 1.5 Hz, 1H, Ar-***H***), 7.21 (t, *J* = 7.6 Hz, 1H, Ar-***H***), 7.17 (td, *J* = 7.6, 1.3 Hz, 1H, Ar-***H***), 7.06 (tdd, *J* = 7.7, 4.1, 2.0 Hz, 2H, Ar-***H***), 6.99 – 6.88 (m, 2H, Ar-***H***), 5.89 – 5.78 (overlapping d, $^2J_{H\text{-}H}$ = 14.8 Hz, $^3J_{H\text{-}H}$ = 9.8 Hz, 2H, ***H3*** and ***H6*** or ***H7***), 5.16 (d, $^3J_{H\text{-}H}$ = 9.9 Hz, 1H, ***H6*** or ***H7***), 4.20 (d, $^2J_{H\text{-}H}$ = 14.8 Hz, 1H, ***H3***), 3.68 (m, 1H, ***H1***), 3.56 (m, 1H, ***H1***), 2.65 (ddd, *J* = 17.3, 6.9, 3.4 Hz, 1H, ***H2***), 2.38 (ddd, *J* = 17.3, 8.5, 3.7 Hz, 1H, ***H2***) ppm.

^{13}C NMR (151 MHz, $CDCl_3$) δ 172.2 (***C***=O), 157.2 (q, $^2J_{C\text{-}F}$ = 36.8 Hz, ***C***OCF_3), 138.2 (***C4/5/8/9***), 137.2 (***C4/5/8/9***), 136.3 (***C4/5/8/9***), 132.3 (***C4/5/8/9***), 131.2 (Ar***C***), 130.9 (Ar***C***), 130.5 (Ar***C***), 130.1 (Ar***C***), 129.9 (Ar***C***), 129.3 (Ar***C***), 129.3 (Ar***C***), 128.8 (Ar***C***), 116.0 (q, $^1J_{C\text{-}F}$ = 287.7 Hz, ***C***F_3), 60.1 (***C6/7***), 55.5 (***C6/7***), 52.5 (***C3***), 35.8 (***C1***), 34.9 (***C2***) ppm.

^{19}F NMR (561 MHz, $CDCl_3$) δ -76.0 (C***F***$_3$CONH) ppm.

ES-MS (MeOH): *m/z* 535.1 $[M+H]^+$, 557.1 $[M+Na]^+$; LC-MS(ES+): 534.601 $[M+H]^+$. HRMS (ES+): *m/z* found 543.9656 $[M+H]^+$ $C_{20}H_{18}O_2N_2Br_2F_3$ requires 534.9662 ($|\Delta m/z| = 0.39$ ppm).

_N_-(3-trifluoroacetamidopropanoyl)-5,6-dihydro-11,12-didehydrodibenzo[*b,f*]azocine[11] (16)

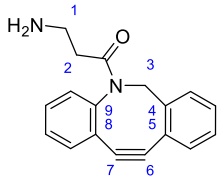


Prepared according to a procedure by Kuzmin *et al.*[11] with minor modifications. A solution of **15** (1.2 g, 2.08 mmol, 1.00 eq.) in THF was added to a solution of potassium *t*-butoxide (0.584 g,

5.21 mmol, 2.50 eq.) in THF (10 mL) at room temperature; the reaction mixture was stirred for 2 hours before a further portion of potassium t-butoxide was added (0.292 g, 0.261 mmol, 1.25 eq.) and allowed to react for 2 hours. Once finished it was diluted with EtOAc (20 mL), washed with 5 % aqueous HCl and brine, then dried over $MgSO_4$, and the solvent was removed under reduced pressure. The crude product was purified by chromatography (hexanes/ethyl acetate, 2:1 to 1:1) to afford 0.76 g (1.83 mmol, 88%) of **16** as a pale yellow/cream powder.

^{1}H NMR (600 MHz, $CDCl_3$) δ 7.67 (d, $^3J_{H\text{-}H}$ = 7.6 Hz, 1H, Ar***H***), 7.45 – 7.36 (m, 4H, Ar***H***), 7.36 – 7.27 (m, 3H, Ar***H***), 7.12 (s, 1H, N***H***), 5.15 (d, $^2J_{H\text{-}H}$ = 14.0 Hz, 1H, ***H3***), 3.73 (d, $^2J_{H\text{-}H}$ = 14.0 Hz, 1H, ***H3***), 3.56 – 3.46 (m, 1H, ***H1***), 3.32 – 3.24 (m, 1H, ***H1***), 2.53 (ddd, *J* = 17.1, 8.5, 3.8 Hz, 1H, ***H2***), 1.98 (ddd, *J* = 17.1, 6.9, 3.3 Hz, 1H, ***H2***) ppm.
^{13}C NMR (151 MHz, $CDCl_3$) δ 171.8 (***C***=O), 157.1 (q, $^2J_{C\text{-}F}$ = 37.0 Hz, ***C***OCF_3), 150.8 (***C4/5/8/9***), 147.8 (***C4/5/8/9***), 132.1 (Ar***C***), 129.1 (Ar***C***), 128.9 (Ar***C***), 128.8 (Ar***C***), 128.5 (Ar***C***), 128.1 (Ar***C***), 127.5 (Ar***C***), 125.9 (Ar***C***), 122.91 (***C4/5/8/9***), 122.89 (***C4/5/8/9***), 115.9 (q, $^1J_{C\text{-}F}$ = 287.8 Hz, ***C***F_3), 115.2 (***C6*** or C***7***), 107.5 (***C6*** or C***7***), 55.8 (***C3***), 35.8 (***C1***), 34.1 (***C2***) ppm.
^{19}F NMR (377 MHz, $CDCl_3$) δ -76.1 (C***F***$_3$CONH) ppm.
ES-MS (MeOH): *m/z* 373.0 $[M+H]^+$, 395.0 $[M+Na]^+$; HRMS (ES+): found (*m/z*) 373.1152 $[M+H]^+$ $C_{20}H_{16}O_2N_2F_3$ requires 373.1158 ($|\Delta m/z|$ = 1.62 ppm).

N-(3-aminopropyl-5,6-dihydro-11,12-didehydrodibenzo[*b*,*f*]azocine[11] (17)



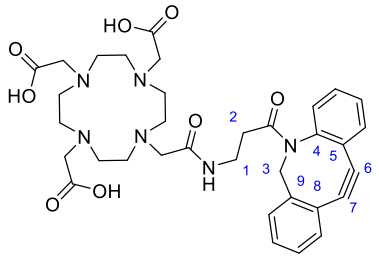
Prepared according to a procedure by Kuzmin *et al.*[11] with minor modifications. A solution of K_2CO_3 (0.148 g, 1.07 mmol, 2.00 eq.) in H_2O (0.7 mL) was added to a solution of **16** (0.20 g, 0.54 mmol, 1.00 eq.) dissolved in MeOH (2.3 mL) and stirred at room temperature followed by TLC (CH_2Cl_2/MeOH 11:4 stained with ninhydrin) for 3 hours. The reaction was stirred at 40 °C for a further hour. The solvents were removed *in vacuo* and the residue was dissolved in 16 mL EtOAc and 4 mL DCM and washed with water (2 × 20 mL) and brine (20 mL), then dried over Na_2SO_4, filtered and the solvent was removed under reduced pressure. The crude product was purified by column chromatography (CH_2Cl_2/MeOH 9:1), (CH_2Cl_2/MeOH/MeCN, 7:2:1) and (CH_2Cl_2/toluene/MeOH/MeCN, 4:3:2:1) to afford 0.041 g (0.147 mmol, 27%) as a yellow powder. R_f = 0.05 (CH_2Cl_2/toluene/MeOH/MeCN, 4:3:2:1).

^{1}H NMR (400 MHz, $CDCl_3$) δ 7.69 (d, $^3J_{H\text{-}H}$ = 7.5 Hz, 1H, Ar***H***), 7.43 – 7.33 (m, 5H, Ar***H***), 7.30 (td, $^3J_{H\text{-}H}$ = 7.4 Hz, $^4J_{H\text{-}H}$ = 1.3 Hz, 1H, Ar***H***), 7.28 – 7.23 (m, 1H, Ar***H***), 5.16 (d, $^2J_{H\text{-}H}$ = 13.8 Hz, 1H,

H3), 3.67 (d, $^{2}J_{H\text{-}H}$ = 13.8 Hz, 1H, ***H3***), 2.84 – 2.68 (m, 2H, ***H1***), 2.41 (ddd, $^{2}J_{H\text{-}H}$ = 15.9 Hz, $^{3}J_{H\text{-}H}$ = 6.9, 5.6 Hz, 1H, ***H2***), 1.97 (dt, $^{2}J_{H\text{-}H}$ = 15.9 Hz, $^{3}J_{H\text{-}H}$ = 6.1 Hz, 1H, ***H2***) ppm. ^{1}H NMR data corresponds to reported literature values.[11]

ES-MS (MeOH): *m/z* 277.1 $[M+H]^{+}$, 295.1 $[M+Na]^{+}$; HRMS (ES+): found (m/z) 277.1333 $[M+H]^{+}$ $C_{18}H_{17}ON_2$ requires 277.1335 ($|\Delta m/z| = 0.97$ ppm).

DOTA-dibenzocyclooctyne (DBCO)/ 1,4,7,10-Tetraazacyclododecane-1,4,7-tris(acetic acid)-10-[3-oxo-3-(5-azadibenzocyclootyne)acetamide][12, 13] (L^4)



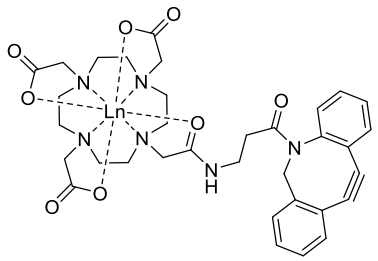
Prepared with minor adaptation from the procedure described by Zeng *et al.*[12] and Liang *et al.* [13] DBCO-amine (40.0 mg, 144 µmol, 1.00 eq.), trimethylamine (224 µL, 1.6 mmol, ~11.0 eq.) and dry DMF (8 mL) were added to a flame-dried flask and stirred for 10 minutes. DOTA-NHS ester (140 mg, 184 µmol, 1.27 eq.) was added and stirred at room temperature overnight. Water (4 mL) was added to the reaction mixture to hydrolyse excess DOTA-NHS ester. The solvents were removed *in vacuo* to yield a pale yellow transparent oil. The residue was dissolved in 3.5 mL (8 H_2O: 2 MeCN) and purified by preparative HPLC (A.1 HPLC conditions method 1). UV-directed fraction collection λ = 220 nm. t_R(prep) = 4.1 mins. Solvent was removed *in vacuo* to yield the product as an off-white solid (66 mg, 69%).

^{1}H NMR (600 MHz, 8 D_2O: 2 CD_3CN) δ 8.56 (br. s/m, 1H, N***H***), 8.00 (d, $^{3}J_{H\text{-}H}$ = 7.5 Hz, 1H, Ar***H***), 7.86-7.71 (m, 6H, Ar***H***), 7.68 (d, $^{3}J_{H\text{-}H}$ = 7.5 Hz, 1H, Ar***H***), 5.42 (d, $^{2}J_{H\text{-}H}$ = 14.2 Hz, 1H, ***H3***), 4.13-3.92 (overlapping d/m, 5H, ***H3***, C$\boldsymbol{H_2}$-arm/C$\boldsymbol{H_2}$-ring), 3.85 (s, 2H), 3.77 – 3.19 (m, 20H, C$\boldsymbol{H_2}$-arm/C$\boldsymbol{H_2}$-ring,, 2 × ***H1***), 2.77 (dt, $^{2}J_{H\text{-}H}$ = 16.0 Hz, $^{3}J_{H\text{-}H}$ = 6.2 Hz, 1H, ***H2***), 2.44 (dt, $^{2}J_{H\text{-}H}$ = 15.9 Hz, $^{3}J_{H\text{-}H}$ = 7.2 Hz, 1H, ***H2***) ppm.

^{13}C NMR (151 MHz, 8 D_2O: 2 CD_3CN) δ 172.3 (***C***OOH), 165.3 (***C***OOH), 150.1 (***C***ON), 147.3 (***C***ON), 131.5 (Ar***C***), 128.71 (Ar***C***), 128.69 (Ar***C***), 128.3 (Ar***C***), 128.0 (Ar***C***), 127.6 (Ar***C***), 126.4 (Ar***C***), 125.1 (Ar***C***), 121.8 (***C4/5/8/9***), 120.9 (***C4/5/8/9***), 113.7 (***C4/5/8/9***), 107.2 (***C4/5/8/9***), 55.5 (br. s, ring/arm), 54.9 (***C3***), 54.8 (***C6/7***), 53.6 (ring/arm), 52.7 (br. s, ring/arm), 50.3 (br. s, ring/arm), 50.0 (br. s, ring/arm), 47.6 (br. s, ring/arm), 34.89 (ring/arm), 34.84 (***C1***), 33.2 (***C2***) ppm.

ES-MS (MeOH): *m/z* 664.2 $[M+H]^{+}$. HRMS (ES+): found (*m/z*): 663.3134 $[M+H]^{+}$; $C_{34}H_{43}O_8N_6$ requires 663.3137 ($|\Delta m/z|$ = 0.41 ppm).

Lanthanide complexation of DOTA-dibenzocyclooctyne (DBCO) (Ln$\mathbf{L^4}$)



Ln = Eu, Tb

To a solution of the ligand $\mathbf{L^4}$ (0.06 mmol, 1.00 eq.) in 3 mL (H_2O/ MeCN, 7:3), the appropriate lanthanide triflate salt was added (0.063 mmol, 1.05 eq.) and the reaction mixture was stirred at 50 °C for 30 minutes. The pH was adjusted to 4/5 by dropwise addition of an aqueous 1 M NaOH solution. The reaction was left to stir at 50 °C for 48 hours. The solvent was removed under reduced pressure and the residue was suspended in water. The pH of this solution was adjusted to 7 by addition of aqueous 1 M NaOH and the solvent was removed under reduced pressure giving the crude as a pale pink powder. The pale pink powder was purified by column chromatography (alumina MeCN/H_2O, 8:2 to 7:3). Excess mass attributed to salts; product used with salts.

(Ln = Eu) From $Eu(OTf)_3$ (37.7 mg, 0.063 mmol) yielded an off white powder (54.6 mg, 0.067 mmol, 112%) R_f = 0.32 (MeCN/H_2O, 8:2).

^{1}H NMR (400 MHz, D_2O) δ 33.5, 33.3, 32.5, 31.4, 31.2, 30.9, 12.4, 12.1, 11.8, -0.5, -1.0, -1.3, -2.0, -2.9, -3.3, -5.6, -5.8, -7.0, -7.5, -7.7, -8.5, -10.8, -11.1, -11.9, -12.8, -13.1, -14.7, -15.2, -15.5, -15.7, -16.1, -17.0 ppm.

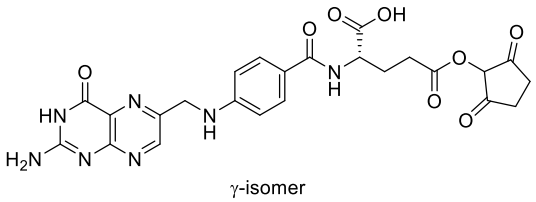
ES-MS (MeOH): *m/z* 811.9 $[M+H]^+$. HRMS (ES+): found (*m/z*): 811.2101 $[M+H]^+$; $C_{34}H_{40}O_8N_6Eu$ requires 811.2101 ($|\Delta m/z|$ = 0.03 ppm).

(Ln = Tb) From $Tb(OTf)_3$ (38.1 mg, 0.063 mmol) yielded an off white powder (75.7 mg, 0.092 mmol, 154%) R_f = 0.32 (MeCN/H_2O, 8:2).

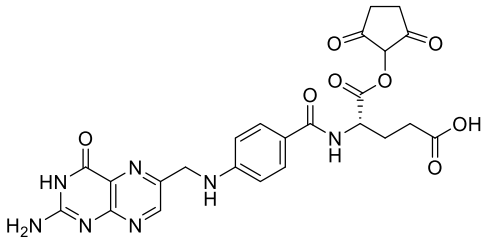
^{1}H NMR (400 MHz, D_2O) δ 251.6, 202.4, 191.6, 172.7, 144.2, 117.4, 111.6, 110.0, 73.6, 59.9, 46.0, 42.6, 25.2, 22.1, 21.5, 20.5, 19.7, 18.1, 17.0, 16.1, 14.5, 14.0, 13.5, 13.1, 12.5, 12.0, 11.1, -26.1, -42.3, -67.7, -79.4, -100.4, -112.8, -127.0, -205.2, -373.7, -379.6, -382.1, -384.8, -398.7, -402.4 ppm.

ES-MS (MeOH): *m/z* 819.1 $[M+H]^+$, 841.1 $[M+Na]^+$.HRMS (ES+): found (*m/z*): 819.2154 $[M+H]^+$; $C_{34}H_{40}O_8N_6{}^{159}Tb$ requires 819.2156 ($|\Delta m/z|$ = 0.20 ppm).

_N_-NHS-folic acid[14, 15] (18)



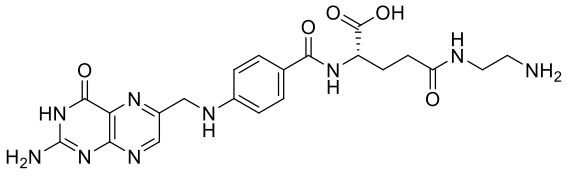
γ-isomer



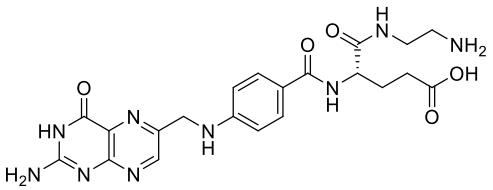
α-isomer

Prepared according to the procedure described by Trindade et al.[14] and Dzwonek et al.[15]
Discontinued due to poor solubility leading to difficulties in HPLC purification.

_N_-ethylene diamine-folic acid[16, 17] (19)



γ-isomer

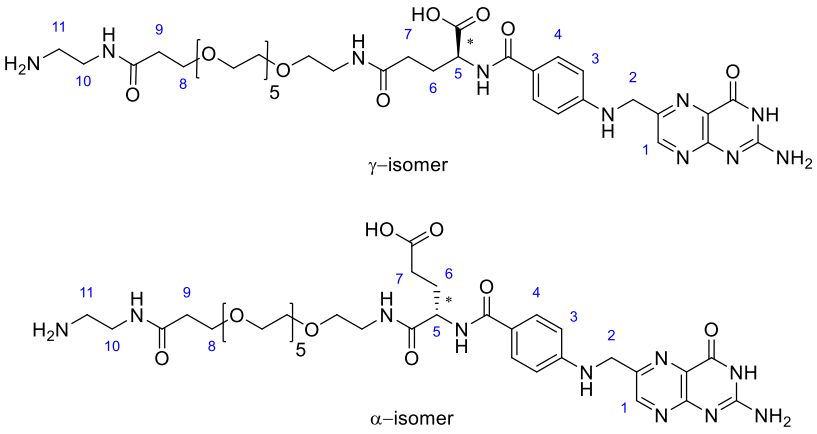


α-isomer

Prepared according to the procedure described by König and Kramer.[16] Discontinued due to poor solubility leading to difficulties in HPLC purification.
ES-MS (MeOH) *m/z* 485.0 $[M+H]^+$.

Prepared according to the procedure described by Rutnakornpituk *et al.*[17] Discontinued due to poor solubility leading to difficulties in HPLC purification.
ES-MS (MeOH) *m/z* 485.0 $[M+H]^+$.

Solid phase synthesis of FA-PEG$_6$-EDA-NH$_2$[18, 19] (20$^{\alpha\gamma}$ mixture)



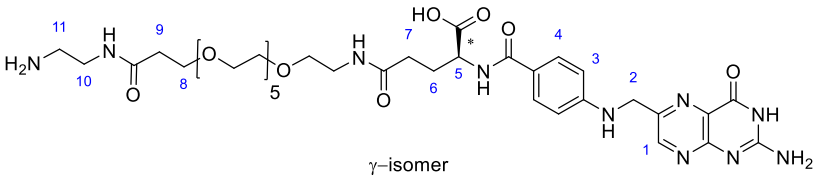
Prepared with minor adaptation from the procedure described by Chen *et al.*[18] and Kularatne *et al.*[19] Refer to Scheme 3.2 for an overview of the synthetic route. The procedure was carried out in parallel batches of four. 1,2-Diaminoethane trityl resin (1.2-1.7 mmol/g, 70 mg, 0.1 mmol) was swollen with DCM (3 mL) for 2 hours and then drained, followed by DMF (3 mL) for 2 hours and then drained in a biotage phase separator column. After swelling the resin, a solution of Fmoc-PEG$_6$-OH (86 mg, 0.15 mmol, 1.50 eq.), HATU (57 mg, 0.15 mmol, 1.50 eq.), and DIPEA (35 µL, 0.2 mmol, 2.00 eq.) in DMF (4 mL) was stirred for 15 minutes before addition to the resin. N_2 was bubbled through the suspension overnight, and the resin was washed with DMF (3 × 15 mL) followed by *i*-PrOH (3 × 15 mL). The resin was then swollen in DMF (5 mL) for at least 30 minutes before the next step. The above resin was incubated with 20% piperidine in DMF (5 mL) for 30 minutes to remove the Fmoc-protection, then followed by washings with DMF (3 × 15 mL) and *i*-PrOH (3 × 15 mL). The resin was then swollen in DMF (5 mL) for at least 30 minutes before the next step. The above sequence was repeated for coupling of folic acid (53 mg, 0.12 mmol, 1.20 eq.). The product was cleaved from the resin using a TFA: H_2O: TIPS mix (95:2.5:2.5) (5 mL) for 2-3 hours at room temperature unstirred. The filtrate was collected, and the resin was washed with DCM (3 × 15 mL) and *i*-PrOH (3 × 10 mL). and the filtrate and washes were concentrated under vacuum. The product was washed with copious amounts of DCM that was removed under reduced pressure, then washed with MeOH and removed. The concentrated product was dissolved in minimal MeOH (1-3 mL) and precipitated in cold diethyl ether (~400 mL) and centrifuged (4000 rpm, 4 °C, 10 minutes) and a yellow solid isolated. The precipitate was purified by HPLC condition 2 either mass-directed or UV-directed fraction collection (λ = 280 nm). t_R (prep) = 4.7 mins.

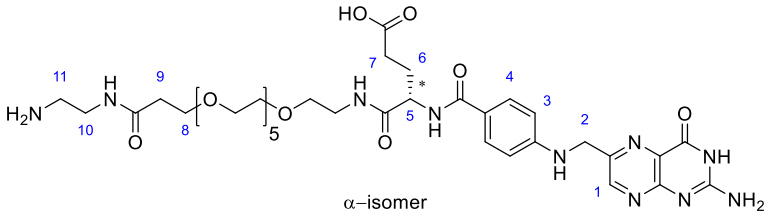
^{1}H NMR (400 MHz, D_2O) δ 8.67 (s, 1H, ***H1***), 7.67 (m, 2H, ***H4***), 6.87 – 6.76 (m, 2H, ***H3***), 4.60 (s, 2H, ***H2***), 4.37 (dt, $^3J_{H\text{-}H}$ = 9.6, 4.7 Hz, 1H, ***H5***), 3.72 (m, 2H, ***H8***), 3.67 – 3.33 (m, 24H, PEG), 3.22 (m, 1H), 3.12 (m, 2H), 2.52 (td, *J* = 6.0, 3.7 Hz, 2H, ***H6/ H7***), 2.46 – 1.99 (m, 4H, ***H6/ H7***) ppm.

ES-MS (MeOH) *m/z* 819.3 $[M+H]^+$; **HRMS** (ES^+) (mixture of regioisomers), found (*m/z*): 819.39874 $[M+H]^+$; $C_{36}H_{55}O_{12}N_{10}$ requires 819.39954. ($|\Delta m/z|$ = 0.98 ppm); (*m/z*): 410.20319 $[M+2H]^{2+}$; $C_{36}H_{56}O_{12}N_{10}$ requires 410.20341. ($|\Delta m/z|$ = 0.55 ppm).

UV-Vis (H_2O) (mixture of regioisomers) λ_{max} = 280 nm (ε = 25266 M^{-1} cm^{-1}).

Solid phase synthesis of FA-PEG$_6$-EDA-NH$_2$[18, 19] (20$^{\alpha}$ or 20$^{\gamma}$)





Prepared with minor adaptation from the procedure described by Chen *et al.*[18] and Kularatne *et al.*[19] Refer to Scheme 3.4 for an overview of the synthetic route. The procedure was carried out in parallel batches of four. 1,2-Diaminoethane trityl resin (1.2-1.7 mmol/g, 70 mg, 0.1 mmol) was swollen with DCM (3 mL) for 2 hours and then drained, followed by DMF (3 mL) for 2 hours and then drained in a biotage phase separator column. After swelling the resin, a solution of Fmoc-PEG$_6$-OH (86 mg, 0.15 mmol, 1.50 eq.), HATU (57 mg, 0.15 mmol, 1.50 eq.), and DIPEA (35 µL, 0.2 mmol, 2.00 eq.) in DMF (4 mL) was stirred for 15 minutes before addition to the resin. N_2 was bubbled through the suspension overnight, and the resin was washed with DMF (3 × 15 mL) followed by *i*-PrOH (3 × 15 mL). The resin was then swollen in DMF (5 mL) for at least 30 minutes before the next step. The above resin was incubated with 20% piperidine in DMF (5 mL) for 30 minutes to remove the Fmoc-protection, then followed by washings with DMF (3 × 15 mL) and *i*-PrOH (3 × 15 mL). The resin was then swollen in DMF (5 mL) for at least 30 minutes before the next step. The above sequence was repeated for two more coupling steps for conjugation of γ-isomer: Fmoc-Glu-OtBu (CAS: 84793-07-7) or α-isomer: Fmoc-Glu(OtBu)-OH (CAS: 71989-18-9) (64 mg, 0.15 mmol, 1.5 eq) and N^{10}-TFA-Ptc-OH (61 mg, 0.15 mmol, 1.50 eq.). The product was cleaved from the resin using a TFA: H_2O: TIPS mix (95:2.5:2.5) (5 mL) for 2-3 hours at room temperature unstirred. The filtrate was collected, and the resin was washed with DCM (3 × 15 mL) and *i*-PrOH (3 × 10 mL). and the filtrate and washes were concentrated under vacuum. The product was washed with copious amounts of DCM that was removed under reduced pressure, then washed with MeOH and removed. The concentrated product was dissolved in minimal MeOH (1-3 mL) and precipitated in cold diethyl ether (~400 mL) and centrifuged (4000 rpm, 4 °C, 10 minutes) and a yellow solid isolated that was

characterised by MS (ES-MS (MeOH) *m/z* 915.3 $[M+H]^+$). The yellow precipitate was stirred with saturated Na_2CO_3 solution at room temperature to cleave the trifluoroacetyl protecting group for ~1 hour followed by MS. The mixture was neutralised to pH 7 with 2M HCl (aq.) and the solvent was removed under reduced pressure. The residue was dialysed for at least 24 hours. The precipitate was purified by HPLC (A.2 HPLC conditions method 2).

(γ-isomer) t_R (prep) = 4.7 mins. (63.2 mg, 0.078 mmol, 19%)

^{1}H NMR (γ-isomer) (600 MHz, D_2O, pH 9) δ 8.64 (s, 1H, ***H1***), 7.69 (m, 2H, ***H4***), 6.85 (m, 2H, ***H3***), 4.62 (s, 2H, ***H2***), 4.37 (dd, $^3J_{H\text{-}H}$ = 9.5, 4.0 Hz, 1H, ***H5***), 3.79 – 3.65 (m, 2H, ***H8***), 3.62 – 3.43 (m, 20H, PEG), 3.38 (q, *J* = 6.3 Hz, 4H, ***H10*** and PEG), 3.29 – 3.14 (m, 2H, PEG), 2.92 (t, $^3J_{H\text{-}H}$ = 5.8 Hz, 2H, ***H11***), 2.52 (t, $^3J_{H\text{-}H}$ = 6.0 Hz, 2H, ***H9***), 2.40 (dt, $^2J_{H\text{-}H}$ = 14.6, $^3J_{H\text{-}H}$ = 7.3 Hz, 1H, ***H7***), 2.34 (dt, $^2J_{H\text{-}H}$ = 14.6, $^3J_{H\text{-}H}$ = 6.9 Hz, 1H, ***H7***), 2.26 (dtd, $^2J_{H\text{-}H}$ = 14.3, $^3J_{H\text{-}H}$ = 7.2, 4.1 Hz, 1H, ***H6***), 2.08 (ddt, $^2J_{H\text{-}H}$ = 14.1, $^3J_{H\text{-}H}$ = 8.8, 7.1 Hz, 1H, ***H6***).

^{13}C NMR (γ-isomer) (151 MHz, D_2O, pH 9) δ 178.6 (***C***OOH), 175.6 (***C***ONH), 174.6 (***C***ONH), 172.7 (***C***ONH), 169.2 (***C***ONH (ring), 155.5, 151.1, 147.9, 147.5 (***C1***), 129.1 (***C4***), 128.2, 121.5 (***C3***), 112.7, 69.4 (PEG), 69.4 (PEG), 69.2 (PEG), 68.6 (PEG), 66.6 (***C8***), 55.2 (***C5***), 45.8 (***C2***), 39.5 (***C11***), 39.3 (***C10***), 38.9, 35.9 (***C9***), 32.7 (***C7***), 27.7 (***C6***).

ES-MS (γ-isomer) (MeOH) *m/z* 819.3 $[M+H]^+$.

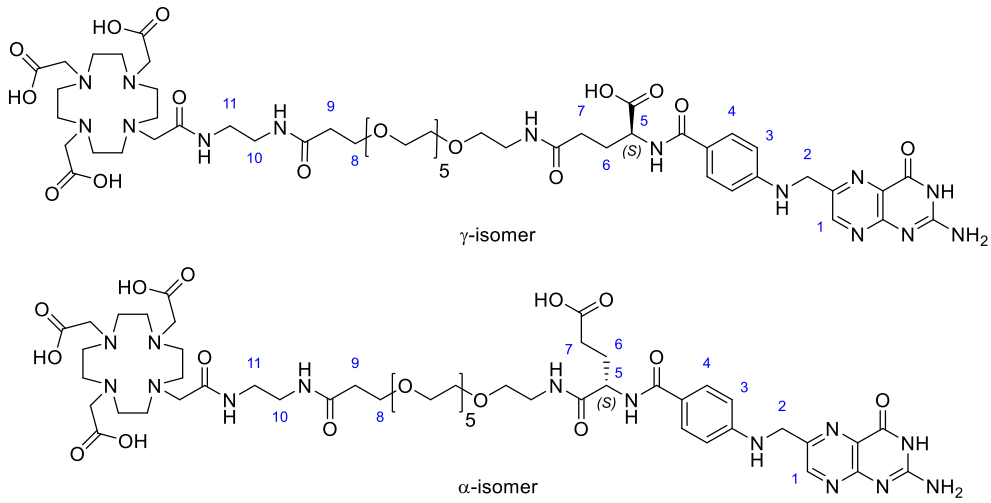
(α-isomer) t_R (prep) = 1.73 mins (crude 0.571g, 0.70 mmol, 174%) (200 mg crude purified by HPLC to give 15.6 mg, 0.019 mmol, 5%)

^{1}H NMR (α-isomer) (600 MHz, D_2O, pH 9) δ 8.62 (s, 1H, ***H1***), 7.69 (m, 2H, ***H4***), 6.82 (m, 2H, ***H3***), 4.58 (s, 2H, ***H2***), 4.39 (dd, $^3J_{H\text{-}H}$ = 8.8, 5.5 Hz, 1H, ***H5***), 3.73 (t, $^3J_{H\text{-}H}$ = 6.0 Hz, 2H, ***H8***), 3.68 – 3.38 (m, 26H, ***H10*** and PEG), 3.01 (t, $^3J_{H\text{-}H}$ = 6.0 Hz, 2H, ***H11***), 2.52 (t, $^3J_{H\text{-}H}$ = 5.9 Hz, 2H, ***H9***), 2.36 (t, *J* = 7.8 Hz, 2H, ***H7***), 2.19 – 2.12 (m, 1H, ***H6***), 2.12 – 2.05 (m, 1H, ***H6***).

^{13}C NMR (α-isomer) (151 MHz, D_2O, pH 9) δ 181.6 (***C***OOH), 174.7 (***C***ONH), 174.5 (***C***ONH), 172.2 (***C***ONH), 169.9 (***C***ONH (ring)), 163.2, 161.0, 155.4, 151.3, 147.8, 147.5 (***C1***), 129.3 (***C4***), 128.1, 120.8, 112.5 (***C3***), 69.6 (PEG), 69.47 (PEG), 69.45 (PEG), 69.43 (PEG), 69.41 (PEG), 68.9 (PEG), 66.5 (***C8***), 55.1 (***C5***), 45.7 (***C2***), 39.4 (***C11***), 39.1 (***C10***), 38.5, 36.0, 35.9 (***C9***), 33.9 (***C7***), 27.7 (***C6***).

ES-MS (α-isomer) (MeOH) *m/z* 819.3 $[M+H]^+$; LC-MS (H_2O) *m/z*: 818.4 $[M+H^+]$.

Folate-PEG$_6$-DOTA conjugate[18, 19] (L$^{5\alpha\gamma}$)



Prepared with minor adaptation from the procedure described by Chen *et al.*[18] and Kularatne *et al.*[19] FA-PEG$_6$-EDA-NH$_2$, **20** (0.150 g, 0.183 mmol 1.00 eq.) was added to a flame-dried flask and dissolved in DMSO (1.8 mL, 0.1 M final concentration). DIPEA (112 µL, 0.641 mmol, 3.50-3.80 eq.) and DOTA-NHS ester (0.153 g, 0.201 mmol, 1.10 eq.) were added and the reaction was stirred at room temperature overnight under an Ar atmosphere. The reaction was monitored by LC-MS and upon completion (~ 24 hours) the unreacted DOTA-NHS ester was cleaved by the addition of water (1 mL) and stirred for 30 minutes. The reaction mixture was concentrated under reduced pressure and the crude product precipitated by dropwise addition into vigorously stirred cold (0 °C) acetone (~ 600 mL). The suspension was centrifuged (4000 rpm, 4 °C, 10 minutes), and the yellow solid isolated. The solid was dissolved in water and freeze-dried to remove trace DMSO and yield the crude product as a yellow powder. The precipitate was purified by HPLC (A.2 HPLC conditions method 2).

(γ-isomer) Crude yield: (63.8 mg, 0.053 mmol, >100%).

^{1}H NMR (γ-isomer) (600 MHz, D_2O, pH 9) δ 8.71 (s, 1H, ***H1***), 7.63 (d, $^3J_{H\text{-}H}$ = 8.6 Hz, 2H, ***H4***), 6.70 (d, $^3J_{H\text{-}H}$ = 8.6 Hz, 2H, ***H3***), 4.53 (s, 2H, ***H2***), 4.38 (dd, $^3J_{H\text{-}H}$ = 9.4, 4.2 Hz, 1H, ***H5***), 3.93 – 2.96 (m, 52H, C***H***$_{2\text{-arm}}$/C***H***$_{2\text{-ring}}$/PEG/ ***H10***/***H9***), 2.54 (t, $^3J_{H\text{-}H}$ = 6.2 Hz, 2H, ***H9***), 2.46 – 2.32 (m, 2H, ***H7***), 2.26 (dtd, $^2J_{H\text{-}H}$ = 14.3, $^3J_{H\text{-}H}$ = 7.4, 4.6 Hz, 1H, ***H6***), 2.14 – 2.05 (m, 1H, ***H6***) ppm. Crude NMR likely to contain DOTA as an impurity.

^{13}C NMR (γ-isomer) (151 MHz, D_2O, pH 9) δ 178.6 (C^5***C***OOH), 178.0, 175.7, 174.0, 172.3, 169.8, 169.0 (C^{5}NH***C***O), 154.4, 150.7, 149.6 (***C1***), 149.1 (***C1***), 129.0 (***C4***), 127.2, 121.3, 112.3 (***C3***), 69.5 (PEG), 69.4 (PEG), 69.3 (PEG), 68.7 (PEG), 66.7 (***C8***), 56.4 (cylen-arm), 56.1 (cylen-arm), 56.0 (cylen-arm), 55.9 (cylen-arm), 55.2 (***C5***), 51.8, 50.8, 49.9, 48.3 (cyclen-ring/***C10***/***C11***), 45.5 (***C2***), 38.9 (cyclen-ring/***C10***/***C11***), 38.5 (cyclen-ring/***C10***/***C11***), 36.0 (***C9***), 32.7 (***C7***), 27.8 (***C6***) ppm.

(α-isomer) Crude yield: (0.221 g, 0.183 mmol, 100%). Approximately 100 mg of the crude was purified HPLC to afford the pure product (5.1 mg, 0.004 mmol, 2%).

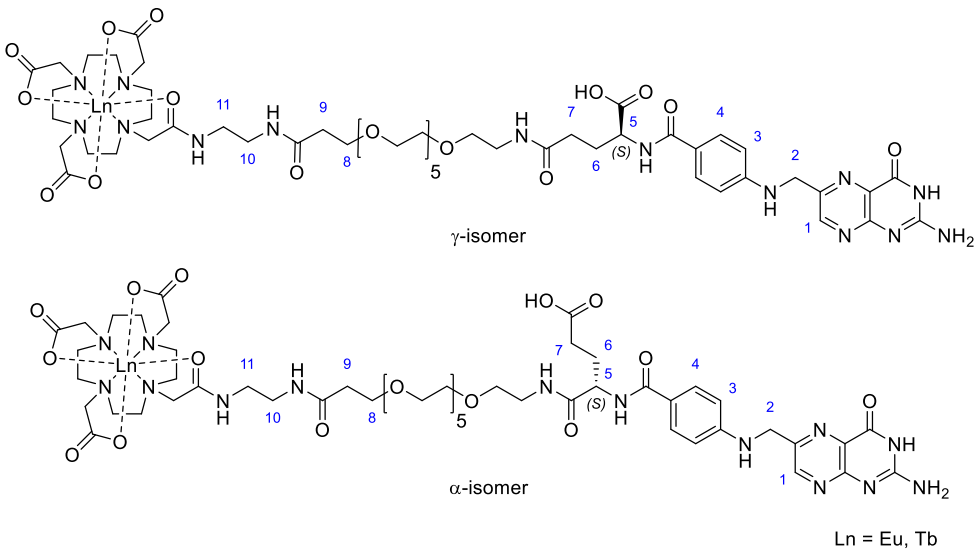
^{1}H NMR (600 MHz, D_2O, pH 9) (α-isomer) δ 8.65 (s, 1H, ***H1***), 7.72 (d, $^{3}J_{H\text{-}H}$ = 8.8 Hz, 2H, ***H4***), 6.87 (d, $^{3}J_{H\text{-}H}$ = 8.8 Hz, 2H, ***H3***), 4.64 (s, 2H, ***H2***), 4.38 (dd, $^{3}J_{H\text{-}H}$ = 8.9, 5.4 Hz, 1H, ***H5***), 3.76 (t, *J* = 6.2 Hz, 2H, ***H8***), 3.72 – 3.17 (m, 30H, C***H***$_{2\text{-ring}}$/ C***H***$_{2\text{-arm}}$/PEG/ ***H10***/ ***H11***), 3.12 (s, 5H, cyclen-ring), 2.90 (br. s, 5H, cyclen-ring), 2.53 (t, $^{3}J_{H\text{-}H}$ = 6.2 Hz, 1H, ***H9***), 2.35 (td, $^{3}J_{H\text{-}H}$ = 7.5, 2.1 Hz, 2H, ***H7***), 2.18 – 2.03 (m, 2H, ***H6***) ppm.

^{13}C NMR (151 MHz, D_2O, pH 9) (α-isomer) δ 181.6 (C^{7}***C***OOH), 174.5, 174.0, 172.6, 171.0, 170.1 (***C***ONH(ring)), 163.5, 155.5, 151.4, 147.9, 147.6 (***C1***), 129.4 (***C4***), 129.1, 128.2, 121.0, 112.7 (***C3***), 69.59 (PEG), 69.56 (PEG), 69.53 (PEG), 69.50 (PEG), 69.47 (PEG), 69.42 (PEG), 69.40 (PEG), 68.9 (PEG), 66.7 (***C8***), 56.9 (cylen-arm), 56.7 (cylen-arm), 56.4 (cylen-arm), 55.0 (***C5***), 51.2, 49.7 (cylen-ring), 49.5 (cylen-ring), 45.8 (***C2***), 39.1 (cyclen-arm), 39.0 (cyclen-ring/***C10***/***C11***), 38.7 (cyclen-ring/***C10***/***C11***), 38.4 (cyclen-ring/***C10***/***C11***), 36.0 (***C9***), 33.9 (***C7***), 27.6 (***C6***) ppm.

ES-MS (MeOH) (mixture of regioisomers) *m/z*: 1205.802 [M+H^{+}]; HRMS (ES^{+}), found (*m/z*): 1205.58023 [M+H^{+}]; $C_{52}H_{81}O_{19}N_{14}$ requires 1205.57969 (|Δ *m/z*| = 0.44 ppm).

UV-Vis (H_2O) (mixture of regioisomers) λ_{max} = 281 nm (ε = 20013 M^{-1} cm^{-1}), 353 nm.

Lanthanide complexation of folate-PEG$_6$-DOTA conjugate, (LnL$^{5\alpha\gamma}$)



To a solution of the ligand, **L$^{5\alpha\gamma}$** (1.00 eq.) in H_2O the appropriate Ln(OTf)$_3$ was added (1.05 eq.) and the reaction mixture was stirred at 60 °C for 30 min. The pH was adjusted to 4 by dropwise addition of an aqueous 1 M NaOH solution. The reaction was then allowed to stir at 60 °C for 48 h. The pH of this solution was adjusted to 7 by addition of aqueous 1 M NaOH. The reaction mixture was

dialysed for at least 24 hours. The solvent was removed under reduced pressure to afford the product as a yellow powder.

(Ln = Eu) From Eu(19.5 mg, 0.014 mmol, 87%)

^{1}H NMR (400 MHz, D_2O) (mixture of regioisomers) δ 33.8, 33.2, 32.1, 31.0, 30.8, 12.3, 11.9, 11.2, -0.0, -0.4, -1.1, -2.0, -3.0, -3.1, -4.8, -5.7, -6.9, -7.6, -7.9, -8.6, -10.5, -11.1, -11.9, -12.5, -14.6, -15.0, -15.4, -16.1, -16.4 ppm. Only major resolved peaks outside the +10 to 0 ppm range are reported.

ES-MS: LC-MS (MeOH) found *m/z* 1354.56 for $[M+H]^+$, 677.97 $[M+2H]^{2+}$. **HRMS** (ES^+) found (m/z): 1355.4972 $[M+H]^+$; $C_{52}H_{78}O_{19}N_{14}{}^{151}Eu$ requires 1355.4787 ($|\Delta m/z|$ = 0.06 ppm)

UV-Vis (H_2O) (mixture of regioisomers): λ_{max} 281 nm.

Luminescence lifetimes: H_2O: 0.59 ms, D_2O: 1.59 ms, q = 0.96.

(Ln = Tb, α-isomer) Purified by HPLC (A.3 HPLC conditions method 3).

From $\mathbf{L^{5\alpha}}$ (65 mg, 0.054 mmol, 1.00 eq.) yielded Tb$\mathbf{L^{5\alpha}}$ (5.4 mg, 0.004 mmol, 7%)

^{1}H NMR (500 MHz, D_2O) δ 252.4, 241.0, 202.6, 189.9, 111.7, 105.0, 76.1, 67.2, 56.1, 47.2, 16.2, 13.2, -49.0, -62.0, -66.4, -77.5, -92.9, -101.1, -111.3, -113.7, -194.9, -210.2, -363.2, -376.0, -392.5 ppm. Only major resolved peaks outside the +10 to -10 ppm range are reported.

HRMS(ES^+) found (m/z): 1361.4822 $[M+H]^+$; $C_{52}H_{78}O_{19}N_{14}{}^{159}Tb$ requires 1361.4816 ($|\Delta m/z|$ = 0.47 ppm)

Luminescence lifetimes: H_2O: 0.52 ms, D_2O: 0.30 ms, q = 0.80.

(Ln = Tb, γ-isomer) Purified by HPLC (A.4 HPLC conditions method 4).

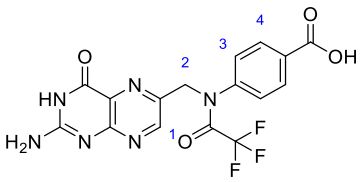
From $\mathbf{L^{5\gamma}}$ (64 mg, 0.054 mmol, 1.00 eq.) yielded Tb$\mathbf{L^{5\gamma}}$ (33.3 mg, 0.025 mmol, 46%)

^{1}H NMR (500 MHz, D_2O) δ 253.0, 242.4, 239.4, 202.0, 189.7, 111.6, 104.8, 76.3, 68.8, 57.0, 48.0, 16.7, 12.6, -66.7, -77.6, -100.8, -110.8, -113.8, -123.2, -196.4, -212.5, -363.3, -376.1, -392.8 ppm. Only major resolved peaks outside the +10 to -10 ppm range are reported.

HRMS(ES^+) found (m/z): 1361.4841 $[M+H]^+$; $C_{52}H_{78}O_{19}N_{14}{}^{159}Tb$ requires 1361.4816 ($|\Delta m/z|$ = 1.90 ppm).

Luminescence lifetimes: H_2O: 0.55 ms, D_2O: 0.35 ms, q = 0.70.

N^{10}-(TFA)-pteroic acid[20] (21)



Prepared by the procedure described by Yamaguchi *et al.*[20] All procedures were carried out in the dark where possible. Pteroic acid (0.50 g, 1.60 mmol, 1.00 eq.) was dried for several hours under high vacuum before use. Trifluoroacetic anhydride (12.5 mL, 89.9 mmol, 56.2 eq.) was added to pteroic acid and stirred at room temperature under Ar for 4 days. The reaction mixture was concentrated under reduced pressure before 3% TFA in water (37.5 mL) was added and the mixture stirred for 2 days at room temperature in the dark. The precipitate was isolated by centrifugation (4700 rpm, 20 min, 4 °C), the solid was resuspended in deionised water (40 mL) and centrifuged a further 3 times (~50 mL water). The solid was dried and afforded a brown solid (0.480 g, 1.17 mmol, 73%). The compound was used directly in the next step without further purification.

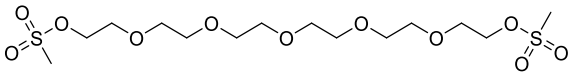
^{1}H NMR (600 MHz, DMSO-d_6/D_2O (8:2)) δ 8.56 (s, 1H, ***H1***), 7.94 (d, $^{3}J_{H\text{-}H}$ = 8.3 Hz, 2H, ***H4***), 7.57 (d, $^{3}J_{H\text{-}H}$ = 8.1 Hz, 2H, ***H3***), 5.09 (s, 2H, ***H2***) ppm.

^{13}C NMR (151 MHz, DMSO-d_6/D_2O (8:2)) δ 167.4 (***C***OOH), 161.7, 156.6 (q, $^{2}J_{C\text{-}F}$ = 35.6 Hz, ***C***OCF_3), 155.9, 154.3, 150.1 (***C1***), 145.5, 143.6, 131.8, 131.2, 131.1 (***C4***), 129.7 (***C3***), 128.7, 121.4, 116.7 (q, $^{1}J_{C\text{-}F}$ = 288.6 Hz, ***C***F_3), 54.4 (***C2***) ppm.

^{19}F NMR (377 MHz, $CDCl_3$) δ -66.2 (C***F***$_3$), 73.9, 74.1 ppm.

ES-MS (MeOH) *m/z* 409.069 $[M+H]^+$, HRMS (ES^+), found (*m/z*): 409.0865 $[M+H]^+$; $C_{16}H_{12}O_4N_6F_3$ requires 409.0867. ($|\Delta m/z|$ =0.43ppm).

3,6,9,12,15-Pentaoxaheptadecane-1,17-diyl dimethanesulfonate/ dimesylate-PEG_5 [21, 22] (22)



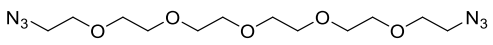
Prepared by the procedure described by Goswami *et al.*[21] and Kohata *et al.*[22] A solution of methanesulfonyl chloride (1.35 mL, 17.5 mmol, 3.00 eq.) in DCM (15 mL) was added dropwise over 30 minutes to a stirred mixture of hexatheylene glycol (1.46 mL, 5.8 mmol, 1.00 eq.) and triethylamine (2.43 mL, 17.5 mmol, 3.00 eq.) in DCM (15 mL) at 0 °C. The mixture was stirred for 2 hours at 0 °C and then at room temperature for a further 2 hours. The solvents were removed under reduced pressure and the residue diluted with DCM (100 mL) and washed with 3% aqueous. HCl (100 mL) and brine (100 mL). The extraction was repeated three times and the combined organic components were dried over Na_2SO_4 and filtered through a celite pad. The filtrate was dried under reduced pressure to afford the product as a colourless oil (2.46 g, 5.61 mmol, 97%).

^{1}H NMR (400 MHz, $CDCl_3$) δ 4.38 – 4.34 (m, 4H, 2 × $CH_2C\boldsymbol{H_2}OMs$), 3.77 – 3.72 (m, 4H, 2 × $C\boldsymbol{H_2}CH_2OMs$), 3.68 – 3.59 (m, 16H), 3.07 (s, 6H, 2 × $SO_3C\boldsymbol{H_3}$) ppm. The ^{1}H NMR data corresponds to reported literature values.[22]

^{13}C NMR (101 MHz, $CDCl_3$) δ 70.70 ($\boldsymbol{C}H_2$), 70.66 ($\boldsymbol{C}H_2$), 70.6 ($\boldsymbol{C}H_2$), 69.5 ($CH_2\boldsymbol{C}H_2OMs$), 69.1 ($\boldsymbol{C}H_2CH_2OMs$), 37.8 ($SO_3\boldsymbol{C}H_3$) ppm.

ES-MS (MeOH) *m/z* 439.2 $[M+H]^+$, 461.2 $[M+Na]^+$.

1,17-diazido-3,6,9,12,15-pentaoxaheptadecane / diazide-PEG$_5$[21, 22] (23)



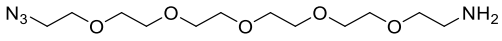
Prepared with minor adaptation from the procedure described by Kohata *et al.*[22] Dimesylate-PEG$_5$, **22** (4.81 g, 10.6 mmol, 1.00 eq.) was dissolved in dry DMF (25 mL) before addition of sodium azide (2.07 g, 46.8 mmol, 2.90 eq.), and the mixture was stirred for 24 h at 65 °C. The reaction mixture was diluted with diethyl ether (80 mL) and filtered through a celite pad. The filtrate was washed with water (15 mL × 2), followed by brine (20 mL × 3). The isolated organic extracts were combined, and solvent was removed *in vacuo*. The residue was redissolved in DCM and the inorganic salts were removed by filtration. The filtrate was evaporated to dryness under reduced pressure, affording the product as a pale yellow oil (2.30 g, 6.92 mmol, 65%).

^{1}H NMR (400 MHz, $CDCl_3$) δ 3.70 – 3.63 (m, 20H), 3.38 (t, $^3J_{H\text{-}H}$ = 5.1 Hz, 4H, $C\boldsymbol{H_2}N_3$) ppm. The ^{1}H NMR data corresponds to reported literature values.[22]

^{13}C NMR (101 MHz, $CDCl_3$) δ 70.85, 70.82, 70.77, 70.73, 70.2, 50.8 ($\boldsymbol{C}H_2N_3$) ppm.

ES-MS (MeOH) *m/z* 355.2 $[M+Na]^+$.

17-Azido-3,6,9,12,15-pentaoxaheptadecan-1-amine/Azide-PEG$_5$-amine[21, 22] (24)



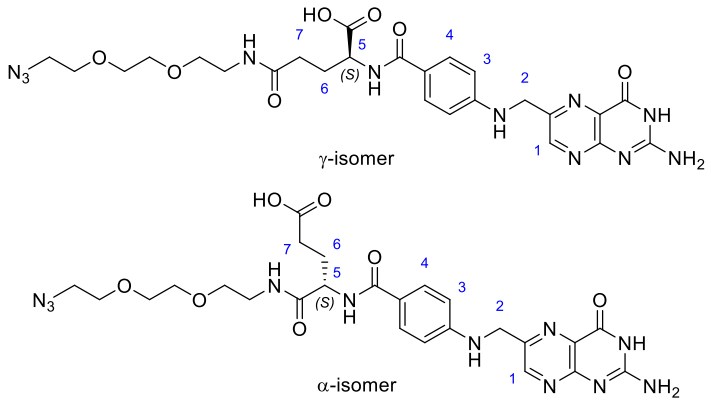
Prepared by the procedure described by Goswami *et al.*[21] and Kohata *et al.*[22] To PEG$_5$-diazide, **23** (2.30 g, 6.92 mmol, 1.00 eq.), 5% aqueous HCl (25 mL) was added and vigorously stirred at room temperature. To this mixture, a solution of triphenyl phosphine (1.63 g, 6.23 mmol, 0.90 eq.) in Et_2O (18 mL) was added dropwise over ~3 hours. The mixture was stirred for a further 24 hours at room temperature. The reaction mixture was washed with ethyl acetate (3 × 100 mL) to remove unreacted starting materials and triphenylphosphine oxide that was formed during the reaction. The aqueous layer was collected, and 20 M potassium hydroxide was added slowly until the pH of the solution was basic (~ pH 12). The product was extracted by washing the aqueous layer with DCM (3 × 100 mL). The organic layer was dried over Na_2SO_4, filtered and the filtrate was dried under reduced pressure to afford the product as a pale yellow oil (1.45 g, 4.73 mmol, 68%).

^{1}H NMR (400 MHz, $CDCl_3$) δ 3.67 – 3.57 (m, 18H, OC***H*****$_2$**C***H*****$_2$**O), 3.48 (t, $^{3}J_{H\text{-}H}$ = 5.2 Hz, 2H, OC***H*****$_2$**CH_2N_3), 3.36 (t, $^{3}J_{H\text{-}H}$ = 5.1 Hz, 2H, C***H*****$_2$**NH_2), 2.84 (t, $^{3}J_{H\text{-}H}$ = 5.2 Hz, 2H, C***H*****$_2$**N_3), 1.42 (s, 2H, N***H*****$_2$**) ppm.

^{13}C NMR (101 MHz, $CDCl_3$) δ 73.5 (O***C***$H_2CH_2N_3$), 70.83, 70.77, 70.73, 70.71, 70.5, 70.2, 50.8 (***C***H_2NH_2), 41.9 (***C***H_2N_3) ppm.

ES-MS (MeOH) *m/z* 307.2 $[M+H]^+$, 329.2 $[M+Na]^+$.

Folate-PEG$_2$-azide (25[a])



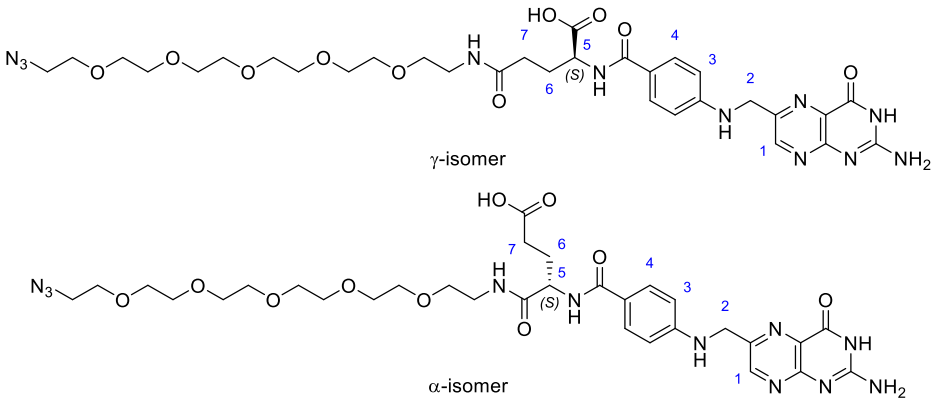
Prepared with minor adaptation from the procedure described by Ke et al.[23] Folic acid (1.00 g, 2.27 mmol, 1.00 eq.) and dicyclohexylcarbodiimide (DCC) (0.935 g, 4.53 mmol, 2.00 eq.) were dissolved in dry DMSO (50 mL) under an inert atmosphere. Pyridine (10 mL) was added to the reaction mixture and stirred for 1 hour before addition of the azide-PEG$_2$-amine (0.40 g, 2.27 mmol, 1.00 eq.). The reaction mixture was stirred in the dark for a further 60 hours. The resulting mixture was then filtered, under an inert atmosphere using a filter cannula, into a flask of vigorously stirring diethyl ether (200 mL) to produce a yellow precipitate. The suspension was continuously agitated with slow stirring and most of the ether was decanted. The yellow solid was washed twice, to remove remaining DMSO, with acetone (60 mL) and diethyl ether (100 mL); stirring was maintained and solvent was decanted each time. Any remaining solvent was then removed *in vacuo* to obtain the product as a fine yellow powder.

^{1}H NMR of a mixture of regioisomers (600 MHz, D_2O, pH 9) δ 8.62 (s, 1H, ***H1***), 7.74 – 7.65 (m, 2H, ***H4***), 6.89 – 6.81 (m, 2H, ***H3***), 4.60 (br. s, 2H, ***H2***), 4.40-4.36 (m, 1H ***H5***), 3.71 – 3.13 (m, 12H, PEG), 2.48 – 2.30 (m, 2H, ***H6/H7***), 2.20 – 2.03 (m, 2H, ***H6/H7***) ppm.

^{13}C NMR (151 MHz, D_2O) δ 181.7 (***C***OOH), 178.7, 175.7, 174.5, 172.6, 170.1, 169.2, 163.5, 155.5, 151.4, 151.1, 147.8, 147.5 (***C1***), 129.3 (***C4***), 129.2 (***C4***), 129.0, 128.2, 121.5, 120.9, 115.1 (***C3***), 112.8 (***C3***), 112.7, 69.6, 69.51, 69.46, 69.3, 69.2, 69.1, 69.0, 68.9, 68.5, 55.2 (***C5***), 55.1 (***C5***), 50.0, 49.9, 45.8 (***C2***), 39.0, 38.9, 33.9 (***C6/C7***), 32.6 (***C6/C7***), 27.5 (***C6/C7***) ppm.

ES-MS (MeOH) *m/z* 598.2 $[M+H]^+$, 620.2 $[M+Na]^+$, LC-MS (MeOH) 597.2 $[M+H]^+$, 1193.5 $[2M+H]^+$.

Folate-PEG$_5$-azide[24] (25^b)



Prepared with minor adaptation from the procedure described by Ke et al.[23] Folic acid (1.30 g, 2.94 mmol, 1.00 eq.) and DCC (1.21 g, 5.88 mmol, 2.00 eq.) were dissolved in dry DMSO (50 mL) under an inert atmosphere. Pyridine (10 mL) was added to the reaction mixture and stirred for 1 hour before addition of the azide-PEG$_5$-amine (0.90 g, 2.94 mmol, 1.00 eq.). The reaction mixture was stirred in the dark for a further 60 hours. The resulting mixture was then filtered, under an inert atmosphere using a filter cannula, into a flask of vigorously stirring diethyl ether (200 mL) to produce a yellow precipitate. The suspension was continuously agitated with slow stirring and most of the ether was decanted. The yellow solid was washed twice, to remove remaining DMSO, with acetone (60 mL) and diethyl ether (100 mL); stirring was maintained and solvent was decanted each time. Any remaining solvent was then removed *in vacuo* to obtain the product as a fine yellow powder.

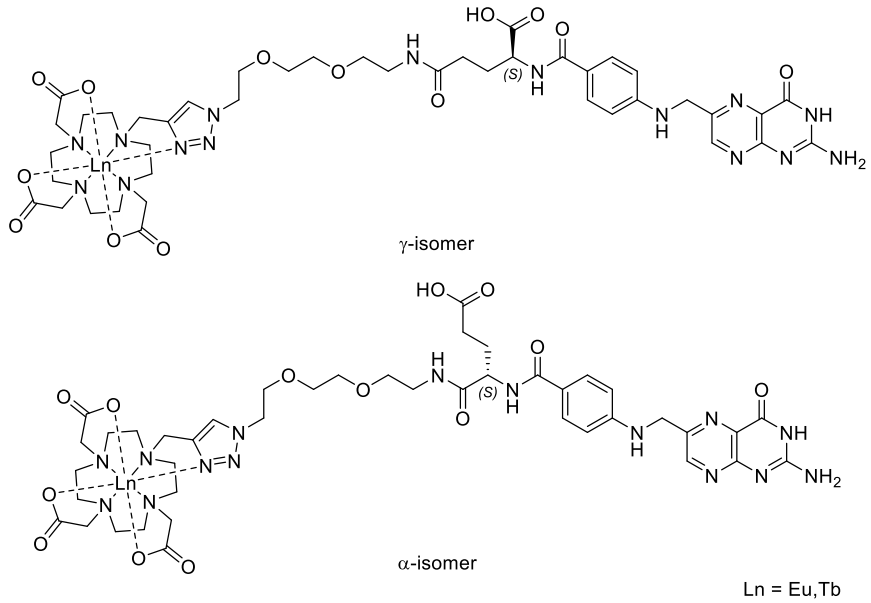
The crude was purified by HPLC (A.5 HPLC conditions method 5) using mass directed or UV-directed fraction collection (λ = 280 nm) t_R (prep) =2.4 mins.

^{1}H NMR of a mixture of regioisomers (400 MHz, D_2O with NH_4OH, pH 9) δ 8.61 (s, 1H, ***H1***), 7.67 (dd, $^3J_{H\text{-}H}$ = 8.9, 7.6 Hz, 2H, ***H4***), 6.81 (overlapping d/dd, $^3J_{H\text{-}H}$ = 8.9 Hz, 2H, ***H3***), 4.58 (s, 2H, ***H2***), 4.40-4.33 (m, 1H, ***H5***), 3.73 – 3.32 (m, 23H, PEG), 3.20 (m, 1H, PEG), 2.44 – 2.29 (m, 2H, ***H6/H7***), 2.27 – 1.98 (m, 2H, ***H6/H7***) ppm.

^{13}C NMR (151 MHz, D_2O with NH_4OH, pH 9) δ 181.62 (***C***OOH), 181.56 (***C***OOH), 178.62 (***C***ONH), 178.55 (***C***ONH), 175.72 (***C***ONH), 175.65 (***C***ONH), 174.50 (***C***ONH), 174.45 (***C***ONH), 171.3 (***C***ONH), 170.2 (***C***ONH), 169.9 (***C***ONH), 169.1 (***C***ONH), 155.2, 151.3, 151.1, 151.0, 150.8, 148.0, 147.9 (***C1***), 147.7 (***C1***), 129.3 (***C4***), 129.2 (***C4***), 129.1 (***C4***), 129.0 (***C4***), 128.0, 122.7, 122.1, 121.4, 120.8, 119.5, 115.10 (***C3***), 115.05 (***C3***), 112.6 (***C3***), 112.5 (***C3***), 69.62 (PEG), 69.59 (PEG), 69.55 (PEG), 69.51 (PEG), 69.47 (PEG), 69.43 (PEG), 69.39 (PEG), 69.3 (PEG), 69.2 (PEG), 69.1 (PEG), 68.91 (PEG), 68.88 (PEG), 68.86 (PEG), 68.7 (PEG), 68.6 (PEG), 55.22 (***C5***), 55.19 (***C5***), 55.04 (***C5***), 54.98 (***C5***), 50.3 (PEG), 50.13 (PEG), 50.08 (PEG), 45.70 (***C2***), 45.67, 39.03, 39.00, 38.9, 33.91 (***C6/C7***), 33.88 (***C6/C7***), 32.7 (***C6/C7***), 32.6 (***C6/C7***), 30.4, 27.84 (***C6/C7***), 27.76 (***C6/C7***), 27.68 (***C6/C7***), 27.66 (***C6/C7***), 23.8 ppm.

ES-MS (MeOH) *m/z* 730.3 $[M+H]^+$, 752.3 $[M+Na]^+$, HRMS (ES^+), found (*m/z*): 730.3262 $[M+H]^+$; $C_{31}H_{44}O_{10}N_{11}$ requires 730.3267. ($|\Delta m/z|$ = 0.74ppm).

Ln.pDO3A clicked to FA-PEG-N_3[25] (Ln$\mathbf{L}^{6a}$**)**



Ln-pDO3A, Ln$\mathbf{L}^1$ (0.150 g, 0.28 mmol, 1.00 eq.), FA-PEG-N_3 (**25**) (0.185 g, 0.31 mmol, 1.10 eq.) and $(CF_3SO_3Cu)_2 \cdot C_6H_6$ (14.2 mg, 0.028 mmol, 0.10 eq.) were combined with MeOH (15 mL) and DMSO (5 mL). The solution was heated at reflux at 80 °C whilst stirring under Ar for 24 hours. The methanol was removed *in vacuo* and the residue was dissolved in water before lyophilisation to aid removal of the DMSO. The solid was dissolved in H_2O (50 mL) and gently stirred with 2-3g CupriSorb™ resin for 24 hours to remove copper. The insoluble CupriSorb™ was removed by filtration and the filtrate was dried *in vacuo*. The compound was purified by HPLC (Eu: A.6 HPLC conditions method 6) and (Tb: A.7 HPLC conditions method 7) and then dried by lyophilisation to afford a yellowy-green powder.

(Ln = Eu) (0.0751 g, 0.066 mmol, 24%)

^{1}H NMR (400 MHz, D_2O/MeOD (95:5)) δ 29.8, 27.5, 26.9, 26.5, 13.4, 11.0, -0.1, -0.9, -4.6, -5.0, -5.7, -6.7, -7.0, -7.2, -8.6, -9.1, -9.4, -12.1, -12.8, -13.6, -14.7, -15.3, -16.3, -18.7, -19.3 ppm. Only major resolved peaks outside the +10 to 0 ppm range are reported.

ES-MS (H_2O) *m/z* 1130.9 $[M+H]^+$, HRMS (ES^+), found (*m/z*): 1130.34559 $[M+H]^+$; $C_{42}H_{57}O_{13}N_{15}{}^{151}Eu$ requires 1130.34532. ($|\Delta m/z|$ = 0.24 ppm); (*m/z*): 565.67626 $[M+2H]^{2+}$; $C_{42}H_{58}O_{13}N_{15}{}^{151}Eu$ requires 565.67630. ($|\Delta m/z|$ = 0.06 ppm).

UV-Vis (H_2O) λ_{max} = 281 nm, ε = 25832 M^{-1} cm^{-1} peaks also at 218 and 342 nm.

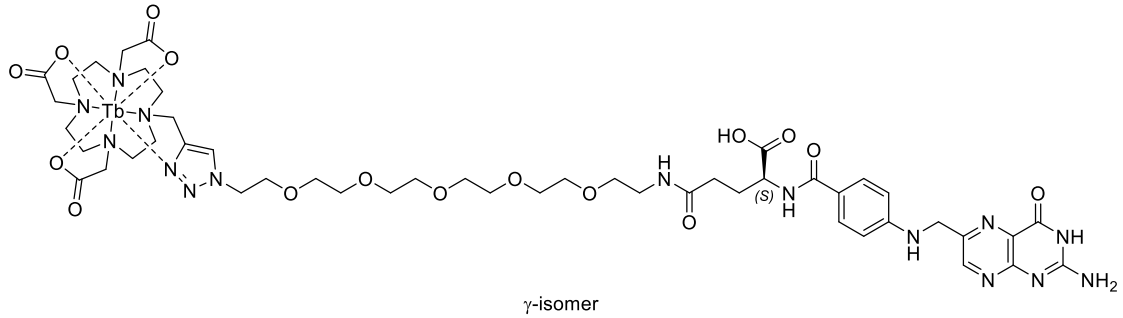
(Ln = Tb) t_R(prep) = 12.62 mins; t_R(ana) = 1.85 mins, (18.5 mg, 0.016 mmol, 4%)

^{1}H NMR (500 MHz, D_2O): δ 318.7, 290.2, 223.6, 220.2, 206.1, 194.7, 179.6, 175.9, 145.5, 116.6, 112.9, 18.5, 14.3, 13.3, 12.0, 11.2, 10.4, -14.4, -19.7, -28.0, -35.1, -40.5, -45.9, -50.1, -60.6, -76.1, -86.8, -90.7, -99.6, -102.5, -131.2, -140.8, -151.2, -152.8, -164.2, -176.4, -330.4, -347.0, -374.1 ppm. Only major resolved peaks outside the +10 to -10 ppm range are reported.

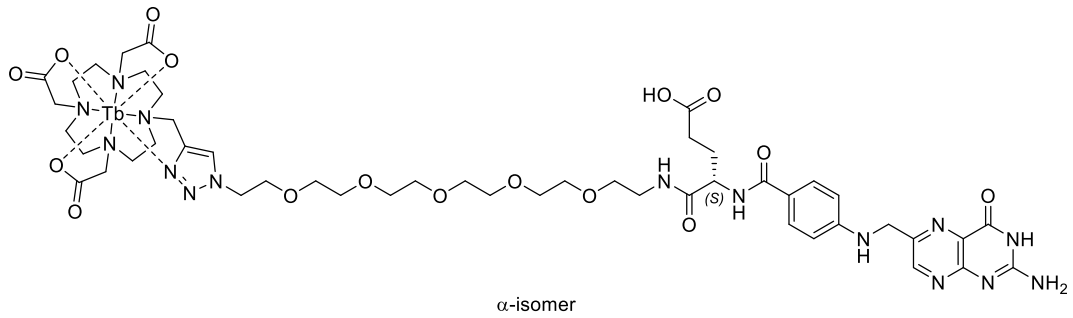
ES-MS (H_2O) *m/z* 1139.7 $[M+H]^+$, 1161.8 $[M+Na]^+$, HRMS (ES^+), found (*m/z*): 1138.35286 $[M+H]^+$; $C_{42}H_{57}O_{13}N_{15}{}^{159}Tb$ requires 1138.35082.(│Δ*m/z*│= 1.79 ppm); (*m/z*): 569.67890 $[M+2H]^{2+}$; $C_{42}H_{58}O_{13}N_{15}{}^{159}Tb$ requires 569.67905 (│Δ*m/z*│= 0.26 ppm).

UV-Vis (H_2O) λ_{max} = 282 nm.

Tb.pDO3A clicked to FA-PEG$_5$-N$_3$[25] (TbL^{6b})



γ-isomer



α-isomer

Tb-pDO3A (0.033 g, 0.062 mmol, 1.00 eq.) and FA-PEG$_5$-N$_3$, **25** (0.054 g, 0.074 mmol, 1.20 eq.) were dissolved in H_2O (3.5 mL). To this, $CuSO_4 \cdot 5H_2O$ (1.54 mg, 0.0062 mmol, 0.10 eq.) (62 µL of 0.1 M solution in H_2O) and sodium ascorbate (6.11 mg, 0.031 mmol, 0.50 eq.) (308 µL of 0.1 M solution in H_2O) were added and heated at 40 °C under Ar for 25 hours monitored by LC-MS. The reaction mixture was diluted in 50 mL H_2O and gently stirred with 2-3g CupriSorb™ resin to remove copper for 24 hours. The insoluble CupriSorb™ was removed by filtration, and the filtrate was dried *in vacuo* to yield the crude as a yellow residue (152 mg, 0.12 mmol, crude 195%). t_R(prep) = 12.34 mins (purification step 1)

Tb-pDO3A (0.031 g, 0.057 mmol, 1.00 eq.) and FA-PEG$_5$-N$_3$ (0.050 g, 0.069 mmol, 1.20 eq.) were dissolved in H_2O (5 mL) and degassed with three freeze-pump-thaw cycles. To this,

$(CuOTf)_2 \cdot C_6H_6$ (5.0 mg, 0.01 mmol, 0.20 eq.) was added and degassed with a further freeze-pump-thaw cycle and heated at 40 °C under Ar for 3.5 days monitored by LC-MS. The reaction mixture was diluted in 50 mL H_2O and gently stirred with 2-3g CupriSorb™ resin to remove copper for 24 hours. The insoluble CupriSorb™ was removed by filtration, and the filtrate was dried *in vacuo* to yield the crude as a yellow residue (106 mg, 0.083 mmol, crude 146%). t_R(prep) = 12.41 mins (purification step 1)

The crude products (258 mg) were combined and purified by HPLC twice (A.8 HPLC conditions method 8). The first HPLC conditions isolated the compound as a mixture of regioisomers from the impurities - t_R(ana) = 2.98 mins. The second HPLC conditions separated the major and minor isomers.

(Ln = Tb)

Major isomer, t_R(prep) = 9.71 mins, t_R(ana) = 0.95 min, (26.6 mg, 0.021 mmol, 18%)

^{1}H NMR (500 MHz, D_2O): δ 322.6, 292.5, 227.0, 222.1, 206.9, 196.1, 181.9, 178.4, 146.4, 118.4, 114.3, 14.6, 12.5, 10.2, -14.1, -19.9, -27.5, -35.2, -41.1, -46.5, -49.9, -60.5, -76.3, -86.8, -90.8, -99.8, -103.5, -132.1, -141.7, -152.0, -154.2, -165.9, -177.9, -333.0, -349.6, -377.7 ppm. Only major resolved peaks outside the +10 to -10 ppm range are reported.

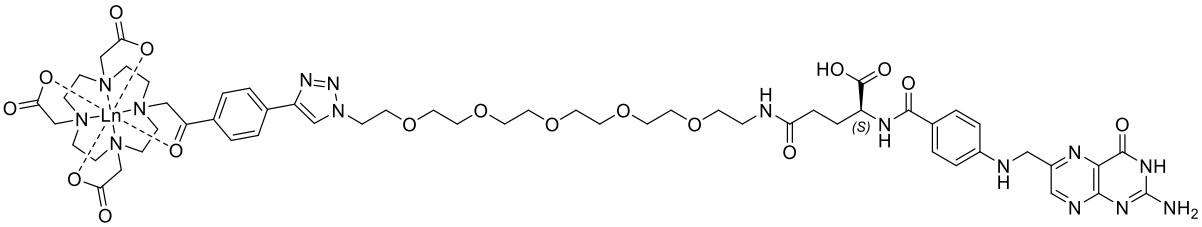
ES-MS (H_2O) (minor isomer) *m/z* 1270.38 $[M+H]^+$, 635.69 $[M+2H]^{2+}$; LC-MS (H_2O) 1266.0 $[M-H]^-$, 634.7 $[M+2H]^{2+}$. HRMS (ES^-), found (*m/z*): 1268.4174 $[M+H]^+$; $C_{48}H_{67}O_{16}N_{15}{}^{159}Tb$ requires 1268.4149.

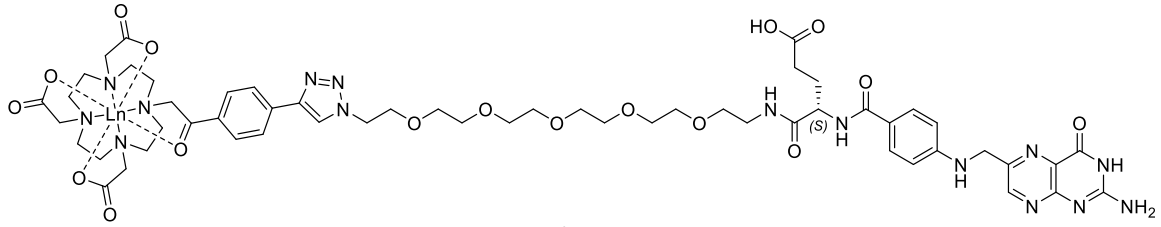
Minor isomer, t_R(prep) = 11.02 mins, t_R(ana) = 1.04 min (17.6 mg, 0.014 mmol, 12%)

^{1}H NMR (500 MHz, D_2O): δ 322.6, 292.6, 227.0, 221.9, 207.0, 196.3, 181.7, 178.2, 146.3, 118.3, 114.2, 14.3, 12.1, -14.3, -20.2, -27.6, -35.4, -41.3, -46.7, -50.0, -60.7, -76.3, -86.8, -90.9, -99.9, -103.6, -132.3, -141.7, -152.3, -154.0, -166.1, -177.8, -332.7, -349.4, -377.6 ppm. Only major resolved peaks outside the +10 to -10 ppm range are reported.

ES-MS (H_2O) (minor isomer) *m/z* 1270.38 $[M+H]^+$, 635.69 $[M+2H]^{2+}$; LC-MS (H_2O) 1267.9 $[M+H]^+$, 634.7 $[M+2H]^{2+}$. HRMS (ES^+), found (*m/z*): 1270.4297 $[M+H]^+$; $C_{48}H_{69}O_{16}N_{15}{}^{159}Tb$ requires 1270.4295 ($|\Delta m/z| = 0.22$ ppm).

Tb-1-(4'-ethynyl-2-acetophenone)-4,7,10-tris(carboxymethyl)-1,4,7,10-tetraazacyclododecane clicked to FA-PEG$_5$-N$_3$ (Ln$\mathbf{L}^7$)





Ln = Eu,Tb

Tb-1-(4'-ethynyl-2-acetophenone)-DO3A (0.0744 g, 0.12 mmol, 1.00 eq.) and FA-PEG$_5$-N$_3$ (0.101 g, 0.14 mmol, 1.20 eq.) were dissolved in H_2O/MeOH/DMSO (5.5 mL, 6:4:1). To this, $CuSO_4.5H_2O$ (2.88 mg, 0.012 mmol, 0.10 eq.) (115 µL of 0.1 M solution in H_2O) and sodium ascorbate (11.4 mg, 0.058 mmol, 0.50 eq.) were added and heated at 40 °C under Ar for 2 days monitored by LC-MS. The reaction mixture was concentrated under reduced pressure and then diluted in H_2O (50 mL) which was removed by lyophilisation. The yellow residue was then dissolved in H_2O (50 mL) and gently stirred with 2-3 g CupriSorb™ resin to remove copper for 24 hours. The insoluble CupriSorb™ was filtered, and the filtrate was dried *in vacuo* to yield the crude as a yellow residue (0.254 g, 0.2 mmol, crude 173%).

(Ln = Eu) From Eu-1-(4'-ethynyl-2-acetophenone)-DO3A (0.0202 g, 0.032 mmol, 1.00 eq.) yielded crude product as yellow powder (68.3 mg, 0.05 mmol, crude 158%).

^{1}H NMR (500 MHz, D_2O) (mixture of regioisomers) δ 45.1, 40.7, 36.9, 35.0, 33.0, 27.6, 26.1, 25.4, 23.0, 19.9, 12.5, 10.9, 1.3, 0.8, 0.3, 0.1, -0.4, -0.8, -1.7, -2.4, -3.1, -3.7, -4.1, -4.7, -5.9, -7.3, -7.9, -8.5, -9.2, -10.5, -11.5, -12.5, -13.1, -15.4, -16.0, -16.4, -18.4, -19.8, -21.2, -22.8, -23.9 ppm. Only major resolved peaks outside the +10 to 0 ppm range are reported.

LC-MS (H_2O) (mixture of regioisomers): 684.3 $[M+2H]^{2+}$, 1367.3 $[M+H]^+$.

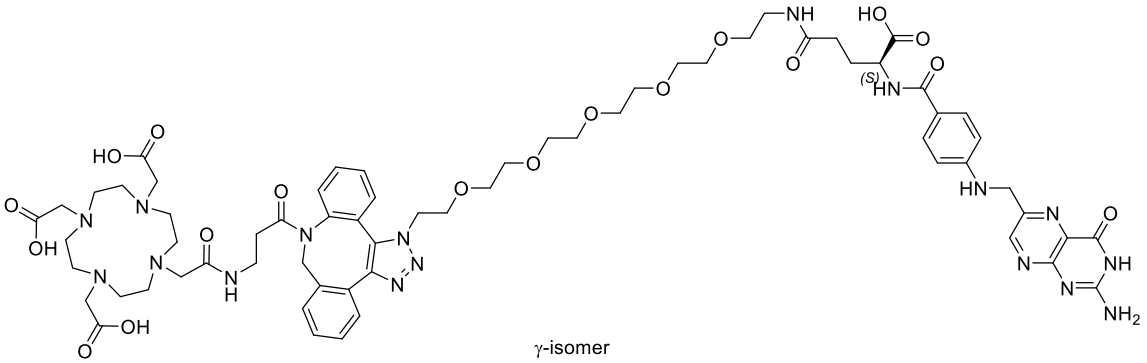
The compound was purified HPLC (A.9 HPLC conditions method 9) isolated the compound as a mixture of regioisomers from the impurities.

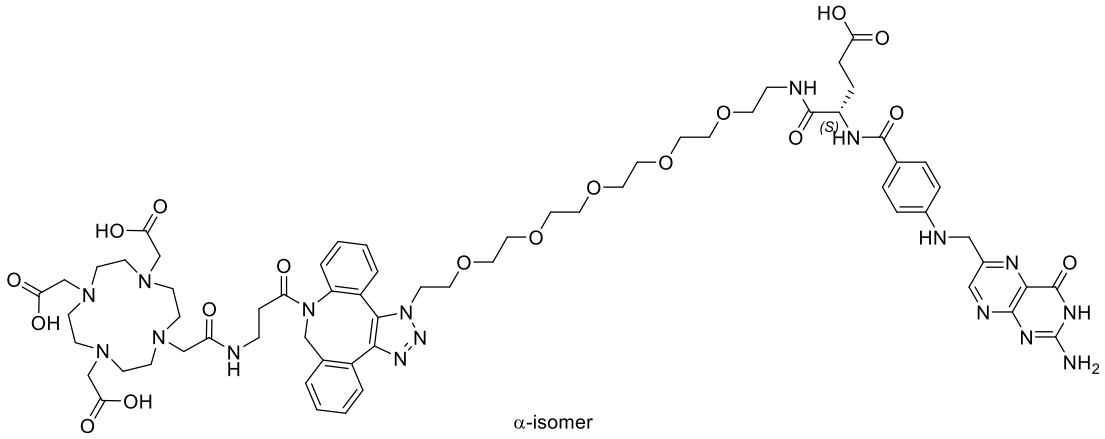
(Ln = Tb) From Tb-ethynylacetophenoneDO3A (50 mg, 0.078 mmol, 1.00 eq.) yielded product as yellow powder (41.1 mg, 0.03 mmol, 39 %) t_R(prep) = 13.4 mins, t_R(ana) = 1.16 mins.

^{1}H NMR (500 MHz, D_2O) (mixture of regioisomers) δ 305.5, 266.4, 257.4, 200.1, 195.8, 176.5, 135.5, 128.0, -18.2, -34.4, -39.8, -53.8, -78.0, -84.9, -95.9, -113.0, -132.3, -142.7, -158.9, -168.6, -185.4, -325.9, -431.3 ppm. Only major resolved peaks outside the +10 to -10 ppm range are reported.

ES-MS (MeOH) (mixture of regioisomers) *m/z* 687.7 $[M+2H]^{2+}$; LC-MS (MeOH) 686.6 $[M+2H]^{2+}$, 1372.5 $[M+H]^+$. HRMS (ES^+), found (*m/z*): 1374.4548 $[M+H]^+$; $C_{55}H_{73}O_{17}N_{15}{}^{159}Tb$ requires 1374.4557 ($|\Delta m/z| = 0.64$ ppm). HRMS (ES^-), found (*m/z*): 1372.4437 $[M-H]^-$; $C_{55}H_{71}O_{17}N_{15}{}^{159}Tb$ requires 1372.4411.

DOTA-DBCO clicked to FA-PEG$_5$-N$_3$ (L^8)

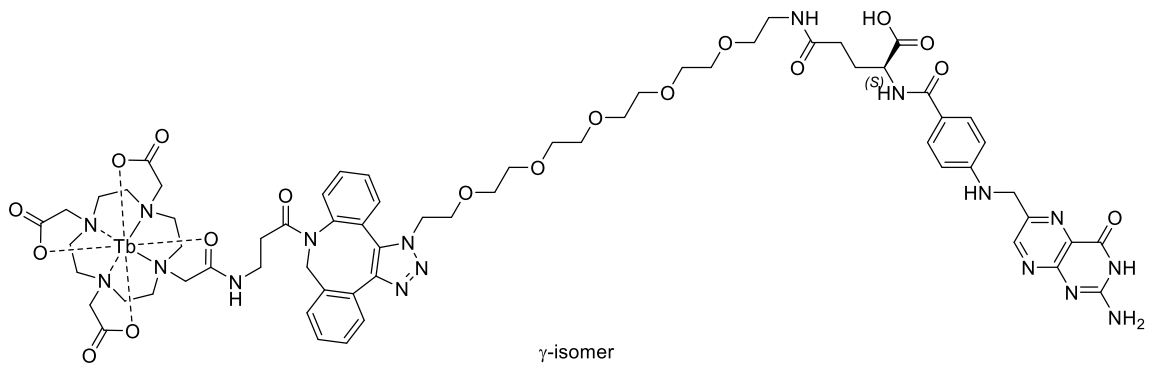


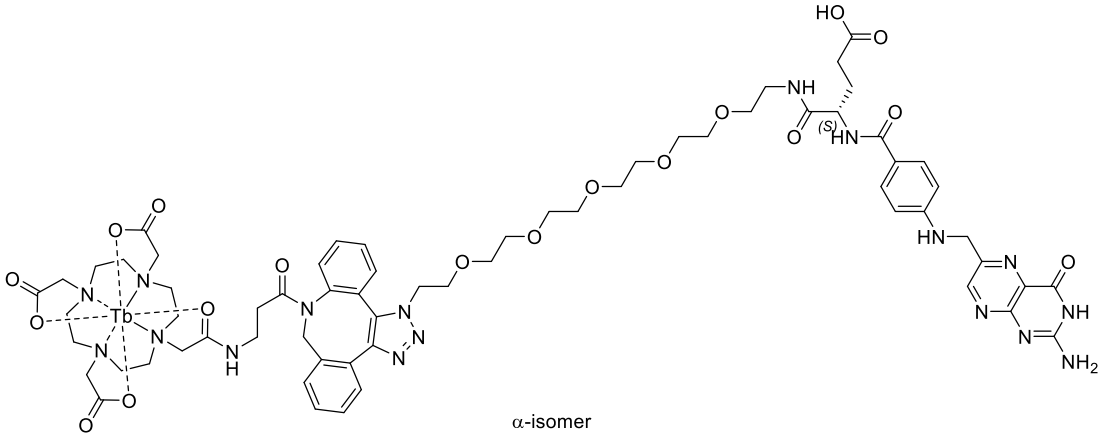


DOTA-DBCO (40mg, 0.05 mmol, 1.00 eq.) was dissolved in H_2O/MeCN (2 mL, 8:2) before FA-PEG$_5$-N$_3$ (36 mg, 0.05 mmol, 1.00 eq.) was added. The reaction mixture was stirred at room temperature and monitored by LC-MS. The reaction reached completion after 7 hours. Solvent was then removed *in vacuo* to yield a crude product as a yellow residue (67 mg, 0.048 mmol, 97%). The product was used in the next reaction without purification.

ES-MS (H_2O/MeCN (8:2)) (mixture of regioisomers) *m/z* 696.7 $[M+2H]^{2+}$, 1392.5 $[M+H]^+$; HRMS (ES^+), found (*m/z*): 1392.6331 $[M+H]^+$; $C_{65}H_{86}O_{18}N_{17}$ requires 1392.6331 ($|\Delta m/z| = 0.05$ ppm).

Tb-DOTA-DBCO clicked to FA-PEG$_5$-N$_3$ (Tb$\mathbf{L^8}$**)**





Method 1: Tb-DOTA-DBCO clicked to FA-PEG$_5$-N$_3$

Crude Tb-DOTA-DBCO, Tb$\mathbf{L^4}$ (59 mg, 0.05 mmol, 1.06 eq.) was dissolved in H_2O/MeCN (2 mL, 8:2). To this, FA-PEG$_5$-N$_3$, **25** (35 mg, 0.047 mmol, 1.00 eq.) was added and the reaction was stirred at room temperature for 24 hours. The reaction mixture was concentrated under reduced pressure and the residue dissolved in H_2O (8 mL) and removed by lyophilisation. The crude was purified by HPLC (A.10 HPLC conditions method 10). (33.7 mg, 0.022 mmol, 44%) t_R(prep) = 14.1 mins, t_R(ana) = 1.48 mins.

^{1}H NMR (500 MHz, D_2O) δ 256.0, 241.6, 202.8, 194.7, 111.4, 105.4, 65.7, 48.9, 45.7, 26.0, 19.7, 16.5, 15.5, 14.0, 13.0, 12.1, 11.9, 10.6, -46.0, -54.8, -67.0, -76.5, -78.7, -101.5, -110.4, -114.3, -125.0, -197.5, -211.4, -365.5, -374.5, -393.6 ppm.

ES-MS (H_2O/MeCN (8:2)) (mixture of regioisomers) *m/z* 1548.4 $[M+H]^+$, 775.2 $[M+2H]^{2+}$; HRMS (ES^+), found (*m/z*): 1570.5191 $[M+Na]^+$; $C_{65}H_{82}O_{18}N_{17}{}^{159}TbNa$ requires 1570.5169 ($|\Delta m/z| =$ 1.40 ppm).

Method 2: Tb-complexation of DOTA-DBCO clicked to FA-PEG$_5$-N$_3$

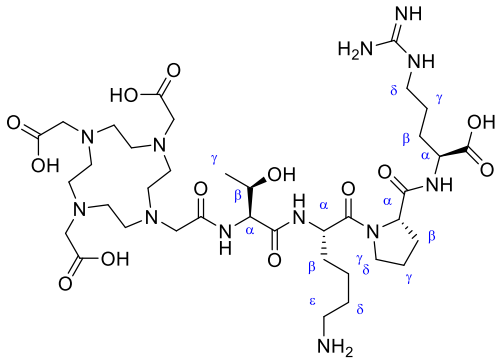
To a solution of the ligand, $\mathbf{L^8}$ (67 mg, 0.048 mmol, 1.00 eq) in H_2O/MeCN (3 mL, 7:3), $Tb(OTf)_3$ (31.4 mg, 0.0505 mmol, 1.08 eq.) was added and the reaction mixture was stirred at 60 °C for 30

min. The pH was adjusted to 4/5 by dropwise addition of an aqueous 1 M NaOH solution. The reaction was left to stir at 60 °C for 48 hours. The solvent was removed under reduced pressure and the residue was suspended in water. The pH of this solution was adjusted to 7 by addition of aqueous 1 M NaOH and the solvent was removed under reduced pressure. The crude was purified by HPLC (A.10 HPLC conditions method 10). (44 mg, 0.028 mmol, 59%) t_R(prep) = 14.0 mins, t_R(ana) = 1.51 mins.

^{1}H NMR (500 MHz, D_2O) δ 256.0, 241.6, 202.8, 194.7, 111.4, 105.4, 65.7, 48.9, 45.7, 26.0, 19.7, 16.5, 15.5, 14.0, 13.0, 12.1, 11.9, 10.6, -46.0, -54.8, -67.0, -76.5, -78.7, -101.5, -110.4, -114.3, -125.0, -197.5, -211.4, -365.5, -374.5, -393.6 ppm.

ES-MS (H_2O/MeCN (8:2)) (mixture of regioisomers) *m/z* 1548.4 $[M+H]^+$, 774.7 $[M+2H]^{2+}$; HRMS (ES^+), found (*m/z*): 1548.5352 $[M+H]^+$; $C_{65}H_{83}O_{18}N_{17}{}^{159}Tb$ requires 1548.5350 ($|\Delta m/z|$ = 0.16 ppm).

(DOTA)-NHCO-Thr-Lys-Pro-Arg-OH (L^9)



The following protected amino acids (1 mmol) (0.2 mol dm^{-3} solutions in DMF) were loaded into the peptide synthesiser in the order shown: N^{α}-Fmoc-Pro-OH (337 mg); N^{α}-Fmoc-Lys(Boc)-OH (468 mg); N^{α}-Fmoc-Thr(^{t}Bu)-OH (397 mg). Synthesis as general procedure using N^{α}-Fmoc-Arg(Pbf)-Wang resin (Sigma) (167 mg, 0.1 mmol, substitution 0.4-0.8 mmol/g) and carried out twice. Crude resin-bound peptide was transferred to a phase separator (Biotage) where it was washed with DMF (3 × 10 mL), DCM (3 × 10 mL) and dried under vacuum for 20 minutes. The resin was swollen with DCM (5 mL) for 2 hours, followed by DMF (5 mL) for 2 hours. After swelling the resin in DMF, anhydrous DMF (3 mL) and triethylamine (139.4 µL, 1 mmol, 10.0 eq.) was added and left for 30 minutes unstirred. DOTA-NHS ester (CheMatech) (0.990 g, 0.13 mmol, 1.30 eq.) was added and N_2 was bubbled through for 3 days. Deionised water (2 mL) was added to hydrolyse any excess DOTA-NHS and left to react for 1 hour. The resin was washed thoroughly with DMF (3 × 10 mL) and DCM (3 × 10 mL) and dried under vacuum for 20 minutes. A cleavage mix of TFA: H_2O: TIPS: 1,3-dimethoxybenzene (5 mL, 92.5: 2.5: 2.5: 2.5) was added to the resin and left unstirred for 3 hours. The filtrate was collected, and the resin washed with DMF (2 × 3 mL), DCM

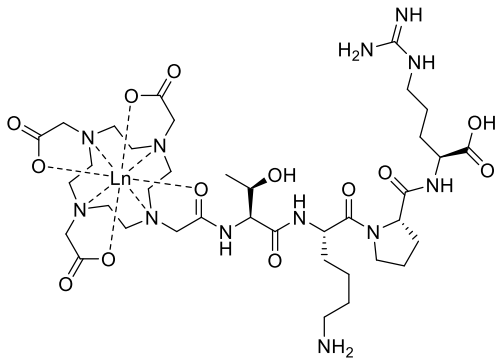
(50 mL) and MeOH (50 mL). Solvents were removed under reduced pressure using toluene to aid removal of DMF. The solid was further purified by HPLC (A.11 HPLC conditions method 11). The solvent was removed under reduced pressure and the compound was obtained as a clear, colourless solid (158 mg, 0.178 mmol, 89%).

^{1}H NMR (500 MHz, D_2O) δ 4.64 (t, $^{3}J_{H\text{-}H}$ = 7.0 Hz, 1H, Lys α), 4.44 (dd, $^{3}J_{H\text{-}H}$ = 8.4, 5.9 Hz, 1H, Pro α), 4.39-4.32 (m, 2H, Thr α and Arg α), 4.30-2.92 (br. overlapping m, 24 H, cyclen ring/arm) 4.19-4.13 (m, 1H, Thr β), 3.89 (dt, $^{2}J_{H\text{-}H}$ = 10.3, $^{3}J_{H\text{-}H}$ = 6.6 Hz, 1H, Pro δ), 3.66 (dt, $^{2}J_{H\text{-}H}$ = 10.3, $^{3}J_{H\text{-}H}$ = 7.0 Hz, 1H, Pro δ), 3.23 (t, $^{3}J_{H\text{-}H}$ = 6.9 Hz, 2H, Arg δ), 3.00 (t, $^{3}J_{H\text{-}H}$ = 7.6 Hz, 2H, Lys ε), 2.36-2.27 (m, 1H, Pro β), 2.08-1.99 (m, 2H, Pro γ), 1.99-1.89 (m, 2H, 1 × Pro β and 1 × Arg β), 1.86-1.63 (m, 7H, Lys β and δ, Arg γ and 1 × Arg β), 1.54-1.43 (m, 2H, Lys γ), 1.21 (d, $^{3}J_{H\text{-}H}$ = 6.4 Hz, 3H, Thr γ) ppm.

^{13}C NMR (126 MHz, D_2O) δ 175.2 (Arg ***C***O), 174.0 (Pro ***C***O), 171.9 (Thr ***C***O), 162.9 (q, $^{2}J_{C\text{-}F}$ = 35.7 Hz, ***C***OCF_3), 156.7 (Arg ε ***C***=*N*), 119.1 (), 116.3 (q, $^{1}J_{C\text{-}F}$ = 291.6 Hz, ***C***F_3), 67.2 (Thr β), 60.3 (Pro α), 58.9 (Thr α), 52.4 (Arg α), 51.5 (Lys α), 48.1 (Pro δ), 40.4 (Arg δ), 39.1 (Lys ε), 30.0 (Lys β/δ), 29.3 (Pro β), 27.5 (Arg β), 26.4 (Lys β/δ), 24.6 (Pro γ), 24.4 (Arg γ), 21.7 (Lys γ), 18.9 (Thr γ) ppm.

ES-MS(MeOH): *m/z* 888.5 $[M+H]^+$; HRMS (ES+), found (*m/z*): 887.4926 $[M+H]^+$; $C_{43}H_{77}N_{13}O_4$ requires: 887.4945 (|Δ *m/z*| = 2.13 ppm)

Lanthanide complexation of DOTA-tuftsin (LnL^{9})



Ln = Eu, Tb, Gd

$Ln(OTf)_3$ (1.00 eq.) was added to a solution of (DOTA)-NHCO-Thr-Lys-Pro-Arg-OH (1.00 eq.) in MeOH (1 mL). The solution was stirred at 60 °C for 30 minutes, the pH was adjusted to 5 using 1M NaOH aqueous solution, and the resultant solution was stirred at 60 °C for a further 48 hours. The MeOH was removed under reduced pressure. The resulting residue was dissolved in water and the pH adjusted to 7 using 1M NaOH solution. The resulting solution was dialysed in a 1000 MWCO Float-a-Lyzer before the solvent was removed to yield the complexes as a colourless powder.

(Ln = Eu) From $Eu(OTf)_3$ (11 mg, 0.018 mmol, 1.00 eq.) yielded a colourless powder (16 mg, 0.015 mmol, 82%).

^{1}H NMR (400 MHz, D_2O) δ 33.25, 31.60, 31.04, 30.76, 30.35, 12.31, 11.57, 10.47, 0.36, -0.27, -1.87, -2.54, -3.17, -3.73, -5.57, -7.33, -7.76, -11.35, -11.64, -12.15, -14.10, -14.46, -15.71, -16.56.

Luminescence lifetimes: H_2O: 0.62 ms, D_2O: 2.26 ms, q = 1.1.

ES-MS(MeOH): *m/z* 1059.2 $[M + Na]^+$, 519.2 $[M + 2H]^{2+}$

(Ln = Tb) From $Tb(OTf)_3$ (14 mg, 0.024 mmol, 1.00 eq.) yielded a colourless powder (15 mg, 0.014 mmol, 59%)

^{1}H NMR (400 MHz, D_2O) δ 265.4, 248.9, 232.5, 218.2, 125.3, 113.5, 111.0, 60.4, 58.2, 50.3, 46.6, 44.0, 35.2, 33.2, 28.3, 23.8, 20.1, -10.1, -15.4, -16.6, -17.3, -21.1, -21.9, -25.6, -31.7,-33.1, -35.2, -58.4, -65.6, -67.6, -71.9, -75.4, -98.7, -106.0, -113.0, -121.1, -131.1, -136.7, -191.5, -204.1, -367.2, -375.0, -388.5, -399.2, -405.2.

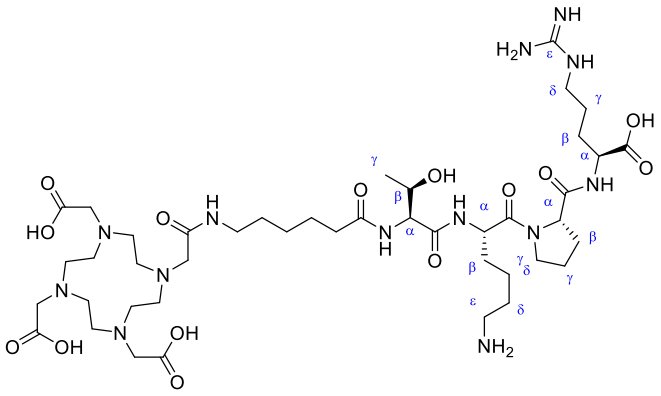
Luminescence lifetimes: H_2O: 1.93 ms, D_2O: 3.22 ms, q = 0.73.

ES-MS(MeOH): *m/z* 1043.26 $[M + H]^+$, 522.15 $[M + 2H]^{2+}$; HRMS (ES^+), found (*m/z*): 1043.3958 $[M+H]^+$; $C_{37}H_{64}O_{13}N_{12}{}^{159}Tb$ requires 1043.3964 ($|\Delta\ m/z|$ = 0.52 ppm).

(Ln = Gd) From $Gd(OTf)_3$ (45 mg, 0.074 mmol, 1.00 eq.) yielded a colourless powder (52.5 mg, 0.050 mmol, 68%)

ES-MS(MeOH): *m/z* 1042.36 $[M + H]^+$, 521.69 $[M + 2H]^{2+}$; HRMS (ES^+), found (*m/z*): 521.7014 $[M+2H]^{2+}$; $C_{37}H_{63}GdO_{13}N_{12}$ requires 521.7014 ($|\Delta\ m/z|$ = 0.4 ppm).

(DOTA)-$NHC_5H_{10}CO$-Thr-Lys-Pro-Arg-OH (L^{10})

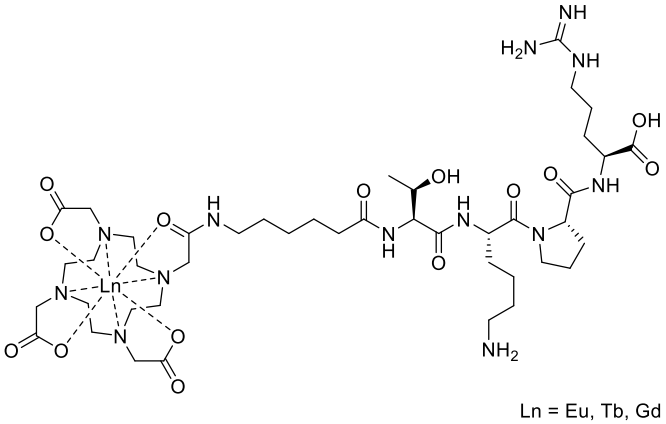


The following protected amino acids (1 mmol) (0.2 mol dm^{-3} solutions in DMF) were loaded into the peptide synthesiser in the order shown: N^{α}-Fmoc-Pro-OH (337 mg); N^{α}-Fmoc-Lys(Boc)-OH (468 mg); N^{α}-Fmoc-Thr(^{t}Bu)-OH (397 mg); Fmoc-$NHC_5H_{10}COOH$ (353 mg) (Fluorochem). Synthesis as general procedure using N^{α}-Fmoc-Arg(Pbf)-Wang resin (Sigma) (167 mg, 0.1 mmol, substitution 0.4-0.8 mmol/g) and carried out twice. Crude resin-bound peptide was transferred to a phase separator (Biotage) where it was washed with DMF (3 × 10 mL), DCM (3 × 10 mL) and dried

under vacuum for 20 minutes. The resin was swollen with DCM (5 mL) for 2 hours, followed by DMF (5 mL) for 2 hours. After swelling the resin in DMF, anhydrous DMF (3 mL) and trimethylamine (139.4 µL, 1 mmol, 10.0 eq.) was added and left for 30 minutes unstirred. DOTA-NHS ester (CheMatech) (0.914 g, 0.12 mmol, 1.20 eq.) was added and N_2 was bubbled through for 3 days. Deionised water (2 mL) was added to hydrolyse any excess DOTA-NHS and left to react for 1 hour. The resin was washed thoroughly with DMF (3 × 10 mL) and DCM (3 × 10 mL) and dried under vacuum for 20 minutes. A cleavage mix of TFA: H_2O: TIPS: 1,3-dimethoxybenzene (5 mL, 92.5: 2.5: 2.5: 2.5) was added to the resin and left unstirred for 3 hours. The filtrate was collected, and the resin washed with DCM (50 mL) and MeOH (50 mL). Solvents were removed under reduced pressure and the crude was dissolved in the minimum amount of MeOH and precipitated with Et_2O. The mixture was centrifuged, and the solid was collected, and the trituration repeated a further two times. The solid was further purified by HPLC (A.11 HPLC conditions method 11). t_R(prep) = 5.52 min, t_R(ana) = 6.40 min. The solvent was removed under reduced pressure and the compound was obtained as a clear, colourless solid (54 mg, 0.054 mmol, 27%).

^{1}H NMR (600 MHz, D_2O) δ 4.58 (dd, *J* = 8.5, 5.5 Hz, 1H), 4.37 (dd, *J* = 8.4, 6.1 Hz, 1H), 4.29 (dd, *J* = 9.1, 4.9 Hz, 1H), 4.24 – 4.19 (m, 1H), 4.10 – 4.03 (m, 1H), 3.79 (dt, *J* = 10.5, 6.6 Hz, 1H), 3.59 (dt, *J* = 10.5, 7.0 Hz, 1H), 2.94 (t, *J* = 7.6 Hz, 3H), 2.28 (tdd, *J* = 22.1, 20.1, 12.0, 4.8 Hz, 4H), 2.04 – 1.84 (m, 5H), 1.76 (ddt, *J* = 14.3, 10.1, 5.2 Hz, 2H), 1.65 (dq, *J* = 13.4, 7.3, 6.2 Hz, 5H), 1.56 (p, *J* = 7.7 Hz, 2H), 1.51 – 1.36 (m, 3H), 1.29 (tt, *J* = 15.2, 7.0 Hz, 3H), 1.13 (d, *J* = 6.3 Hz, 3H) ppm.
LC MS (MeOH): *m/z* 1000.6 $[M+H]^+$, 500.8 $[M+2H]^{2+}$; HRMS (ES+): found (*m/z*): 1000.5790 $[M+H]^+$; $C_{43}H_{77}N_{13}O_4$ requires: 1000.5786 ($|\Delta\ m/z|$ = 0.47 ppm).

Lanthanide complexation of (DOTA)-NHC$_5$H$_{10}$CO-Thr-Lys-Pro-Arg-OH (LnL^{10})



$Ln(OTf)_3$ (1.00 eq.) was added to a solution of (DOTA)-NHC$_5$H$_{10}$CO-Thr-Lys-Pro-Arg-OH (1.00 eq.) in MeOH (600 µL). The solution was stirred at 60 °C for 30 minutes, the pH was adjusted to 5 using 1M NaOH aqueous solution, and the resultant solution was stirred at 60 °C for a further 48 hours. The MeOH was removed under reduced pressure. The resulting residue was dissolved in water

and the pH adjusted to 7 using 1M NaOH solution. The resulting solution was dialysed in a 1000 MWCO Float-a-Lyzer before the solvent was removed to yield the complexes as a colourless powder.

(Ln = Eu) From $Eu(OTf)_3$ (15 mg, 0.025 mmol, 1.00 eq.) yielded a colourless powder (21 mg, 0.018 mmol, 72%).

^{1}H NMR (400 MHz, D_2O) δ 33.0, 32.5, 31.6, 12.7, 12.1, 0.1, -0.4, -1.8, -2.7, -4.0, -5.1, -6.0, -6.6, -7.2, -7.8, -9.9, -10.7, -12.5, -12.8, -15.0, -16.0 ppm.

ES-MS (MeOH): *m/z* 575.7 $[M+2H]^{2+}$ 586.7 $[M+Na+H]^{2+}$ LC-MS (MeOH): *m/z* 575.7 $[M+2H]^{2+}$

Luminescence lifetimes: H_2O: 0.56 ms, D_2O: 2.32 ms, q = 1.3.

(Ln = Tb) From $Tb(OTf)_3$ (9 mg, 0.029 mmol, 1.00 eq.) yielded a colourless powder (14 mg, 0.012 mmol, 88%)

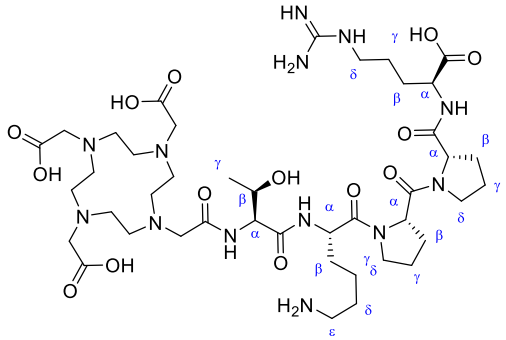
^{1}H NMR (400 MHz, D_2O) δ 258.4, 248.2, 242.2, 194.3, 180.1, 107.3, 102.2, 77.5, 55.6, 53.4, 25.3, 20.2, 18.5, 14.0, -73.6, -79.5, -82.8, -102.8, -109.4, -111.9, -117.2, -374.4, -384.8, -394.2 ppm.

ES-MS (MeOH): *m/z* 1157.7 $[M + H]^+$, 579.4 $[M + 2H]^{2+}$; HRMS (ES^+), found (*m/z*): 578.7442 $[M+2H]^{2+}$; $C_{43}H_{76}O_{14}N_{13}{}^{159}Tb$ requires 578.7439 ($|\Delta\ m/z|$ = 0.59 ppm).

(Ln = Gd) From $Gd(OTf)_3$ (17 mg, 0.029 mmol, 1.00 eq.) yielded a colourless powder (27 mg, 0.023 mmol, 84%)

ES-MS(MeOH): 577.3 $[M+2H]^{2+}$. HRMS (ES^-), found (*m/z*): 1153.4642 $[M-H]^-$; $C_{43}H_{73}O_{14}N_{13}Gd$ requires 1153.4646 ($|\Delta\ m/z|$ = 0.35 ppm).

(DOTA)-NHCO-Thr-Lys-Pro-Pro-Arg-OH (L^{11})



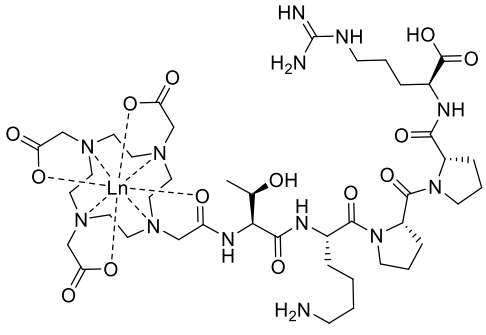
The following protected amino acids (1 mmol) (0.2 mol dm^{-3} solutions in DMF) were loaded into the peptide synthesiser in the order shown: N^{α}-Fmoc-Pro-OH (674 mg); N^{α}-Fmoc-Lys(Boc)-OH (468 mg); N^{α}-Fmoc-Thr(^{t}Bu)-OH (397 mg). Synthesis as general procedure using N^{α}-Fmoc-Arg(Pbf)-Wang resin (Sigma) (167 mg, 0.1 mmol, substitution 0.4-0.8 mmol/g) and carried out twice. Crude resin-bound peptide was transferred to a phase separator (Biotage) where it was washed with DMF (3 × 10 mL), DCM (3 × 10 mL) and dried under vacuum for 20 minutes. The resin was

swollen with DCM (5 mL) for 2 hours, followed by DMF (5 mL) for 2 hours. After swelling the resin in DMF, anhydrous DMF (3 mL) and trimethylamine (139.4 µL, 1 mmol, 10.0 eq.) was added and left for 30 minutes unstirred. DOTA-NHS ester (CheMatech) (0.914 g, 0.13 mmol, 1.30 eq.) was added and N_2 was bubbled through for 3 days. Deionised water (2 mL) was added to hydrolyse any excess DOTA-NHS and left to react for 1 hour. The resin was washed thoroughly with DMF (3 × 10 mL) and DCM (3 × 10 mL) and dried under vacuum for 20 minutes. A cleavage mix of TFA: H_2O: TIPS: 1,3-dimethoxybenzene (5 mL, 92.5: 2.5: 2.5: 2.5) was added to the resin and left unstirred for 3 hours. The filtrate was collected, and the resin washed with DCM (50 mL) and MeOH (50 mL). Solvents were removed under reduced pressure. The solid was further purified by HPLC (A.11 HPLC conditions method 11). The solvent was removed under reduced pressure and the compound was obtained as a clear, colourless solid (140 mg, 0.14 mmol, 71%). t_R (prep-DOTA-pentapeptide) t_R (ana)= 14.84 min.

^{1}H NMR (500 MHz, D_2O) δ 4.61 (dd, *J* = 8.4, 6.0 Hz, 1H), 4.55 (dd, *J* = 8.3, 5.7 Hz, 1H), 4.36 (dd, *J* = 8.7, 4.8 Hz, 1H), 4.29 – 4.24 (m, 2H), 4.12 – 4.05 (m, 1H), 3.80 (dt, *J* = 10.1, 6.6 Hz, 1H), 3.70 (dt, *J* = 10.1, 7.0 Hz, 1H), 3.56 (ddt, *J* = 17.3, 10.1, 6.8 Hz, 2H), 3.12 (t, *J* = 6.9 Hz, 2H), 2.90 (t, *J* = 7.6 Hz, 2H), 2.27 (ddt, *J* = 13.1, 8.6, 6.8 Hz, 1H), 2.20 (ddd, *J* = 12.6, 8.3, 5.9 Hz, 1H), 1.95 (tdd, *J* = 14.5, 6.9, 2.5 Hz, 4H), 1.90 – 1.78 (m, 2H), 1.71 (pd, *J* = 8.9, 8.1, 3.3 Hz, 1H), 1.62 – 1.54 (m, 3H), 1.45 – 1.30 (m, 2H), 1.11 (d, *J* = 6.4 Hz, 3H).

ES-MS(MeOH): *m/z* 984.654 $[M + H]^+$, 492.796 $[M + 2H]^{2+}$ HRMS (ES^+), found (*m/z*): 984.5456 $[M+H^+]$; $C_{42}H_{74}O_{14}N_{13}$ requires 984.5473 (|Δ *m/z*| = 1.70 ppm).

Lanthanide complexation of DOTA-pentapeptide (Ln$\mathbf{L^{11}}$)



$Ln(OTf)_3$ (1.00 eq.) was added to a solution of (DOTA)-NHCO-Thr-Lys-Pro-Pro-Arg-OH (1.00 eq.) in MeOH (1 mL). The solution was stirred at 60 °C for 30 minutes, the pH was adjusted to 5 using 1M NaOH aqueous solution, and the resultant solution was stirred at 60 °C for a further 48 hours. The MeOH was removed under reduced pressure. The resulting residue was dissolved in water and the pH adjusted to 7 using 1M NaOH solution. The resulting solution was dialysed in a 1000 MWCO Float-a-Lyzer before the solvent was removed to yield the complexes as a colourless powder.

(Ln = Eu) From $Eu(OTf)_3$ (26 mg, 0.043 mmol, 1.00 eq.) yielded a colourless powder (41.3 mg, 0.036 mmol, 86%).

^{1}H NMR (400 MHz, D_2O) δ 33.7, 33.0, 32.4, 31.4, 30.9, 30.6, 12.1, 11.6, 10.5, 4.8, 0.3, -0.4, -1.9, -2.6, -3.3, -3.7, -4.4, -5.6, -7.3, -7.4, -7.8, -11.4, -11.7, -12.2, -13.3, -14.2, -14.6, -15.7, -16.6. Luminescence lifetimes: H_2O: 0.61 ms, D_2O: 2.17 ms, q = 1.1.

ES-MS(MeOH): *m/z* 567.76 $[M + 2H]^{2+}$ LC-MS (MeOH): *m/z* 1133.11 $[M+H]^+$, 567.072 $[M+2H]^{2+}$. HRMS (ES^+), found (*m/z*): 1134.4480 $[M+H^+$, $C_{42}H_{71}O_{14}N_{13}Eu$ requires 1134.4455 ($|\Delta$ *m/z*$|$ = 2.14 ppm).

(Ln = Tb) From $Tb(OTf)_3$ (32 mg, 0.053 mmol) yielded a colourless powder (35.5 mg, 0.031 mmol, 58%)

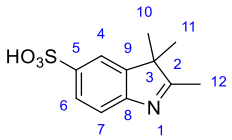
^{1}H NMR (400 MHz, D_2O) δ 269.3, 253.5, 230.8, 220.0, 124.5, 112.7, 110.2, 72.3, 63.3, 48.0, 44.0, 35.6, 31.9, 28.3, 22.2, 19.4, 16.6, 15.6, 14.8, 13.3, 11.3, 10.5, -16.9, -18.8, -21.9, -24.8, -27.2, -35.0, -37.4, -59.5, -66.5, -72.6, -74.8, -99.5, -106.8, -112.8, -121.9, -130.8, -136.3, -368.5, -376.1, -399.7 ppm. Luminescence lifetimes: H_2O: 1.82 ms, D_2O: 3.29 ms, q = 0.9.

ES-MS(MeOH): *m/z* 570.78 $[M+2H]^{2+}$, HRMS (ES^-), found (*m/z*): 1138.470 $[M+H^-]$; $C_{42}H_{69}O_{14}N_{13}{}^{159}Tb$ requires 1138.4346 ($|\Delta$ *m/z*$|$ = 2.16 ppm).

(Ln = Gd) From $Gd(OTf)_3$ (26 mg, 0.043 mmol) yielded a colourless powder (46.4 mg, 0.041 mmol, 96%)

ES-MS(MeOH): *m/z* 569.33 $[M + 2H]^{2+}$ LC-MS (MeOH): *m/z* 1138.094 $[M+H]^+$, 569.599 $[M+2H]^{2+}$. HRMS (ES^+), found (m/z): 1139.4506 $[M+H^+]$; $C_{42}H_{71}O_{14}N_{13}Gd$ requires 1139.4479 ($|\Delta$ *m/z*$|$ = 2.6 ppm).

2,3,3-trimethyl-*3H*-indole-5-sulfonic acid[16, 26] (26)

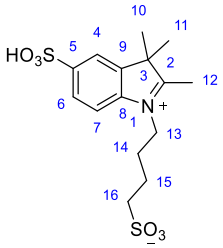


Prepared with minor adaptation from the procedure described by Pham *et al.*[26] and König *et al.*[16] Hydrazinobenzenesulfonic acid (5.00 g, 26.6 mmol, 1.00 eq.), sodium acetate (4.36 g, 53.2 mmol, 2.00 eq.) and 3-methyl-butan-2-one (8.40 mL, 78.4 mmol, 2.95 eq.) were stirred in glacial acetic acid (30 mL) at 130 °C for 5 hours under N_2. After cooling to room temperature, Et_2O was added carefully to the stirring red solution until a precipitate was observed. The precipitate was isolated *via* filtration, then washed with copious amounts of Et_2O. The solid material was collected and dried *in vacuo* to yield 2,3,3-trimethyl-*3H*-indole-5-sulfonic acid as a pink-brown powder (10.54 g, 44.0 mmol, 166%). The crude contained acetic acid as an impurity and was used in the next step without further purification.

A small portion of the crude was purified further by dissolving in minimal MeOH and precipitation with excess Et_2O. The solid was isolated by centrifugation (4000 rpm, 4 °C, 5 minutes), discarding the supernatant. This solid was triturated a further two times from MeOH and Et_2O, centrifuged and dried under reduced pressure.

^{1}H NMR (400 MHz, D_2O) δ 7.82 (d, $^4J_{H\text{-}H}$ = 1.8 Hz, 1H, ***H4***), 7.78 (dd, $^3J_{H\text{-}H}$ = 8.1 Hz, $^4J_{H\text{-}H}$ = 1.9 Hz, 1H, ***H6***), 7.53 (d, $^3J_{H\text{-}H}$ = 8.1 Hz, 1H, ***H7***), 1.93 (s, 3H, ***H12***), 1.28 (s, 6H, ***H10***/***H11***) ppm.
^{13}C NMR (101 MHz, D_2O) δ 194.8, 181.5 (***C2***), 154.1 (***C5***), 146.4 (***C9***), 139.7 (***C8***), 125.6 (***C6***), 119.3 (***C4***), 118.9 (***C7***), 54.2 (***C3***), 23.3 (***C12***), 21.8 (***C10***/***C11***) ppm.
ES-MS (MeOH) *m/z*: 240.0 $[M+H^+]$, 262.0 $[M+Na]^+$,238.0 $[M-H]^-$.

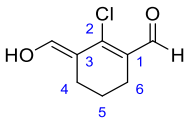
5-sulfo-1-(4-sulfobutyl)-2,3,3-trimethyl-3H-indolium betaine[26, 27] (27)



Prepared with minor adaptation from the procedure described by Pham *et al.*[26] and Mujumdar *et al.*[27] 2,3,3-Trimethyl-3*H*-indole-5-sulfonic acid, **26** (4.00 g, 16.7 mmol, 1.00 eq.) and 1,4-butanesultone (2.05 mL, 20.0 mmol, 1.20 eq.) were suspended in 1,2-dichlorobenzene (25 mL) and stirred at 110 °C for 16 hours under Ar. After cooling to room temperature, the suspension was centrifuged (4000 rpm, 4 °C, 10 minutes), and the supernatant was discarded. The solid pellet was dissolved in minimal H_2O (~5 mL) and precipitated with *i*PrOH (~200 mL) and centrifuged (4000 rpm, 4 °C, 10 minutes), discarding the supernatant, this was carried out twice. The solid was transferred using H_2O and the solvent was removed to afford the product as a dark pink powder (3.03 g, 8.07 mmol, 48%).

^{1}H NMR (500 MHz, D_2O) δ 8.14 (d, $^4J_{H\text{-}H}$ = 1.7 Hz, 1H, ***H4***), 8.05 (dd, $^3J_{H\text{-}H}$ = 8.4 Hz, $^4J_{H\text{-}H}$ = 1.7 Hz, 1H, ***H6***), 7.94 (d, $^3J_{H\text{-}H}$ = 8.5 Hz, 1H, ***H7***), 4.57 (t, $^3J_{H\text{-}H}$ = 7.8 Hz, 2H, ***H13***), 2.99 (t, $^3J_{H\text{-}H}$ = 7.6 Hz, 2H, ***H16***), 2.17 – 2.11 (m, 2H, ***H14***), 1.99 -1.88 (m, 2H, ***H15***), 1.63 (s, 6H, ***H10***/***H11***) ppm.
^{13}C NMR (126 MHz, D_2O) δ 199.3 (N=***C2***), 174.7, 144.0 (***C8***), 142.8 (***C5***), 142.6 (***C9***), 126.9 (***C6***), 120.9 (***C4***), 115.8 (***C7***), 64.8, 54.9 (***C3***), 50.5, 49.9 (***C16***), 47.7 (***C13***), 26.6, 25.8 (***C14***), 21.5 (***C10***/***C11***), 21.4 (***C15***), 20.8, 20.4 ppm.
ES-MS (MeOH) *m/z* 376.5 $[M+H]^+$, 398.5 $[M+Na]^+$, 374.6 $[M-H]^-$; HRMS (ES^-), found (*m/z*): 374.07375 $[M-H]^-$; $C_{15}H_{20}O_6N^{32}S_2^-$ requires 374.07375 ($|\Delta m/z| = 0.00$ ppm).

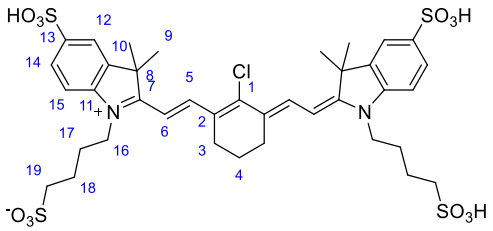
(E)-2-chloro-3-(hydroxymethylene)cyclohex-1-enecarbaldehyde[28, 29] (28)



Prepared with minor adaptation from the procedure described by An *et al.*[28] and Sim *et al.*[29] Phosphoryl chloride (17 mL, 0.18 mol, 3.60 eq.) was dissolved in anhydrous DCM (17 mL) and added dropwise to a flame dried Schlenk flask with anhydrous DMF (25 mL, 0.32 mol, 6.40 eq.) at 0 °C whilst stirring. After stirring for 30 minutes as 0 °C, cyclohexanone (5.25 mL, 0.05 mol, 1.00 eq.) was added and the mixture was heated to 50 °C for 6 hours. The reaction mixture was allowed to cool to room temperature before being poured onto ice (80 g) and stirred overnight with a surrounding container of dry ice. The mixture was filtered through a celite pad to obtain a pale-yellow precipitate. The solid was collected and dissolved in acetone and filtered again to remove any celite. The solvent was removed *in vacuo* and the solid was recrystallised from a small volume of hot acetone. The yellow precipitate was obtained *via* filtration and dried under vacuum (5.75 g, 0.033 mol, 66%). The compound was prepared as needed and used immediately in the next step as it does not store well.

^{1}H NMR (400 MHz, DMSO-d_6) δ 10.86 (br. s, 1H, enol O***H***), 10.16 (s, 1H, CO***H***), 7.61 (s, 1H, enol ***H***), 2.35 (t, $^3J_{H\text{-}H}$ = 6.2 Hz, 4H, ***H4***/***H6***), 1.57 (p, $^3J_{H\text{-}H}$ = 6.2 Hz, 2H, ***H5***) ppm.
^{13}C NMR (126 MHz, DMSO-***d*$_6$**) δ 189.6 (br. s), 149.7, 146.3 (br. s), 127.4 (br. s), 112.9 (br. s), 23.8 (***C4***/***C6***), 20.1 (***C5***) ppm.
ES-MS (MeOH): *m/z* 171.0 $[M\text{-}H]^-$; LC-MS (MeOH) found *m/z* 173.0 $[M+H]^+$. **HRMS**(ESI^+) found (*m/z*): 173.0366 $[M+H]^+$; $C_8H_{10}O_2Cl$ requires 173.0364 ($|\Delta m/z|$ = 1.02 ppm).

5,5'-sulfo *meso*-chloro dye[16] (PA-2)



Prepared using the procedure described by König *et al.*[16] **27** (1.50 g, 4.00 mmol, 2.10 eq.), **28** (0.328 g, 1.90 mmol, 1.00 eq.) and sodium acetate (0.312 g, 3.8 mmol, 2.00 eq.) were suspended in MeOH (48 mL) before acetic anhydride (48 mL) was added and the reaction mixture was heated to 80 °C for 3 hours. After cooling to room temperature, Et_2O was added until a precipitate formed. The precipitate was isolated by centrifugation (4750 rpm, 4 °C, 15 minutes), dissolved in a small amount of H_2O, and precipitated with an excess of 2-propanol. The solid was separated by centrifugation and the trituration was repeated in total three times using minimal H_2O and excess

2-propanol. The solid was isolated and dried under reduced pressure to afford the product as a green solid (1.01 g, 1.06 mmol, 56%).

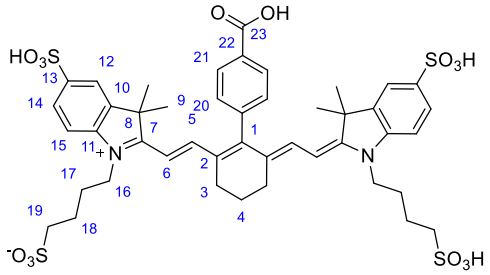
^{1}H NMR (500 MHz, D_2O) δ 8.31 (d, $^{3}J_{H\text{-}H}$ = 13.9 Hz, 2H, ***H5***), 7.88 (d, $^{4}J_{H\text{-}H}$ = 1.7 Hz, 2H, ***H12***), 7.78 (dd, $^{3}J_{H\text{-}H}$ = 8.4 Hz, $^{4}J_{H\text{-}H}$ = 1.8 Hz, 2H, ***H14***), 7.33 (d, $^{3}J_{H\text{-}H}$ = 8.4 Hz, 2H, ***H15***), 6.23 (d, $^{3}J_{H\text{-}H}$ = 14.0 Hz, 2H, ***H6***), 4.16 (br. t, 4H, ***H16***), 2.96 (t, $^{3}J_{H\text{-}H}$ = 7.6 Hz, 4H, ***H19***), 2.54 (br. s, 4H, ***H3***), 1.99-1.91 (m, 4H, ***H17***/***H18***), 1.91-1.83(m, 4H, ***H17***/***H18***), 1.77 (m, 2H, ***H4***), 1.71 (s, 12H, ***H9***) ppm.

^{13}C NMR (126 MHz, D_2O) δ 173.5 (***C7***), 150.3 (***C2***), 144.7 (***C5***), 144.3 (***C13***), 141.8 (***C10***), 139.0 (***C11***), 128.3 (***C1***), 126.5 (***C14***), 119.8 (***C12***), 110.9 (***C15***), 102.0 (***C6***), 50.4 (***C19***), 49.2 (***C8***), 43.8 (***C16***), 27.1 (***C9***), 25.8 (***C3***), 25.6 (***C9***, ***C17***), 21.7 (***C18***), 20.3 (***C4***) ppm.

LC-MS (MeOH) *m/z* 886.3 $[M\text{-}H]^{-}$, 442.2 $[M\text{-}2H]^{2-}$.

UV-Vis (H_2O): λ_{max} 782 nm.

Heptamethine cyanine dye[16, 30] (PA-3)



Prepared with minor adaptation from the procedure described by Lee *et al.*[30] and König *et al.*[16] **PA-2** (0.40 g, 0.42 mmol, 1.00 eq.) and 4-carboxyphenylboronic acid (0.125 g, 0.76 mmol, 1.80 eq.) were dissolved in degassed H_2O (~50 mL) and heated under reflux in the presence of $Pd(PPh_3)_4$ (0.032 g, 0.027 mmol, 0.06 eq.) for 18-24 hours under Ar in the dark. The reaction progress was monitored by TLC using alumina plates with MeCN/ H_2O (7:3) until the *meso*-chloro dye disappeared. The reaction mixture was then cooled to room temperature, and H_2O was removed *in vacuo*. The solid was isolated by trituration with minimal MeOH and excess acetone and centrifuged (4750 rpm, 15 minutes, 4 °C), discarding the supernatant. The trituration was repeated once more and the precipitate was dried under high vacuum to yield a dark green powder (0.34 g, 0.354 mmol, 85%).

^{1}H NMR (600 MHz, DMSO-d_6) δ 8.19 (d, $^{2}J_{H\text{-}H}$ = 8.0 Hz, 2H, ***H21***), 7.62 – 7.56 (m, 4H, ***H12***/***H14***), 7.41 (d, $^{2}J_{H\text{-}H}$ = 8.0 Hz, 2H, ***H15***), 7.30 (d, $^{2}J_{H\text{-}H}$ = 8.2 Hz, 2H, ***H20***), 7.01 (d, $^{3}J_{H\text{-}H}$ = 13.9 Hz, 2H, ***H6***), 6.27 (d, $^{3}J_{H\text{-}H}$ = 14.1 Hz, 2H, ***H5***), 4.12 (br. t, $^{3}J_{H\text{-}H}$ = 7.3 Hz, 4H, ***H16***), 2.71 (t, $^{3}J_{H\text{-}H}$ = 6.2 Hz, 4H, ***H3***), 2.58 (t, *J* = 7.2 Hz, 4H, ***H19***), 2.00 – 1.94 (m, 2H, ***H4***), 1.79 – 1.67 (m, 8H, ***H17***/***H18***), 1.10 (s, 12H, ***H9***) ppm.

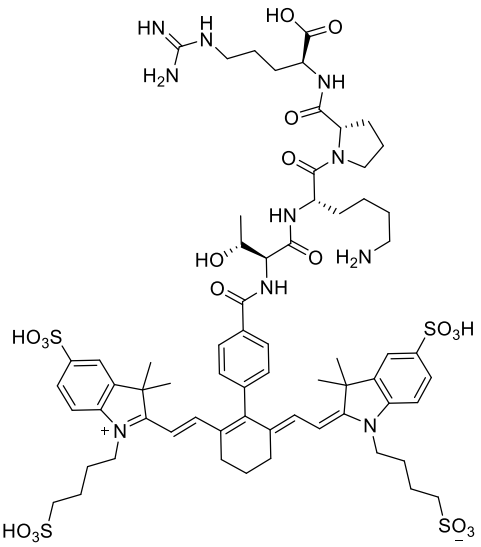
^{13}C NMR (151 MHz, DMSO-d_6) δ 171.3 (**C*7***), 166.9 (**C*23***), 159.8 (**C*1***), 146.5 (**C*6***), 145.1, 143.3, 142.0, 139.9, 131.0 (**C*2***), 130.4, 129.54 (**C*20***), 129.50 (**C*21***), 126.1 (**C14**), 119.7 (**C*12***), 110.2

(**C*15***), 100.7 (**C*5***), 50.7 (***C19***), 48.2 (**C*8***), 43.5 (**C*16***), 26.9 (**C*9***), 25.8 (**C*17*/C*18***), 25.3, 24.1 (**C*3***), 22.3 (**C*17*/C*18***), 20.8 (**C*4***) ppm.

ES-MS (MeOH): found *m/z* 971 $[M-H]^-$, **LC-MS** (MeOH) *m/z* 973.2 $[M+H]^+$.

UV-Vis (H_2O): λ_{max} 760 nm.

Heptamethine cyanine attached to tuftsin (PA-4)



The procedure was adapted from solid-phase synthesis protocols. To the tuftsin peptide conjugated resin (~0.15 mmol, 1.00 eq.) DCM (5 mL) was added to swell the resin for 2 hours followed by DMF (5 mL) for 2 hours in a biotage phase separator. A solution of heptamethine cyanine dye (0.204 g, 0.21 mmol, 1.40 eq.), HATU (0.086 g, 0.225 mmol, 1.50 eq.) and DIPEA (52.3 µL, 0.3 mmol, 2.00 eq.) in DMF (3 mL) was stirred for 10 minutes to preactivate. The activated mixture was added to the drained swollen resin and bubbled with N_2 to agitate the mixture for 3 days. Following completion, the resin was washed with DMF (3 × 10 mL) and iPrOH (3 × 10 mL) and dried in the isolute column under vacuum for 20 minutes. The product was cleaved from the resin using cleavage cocktail (TFA: H_2O: TIPS (8 mL, 95:2.5:2.5)). The resin was washed with DCM (3 × 5 mL), *i*-PrOH (3 × 10 mL) and H_2O (2 × 5 mL) before being concentrated under reduced pressure. The concentrated solution (~13 mL) was triturated in Et_2O (~ 400 mL) to afford a green precipitate and centrifuged (4750 rpm, 4 °C, 15 minutes). The supernatant was discarded, and the crude product was dried to yield a fine green powder (0.195 g, 0.13 mmol, crude 89%). The precipitate was further purified by HPLC (A.12 HPLC conditions method 12) to yield the product as a fine green powder.

LC-MS (MeOH) *m/z* 1456.3 $[M+H]^+$; 728.4 $[M+2H]^{2+}$. HRMS (ESI^+), found (*m/z*): 728.2701 $[M+2H]^{2+}$; $C_{66}H_{92}O_{19}N_{10}S_4$ requires 728.2694 ($|\Delta m/z| = 0.73$ ppm).

UV-Vis (H_2O): λ_{max} 764 nm.

7.2 References

1. X. L. Dean-Ben, A. Buehler, V. Ntziachristos and D. Razansky, *IEEE Trans. Med. Imaging*, 2012, **31**, 1922-1928.
2. A. Dadabhoy, S. Faulkner and P. G. Sammes, *J. Chem. Soc., Perkin Trans. 2* , 2002, 348-357.
3. M. Jauregui, W. S. Perry, C. Allain, L. R. Vidler, M. C. Willis, A. M. Kenwright, J. S. Snaith, G. J. Stasiuk, M. P. Lowe and S. Faulkner, *Dalton Trans.*, 2009, 6283-6285.
4. L. Tear, PhD thesis, University of Oxford, 2018.
5. C. Wu, X. Xin, Z. M. Fu, L. Y. Xie, K. J. Liu, Z. Wang, W. Y. Li, Z. H. Yuan and W. M. He, *Green Chem.*, 2017, **19**, 1983-1989.
6. R. C. Chadwick, S. Van Gyzen, S. Liogier and A. Adronov, *Synthesis*, 2014, **46**, 669-677.
7. T. Cruchter, K. Harms and E. Meggers, *Chem. Eur. J.*, 2013, **19**, 16682-16689.
8. E. Murrell, M. S. Kovacs and L. G. Luyt, *ChemMedChem*, 2018, **13**, 1625-1628.
9. G. Naturale, M. Lamblin, C. Commandeur, F. X. Felpin and J. Dessolin, *Eur. J. Org. Chem.*, 2012, **2012**, 5774-5788.
10. M. S. Cherevin, Z. P. Zubreichuk, L. A. Popova, T. G. Gulevich and V. A. Knizhnikov, *Russ. J. Gen. Chem.*, 2007, **77**, 1576-1579.
11. A. Kuzmin, A. Poloukhtine, M. A. Wolfert and V. V. Popik, *Bioconjugate Chem.*, 2010, **21**, 2076-2085.
12. D. X. Zeng, N. S. Lee, Y. J. Liu, D. Zhou, C. S. Dence, K. L. Wooley, J. A. Katzenellenbogen and M. J. Welch, *ACS Nano*, 2012, **6**, 5209-5219.
13. Y. Liang, X. Jiang, R. Yuan, Y. Zhou, C. X. Ji, L. M. Yang, H. F. Chen and Q. Wang, *Anal. Chem.*, 2017, **89**, 538-543.
14. A. F. Trindade, R. F. M. Frade, E. M. S. Macoas, C. Graca, C. A. B. Rodrigues, J. M. G. Martinho and C. A. M. Afonso, *Org. Biomol. Chem.*, 2014, **12**, 3181-3190.
15. M. Dzwonek, D. Zalubiniak, P. Piatek, G. Cichowicz, S. Meczynska-Wielgosz, T. Stepkowski, M. Kruszewski, A. Wieckowska and R. Bilewicz, *RSC Adv.*, 2018, **8**, 14947-14957.
16. S. G. Konig and R. Kramer, *Chem. Eur. J.*, 2017, **23**, 9306-9312.
17. M. Rutnakornpituk, N. Puangsin, P. Theamdee, B. Rutnakornpituk and U. Wichai, *Polymer*, 2011, **52**, 987-995.
18. Q. S. Chen, X. J. Meng, P. McQuade, D. Rubins, S. A. Lin, Z. Z. Zeng, H. Haley, P. Miller, D. G. Trotter and P. S. Low, *Mol. Pharmaceutics*, 2017, **14**, 4353-4361.
19. S. A. Kularatne, M. J. Belanger, X. J. Meng, B. M. Connolly, A. Vanko, D. L. Suresch, I. Guenther, S. B. Wang, P. S. Low, P. McQuade and D. G. Trotter, *Mol. Pharmaceutics*, 2013, **10**, 3103-3111.

20. A. Yamaguchi, Y. Anami, S. Y. Y. Ha, T. J. Roeder, W. Xiong, J. Lee, N. T. Ueno, N. Y. Zhang, Z. Q. An and K. Tsuchikama, *Bioorg. Med. Chem.*, 2021, **32**, DOI: 10.1016/j.bmc.2021.116013.
21. L. N. Goswami, Z. H. Houston, S. J. Sarma, S. S. Jalisatgi and M. F. Hawthorne, *Org. Biomol. Chem.*, 2013, **11**, 1116-1126.
22. A. Kohata, P. K. Hashim, K. Okuro and T. Aida, *J. Am. Chem. Soc.*, 2019, **141**, 2862-2866.
23. M. R. Ke, S. L. Yeung, D. K. P. Ng, W. P. Fong and P. C. Lo, *J. Med. Chem.*, 2013, **56**, 8475-8483.
24. T. Legigan, J. Clarhaut, I. Tranoy-Opalinski, A. Monvoisin, B. Renoux, M. Thomas, A. Le Pape, S. Lerondel and S. Papot, *Angew. Chem. Int. Ed.*, 2012, **51**, 11606-11610.
25. V. Hong, S. I. Presolski, C. Ma and M. G. Finn, *Angew. Chem. Int. Ed.*, 2009, **48**, 9879-9883.
26. W. Pham, Z. Medarova and A. Moore, *Bioconjugate Chem.*, 2005, **16**, 735-740.
27. R. B. Mujumdar, L. A. Ernst, S. R. Mujumdar, C. J. Lewis and A. S. Waggoner, *Bioconjugate Chem.*, 1993, **4**, 105-111.
28. H. W. An, S. L. Qiao, C. Y. Hou, Y. X. Lin, L. L. Li, H. Y. Xie, Y. Wang, L. Wang and H. Wang, *Chem. Commun.*, 2015, **51**, 13488-13491.
29. N. Sim, S. Gottschalk, R. Pal, M. Delbianco, O. Degtyaruk, D. Razansky, G. G. Westmeyer, V. Ntziachristos, D. Parker and A. Mishra, *Chem. Commun.*, 2015, **51**, 15149-15152.
30. H. Lee, J. C. Mason and S. Achilefu, *J. Org. Chem.*, 2006, **71**, 7862-7865.

A. Appendix - HPLC conditions

HPLC was performed using a MilliQ® water (Milipore, Merck) and HPLC-grade solvents were used. Temperature used for HPLC was ambient unless otherwise stated. Sample diluent was H_2O/MeCN (95: 5) unless otherwise state at a concentration of 50-100 mg/mL and filtered (nylon, 0.45 µm).

Waters HPLC:

Waters Autopurification system, equipped with an ACQUITY QDa performance mass spectrometer and UV-Vis absorption spectrometer. UV-Vis absorption were acquired on the HPLC.

Analytical HPLC:Samples were injected in 5 µL aliquots using either Sunfire® C_{18} column (5µm, 4.6 × 150 mm) with a flow rate of 1 mL/min, or Waters X-bridge® C_{18} column (5 µm, 4.6 mm × 50 mm) with a flow rate of 1 mL/min and an injection loop of 0.02 mL.

Semi-preparative HPLC was performed with the Sunfire® Prep C_{18} OBD™ column (5µm, 19 mm × 150 mm), an injection loop of 1 mL and a flow rate of between 10-25 mL/min; or with the X-bridge® BEH C_{18} OBD™ Prep Column, 130 Å (5µm, 19 mm × 100 mm). Samples were injected in 750 µL aliquots with mass or wavelength-directed purification.

Agilent HPLC:

An Agilent 1260 Infinity II system fitted with a G7157A autosampler, G1364 E 1260 FC-PS (fraction collector), G7114A 1260 VWD with an injection loop of 5 mL and a flow rate of between 10-25 mL/min. Semi-preparative HPLC was performed using the X-bridge® BEH C_{18} OBD™ Prep Column, 130 Å (5µm, 19 mm × 100 mm) or Agilent Prep Column C18, 100 Å (5µm, 21.2 mm × 50 mm).

External HPLC purification:

Compounds that were purified externally were performed by staff at GSK. Instruments for preparative HPLC included: Waters ‘Silver’ MDAP, Waters ‘Platinum’ MDAP and Waters ‘Scarlet’ MDAP. The following preparative columns were used: XBridge BEH C18 OBD Prep Column (5µm, 150 x 30 mm), Zorbax SB-Phenyl (5 µm, 150 mm × 30 mm), CSH C18 (5µm, 150 × 30 mm) and CSH Fluoro-Phenyl (5µm, 150 × 30 mm).

Instruments for analytical HPLC included: Shimadzu 'Achiral Toolbox' UHPLC-MS and Waters 'Purple' XEVO UPLC-QTOF-MS. The following analytical columns were used: BEH C18 (1.7µm, 30 mm × 2.1 mm), Zorbax Phenyl (3.5 µm, 30 mm × 2.1 mm), Acquity UPLC CSH C18 (1.7µm, 100 mm × 2.1 mm) and CSH Fluorophenyl (1.7 µm, 50 mm × 2.1 mm).

A.1 HPLC conditions method 1

Instrument name: Agilent

Column: Agilent Prep Column C18, 100 Å (5µm, 21.2 mm × 50 mm)

Mobile phase A: H_2O + 0.1% v/v formic acid

Mobile phase B: MeCN + 0.1% v/v formic acid

Injection Volume: varied volume, typically 750 µL

Collection Mode: UV (DAD)

Time (min)	%A	%B	Flow rate (mL/min)
0.0	95	5	25
1.0	95	5	25
10.0	5	95	25
14.9	5	95	25
15.0	95	5	25

A.2 HPLC conditions method 2

Instrument name: Waters or Agilent

Column: XBridge BEH C18 OBD Prep Column, 130Å (5 µm, 19 mm × 100 mm)

Mobile phase A: H_2O + 50 µL/L NH_4OH;

Mobile phase B: MeCN + 50 µL/L NH_4OH

Injection Volume: varied volume, typically 750 µL

Collection Mode: UV (DAD) (Agilent/Waters) and/or MS(+/-) (Waters)

Time(min)	A%	B%	Flow rate (mL/min)
0.0	95	5	25
2.0	95	5	25
12.0	60	40	25
13.5	5	95	25
14.0	5	95	25
14.5	95	5	25
15.0	95	5	25

A.3 HPLC conditions method 3

62 mg of sample was dissolved in 4.53 mL DMSO.

Instrument Name: Waters 'Silver' MDAP

Column: XBridge BEH C18 OBD Prep Column, (5µm, 150 × 30 mm)

Mobile phase A: H_2O + 0.1% formic acid

Mobile phase B: MeOH

Injection Volume: varied volume, typically 700 µL

Collection Mode: UV (DAD) and/or MS(+/-)

The gradient was delivered by two pumps in order to use at-column dilution when injecting the sample. The gradient program used for the purification is summarised below:

Chromatographic Pump			**Regeneration Pump**			
Time (mins)	**%B**	**Flow Rate (mL/min)**	**Time (mins)**	**%B**	**Flow Rate (mL/min)**	**Total flow rate (mL/min)**
0.0	15	4	0.0	10	36	40
4.0	15	4	4.0	10	36	40
4.5	15	20	4.5	15	20	40
16.0	45	20	16.0	45	20	40
16.5	60	20	16.5	60	20	40
16.6	100	20	16.6	100	20	40
19.0	100	20	19.0	100	20	40

Analytical Method Details

Instrument Name: Shimadzu 'Achiral Toolbox' UHPLC-MS

Column: BEH C18 (1.7µm, 30 mm × 2.1 mm)

Mobile phase A: H_2O + 0.1% Formic acid

Mobile phase B: MeOH

Temperature (°C): 30

Sample Diluent: DMSO

Injection Volume (µL): 0.5

Time (mins)	%A	%B	Flow rate (mL/min)
0.00	99	1	0.8
2.35	5	95	0.8
2.75	5	95	0.8
2.85	5	95	0.8
3.50	99	1	0.8

A.4 HPLC conditions method 4

85 mg of sample was dissolved in 4.53 mL DMSO.

Instrument Name: Waters 'Silver' MDAP

Column: XBridge BEH C18 OBD Prep Column, (5µm, 150 × 30 mm)

Mobile phase A: H_2O + 0.1% v/v formic acid

Mobile phase B: MeOH

Injection Volume: varied volume, typically 500 µL

The gradient was delivered by two pumps in order to use at-column dilution when injecting the sample.

The gradient program used for the purification is summarised below:

Chromatographic Pump			Regeneration Pump			
Time (mins)	**%B**	**Flow Rate (mL/min)**	**Time (mins)**	**%B**	**Flow Rate (mL/min)**	**Total Flow rate (mL/min)**
0.0	15	4	0.0	5	36	40
4.0	15	4	4.0	5	36	40
4.5	15	20	4.5	15	20	40
16.0	45	20	16.0	45	20	40
16.5	60	20	16.5	60	20	40
16.6	100	20	16.6	100	20	40
19.0	100	20	19.0	100	20	40

Analytical Method Details

Instrument Name: Shimadzu 'Achiral Toolbox' UHPLC-MS

Column: BEH C18 (1.7 µm, 30 mm × 2.1 mm)

Mobile phase A: H_2O + 0.1% v/v formic acid

Mobile phase B: MeOH

Temperature (°C): 30

Sample Diluent: DMSO

Injection Volume (µL): 0.5

Time (mins)	%A	%B	Flow Rate (mL/min)
0.00	1	1	0.8
2.35	95	95	0.8
2.75	95	95	0.8
2.85	95	95	0.8
3.50	1	1	0.8

A.5 HPLC conditions method 5

Instruments: Waters or Agilent

Column: XBridge BEH C18 OBD Prep Column, 130Å (5 µm, 19 mm × 100 mm)

Mobile phase A: H_2O + 50 µL/L NH_4OH

Mobile phase B: MeCN + 50 µL/L NH_4OH

Collection Mode: UV (DAD) (Agilent) and/or MS(+/-) (Water)

Time (min)	A %	B %	Flow (mL/min)
0.0	95	5	25
5.0	50	50	25
5.5	5	95	25
6.5	5	95	25
9.0	95	5	25
10.0	95	5	25

A.6 HPLC conditions method 6

Instrument: Waters

Column: Sunfire Prep C18 OBD column (5µm, 19 mm × 150 mm)

Mobile phase A: H_2O + 0.1% v/v formic acid;

Mobile phase B: MeOH + 0.1 % v/v formic acid

Collection Mode: UV (DAD) and/or MS(+/-)

Time(min)	A%	%B	Flow rate (mL/min)
0.0	95	5	10
1.0	90	10	10
8.0	25	75	10
8.9	5	95	10
9.0	95	5	10
30.0	95	5	10

A.7 HPLC conditions method 7

120 mg of sample was dissolved in 11.7 mL DMSO: water: MeOH (1:1:1)

Instrument name: Waters 'Silver' MDAP

Column: Zorbax SB-Phenyl (5 µm, 150 mm × 30 mm)

Mobile phase A: H_2O + 0.1% v/v TFA acid

Mobile phase B: MeOH

Injection Volume: varied volume, typically 2000 µL

Collection Mode: Fractionation by MS(+/-)

The gradient was delivered by two pumps in order to use at-column dilution when injecting the sample. The gradient program used for the program is summarised below:

Chromatographic Pump:			**Regeneration Pump:**			
Time (mins)	**%B**	**Flow rate (ml/min)**	**Time (mins)**	**%B**	**Flow rate (mL/min)**	**Total Flow rate (mL/min)**
0.0	30	4	0.0	20	36	40
4.0	30	4	4.0	20	36	40
4.5	30	20	4.5	30	20	40
16.0	55	20	16.0	55	20	40
16.5	80	20	16.5	80	20	40
16.6	100	20	16.6	100	20	40
19.0	100	20	19.0	100	20	40

Analytical Method Details

Instrument name: Shimadzu 'Achiral Toolbox' UHPLC-MS

Column: Zorbax Phenyl (3.5 μm, 30 mm × 2.1 mm)

Mobile phase A: H_2O + 0.1% v/v TFA acid

Mobile phase B: MeOH

Temperature (°C): 30

Sample diluent: DMSO

Injection volume (μL): 0.5

Flow rate (mL/min): 1.1 (raised 1.8 between 4.71 and 5.39 min)

Time (mins)	**%A**	**%B**
0.00	100	0
4.70	0	100
5.40	0	100
5.45	100	0
5.60	100	0

A.8 HPLC conditions method 8

Purification step 1:

156 mg of sample (from $CuSO_4 \cdot 5H_2O$) was dissolved in 7 mL DMSO.

107 mg of sample (from $(CuOTf)_2 \cdot C_6H_6$) was dissolved in 5 mL DMSO.

Instrument Name: Waters 'Platinum' MDAP

Column: CSH C18 (5μm, 150 × 30 mm)

Mobile Phase A: H_2O + 0.1% v/v formic acid

Mobile Phase B: MeCN + 0.1% v/v formic Acid

Injection Volume: 1500 μL

Collection Mode: Fractionation by MS(+)

The gradient was delivered by two pumps in order to use at-column dilution when injecting the sample. The gradient program used for the purification is summarised below:

Chromatographic Pump:			**Regeneration Pump:**			
Time (mins)	**%B**	**Flow rate (ml/min)**	**Time (mins)**	**%B**	**Flow rate (mL/min)**	**Total Flow rate (mL/min)**
0.0	3	4	0.0	0	36	40
4.0	3	4	4.0	0	36	40
4.5	3	20	4.5	3	20	40
16.0	30	20	16.0	30	20	40
16.5	75	20	16.5	75	20	40
16.6	100	20	16.6	100	20	40
19.0	100	20	19.0	100	20	40

Analytical Method Details

Instrument Name: Waters 'Purple' XEVO UPLC-QTOF-MS

Column: Acquity UPLC CSH C18 (1.7μm, 100 mm × 2.1 mm)

Mobile phase A: H_2O + 0.1% v/v formic acid

Mobile phase B: MeCN + 0.1% v/v formic Acid

Temperature (°C): 50

Sample Diluent: DMSO

Injection Volume (µL): 0.2

Times (mins)	%A	%B	Flow rate (mL/min)
0	97	3	0.8
0.2	97	3	0.8
18.0	0	100	0.8
19.0	5	95	0.8
20.0	97	3	0.8

Purification Step 2:

54.6 mg of sample was dissolved in 3 mL DMSO.

Instrument Name: Waters 'Platinum' MDAP

Column: CSH Fluoro-Phenyl (5µm, 150 × 30 mm)

Mobile phase A: H_2O + 0.1% v/v formic acid

Mobile phase B: MeCN + 0.1% v/v formic Acid

Injection Volume: 720 µL

The gradient was delivered by two pumps in order to use at-column dilution when injecting the sample. The gradient program used for the purification is summarised below:

Chromatographic Pump:			**Regeneration Pump:**			
Time (mins)	**%B**	**Flow rate (mL/min)**	**Time (mins)**	**%B**	**Flow rate (mL/min)**	**Total Flow rate (mL/min)**
0.0	10	4	0	3	36	40
4.0	10	4	4	3	36	40
4.5	10	20	4.5	10	20	40
16.0	40	20	16	40	20	40
16.5	75	20	16.5	75	20	40
16.6	100	20	16.6	100	20	40
19.0	100	20	19	100	20	40

Analytical Method Details

Instrument Name: Shimadzu 'Achiral Toolbox' UHPLC-MS

Column: CSH Fluorophenyl (1.7 μm, 50 mm × 2.1 mm)

Temperature (°C): 30

Mobile phase A: H_2O + 0.1% v/v formic acid

Mobile phase B: MeCN

Sample Diluent: DMSO

Injection Volume (μL): 0.5

Times (mins)	%A	%B	Flow rate (mL/min)
0.00	97	3	0.8
2.35	5	95	0.8
2.75	5	95	0.8
2.85	97	3	0.8
3.50	97	3	0.8

A.9 HPLC conditions method 9

254 mg of sample was dissolved in 12 mL DMSO:H_2O 2:10.

Instrument Name: Waters 'Scarlet' MDAP

Column: XBridge BEH C18 OBD Prep Column (5μm, 150 × 30 mm)

Mobile Phase A: H_2O + 0.1% v/v formic acid

Mobile Phase B: MeOH

Injection Volume: 1000 μL

Time (mins)	%A	%B	Flow Rate (mL/min)
0.0	90	10	40
4.0	90	10	40
4.5	90	10	40
16.0	50	50	40
16.5	40	60	40
16.6	0	100	40
19.0	0	100	40

Analytical Method Details

Instrument Name: Shimadzu 'Achiral Toolbox' UHPLC-MS

Column: BEH C18 (1.7µm, 30 mm × 2.1 mm)

Mobile phase A: H_2O + 0.1% v/v formic acid

Mobile phase B: MeOH

Temperature (°C): 30

Sample Diluent: Crude Analysis: DMSO, Post Prep Analysis: DMSO/H_2O (1:1)

Injection Volume (µL): 0.5

Time (mins)	%B	Flow Rate (mL/min)
0.00	1	0.8
2.35	95	0.8
2.75	95	0.8
2.85	95	0.8
3.50	1	0.8

A.10 HPLC conditions method 10

170 mg of sample was dissolved in 2.55 mL DMSO (Method 1: Tb-DOTA-DBCO clicked to FA-PEG_5-N_3).

170 mg of sample was dissolved in 3.2 mL DMSO (Method 2: Tb-complexation of DOTA-DBCO clicked to FA-PEG_5-N_3).

Instrument Name: Waters 'Silver' MDAP

Column: XBridge BEH C18 OBD Prep Column (5µm, 150 × 30 mm)

Mobile Phase A: H_2O + 0.1% v/v formic acid

Mobile Phase B: MeOH

Injection Volume: varied volume, typically 500 µL

Collection Mode: UV (DAD) and MS(+/-)

The gradient was delivered by two pumps in order to use at-column dilution when injecting the sample. The gradient program used for the purification is summarised below:

Chromatographic Pump			Regeneration Pump			
Time (mins)	**%B**	**Flow Rate (mL/min)**	**Time (mins)**	**%B**	**Flow Rate (mL/min)**	**Total Flow rate (mL/min)**
0.0	25	4	0	15	36	40
4.0	25	4	4	15	36	40
4.5	25	20	4.5	25	20	40
16.0	60	20	16	60	20	40
16.5	80	20	16.5	80	20	40
16.6	100	20	16.6	100	20	40
100.0	100	20	100	100	20	40

Analytical Method Details

Instrument Name: Shimadzu 'Achiral Toolbox' UHPLC-MS

Column: BEH C18 (1.7µm, 30 mm × 2.1 mm)

Mobile phase A: H_2O + 0.1% v/v formic acid

Mobile phase B: MeOH

Temperature (°C): 30

Sample Diluent: DMSO

Injection Volume (µL): 0.5

Time (mins)	%A	%B	Flow rate (mL/min)
0	99	1	0.8
2.35	5	95	0.8
2.75	5	95	0.8
2.85	5	95	0.8
3.5	99	1	0.8

A.11 HPLC conditions method 11

Instrument name: Waters

Column: Sunfire Prep C18 OBD column (5µm, 19 mm × 150 mm)

Mobile Phase A: H_2O + 0.1 % v/v TFA

Mobile phase B: MeOH + 0.1 % TFA

Collection Mode: MS(+/-)

Time (min)	A%	B%	Flow (mL/min)
0.0	95	5	20
1.0	95	5	20
16.0	40	60	20
17.0	5	95	20
19.0	5	95	20
19.5	95	5	20
20.0	95	5	20

Analytical Method Details

Instrument name: Waters

Column: Sunfire C18 column (5µm, 4.6 × 150 mm)

Mobile Phase A: H_2O + 0.1 % v/v TFA

Mobile phase B: MeOH + 0.1 % TFA

Time (min)	A%	B%	Flow (mL/min)
0.0	95	5	1.0
1.0	95	5	1.0
16.0	40	60	1.0
17.0	5	95	1.0
19.0	5	95	1.0
19.5	95	5	1.0
20.0	95	5	1.0

A.12 HPLC conditions method 12

Instrument name: Agilent

Column: XBridge BEH C18 OBD Prep Column, 130Å (5 µm, 19 mm × 100 mm)

Mobile phase A: H_2O + 0.1% v/v formic acid

Mobile phase B: MeOH + 0.1% v/v formic acid

Collection Mode: UV (DAD)

Time (mins)	A%	B%	Flow rate (mL/min)
0.0	95	5	25
1.0	95	5	25
16.0	5	95	25
18.0	5	95	25
19.0	95	5	25
20.0	95	5	25